In compliance with the
Canadian Privacy Legislation
some supporting forms
may have been removed from
this dissertation.

While these forms may be included
in the document page count,
their removal does not represent
any loss of content from the dissertation.

University of Alberta

# Eulerian-Lagrangian Model of Turbulent Mixing for Silver Halide Precipitation

by

Gary L. Anthieren ©

A thesis submitted to the Faculty of Graduate Studies and Research in partial fulfillment of the requirements for the degree of Master of Science
in
Chemical Engineering

Department of Chemical and Materials Engineering

Edmonton, Alberta
Fall 2003

National Library
of Canada

Acquisitions and
Bibliographic Services

395 Wellington Street
Ottawa ON K1A 0N4
Canada

Bibliothèque nationale
du Canada

Acquisisitons et
services bibliographiques

395, rue Wellington
Ottawa ON K1A 0N4
Canada

*Your file Votre référence*
*ISBN: 0-612-87711-6*
*Our file Notre référence*
*ISBN: 0-612-87711-6*

The author has granted a non-exclusive licence allowing the National Library of Canada to reproduce, loan, distribute or sell copies of this thesis in microform, paper or electronic formats.

The author retains ownership of the copyright in this thesis. Neither the thesis nor substantial extracts from it may be printed or otherwise reproduced without the author's permission.

L'auteur a accordé une licence non exclusive permettant à la Bibliothèque nationale du Canada de reproduire, prêter, distribuer ou vendre des copies de cette thèse sous la forme de microfiche/film, de reproduction sur papier ou sur format électronique.

L'auteur conserve la propriété du droit d'auteur qui protège cette thèse. Ni la thèse ni des extraits substantiels de celle-ci ne doivent être imprimés ou aturement reproduits sans son autorisation.

Canada

**University of Alberta**

**Library Release Form**

**Name of Author:** Gary L. Anthieren

**Title of Thesis:** Eulerian-Lagrangian Model of Turbulent Mixing for Silver Halide Precipitation

**Degree:** Master of Science

**Year this Degree Granted:** 2003

Permission is hereby granted to the University of Alberta Library to reproduce single copies of this thesis and to lend or sell such copies for private, scholarly or scientific research purposes only.

The author reserves all other publication and other rights in association with the copyright in the thesis, and except as herein before provided, neither the thesis nor any substantial portion thereof may be printed or otherwise reproduced in any material form whatever without the author's prior written permission.

Date: Sept. 24 2003

## University of Alberta

## Faculty of Graduate Studies and Research

The undersigned certify that they have read, and recommend to the Faculty of Graduate Studies and Research for acceptance, a thesis entitled **Eulerian-Lagrangian Model of Turbulent Mixing for Silver Halide Precipitation** submitted by **Gary L. Anthieren** in partial fulfillment of the requirements for the degree of **Master of Science in Chemical Engineering**.

Dated by Supervisor: Sept 22, 2003

# Abstract

A fully mechanistic model was developed to simulate the turbulent mixing and crystallization of silver bromide in a semi-batch reactor. Instantaneous primary nucleation, multiple species thermodynamic equilibria, size-dependent growth kinetics, discretized population balances and accurate modeling of turbulent flow in a stirred tank are coupled for the first time in this model.

Preliminary model validation focused on predicting the crystal size distribution (CSD) of seeded and unseeded precipitations in the micro-mixing controlled regime. Difficulties in predicting the dissolution of nuclei using a geometric length scale led to the design of a novel symmetric geometric length scale. This significantly improved the model's ability to predict the CSD. Comparisons of the predicted and experimental CSD show excellent agreement for unimodal distributions when using the kinetic parameters measured by Wey and Strong (1977). The predicted and experimental CSD also show excellent agreement for unimodal and bimodal distributions when using the kinetic constant and physical properties optimized within known experimental ranges. In addition, the precipitation model has shown that excluding crystal growth from the highly supersaturated feed plume is an acceptable simplification and greatly decreases the computational time required by the model.

The model was experimentally validated for two impeller diameters, two feed concentrations, three feed pipe diameters and seven volumetric feed rates.

All experimental results were independent of feed pipe diameter. The experimental results provided clear evidence that precipitation results should be plotted against molar feed rate rather than volumetric feed rate as is usually done in the mixing literature. When nucleation was not limited by the local supply of halide, comparisons between the model predictions and experiments showed excellent agreement and revealed that the number of nuclei produced prior to stable crystal formation is the primary precipitation quantity affected by mixing. A new mixing limit was identified for cases where nucleation is limited by the local supply of halide. This is termed the convective-stoichiometric limit of mixing. It occurs for large molar feed rates and results in incomplete nucleation in the feed plume. Also, a precipitation scaling protocol based on constant power input per unit volume is used to investigate scale-up of the precipitation conditions used in this study.

# Acknowledgements

I am thankful to several people for their contributions, support and assistance during this project. First, my greatest thanks go to Dr. Suzanne Kresta, my supervisor at the University of Alberta, for her continual motivation and guidance in this project. Her insightful ideas and expertise helped make this project a success. I would also like to thank Dr. Katrin Parsiegla, my supervisor from the Eastman Kodak Company, for sharing her advice and knowledge. I am grateful to Katrin and her husband Carl for including me in their lives during my three month stay in Rochester, NY. Many nights out for dinner, trips to the hang gliding sight and sight seeing made my stay there enjoyable. As well, I would like to thank my colleagues in the mixing group, especially Vesselina and Sujit for their company while spending time in the office.

This study was made possible by financial contributions from the Eastman Kodak Company and the Natural Sciences and Engineering Research Council of Canada (NSERC). Financial assistance from the Department of Chemical Engineering and the University of Alberta in the form of assistantships and scholarships was also greatly appreciated.

Finally, my deepest appreciation and thanks go to my lovely wife Trish for her support and encouragement. Many times her smile, thoughtfulness, and positive attitude helped keep me motivated. My appreciation also extends to my parents, family and in-laws whose love and support brought me to where I am today.

## Table of Contents

Chapter 1 1

Introduction 1

**1.1 Crystallization Fundamentals** **2**
  *1.1.1 Precipitation Process* *3*
  *1.1.2 Supersaturation* *4*
  *1.1.3 Nucleation* *5*
    Primary Homogeneous Nucleation 6
    Primary Heterogeneous Nucleation 9
    Secondary Nucleation 9
  *1.1.4 Crystal Growth* *10*
    Diffusion-Reaction Theory 10
  *1.1.5 Agglomeration* *17*
  *1.1.6 Precipitation Techniques* *17*
    Double-jet Addition 18
**1.2 The Population Balance** **19**
  *1.2.1 Errors Associated with Discrete Crystal Growth* *20*
    State of the Population Balance 24
**1.3 Mixing Fundamentals** **25**
  *1.3.1 Turbulence* *26*
  *1.3.2 Different Scales of Mixing* *29*
**1.4 Models of Mixing** **34**
  *1.4.1 Micromixing Model* *34*
  *1.4.2 Mesomixing Models* *36*
    Turbulent Dispersion Mesomixing 37
    Inertial-Convective Mesomixing 37
**1.5 Stirred Tank Reactor** **38**
**1.6 Previous Models of Silver Halide Precipitation** **44**
**1.7 Conclusions** **47**

**Chapter 2** 49

**Model Development** 49

**2.1 Model Overview** 50
**2.2 Mixing Model** 52
- *2.2.1 Eulerian Flow Field Model (fixed frame)* 52
  - *Zone 1: Impeller Swept Volume* 55
  - *Zone 2: Impeller Discharge Stream* 55
  - *Zones 3 and 4: Wall Jets* 58
  - *Zones 5 and 9: Top Surface* 59
  - *Zones 6 and 10: Bottom Surface* 59
  - *Zones 7 and 8: Top and Bottom Returns to the Discharge Stream* 60
  - *Zones 11 and 12: Top and Bottom Returns to the Impeller Volume* 60
- *2.2.2 Coupling the Eulerian and Lagrangian Fields* 65
- *2.2.3 Lagrangian Mixing Model (moving frame)* 68

**2.3 Double-jet Addition Precipitation Model** 74
- *2.3.1 Complex Species Equilibria* 74
  - New Solution Strategy 78
- *2.3.2 Nucleation Model* 80
  - Implementing the Nucleation Model 81
- *2.3.3 Growth Model* 81
- *2.3.4 Crystal Population Balance* 82
  - Length Scale Discretization 83
  - New Discretization Method 83
  - Implementing the Population Balance 85
- *2.3.5 Material Balances* 87
- *2.3.6 Equation Solving Technique* 89

**2.4 Conclusions** 90

**Chapter 3** 91

**Precipitation Experiments** 91

**3.1 Introduction** 92
**3.2 Experimental Method and Conditions** 92
*3.2.1 Apparatus* 92
**3.3 Precipitation Conditions** 96
*3.3.1 Crystal Size Distribution* 97
Sampling 97
Measurement and Analysis 99
*3.3.2 Mixing Conditions* 105
**3.4 Micromixing Analysis** 108
*3.4.1 Seeded Experiments* 109
Precipitation Conditions 110
Results and Discussion 111
*3.4.2 Nucleation Experiments* 114
Precipitation Conditions 115
Results and Discussion 115
**3.5 Precipitation Model Validation** 119
*3.5.1 Seeded Precipitation Validation* 120
Parameter Optimization: Sensitivity Analysis 122
*3.5.2 Unseeded Precipitation Validation: Nucleation Model* 126
*3.5.3 Validation Summary* 131
**3.6 Modifications Made to the Precipitation Model** 132
**3.7 Conclusions** 133

Chapter 4 135

**Mesomixing Analysis: Experiments and Simulations** **135**

**4.1 Features of the Precipitation and Mixing Processes** **136**

*4.1.1 Application to Double-jet Precipitations* *137*

**4.2 Ideal Double-jet Precipitations** **144**

**4.3 Mesomixing Analysis** **146**

*4.3.1 Variable Feed Rate Experiments* *147*

Precipitation Conditions 147

Repeatability 149

Results and Discussion 149

*4.3.2 Variable Feed Pipe Diameter Experiments* *154*

**4.4 Model Prediction** **158**

*4.4.1 Deviation from Ideal Double-jet Precipitations* *160*

*4.4.2 Correlation with Molar Feed Rate* *161*

Lagrangian Mixing Description 162

**4.5 Mixing Effects on Double-jet Precipitations** **165**

*4.5.1 Mixing Rate* *165*

*4.5.2 Convective-Stoichiometric Limited Mixing* *167*

**4.6 Precipitation Scale-up Protocol** **168**

**4.7 Conclusions** **171**

**References** **174**

Appendix A: Length Scale and Population Balance Discretization 181

Appendix B: Complete Experimental and Simulated Results 204

Appendix C: Data Treatment and Statistical Transformations 252

Appendix D: Logic Diagrams for PreSim.V50 Source Code 266

Appendix E: Analytical Solutions for the Population Balance Equation 317

## List of Tables

Table 1.1 Summary: Evaluation of various population balance methods. 25
Table 1.2 Dimensions of the stirred tank reactor. 39
Table 1.3 Summary: Key model equations. 48
Table 2.1 Definition and associated equations for the Eulerian Flow Field Model. 61
Table 2.2 Eulerian Flow Field Model for the kettle geometry used in this study (Rushton turbine, T = 0.2 m, $H_o$ = T/2, D = T/4, N = 16.7 rps). 63
Table 2.3 Least squares regression coefficients used to describe the silver and halide activities. 79
Table 3.1 Minimum, maximum and selected impeller rotational speeds. 107
Table 3.2 Hydrodynamic quantities. 107
Table 3.3 Characteristic mixing time constants. 108
Table 3.4 Minimum required feed rate for turbulent dispersion mesomixing. 108
Table 3.5 Estimated silver halide consumption by seed crystals at renucleation. 110
Table 3.6 Summary: Mixing Conditions - Seeded experiments. 111
Table 3.7 Summary: Mixing Conditions - Nucleation experiments. 115
Table 3.8 Summary: Kinetic parameters and physical properties used in the precipitation model. Parameter sets are given in order of decreasing ability to predict unimodal crystal distributions. 132
Table 4.1 Periods of the Double-jet Precipitation Process. 139
Table 4.2 Summary: Mesomixing Conditions - Variable feed rate experiments. 148
Table 4.3 Summary: Mesomixing Conditions - Variable feed pipe diameter experiments I. 155
Table 4.4 Summary: Mesomixing Conditions - Variable feed pipe diameter experiments II. 156

Table 4.5 Index of mixing limitations on the precipitation products for various molar feed rates. 171

## List of Figures

| | | |
|---|---|---|
| Figure 1.1 | Supersaturation profile during the three stages of the precipitation process. | 4 |
| Figure 1.2 | Nucleation terminology (Mullin 2001). | 6 |
| Figure 1.3 | Interaction of volume and surface free energy change for homogeneous primary nucleation (Mullin 2001). | 8 |
| Figure 1.4 | Schematic of the driving forces involved in the surface integration-diffusion growth process (Mullin 2001). | 11 |
| Figure 1.5 | Crystal growth rate expression combing bulk diffusion and surface integration (Wey and Strong 1977a). | 13 |
| Figure 1.6 | Crystal growth rate expression combing bulk diffusion, surface integration and crystal size solubility. | 15 |
| Figure 1.7 | The relationship between particle size and solubility (Mullin 2001). | 16 |
| Figure 1.8 | Possibilities for introducing reactant streams to a precipitation vessel (Mullin 2001). (a) Single-jet surface addition, (b) Single-jet impeller addition, (c) Double-jet surface addition, and (d) Premixed impeller addition. | 18 |
| Figure 1.9 | Discretization of the crystal size distribution with crystal length as the internal coordinate. | 21 |
| Figure 1.10 | Kinetic energy spectrum E and concentration fluctuation spectrum $E_c$ of turbulence. | 27 |
| Figure 1.11 | Schematic representation of radial turbulent dispersion of a feed stream (reproduced from Baldyga and Bourne 1999). | 31 |
| Figure 1.12 | A schematic representation of the inertial-convective disintegration of a fluid element in series with micromixing (reproduced from Baldyga and Bourne 1999). | 32 |
| Figure 1.13 | The stirred tank reactor equipped with a radial pumping, six-bladed Rushton turbine. | 39 |

Figure 1.14 CFD simulated flow field for a Ruston turbine with T = 2 m, D = T/3, C = T/4, and N = 10.5 rps. (a) $H_o$ = T/2, and (b) $H_f$ = T 41

Figure 1.15 Decay of dimensionless radial velocity on impeller centerline: for D = T/3. (data from Kresta and Wood, 1991) 42

Figure 1.16 Decay of dimensionless turbulence kinetic energy on impeller centerline. (data from Kresta and Wood, 1991) 43

Figure 1.17 Decay of dimensionless turbulence kinetic energy dissipation on impeller centerline. (data from Kresta and Wood, 1991) 44

Figure 2.1 A brief outline of the logic used in the precipitation model. 51

Figure 2.2 Circulation pattern for a fully baffled stirred tank reactor with a Rushton turbine divided into zones of similar hydrodynamic properties (D = T/3, C = T/4). a) Initial fill height of $H_o$ = T/2, b) Final fill height of $H_f$ = T. 54

Figure 2.3 Comparison of predicted and experimental decay of maximum dimensionless velocity on the impeller centerline (data taken from Kresta and Wood 1991). 56

Figure 2.4 Comparison of predicted and experimental decay of maximum dimensionless turbulent kinetic energy dissipation on the impeller centerline (data taken from Kresta and Wood 1991). 57

Figure 2.5 Comparison of predicted and experimental decay of maximum dimensionless turbulent kinetic energy on the impeller centerline (data taken from Kresta and Wood 1991). 58

Figure 2.6 Lagrangian path of a discrete feed volume (DFV). a) Entering at the impeller tip, b) Dividing and entering the wall jets, c) Exiting the wall jets, d) Dividing and entering the return streams, d) Terminating due to re-entering the impeller discharge stream, e) Terminating due to entering the impeller swept volume. 66

Figure 2.7 Modified Lagrangian path of a discrete feed volume (DFV). a) Entering at the top surface, b) Traveling downwards and then terminating due to entering the impeller discharge stream. 67

Figure 2.8 Dotted boundaries illustrate the immediate local surrounding solution available to mix with each discrete feed volume (DFV). 68

Figure 2.9 Inertial-convective mesomixing process. Mesomixing limits the volume of fluid at a relevant concentration scale (dashed boundaries) to a fraction of the maximum potential volume (dotted boundaries) available for micromixing to proceed in. 72

Figure 2.10 Radial and axial discretization of the feed plume for turbulent dispersion mesomixing. Mean volume fraction radii ($r_{a,i}$) are used to describe the rate of expansion for each ring. 72

Figure 2.11 Local micro- and mesomixed volume growth for each mixing model invoked under identical turbulence conditions ($Q_{feed} = 7.5\text{x}10^{-7}$ m$^3$/s, $Q_{zone} = 1.5\text{x}10^{-3}$ m$^3$/s, $U_{zone} = 0.085$ m/s, $\varepsilon = 1.0$ W/kg, $k = 0.1$ J/kg). a) Micromixing controlled, b) Micromixing limited by inertial-convective mesomixing, c) and d) Micromixing limited by turbulent dispersion mesomixing modeled using 1 and 3 integration rings, respectively. 73

Figure 2.12 Agreement of the thermodynamic equilibrium model with published data. 77

Figure 2.13 Comparison of calculated and approximated activities showing the deviation when in excess by less than 0.0002 mol/L. a) and b) Silver activity, and c) and d) Bromide activity. (b) and (d) are expanded scales. 79

Figure 2.14 Percent error in the approximated activities becomes unacceptable when in excess by less than 0.0002mol/L. a) Excess silver, and b) Excess halide. 80

Figure 2.15 Possible length scale discretization methods. a) Linear discretization illustrating low resolution of small crystal sizes and high resolution of large crystal sizes, b) Geometric discretization illustrating adequate resolution for all sizes but not extending to zero, and c) Symmetric geometric discretization illustrating adequate resolution for all sizes with the highest resolution at the point of symmetry ($L_{Ps}$) and extending to zero. 84

Figure 2.16 Agreement of the population balance method of Hounslow et al. (1988) modified for use with a symmetric geometric length scale with analytical solutions for typical conditions ($\mu$ = 0.117 $\mu$m, $\sigma$ = 0.021 $\mu$m, G = 4.0 Å/s, $L_{Ps}$ = 0.00435 $\mu$m, $L_P$ = 2.0 $\mu$m, P = 200).87

Figure 3.1 Experimental apparatus used for the Balanced Double-Jet precipitation. (1) Constant temperature bath, (2) Reaction kettle, (3) Impeller and drive, (4) Initial fill height, (5) Final fill height. 93

Figure 3.2 Experimental apparatus used for monitoring and controlling the precipitation. (1) Temperature probe, (2) Ag/AgBr electrode, (3) Ag/AgCl reference electrode, (4) pH probe, (5) Feed plume path. 94

Figure 3.3 Feed addition points for the precipitation. (a) Impeller feed, (b) Surface feed, and (c) Detail of feed pipe design. 95

Figure 3.4 Example electron micrographs used in the Ultrafine Electron Image Analysis (EIA). a) Magnification of 2000x, b) Magnification of 6700x. 100

Figure 3.5a Comparison of identical crystal size distributions ($\mu$ = 0.10 $\mu$m, $\sigma$ = 0.01 $\mu$m), for total crystal counts of $1\times10^9$, $2\times10^9$ and $2\times10^9$, with size intervals of 2.5 and 5.0, and 0.025L nm, respectively. 102

Figure 3.5b Comparison of identical normalized crystal size distributions ($\mu$ = 0.10 $\mu$m, $\sigma$ = 0.01 $\mu$m), for total crystal counts of $1\times10^9$, $2\times10^9$ and $2\times10^9$, with size intervals of 2.5 and 5.0, and 0.025L nm, respectively. 103

Figure 3.5c Comparison of identical normalized crystal density functions ($\mu$ = 0.10 $\mu$m, $\sigma$ = 0.01 $\mu$m), for total crystal counts of $1\times10^9$, $2\times10^9$ and $2\times10^9$, with size intervals of 2.5 and 5.0, and 0.025L nm, respectively. 104

Figure 3.6 Comparison of Electron Image Analysis Measurements for Two Identical Samples. 105

Figure 3.7 CSD time evolution for Seeded Micromixing Analysis - MM12. 112
Figure 3.8 Comparison of CSD time evolutions for the same seed distribution under identical mixing conditions. 113
Figure 3.9 Comparison of CSD time evolutions for the same seed distribution but under different mixing conditions. 114
Figure 3.10 CSD time evolution for Nucleated Micromixing Analysis - MM14. 116
Figure 3.11 Comparison of CSD time evolutions for the same nucleation conditions under identical mixing conditions. 117
Figure 3.12 Comparison of CSD time evolutions for the same nucleation conditions but under identical mixing conditions. 118
Figure 3.13 Comparison of CSD time evolutions for nucleation under different mixing conditions. 119
Figure 3.14 Satisfactory agreement between the model predictions and experimental results for the bimodal seed crystal distribution (MM12) validates the thermodynamic equilibrium, material balances and population balances. 121
Figure 3.15 Increased agreement between the model predictions and experimental results for the pseudo-unimodal seed crystal distribution (MM14R, t > 3 minutes) validates the growth kinetics measured by Wey and Strong (1977a) for unimodal distributions larger than 0.047 μm. 122
Figure 3.16 Cumulative error in the model predictions for the bimodal seed distribution at an interfacial tension of 0.11 N/m. 124
Figure 3.17 Cumulative error in the model predictions for the pseudo-unimodal seed distribution at an interfacial tension of 0.11 N/m. 124
Figure 3.18 Excellent agreement of the model predictions and experimental results using the optimized parameters. 125
Figure 3.19 Excellent agreement of the model predictions and experimental results using the optimized parameters. 125

Figure 3.20 Agreement of the model predictions and experimental results for the nucleation event using the original parameters and a critical supersaturation of 3.7 (first sample error = 0.13). 127

Figure 3.21 Agreement of the model predictions and experimental results for the nucleation event using the optimized parameters and a critical supersaturation of 2.1 (first sample error = 0.44). 128

Figure 3.22 Excellent agreement of the model predictions and mean crystal length at 6 minutes for various feed rates using the original parameters. 129

Figure 3.23 Agreement of the model predictions and mean crystal length at 6 minutes for various feed rates using the optimized parameters. 129

Figure 3.24 Poor agreement of the model predictions and population variance at 6 minutes for various feed rates using the original parameters. 130

Figure 3.25 Poor agreement of the model predictions and population variance at 6 minutes for various feed rates using the optimized parameters. 130

Figure 4.1 Supersaturation and stable crystal count during the periods of the double-jet precipitation process. a) Dissolution period ($<t_1$), b) Nucleation period ($t_1$ to $t_2$), c) Transient period ($t_2$ to $t_3$), and d) Growth period ($>t_3$). 141

Figure 4.2 Formation of the stable crystal population during the periods of the double-jet precipitation process. As the supersaturation in the kettle changes, the critical crystal length varies about the constant nuclei length. a) Dissolution period - all nuclei are unstable and dissolve ($L_N < L_C$), b) Nucleation period - newly formed nuclei are stable and grow, while all previously formed nuclei are unstable and continue to dissolve ($L_N > L_C$), c) Transient Period - excess nuclei previously formed become unstable and dissolve, while stable crystals continue to grow($L_N < L_C$), and d) Growth period - nuclei are unstable and dissolve rapidly, while stable crystals continue to grow ($L_N << L_C$). 142

Figure 4.3 Relationship between growth of the mixing plume volume fraction and the resulting nucleation rate normalized by the ideal nucleation rate. a) Slow mixing and b) Fast mixing. The end of the dissolution period is denoted $t_d$ and occurs later for slow mixing. 144

Figure 4.4 Effect of molar addition rate on the stable number of crystals at the end of the nucleation period and on the number of dissolving nuclei at the end of the dissolution period for ideal mixing conditions. 145

Figure 4.5 Dependence of mean crystal length on molar feed rate for ideal double-jet precipitations at a precipitation time of 6 minutes. 146

Figure 4.6 Comparison of micromixing controlled (MM14, MM16, Qs4.02) and mesomixing controlled crystal size distributions. 149

Figure 4.7 Variation in mean crystal length for two feed concentrations over a range of volumetric feed rates at a sample time of 6 minutes. 150

Figure 4.8 Variation in mean crystal length for two feed concentrations over a range of molar feed rates at a sample time of 6 minutes. 151

Figure 4.9 Variation in mean crystal length for two feed concentrations over a range of molar feed rates at a sample time of 6 minutes (linear-log scale). 152

Figure 4.10 Variation in coefficient of variation for two feed concentrations over a range of molar feed rates at a sample time of 6 minutes. 153

Figure 4.11 Variation in total crystal count for two feed concentrations over a range of molar feed rates. 154

Figure 4.12 Comparison of CSD time evolutions for feed pipe diameters of 0.8 and 4.8 mm, and a feed rate of 115.38 ml/min. 156

Figure 4.13 Comparison of CSD time evolutions for feed pipe diameters of 0.8 and 4.8 mm, and a feed rate of 65.22 ml/min. 157

Figure 4.14 Comparison of the theoretical model predictions and the experimental results of the variable feed rate mesomixing analysis. 159

Figure 4.15 Comparison of the theoretical model predictions and the experimental results of the variable feed rate mesomixing analysis at precipitation time of 6 minutes. 159

Figure 4.16 Number of nuclei captured in the process of dissolution, as taken from the simulation results. 160

Figure 4.17 Normalized nucleation rate for two different volumetric feed rates, both having a molar feed rate of 0.0225 mol/min. 161

Figure 4.18 Lagrangian description of the precipitation and mixing processes within a discrete feed volume. (a) Entering as pure reactant, (b) Mixing with the surrounding reactant and nucleating to relieve the high supersaturation, (c) Nuclei released into the kettle where crystal growth begins, and (d) Mixing and nucleation are completed. 162

Figure 4.19 Lagrangian evolution of the mixed reaction volume for a molar feed rate of 0.0028 mol/min. a) Concentrated feed, and b) Diluted feed. Units for each quantity are given in the legend. 164

Figure 4.20 Increasing the local turbulence by relocating the feed point to the impeller tip results in the precipitation approaching the ideal limit. 166

Figure 4.21 Increasing the local turbulence by raising the impeller rotational speed results in each precipitation product approaching the respective ideal limit. 166

Figure 4.22 Effect of reactant stoichiometric imbalance on nucleation near the feed point. Silver reactant concentration is proportional to the shading. a) At low molar feed rates there is rapid and complete nucleation within the feed plume, b) At moderate feed rates there is complete nucleation in the feed plume, and c) At high molar feed rates nucleation is incomplete due to limited amounts of the reactant in the surrounding solution. 168

Figure 4.23 Precipitation scale-up based on constant power input per unit volume. Predicted results for the small and large scale are identical. Large scale based on a scale-up factor of 10. 170
Figure 4.24 Predicted precipitation scale-up based on constant impeller rotational speed. Large scale based on a scale-up factor of 10. 170

## List of Symbols

| | |
|---|---|
| $a$ | internal feed pipe radius, m |
| $a$ | solute activity, mol L$^{-1}$ |
| $A$ | surface area of a crystal, m$^{2}$ |
| $a_e$ | solute activity at equilibrium, mol L$^{-1}$ |
| $B_o$ | nucleation rate, m$^{-3}$ m$^{-1}$ s$^{-1}$ |
| $\bar{B}_{o,i}$ | instantaneous nucleation rate, m$^{-3}$ s$^{-1}$ |
| $C$ | concentration, mol L$^{-1}$ *or* mol m$^{-3}$ |
| $C$ | off-bottom impeller clearance, m |
| $C_e$ | solute concentration at equilibrium, mol L$^{-1}$ *or* mol m$^{-3}$ |
| $C_f$ | feed concentration, mol L$^{-1}$ *or* mol m$^{-3}$ |
| $C_i$ | solute concentration at the crystal-solution interface, mol L$^{-1}$ *or* mol m$^{-3}$ |
| $C_L$ | effective concentration at equilibrium for crystal size L, mol L$^{-1}$ *or* mol m$^{-3}$ |
| $C_{rel}$ | solute concentration relieved due to nucleation, mol L$^{-1}$ *or* mol m$^{-3}$ |
| $C_s$ | solubility of solute, mol L$^{-1}$ *or* mol m$^{-3}$ |
| $C_{Sc}$ | solute concentration at the critical supersaturation limit, mol L$^{-1}$ *or* mol m$^{-3}$ |
| $C_T$ | total solute concentration, mol L$^{-1}$ *or* mol m$^{-3}$ |
| $D$ | impeller diameter, m |
| $\Delta C$ | concentration driving force, mol m$^{-3}$ |
| $\Delta G$ | overall excess free energy, J mol$^{-1}$ |
| $\Delta G_{crit}$ | critical overall excess free energy, J mol$^{-1}$ |
| $\Delta G_v$ | free energy of transformation, J mol$^{-1}$ m$^{-3}$ |
| $\Delta G_S$ | surface excess free energy, J mol$^{-1}$ |
| $\Delta G_V$ | volume excess free energy, J mol$^{-1}$ |
| $D_H$ | impeller blade height, m |
| $\Delta L_i$ | spacing of *ith* size interval, m |

| | |
|---|---|
| $D_{mol}$ | molecular diffusion coefficient, $m^2\ s^{-1}$ |
| $D_o$ | crystal death rate, $m^{-3}\ m^{-1}\ s^{-1}$ |
| $D_P$ | feed pipe diameter, mm |
| $D_t$ | turbulent diffusivity ($0.1k^2/\varepsilon$), $m^2\ s^{-1}$ |
| $\Delta t_E$ | time step used for updating the Eulerian Flow Field model, s |
| $D_W$ | impeller blade width, m |
| $E$ | engulfment intensity parameter, $s^{-1}$ |
| $G$ | linear crystal growth rate, $m\ s^{-1}$ |
| $H_f$ | final fluid height, m |
| $H_o$ | initial fluid height, m |
| $i$ | interval index (relative to zero or the symmetric interval) |
| $I$ | number of integration rings used for the TD mesomixing model |
| $k$ | turbulent kinetic energy, $J\ kg^{-1}$ |
| $K$ | rate constant for surface integration, $m^4\ mol^{-1}\ s^{-1}$ |
| $k_d$ | mass transfer coefficient, $kg\ m\ mol^{-1}\ s^{-1}$ |
| $k_m$ | mass transfer coefficient, $kg\ m\ mol^{-1}\ s^{-1}$ |
| $k_r$ | rate constant for surface integration, $kg\ m\ mol^{-1}\ s^{-1}$ |
| $K_{SP}$ | solubility product, $mol^2\ L^{-2}$ |
| $L$ | cubic crystal edge length, m |
| $\ell$ | characteristic length scale of turbulence, m |
| $L_c$ | critical cubic crystal edge length, m |
| $L_D$ | characteristic length scale for turbulent dispersion, m |
| $L_i$ | characteristic length of *ith* size interval, m |
| $\ell_i$ | upper length limit of *ith* size interval, m |
| $L_{Ps\text{-}i,\ eff}$ | effective characteristic length of *ith* size interval ($r^i L_{Ps}$), m |
| $m$ | mass of solid deposited on the crystal surface, kg |
| $M$ | molar mass of solute, $kg\ mol^{-1}$ |
| $n$ | crystal count per size interval per unit size, $m^{-3}\ m^{-1}$ |

| | |
|---|---|
| $N$ | cumulative under-size crystal count, $m^{-3}$ |
| $\mathrm{N}$ | impeller rotational speed, rps |
| $\tilde{n}$ | relative crystal count per size interval per unit size, $(\tilde{N}/\Delta L)$, $m^{-3}$ |
| $N_i$ | crystal count per size interval $(\Delta N)$, $m^{-3}$ |
| $\tilde{N}_i$ | relative crystal count per size interval, $(\Delta N/N_T)$, $m^{-3}$ |
| $N_P$ | impeller power number |
| $N_Q$ | impeller flow number |
| $N_T$ | total crystal count, $m^{-3}$ |
| P | impeller power requirement, W |
| P | total number of size intervals |
| pAg | silver ion concentration, $(-\log_{10}([Ag^+]))$, mol $L^{-1}$ |
| pBr | bromide ion concentration, $(-\log_{10}([Br^-]))$, mol $L^{-1}$ |
| Pn | nucleation interval index |
| Ps | symmetric interval index |
| Q | impeller pumping capacity, $m^3\ s^{-1}$ |
| Q | volumetric flow rate, $m^3\ s^{-1}$ |
| $Q_f$ | volumetric feed rate, $m^3\ s^{-1}$ |
| r | common geometric factor |
| R | molar reactant addition rate per unit volume, mol $s^{-1}\ m^{-3}$ |
| Re | Reynolds number |
| $R_g$ | universal gas constant, N m $mol^{-1}\ K^{-1}$ |
| S | supersaturation ratio |
| Sc | Schmidt number |
| $S_{crit}$ | critical supersaturation ratio |
| $S_{FW}$ | fraction of the impeller discharge entering the upper wall-jet |
| t | time, s |
| T | tank diameter, m |
| $t_C$ | characteristic circulation time, s |

| | |
|---|---|
| $t_D$ | characteristic turbulent dispersion mesomixing time, s |
| $t_{diffusion}$ | characteristic diffusion time, s |
| $t_f$ | feed time, s *or* min |
| $t_K$ | Kolmogorov turbulent time scale, s |
| $T_k$ | absolute temperature, K |
| $t_M$ | characteristic micromixing time, s |
| $t_S$ | characteristic inertial-convective mesomixing time, s |
| u | turbulent fluctuating velocity, m $s^{-1}$ |
| U | mean local velocity, m $s^{-1}$ |
| $U_f$ | feed velocity, m $s^{-1}$ |
| $u_K$ | Kolmogorov turbulent fluctuating velocity, m $s^{-1}$ |
| $V_{DFV}$ | volume of micromixed fluid, $m^3$ |
| $V_k$ | volume of zone in the EFM, $m^{-3}$ |
| $V_m$ | molar volume of solute, $m^3$ $s^{-1}$ |
| $V_m$ | volume of micromixed fluid, $m^3$ |
| $V_T$ | tank volume, $m^3$ |
| W | baffle width, m |
| $X_{DFV}$ | local volume fraction of micromixed fluid |
| $X_f$ | volume fraction of fluid containing the feed reactant |
| $X_m$ | volume fraction of micromixed fluid |
| $X_N$ | stable nucleation efficiency |
| $X_u$ | volume fraction of mesomixed fluid |
| Z | number of stable nuclei, $m^{-3}$ |

### *Greek*

| | |
|---|---|
| $\beta$ | stability constant |
| $\Delta\mu$ | chemical potential driving force, J mol$^{-1}$ |
| $\varepsilon$ | rate of kinetic energy dissipation, W kg$^{-1}$ |
| $\gamma$ | activity coefficient |
| $\gamma_e$ | activity coefficient at equilibrium |
| $\lambda_B$ | Batchelor microscale, m |
| $\Lambda_c$ | integral scale of concentration fluctuations, m |
| $\lambda_K$ | Kolmogorov turbulent length scale, m |
| $\mu$ | mean crystal length, m |
| $\nu$ | kinematic viscosity, m$^2$ s$^{-1}$ |
| $\nu$ | number of moles of ions formed from one mole of electrolyte |
| $\theta_B$ | characteristic vessel blend time, s |
| $\rho$ | crystal density, kg m$^{-3}$ |
| $\sigma$ | interfacial tension (surface energy) of solute, N m$^{-1}$ |
| $\sigma$ | standard deviation, m |
| $\xi$ | ratio of relative resistance of diffusion to surface integration |

# Chapter 1

## Introduction

Silver halide precipitation is fundamental to the photographic industry. The sensitivity of photographic materials depends strongly on the precise control of average crystal characteristics such as shape, size, thickness and halide composition. In order to improve the control of these characteristics an understanding of the elementary thermodynamic and kinetic processes, and the influence of local mixing conditions on these processes during precipitation is required.

The majority of silver halides are precipitated using controlled double-jet reactant addition into a stirred tank reactor. It is well known that spatial inhomogeneities in species concentration, and therefore supersaturation, may exist in stirred tank reactors and affect product quality. Consequently, the scale-up of a given photographic emulsion is not trivial, and to a certain extent, processes must be reformulated for use on larger scales. Often compromises between key mixing parameters such as feed time and mixing rate must be made during scale-up despite exact geometric similarity. As a result, the lack of scaleability from the laboratory to industrial scale observed in some silver halide precipitations is simply due to the use of different mixing processes at different scales.

In this work, a fully mechanistic model of silver halide precipitation and turbulent mixing in a stirred tank reactor was developed and then used to study the effects of mixing and scale-up on crystal product characteristics: in particular the crystal size distribution. In this chapter, the fundamental theories that underpin the model are presented and explained.

## 1.2 Crystallization Fundamentals

In reactive crystallization, a solution of one reactant is fed into a stirred solution of the other causing concentrations exceeding the thermodynamic equilibrium solubility limit. Ensuing chemical reaction forms the crystallizing substance to relieve the greater than equilibrium amount of dissolved solute, defined as the excess supersaturation. Initially the crystallizing substance forms molecules and complexes, which then leads to the formation and growth of nuclei.

### *1.2.1 Precipitation Process*

Precipitation often refers to the fast, and possibly irreversible, crystallization of a virtually insoluble substance produced by a chemical reaction. Precipitations are usually initiated at high supersaturations, which results in nearly instantaneous nucleation and the consequent production of large numbers of very small crystals. Although precipitation, like all other crystallization processes, proceeds through supersaturation, nucleation and growth, it is also affected by agglomeration and ageing. Agglomeration is the tendency of small particles to cluster while in solution soon after nucleation. Ageing refers to all irreversible changes that are made to the precipitate size distribution during the process, such as Ostwald ripening.

A common method for producing a precipitate is to rapidly mix two reactant solutions together in a stirred vessel. Immediately after the reactant addition begins, the vessel's supersaturation rapidly increases and exceeds the critical limit required for primary nucleation. Primary nucleation, both homogeneous and heterogeneous, along with nuclei growth continue until sufficient crystal surface area is available to cause a rapid decrease in supersaturation due to consumption by crystal growth. This is referred to as the nucleation period. Once the supersaturation drops below the critical limit, the process enters the transient period. During this period some of the smaller nuclei become unstable and dissolve into solution according to the Gibbs-Thompson effect ( 1.23 ). This effect states that the stable crystal size is inversely related to supersaturation. In turn, the increase in supersaturation owing to the dissolution of small crystals causes the solution to become supersaturated with respect to the larger crystals present. Thus, the larger crystals grow at the expense of the smaller crystals. This is known as Ostwald ripening. For the remainder of the precipitation, the supersaturation and stable number of crystals become relatively constant and the added reactants effectively serve only to grow the stable crystals. During this period all of the nuclei formed continuously in the high supersaturation region near the feed point become unstable in the bulk solution and rapidly dissolve. This is the growth period.

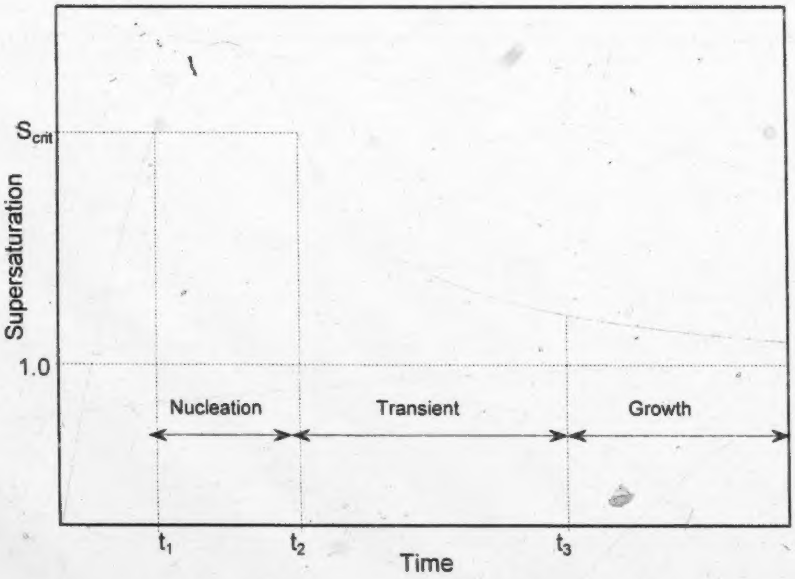

**Figure 1.1** Supersaturation profile during the three stages of the precipitation process.

### *1.2.2 Supersaturation*

Among the most usual expressions for supersaturation are the concentration driving force $\Delta C$, and the supersaturation ratio S. These expressions are given by

$$\Delta C = C - C_e \tag{1.1}$$

$$S = \frac{C}{C_e} \tag{1.2}$$

where C is the solute concentration in the bulk solution and $C_e$ is the equilibrium concentration at the given process temperature. It should be noted that neither of these expressions is the true thermodynamic expression.

The fundamental driving force for crystallization is the difference in chemical potential, $\Delta\mu$, between the precipitating substance in solution and the crystal. This may be written for a binary solution in dimensionless form as (Mullin 2001)

$$\frac{\Delta\mu}{R_g T_k} = \ln\left(\frac{a}{a_e}\right) \tag{1.3}$$

where a and $a_e$ are the activities of the supersaturated and saturated solutions respectively, $R_g$ is the universal gas constant and $T_k$ is the absolute temperature.

The fundamental supersaturation ratio S is then

$$S = \frac{a}{a_e} = \frac{\gamma C}{\gamma_e C_e} \tag{1.4}$$

where the ratio of activity coefficients $\gamma/\gamma_e$ is unity for ideal solutions.

### *1.2.3 Nucleation*

Supersaturation alone is not sufficient for a solution to crystallize. Minute solid bodies, either seed crystals or nuclei, must exist to initiate the crystallization. Nucleation occurs either spontaneously, in the absence of seeding, or may be induced by foreign particles or seed crystals.

To avoid confusion arising from the nucleation nomenclature, the terminology provided by Mullin (2001) will be used (Figure 1.2). The term ‘primary’ will be reserved for nucleation in systems that do not already contain crystals of the same material. Primary nucleation may be either homogeneous (no particles present) or heterogeneous (induced by foreign particles). Nuclei can also be generated in the vicinity of crystals of the same material when present in a supersaturated system; this behavior will be referred to as ‘secondary’ nucleation.

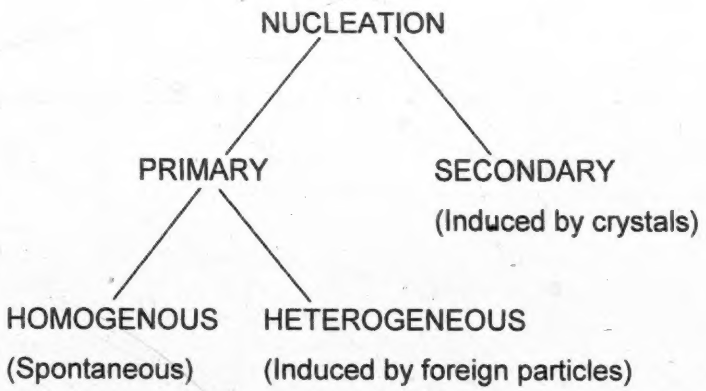

**Figure 1.2** Nucleation terminology (Mullin 2001).

## Primary Homogeneous Nucleation

In primary homogeneous nucleation, it is believed that clusters of solute molecules are formed by a sequence of bimolecular additions in the supersaturated solution. If the cluster grows beyond a critical size, it becomes a stable nucleus. Several free energy changes are associated with the process of homogeneous nucleation.

The overall excess free energy $\Delta G$ between a small solid particle of solute and solute in solution is equal to the sum of the surface excess free energy $\Delta G_S$ and the volume excess free energy $\Delta G_V$ (Mullin 2001).

$$\Delta G = \Delta G_s + \Delta G_v = 6L^2\sigma + L^3\Delta G_v \quad (1.5)$$

Here L is the cubic edge length of the nucleus, $\sigma$ is the interfacial tension (surface energy) and $\Delta G_v$ is the free energy change of the transformation per unit volume of crystal formed. The two terms in the above equation are of opposite sign and depend on different orders of crystal length, thus the free energy of formation has a maximum at some critical crystal size $L_c$ (Figure 1.3). This critical length is found by maximizing Equation ( 1.5 ). Setting $d\Delta G/dL$ to zero gives

$$L_c = \frac{-4\sigma}{\Delta G_v} \quad (1.6)$$

And from Equations ( 1.5 ) and ( 1.6 ):

$$\Delta G_{crit} = \frac{32\sigma^3}{(\Delta G_v)^2} = 2\sigma L_c^2 \quad (1.7)$$

The thermodynamic tendency of a nucleus to reduce its free energy dictates its behavior. According to Figure 1.3, particles smaller than the critical length will dissolve, while larger particles will grow.

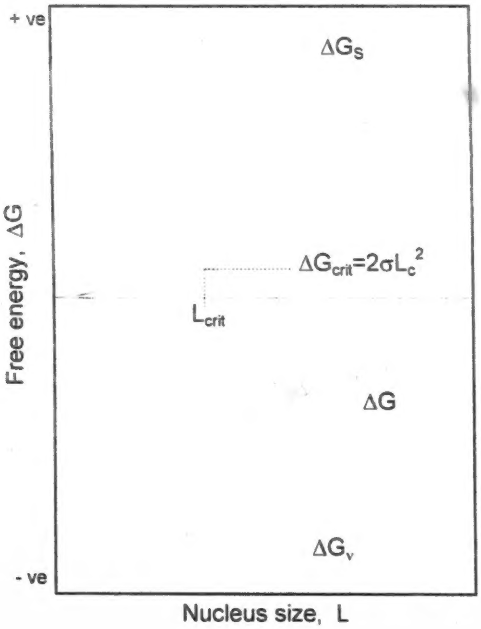

**Figure 1.3** Interaction of volume and surface free energy change for homogeneous primary nucleation (Mullin 2001).

The amount of energy required to produce a stable nucleus $\Delta G_{crit}$ can be related to the supersaturation level of the solution through the Gibbs-Thompson relation (Ostwald 1900). The relationship between cubic particle size and solubility can be expressed as

$$\ln S = \frac{4\sigma M}{\nu R_g T_k \rho L} \qquad (1.8)$$

where S is defined by Equation ( 1.2 ), M is the molar mass of the solid in solution and $\rho$ is the density of the solid. The quantity $\nu$ represents the number of moles of ions formed from one mole of electrolyte. For a non-electrolyte, $\nu = 1$. Using this relation with Equation ( 1.6 ) gives

$$-\Delta G_v = \frac{4\sigma}{L_c} = \frac{\nu R_g T_k \rho \ln S_c}{M} \qquad (1.9)$$

And from Equation ( 1.7 )

$$\Delta G_{crit} = \frac{32\sigma^3 M^2}{\left(\nu R_g T_k \rho \ln S_c\right)^2} \qquad (1.10)$$

This expression suggests that three main variables will govern the rate of homogeneous primary nucleation; interfacial tension $\sigma$, temperature $T_k$, and supersaturation S.

### Primary Heterogeneous Nucleation

Primary heterogeneous nucleation begins to occur at lower supersaturations than homogeneous nucleation due to a reduction in the overall free energy required relative to that of homogeneous nucleation. The overall free energy is reduced due to a decrease in the interfacial energy caused by a partial affinity between the crystalline solid and the foreign particle surface. For the case of complete non-affinity, the required overall free energy of heterogeneous nucleation is the same as that required for primary homogeneous nucleation. For the case of complete affinity the required excess free energy is zero. This case corresponds to the seeding of a supersaturated solution with crystals of the solute, meaning that no nuclei need to be formed (Mullin 2001).

In practice, it is virtually impossible to achieve systems entirely free of foreign particles. Nielsen (1957) concluded that heterogeneous nucleation occurs at low supersaturations, but at high supersaturations nucleation is completely dominated by homogeneous nucleation. Berry and Skillman (1968) then concluded that typical photographic emulsions using high supersaturations are dominated by homogeneous nucleation.

### Secondary Nucleation

Secondary nucleation occurs when crystals of the solute are already present in the supersaturated solution. Secondary nucleation can occur by attrition or breakage (Strickland-Constable 1968), or by the shearing of weak outgrowths or loosely bonded units from the crystal surface by fluid shear (Powers 1963). Primary nucleation usually dominates at the high levels of supersaturation used for silver halide precipitation.

### *1.2.4 Crystal Growth*

Immediately after a stable nucleus has been formed in a supersaturated solution it begins to grow. Of the many proposed crystal growth mechanisms in the literature, all may be broadly grouped into three main classes: surface energy, diffusion and adsorption. Surface energy theories are based on the hypothesis that crystals grow assuming a shape that minimizes their surface energy (Gibbs 1948). Diffusion theories are based on the hypothesis that material is deposited on the crystal surface at a rate proportional to the concentration gradient between the crystal surface and the bulk solution (Noyes and Whitney 1897). Lastly, Volmer (1939) suggested that crystal growth was a discontinuation process, where adsorption added to the crystal layer by layer. The former theory, although not completely abandoned, has mostly become obsolete, while significant advancements have been made in both the diffusion and adsorption layer theories.

#### Diffusion-Reaction Theory

Noyes and Whitney (1897) proposed that crystal growth was essentially a diffusional process. They assumed that material was deposited or removed from the crystal surface in proportion to the difference between concentrations of the solute at the crystal surface and the bulk solution. The suggested form follows

$$\frac{dm}{dt} = k_m A(C - C_e) \qquad (1.11)$$

where m is the mass of the solid deposited in time t, $k_m$ is the coefficient of mass transfer, A is the surface area available for deposition, C is the bulk concentration and $C_e$ is the equilibrium concentration at the given temperature. A significant improvement was made by Berthoud (1912) and Valeton (1924), who both suggested that two steps are involved in the process. Firstly, there is a transport of the solute from the bulk solution to the crystal surface, which is followed by a first order reaction when the molecules arrange themselves in the lattice. Each step occurs under a different driving force as given below and shown in Figure 1.4.

$$\frac{dm}{dt} = k_d A(C - C_i) \qquad (1.12)$$

$$\frac{dm}{dt} = k_r A(C_i - C_e) \qquad (1.13)$$

where $k_d$ is the coefficient of mass transfer, $k_r$ is the rate constant for the surface integration reaction and $C_i$ is the solute concentration at the crystal-solution interface.

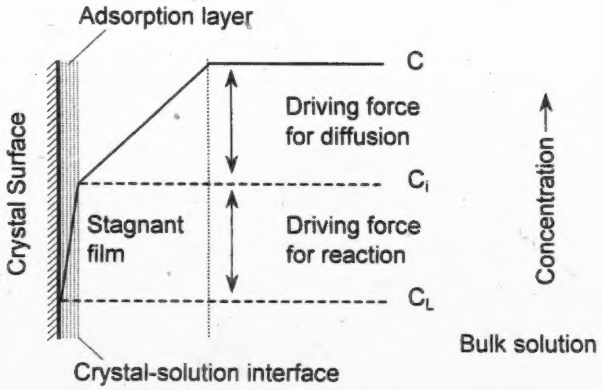
Adsorption layer
C
Driving force for diffusion
Crystal Surface
$C_i$
Stagnant film
Driving force for reaction
Concentration →
$C_L$
Bulk solution
Crystal-solution interface

**Figure 1.4** Schematic of the driving forces involved in the surface integration-diffusion growth process (Mullin 2001).

Assuming that the crystallization process is entirely diffusion or surface integration controlled, it should be possible to determine the growth rate from first principles. In the case of diffusion controlled growth the molar flux F is proportional to the concentration gradient dC/dx according to

$$F = D_{mol}\frac{dC}{dx} \qquad (1.14)$$

where x is the diffusion path length and $D_{mol}$ is the molecular diffusivity of the solute in the solution. Thus, the rate of diffusion dn/dt to a cubic surface, where $\ell$ is the distance from the center of the cube, is

$$\frac{dn}{dt} = 24\ell^2 D_{mol}\frac{dC}{d\ell} \qquad (1.15)$$

At any instant the rate of diffusion is constant, therefore Equation ( 1.15 ) can be integrated, giving

$$\frac{dn}{dt} = \frac{24D_{mol}(C_2 - C_1)}{\frac{1}{\ell_1} - \frac{1}{\ell_2}} \qquad (1.16)$$

$C_2$ equals the equilibrium concentration, $C_1$ equals the bulk concentration, $\ell_1$ equals the surface of the cube and $\ell_2$ is much greater than $\ell_1$. Using $L = 2\ell$, and setting the rate of diffusion equal to the rate of consumption by growth, Equation ( 1.16 ) becomes

$$\frac{dn}{dt} = 12D_{mol}L(C - C_e) = 3L^2\frac{\rho}{M}\frac{dL}{dt} \qquad (1.17)$$

where M is the molar mass of the solute and ρ is the crystal density. Rearranging Equation ( 1.17 ) for the linear growth rate dL/dt or G, gives

$$G = \frac{4D_{mol}M}{\rho L}(C - C_e) = \frac{dL}{dt} \qquad (1.18)$$

Wey and Strong (1977a) combined Equation ( 1.18 ) with an empirical growth rate expression for the surface integration step ( 1.19 ) to propose a growth model that includes both the bulk diffusion and surface integration processes (Figure 1.5).

$$G = K(C_i - C_e)^m \qquad (1.19)$$

where K is the rate constant for the surface integration step and m is the order of the surface integration, taken to be unity.

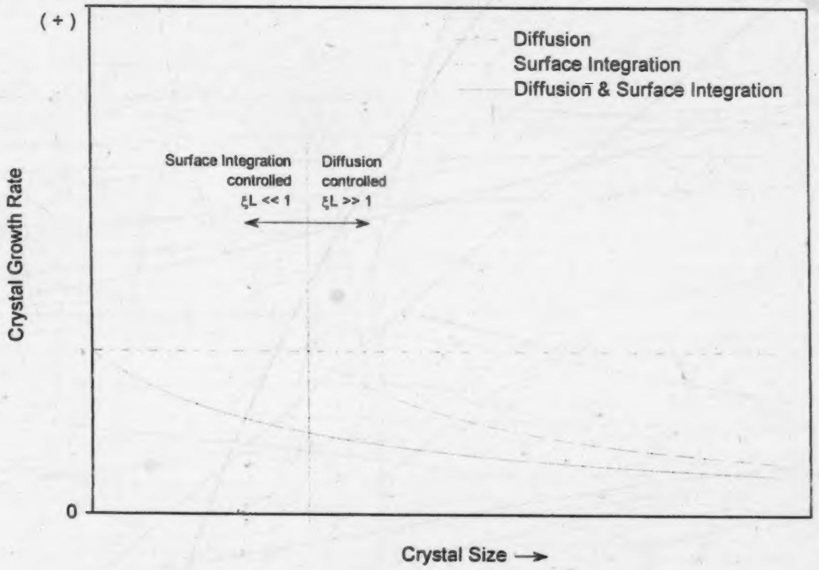

**Figure 1.5** Crystal growth rate expression combing bulk diffusion and surface integration (Wey and Strong 1977a).

Equations ( 1.18 ) and ( 1.19 ) were combined to eliminate the interface solute concentration after replacing the equilibrium concentration with the interface concentration in Equation ( 1.18 ). The result was

$$G = \frac{g}{1+\xi L} \qquad (1.20)$$

where

$$g = K(C - C_e) \qquad (1.21)$$

$$\xi = \frac{\rho K}{4D_{mol}M} \qquad (1.22)$$

Here, g represents a size independent growth rate when surface integration is controlling and $\xi$ represents the ratio of relative resistance of diffusion to surface integration. When $\xi L \ll 1$, growth is controlled by surface integration and when $\xi L \gg 1$, by diffusion.

Later Wey and Strong (1977b) modified their previous growth rate expression to include the influence of the Gibbs-Thompson effect (Figure 1.6). This relationship describes the solubility of small crystals as a function of their size. First derived by Thompson (1871) for vapor-liquid systems and later modified by Ostwald (1900) for solid-liquid systems, it takes the form

$$C_L = C_e \exp\left(\frac{4\sigma M}{\nu R_g T_k \rho L}\right) \qquad (1.23)$$

where $C_L$ is the effective equilibrium concentration for crystals of size L, $\sigma$ is the interfacial tension, $R_g$ is the universal gas constant and $T_K$ is the absolute temperature. The quantity $\nu$ represents the number of moles of ions formed from one mole of electrolyte. The final modified growth rate expression is then

$$G = \frac{K(C - C_L)}{1 + \xi L} \qquad (1.24)$$

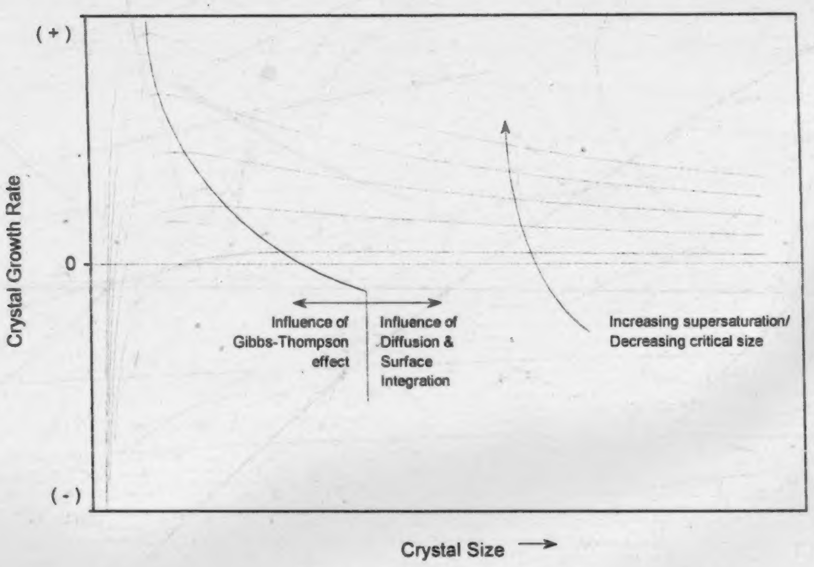

**Figure 1.6** Crystal growth rate expression combing bulk diffusion, surface integration and crystal size solubility.

The Gibbs-Thompson effect implies some interesting consequences for the crystal growth process. For instance, it suggests that the equilibrium concentration associated with small crystals $C_L$ is always greater than that of large crystals $C_e$. Thus, in identical environments the driving force for the growth of small crystals $C\text{-}C_L$ would be less than that for large crystals $C\text{-}C_e$. In fact, as the effect becomes more pronounced at smaller crystal sizes, the driving force would become negative for sizes below the critical size. The critical size can be found by Equation ( 1.23 ), when the bulk concentration equals $C_L$.

$$L_c = \frac{4\sigma M}{\nu R_g T_k \rho \ln\left(C/C_e\right)} = \frac{4\sigma M}{\nu R_g T_k \rho \ln(S)} \qquad (1.25)$$

These opposite driving forces for small and large crystals lead to the process known as Ostwald ripening (Ostwald 1896). The crystals present that are smaller than $L_c$ spontaneously dissolve since their effective driving force is negative. The solution becomes supersaturated with respect to the larger crystals and solute is deposited on them. Therefore, the large crystals grow at the expense of the small crystals.

The derivation of the Gibbs-Thompson effect involves many assumptions, some of which may not be always valid. For example, the interfacial tension and crystal density are implicitly assumed to be independent of crystal size. When a particle comprises only a few molecules, the distinction between interfacial energy and lattice energy loses sense and should be accounted for (Harbury 1946). The Gibbs-Thompson effect also predicts an exponential increase in solubility as the crystal size tends to zero. To compensate for this, Knapp (1922) suggested that the total interfacial tension should be the sum of the normal interfacial energy plus the surface electrical charge. This results in the elimination of the Gibbs-Thompson effect at small sizes (Figure 1.7); a result supported by the work of Harbury (1946).

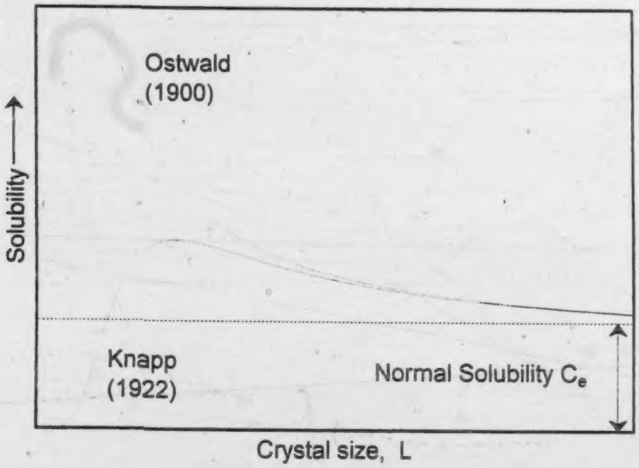

**Figure 1.7** The relationship between particle size and solubility (Mullin 2001).

### 1.2.5 Agglomeration

Small particles have a tendency to cluster together while in solution. The factors controlling the colloidal stability of small particles are the van der Waals attractive forces and the electrostatic repulsion forces. When agglomeration occurs it may result in flocculation, coagulation or coalescence (Antoniades and Wey 1992). Here flocculation will refer to small, loosely held aggregates of noncontacting colloid particles. In this case the attractive forces are almost counterbalanced by the repulsive forces, thus preventing particle contact and making the process easily reversible. In contrast, coagulation refers to the tight agglomeration of colloidal particles. These aggregates are held closely together by van der Waals forces and ionic bonding between contacting surfaces, thus making the process only partially reversible. Lastly, coalescence refers to when at least two colloidal particles combine to form a new particle.

Although some types of agglomeration have been observed in silver halide precipitations, they are rare in the presence of gelatin (Antoniades and Wey 1992), which is a natural stabilizer. With adequate levels of gelatin in solution, silver halide particles are peptized through steric stabilization by the surface adsorption of gelatin, thus preventing agglomeration.

### 1.2.6 Precipitation Techniques

Precipitation processes generally involve the creation of highly supersaturated systems and the main practical difficulty is to maintain reasonably uniform conditions throughout the vessel. The formation of local inhomogeneities such as reactants in non-stoichiometric amounts and undesirable pH levels can affect the product distribution. Therefore, the method used to mix the reactants is of critical importance. Moreover, the position of the reactant addition point is also very important and can greatly influence the product distribution. Various methods can be used for introducing the reactants, each having a distinct influence on the product distribution (Figure 1.8). For example, a single-jet addition of reactant B can be added at either the fluid surface (Figure 1.8a) or in the intensely mixed impeller region (Figure 1.8b) of a vessel containing A. The latter often leads to smaller product crystal sizes since good mixing at the feed point increases the supersaturation and accordingly, the nucleation rate (Baldyga et al. 1995). Alternatively, both reactants may be simultaneously introduced to the reaction vessel using double-jet addition at either the surface or the impeller (Figure 1.8c, impeller feed point not shown). Finally, the reactants can be premixed to allow better control of the initial supersaturation levels (Figure 1.8d). This option improves reactor scaleability by allowing a simple increase or decrease in the number of feed premixing units, rather than the complex scale-up of a single unit (Jézéquel 2001).

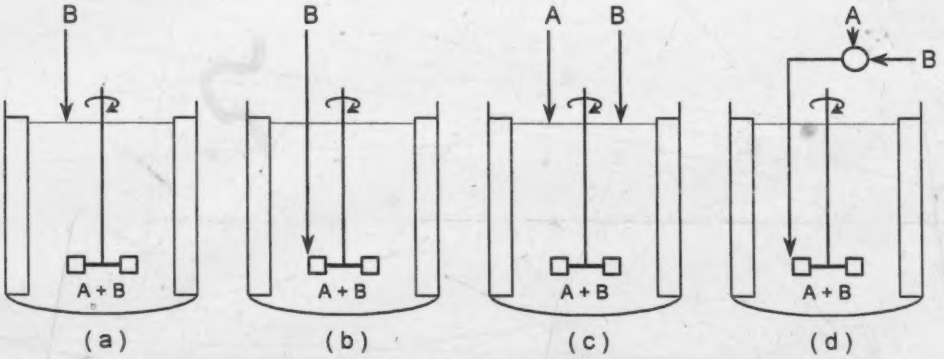

**Figure 1.8** Possibilities for introducing reactant streams to a precipitation vessel (Mullin 2001). (a) Single-jet surface addition, (b) Single-jet impeller addition, (c) Double-jet surface addition, and (d) Premixed impeller addition.

## Double-jet Addition

By tradition, most commercial photographic emulsions are made using controlled double-jet addition of silver nitrate and halide solutions to an agitated vessel containing an aqueous solution of gelatin and excess halide. Controlled double-jet precipitation attempts to control primary nucleation, crystal growth, ripening and agglomeration by maintaining the starting solution temperature and solubility. For common precipitations the solubility is determined by the concentration of halide ions. Hence, the silver nitrate solution is added at a constant rate, while the halide solution addition is controlled to keep the halide ion concentration constant. Ripening is reduced by continuous reactant addition and agglomeration is reduced by the stabilizing properties of the gelatin.

## 1.3 The Population Balance

The complete mathematical description of a crystal size distribution (CSD) simultaneously undergoing nucleation, growth and agglomeration for a well mixed batch system of constant volume is given by Randolph and Larson (1971) as

$$\frac{\partial n}{\partial t}+\frac{\partial (Gn)}{\partial L}=B_o-D_o \qquad (1.26)$$

In this equation n is the crystal number density function, G is the crystal growth rate expressed as a function of crystal size L, and $B_o$ and $D_o$ are the birth and death rates associated with nucleation, agglomeration and breakage. The crystal number density function represents the number of crystals per unit size, and is defined as

$$\lim_{\Delta L\to 0}\frac{\Delta N}{\Delta L}=\frac{dN}{dL}=n \qquad (1.27)$$

where $N$ is the cumulative under-size crystal count and $\Delta N$, hereafter denoted as $N_i$, is the number of crystals appearing in the size interval $\Delta L$. Therefore, the number of crystals in a given size interval is

$$N_i=\int_{\ell_{i-1}}^{\ell_i} n\,dL \qquad (1.28)$$

where $\ell_{i-1}$ and $\ell_i$ are the lower and upper limits of the *ith* size interval, respectively.

Rigorous modeling of the population balance usually leads to an integro-partial-differential equation that cannot be solved analytically. Among the various numerical techniques available for solving the population balance equations, a discretization method that considers particles of similar sizes to exist in groups that interact collectively with other groups has emerged as an efficient solution method. This method converts the intractable integro-partial-differential equation into a set of first order ordinary differential equations.

### *1.3.1 Errors Associated with Discrete Crystal Growth*

Most often, the description of pure crystal growth requires the discretization of Equation ( 1.26 ) with respect to crystal size, as shown in Figure 1.9, where $\ell_i$ and $L_i$ are the upper limit and characteristic size of the *ith* interval, respectively. Assuming that a crystal size distribution can be represented by this idealized density function, then in a given time interval dt, some number of particles $dN_{in}$ will grow into the *ith* size interval from the i-1*th* size interval

$$\begin{aligned} dN_{in} &= G(\ell_{i-1})n(\ell_{i-1},t)dt \\ &= \frac{N_{i-1}}{\Delta L_{i-1}}G(\ell_{i-1})dt \end{aligned} \qquad (1.29)$$

Likewise, a number of particles will grow out of the *ith* size interval into the i+1*th* size interval

$$\begin{aligned} dN_{out} &= G(\ell_i)n(\ell_i,t)dt \\ &= \frac{N_i}{\Delta L_i}G(\ell_i)dt \end{aligned} \qquad (1.30)$$

Combining Equations ( 1.29 ) and ( 1.30 ) gives the overall rate of change for the *ith* size interval

$$\begin{aligned} \frac{dN_i}{dt} &= \frac{G(\ell_{i-1})N_{i-1}}{\Delta L_{i-1}} - \frac{G(\ell_i)N_i}{\Delta L_i} \\ &= \frac{r}{(r-1)\ell_i}\left(rG(\ell_{i-1})N_{i-1} - G(\ell_i)N_i\right) \end{aligned} \qquad (1.31)$$

where r is the ratio common geometric factor for the length scale discretization

$$r = \frac{\Delta L_i}{\Delta L_{i-1}} = \frac{\ell_i}{\ell_{i-1}} = \frac{L_i}{L_{i-1}} \qquad (1.32)$$

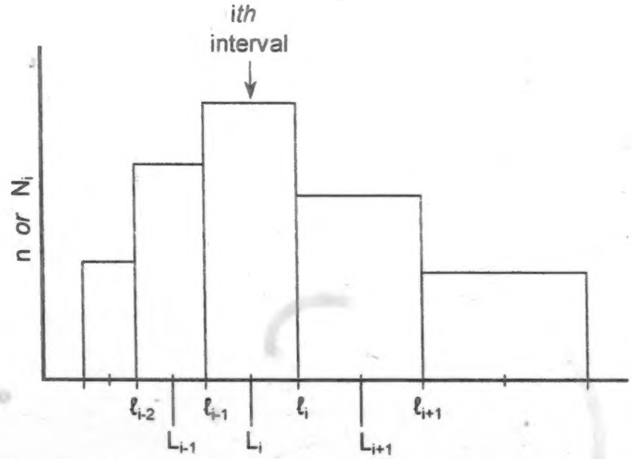

**Figure 1.9** Discretization of the crystal size distribution with crystal length as the internal coordinate.

Hounslow et al. (1988) used a size-independent growth rate to quantify the error associated with Equation ( 1.31 ), for a geometric discretization of $r = \sqrt[3]{2}$, and using the rates of change of the first, second and third moments in the distribution. They determined that the rates of change for the distribution length, area and volume were 13, 28 and 45 % too high, respectively. Thus, this method would result in a general dispersion of the distribution towards larger crystal sizes.

To begin a series of investigations into analyzing the precipitation processes, Marchal et al. (1988) first used the method of classes to formulate the rate of change in the population due to growth. They proposed the following method

$$n(\ell_i) = \frac{\frac{N_{i+1}}{\Delta L_{i+1}} + \frac{N_i}{\Delta L_i}}{2}$$

$$\frac{dN_i}{dt} = \frac{G(\ell_{i-1})}{2\Delta L_{i-1}} N_{i-1} + \left( \frac{G(\ell_{i-1}) - G(\ell_i)}{2\Delta L_i} \right) N_i - \frac{G(\ell_i)}{2\Delta L_{i+1}} N_{i+1}$$
$$\frac{dN_i}{dt} = \frac{r}{2\ell_i (r-1)} \left( r\,G(\ell_{i-1}) N_{i-1} + (G(\ell_{i-1}) - G(\ell_i)) N_i - \frac{G(\ell_i) N_{i+1}}{r} \right) \tag{1.33}$$

Hounslow et al. (1988) showed that this method over predicted the rate of change in the first, second and third moments of the distributions by 1.3, 4.1 and 8.7 %, respectively. Later, David et al. (1991) continued with the method of classes, but used a different expression for approximating the density function that accounted for non-constant interval sizing.

$$n(\ell_i) = \frac{\frac{\Delta L_i}{\Delta L_{i+1}} N_{i+1} + \frac{\Delta L_{i+1}}{\Delta L_i} N_i}{\Delta L_{i+1} + \Delta L_i}$$

$$\frac{dN_i}{dt} = \frac{\Delta L_i}{\Delta L_{i-1}} \frac{G(\ell_{i-1}) N_{i-1}}{(\Delta L_i + \Delta L_{i-1})} + \left( \frac{G(\ell_{i-1})}{(\Delta L_i + \Delta L_{i-1})} \frac{\Delta L_{i-1}}{\Delta L_i} - \frac{G(\ell_i)}{(\Delta L_{i+1} + \Delta L_i)} \frac{\Delta L_{i+1}}{\Delta L_i} \right) N_i - \frac{\Delta L_i}{\Delta L_{i+1}} \frac{G(\ell_i) N_{i+1}}{(\Delta L_{i+1} + \Delta L_i)}$$
$$\frac{dN_i}{dt} = \frac{r}{\ell_i (r^2 - 1)} \left( r^2 G(\ell_{i-1}) N_{i-1} + (G(\ell_{i-1}) - r\,G(\ell_i)) N_i - \frac{G(\ell_i) N_{i+1}}{r} \right) \tag{1.34}$$

This method over predicts the rate of change in the first, second and third moments of the distributions by 2.7, 6.8 and 12.8 %, respectively. Surprisingly, the method used to account for non-constant interval sizing increased the error associated with Equation ( 1.34 ) compared to Equation ( 1.33 ).

Following this, Muhr et al. (1995) used the method of finite differences to simulate the precipitation of silver bromide.

$$\frac{dn(\ell_i)}{dt} = G(\ell_i) \frac{n(\ell_{i+1}) - n(\ell_{i-1})}{\ell_{i-1} - \ell_{i+1}} + n(\ell_i) \frac{G(\ell_{i+1}) - G(\ell_{i-1})}{\ell_{i-1} - \ell_{i+1}} \tag{1.35}$$

Muhr et al. (1996) pointed out that Equations ( 1.34 ) and ( 1.35 ) can be quite similar depending on the choice of the above finite difference approximation or of the approximation for $n(\ell_i)$. Muhr et al. (1996) also pointed out that both equations have the potential to produce negative values in the size distribution, which is not physically possible. They proposed using first order upwinding to circumvent this problem. First order upwinding was adapted from tracer transport problems in fluid mechanics and was selected for its ability to avoid negative values in the tracer concentration. The first order upwinding, finite difference result for a linear discretization is

$$\begin{aligned} \frac{dn_i}{dt} &= \frac{G(\ell_{i-1})n_{i-1} - G(\ell_i)n_i}{\ell_i - \ell_{i-1}} \qquad \text{if} \quad G(\ell) > 0 \\ \frac{dn_i}{dt} &= \frac{G(\ell_i)n_i - G(\ell_{i+1})n_{i+1}}{\ell_{i+1} - \ell_i} \qquad \text{if} \quad G(\ell) < 0 \end{aligned} \tag{1.36}$$

where the growth rates on each side of the zero growth rate point are expressed as

$$G_L\Big|_0 = \frac{G(\ell_{-1}) + G(\ell_0)}{2} \quad \text{and} \quad G_R\Big|_0 = \frac{G(\ell_0) + G(\ell_1)}{2} \tag{1.37}$$

along with

$$\begin{aligned} n_L &= n_{-1} \quad \text{for} \quad G_L \geq 0 \\ n_L &= n_0 \quad \text{for} \quad G_L < 0 \\ n_R &= n_0 \quad \text{for} \quad G_R \geq 0 \\ n_R &= n_1 \quad \text{for} \quad G_R < 0 \end{aligned} \tag{1.38}$$

where the rate of change is

$$\left.\frac{dn}{dt}\right|_0 = \frac{G_L n_L - G_R n_R}{\ell_0 - \ell_{-1}} \tag{1.39}$$

For the case of the simple approximation of the number density function in Equation ( 1.29 ), this method becomes similar to that given in Equation( 1.31 ).

Hounslow et al. (1988) presented an alternative to previous discretized population balance equations by choosing constants that force the correct prediction of the zeroth, first and second moments of the distribution. The resulting equation has the form

$$\frac{dN_i}{dt}=\frac{2G}{(1+r)\ell_i}\left(\frac{r}{r^2-1}N_{i-1}+N_i-\frac{r}{r^2-1}N_{i+1}\right) \qquad (1.40)$$

Furthermore, error in predicting the rate of change of the third moment is only 1.8%. Hounslow (1990) then extended the method for size-dependent growth rates.

$$\frac{dN_i}{dt}=\frac{2}{(1+r)\ell_i}\left(\frac{r}{r^2-1}G_{i-1}N_{i-1}+G_iN_i-\frac{r}{r^2-1}G_{i+1}N_{i+1}\right) \qquad (1.41)$$

This discretized population balance has the potential to produce negative crystal size distributions, but meaningful results can be obtained by simply setting the negative values to zero.

## State of the Population Balance

Based on the previous evaluations of the various population balance methods, the approach proposed by Hounslow et al. (1988) will be adopted as it most accurately predicts the changes due to growth in the crystal distribution. Table 1.1 summarizes analytical calculations of the error in predicting the rates of change in the moments of the distributions for size-independent growth.

**Table 1.1** Summary: Evaluation of various population balance methods.

| Proposed by: | Percent Error in Predicting the Rate of Change in the j*th* Moment of the Distribution [a] | | |
|---|---|---|---|
| | Total Length ( j = 1) | Total Area ( j = 2) | Total Volume ( j = 3) |
| Basic Approach<br>Equation ( 1.31 ) | 13% | 28% | 45% |
| Marchal et al. (1988)<br>Equation ( 1.33 ) | 1.3% | 4.1% | 8.7% |
| David et al. (1991)<br>Equation ( 1.34 ) | 2.7% | 6.8% | 12.8% |
| Hounslow et al. (1988)<br>Equation ( 1.40 ) | 0% | 0% | 1.8% |

[a] j*th* Moment: $m_j = \sum_i L_i^j N_i$

A general discussion of crystal size distributions and other population balance methods is given by Ramkrishna (1985). For a detailed discussion of the crystal size distributions and population balance methods used in this work refer to Section 2.3.4 and Appendix A.

## 1.4 Mixing Fundamentals

The precipitation of silver halide crystals relies upon a single, nearly instantaneous reaction to first form nuclei, followed by relatively slower crystal growth. Both steps are molecular scale processes and require the reactants to be intimately mixed. Since nucleation is practically instantaneous when compared to molecular scale mixing, or *micromixing*, the precipitation products are strongly influenced by the rate and extent of micromixing. In addition, the products will be influenced by the local environment for micromixing, which is indirectly determined by the turbulence properties and bulk flow field in the reaction vessel.

### 1.4.1 Turbulence

The main feature of turbulence is its ability to rapidly mix and transport species, momentum and energy. Turbulence caused by large scale chaotic motions results in fluxes much greater than molecular fluxes in laminar systems with equivalent velocity and length scales.

The turbulence intensity is characterized by a fluctuating velocity at each point in the flow field. The kinetic energy associated with these fluctuating velocities is maintained by power input to the system and is dissipated to internal energy through the action of viscosity. The rate of turbulent kinetic energy dissipation per unit mass of the system, $\varepsilon$ (W/kg), is a key variable in the description of classical turbulence. The rate of turbulent kinetic energy dissipation and its relationship with the various mixing rates is discussed in the following sections.

The structure and dynamics of turbulence are often characterized using time and length scales. The distinction between large and small scales can be seen in the energy spectrum E, and in the concentration spectrum $E_c$ of turbulence (Figure 1.10). The energy spectrum represents the distribution of turbulent kinetic energy over various length scales $\ell$ expressed in terms of wave numbers $k = 2\pi/\ell$. In turbulent liquids energy is introduced at large scales and is dissipated at small scales.

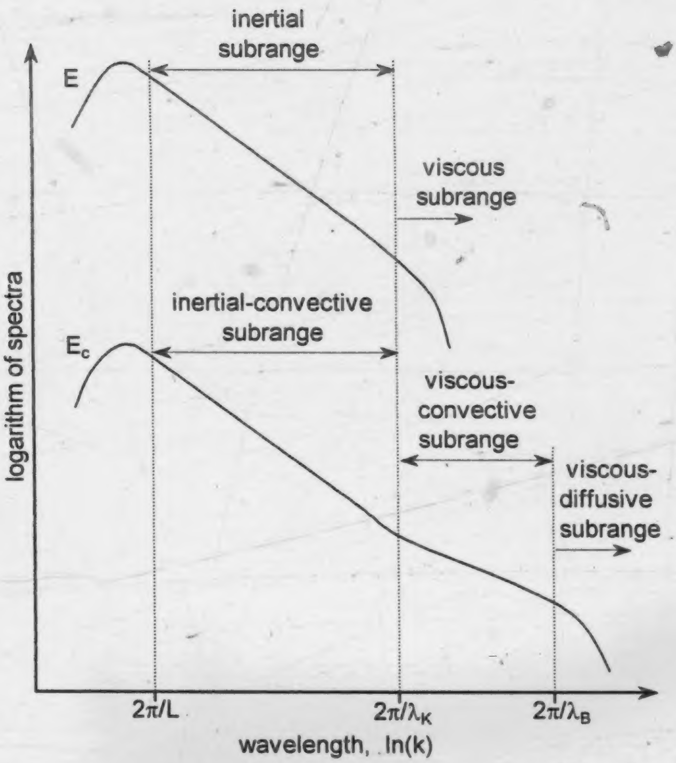

**Figure 1.10** Kinetic energy spectrum E and concentration fluctuation spectrum $E_c$ of turbulence.

In agitated vessels the power input to the system is maintained by the impeller rotation. The local dissipation rate of this energy is given by

$$\varepsilon = A\frac{u^3}{\ell} \tag{1.42}$$

where the constant A is unity for the case of local isotropy, u is the local fluctuating velocity and $\ell$ is the characteristic local integral length scale. Kresta and Wood (1991) suggest that near the impeller the characteristic length scale should be the diameter of the trailing vortices (L = D/10) created by the blade passages. Kresta and Wood (1991) also state that the characteristic length scale changes from the impeller to the bulk of the vessel. Kresta et al. (2001) suggest that the characteristic length may be related to the width of the wall baffles or the wall jet (L = T/10) in the bulk of the vessel.

If the flow is in equilibrium, the rate at which energy enters on the largest scales is exactly equal to the rate at which it is dissipated at the smallest scales. At the smallest scales of motion, the vessel geometry no longer determines the size or orientation of the turbulent eddies, but rather the fluid viscosity becomes important. Kolmogorov defined turbulent scales for length $\lambda_K$, velocity $u_K$, and time $t_K$, which would represent the smallest turbulent eddies. At the Kolmogorov scale the rate of energy dissipation is given by

$$\varepsilon = \frac{u_K{}^3}{\lambda_K} \qquad (1.43)$$

Note that the constant A is unity, indicating isotropic turbulence. By definition the Reynolds number at the Kolmogorov scale is unity, and thus the viscous and inertial forces are of equal magnitude.

$$Re_K = \frac{\lambda_K u_K}{\nu} = 1 \qquad (1.44)$$

thus

$$u_K = \frac{\nu}{\lambda_K} \qquad (1.45)$$

This allows Equation ( 1.43 ) to be rewritten as

$$\lambda_K = \left(\frac{\nu^3}{\varepsilon}\right)^{1/4} \qquad (1.46)$$

giving the Kolmogorov timescale, $\lambda_K/u_K$, as

$$t_K = \left(\frac{\nu}{\varepsilon}\right)^{1/2} \qquad (1.47)$$

Batchelor (1959) derived an expression for the smallest possible scalar striation based on the thought that for diffusion time scales longer than the Kolmogorov scale, turbulence would continue to reduce the scale of segregation before diffusion could be completed. Only once the scalar could diffuse through the lamella at the same rate as the viscous dissipation scale could diffuse momentum would the concentration striations disappear. The penetration depth of a scalar by diffusion in one Kolmogorov time scale is

$$\lambda_B = \sqrt{D_{mol} t_K} = \frac{\lambda_K}{\sqrt{Sc}} \qquad (1.48)$$

where $D_{mol}$ is the diffusion coefficient of the scalar and Sc is the Schmidt number.

## 1.4.2 Different Scales of Mixing

The complicated process of turbulent mixing can be described in terms of three simpler stages based on the scale of operation: *macro*mixing, *meso*mixing and *micro*mixing (Baldyga and Pohorecki 1995). Macromixing acts on the scale of the whole vessel and conveys the volume undergoing mesomixing and micromixing through regions of varying turbulence and concentration. The characteristic macromixing time in a stirred tank can be expressed as the mean circulation time $t_C$ or the blend time of the vessel $\theta_B$.

$$t_C = \frac{V_T}{N_Q N D^3} \qquad (1.49)$$

$$\theta_B = \frac{5.2}{N N_P^{1/3}} \left( \frac{T}{D} \right)^2 \qquad (1.50)$$

where $V_T$ is the fluid volume in the tank, $N_Q$ and $N_P$ are the characteristic flow and power numbers of the impeller, respectively, N is the impeller rotational speed, D is the impeller diameter and T is the vessel diameter.

Mesomixing deals with the coarse scale turbulent exchange between a fresh feed and its surroundings (Figure 1.11). Additional inhomogeneity arising from this interaction can influence the overall yield and selectivity of a complex reaction. Consider the inhomogeneity that appears at high feed rates in the form of a feed plume. This plume of fresh feed is large relative to the micromixing scale but is small compared to the scale of the vessel. The turbulent dispersion of this plume transverse to the direction of flow is called mesomixing. The characteristic time constant describing this dispersion from for a point source is

$$t_D = \frac{Q_f}{UD_t} \qquad (1.51)$$

where $Q_f$ is the volumetric feed rate, $U$ is the mean velocity of the surroundings and $D_t$ is the turbulent diffusivity. The assumption of a point source is possible when (Baldyga and Bourne 1993)

$$a \ll L_D \ll T \qquad (1.52)$$

where $a$ is the internal radius of the feed pipe, $T$ is the scale of the system and

$$L_D = \left(\frac{Q_f}{U}\right)^{1/2} \qquad (1.53)$$

is the characteristic length scale for dispersion. The feed is a local finite source if $a \ll T$ and $a \approx L_D$ or $a > L_D$. In this case, the following additional parameter are required to fully describe the process; the velocity ratio

$$R_u = \frac{U_f}{U} \qquad (1.54)$$

where $U_f$ is the mean velocity exiting the feed pipe. Using this velocity ratio in Equation ( 1.51 ) yields a second time constant that can also be used to define the process when the feed velocity dominates dispersion

$$t_{D1} = \frac{a^2}{D_t} \qquad (1.55)$$

The turbulent diffusivity can be expressed as a function of the turbulent kinetic energy k and its dissipation ε by

$$D_t = 0.1\frac{k^2}{\varepsilon} \qquad (1.56)$$

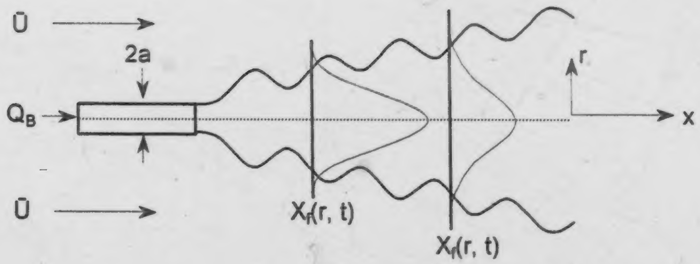

**Figure 1.11** Schematic representation of radial turbulent dispersion of a feed stream (reproduced from Baldyga and Bourne 1999).

Another aspect of mesomixing is related to the inertial-convective process where the coarse scale concentration variance is decayed by the disintegration of large eddies to the Kolmogorov scale ( Figure 1.12). This process proceeds without any direct effect of molecular mixing; however, it does directly affect the environment in which micromixing proceeds. The characteristic time constant describing the reduction in this additional inhomogeneity (Corrsin 1964) is given by

$$t_s = A\left(\frac{\Lambda_c^2}{\varepsilon}\right)^{1/3} \qquad (1.57)$$

where A is a constant of value 1 to 2 and $\Lambda_c$ is the integral scale of concentration fluctuations. $\Lambda_c$ can be taken as the initial concentration fluctuation scale $\Lambda_{co}$, which can be estimated as the feed pipe radius or as $\sqrt{Q_f/\pi U}$ (Baldyga and Bourne 1999).

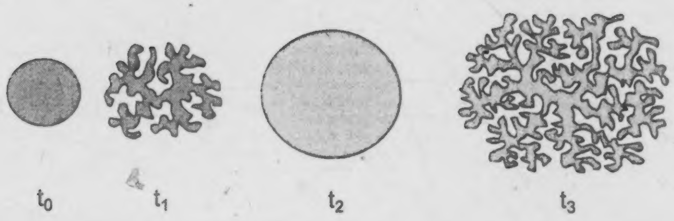

**Figure 1.12** A schematic representation of the inertial-convective disintegration of a fluid element in series with micromixing (reproduced from Baldyga and Bourne 1999).

Micromixing is the smallest of the turbulent mixing scales and is concerned with attaining homogeneity on the molecular scale. It comprises the viscous-convective deformation of fluid elements followed by molecular diffusion (Baldyga and Pohorecki 1995). The effect of accelerating the molecular diffusion by the viscous-convective process is considered to be a significant feature of micromixing. Since chemical reaction requires that molecules be in intimate contact prior to reacting, the micromixing process has the potential to influence the yield and selectivity of fast or instantaneous reactions.

Baldyga and Pohorecki (1995) use the turbulent kinetic energy and concentration fluctuation spectra (Figure 1.10) to distinguish between the different mechanisms of micromixing. Depending on the range of eddy sizes, $\ell$, or wavelengths, k, one of the three subranges applies.

i. In the inertial-convective subrange ($\lambda_K < \ell < L$) large fluid elements are deformed and broken up by fluid motion and their scale is reduced. This process proceeds without any direct effect of molecular mixing and can be identified with the process of inertial-convective mesomixing.

ii. In the viscous-convective subrange ($\lambda_B < \ell < \lambda_K$) eddies are subjected to laminar strain. Since this depends on viscosity, there is a reduction in scale by viscous deformation. The scales become small enough that molecular diffusion begins to be active.

iii. In the viscous-diffusive subrange ($\ell < \lambda_B$) laminar strain and molecular diffusion are equally important. As the scales become even smaller, molecular diffusion rapidly dissipates the concentration variation.

Baldyga and Rohani (1987) showed that for Schmidt numbers much less than 4000, the viscous-diffusive effects are negligible and the intensity of micromixing is represented by the engulfment intensity parameter E

$$E = 0.058\left(\frac{\varepsilon}{\nu}\right)^{½} \qquad (1.58)$$

The characteristic time constant describing mixing by engulfment is approximately equal to $E^{-1}$. The exact definition of the micromixing timescale is

$$t_M = 12\left(\frac{\nu}{\varepsilon}\right)^{½} \qquad (1.59)$$

which is proportional to the Kolmogorov time scale given in Equation ( 1.47 ).

Comparing the characteristic time constants for the various types of mesomixing to the characteristic time constant of micromixing determines which is the controlling mechanism. Baldyga and Bourne (1999) give the parameters used for evaluating the relative importance of point source turbulent dispersion, finite source turbulent dispersion, and inertial-convective mesomixing as, respectively

$$Q_m = \frac{t_D}{t_M}, \qquad Q_{m1} = \frac{t_{D1}}{t_M}, \qquad M = \frac{t_S}{t_M} \qquad (1.60)$$

If $Q_m$, $Q_{m1}$, or M is greater than 1 then mesomixing is the rate-limiting step. For a value of approximately 1, both mesomixing and micromixing must be considered. Where all values are much less than 1, micromixing is the rate-limiting mechanism.

Macromixing can affect the micromixing and mesomixing processes when the feed time, $t_f$, in a semi-batch reactor or the mean residence time, $\bar{t}$, in a CSTR is of the same magnitude as the mean circulation time, $t_C$, or less. In this case the relevant scale of inhomogeneity is that of the vessel and well mixed conditions in the bulk cannot be assumed.

## 1.5 Models of Mixing

In this study, the coupling of Eulerian and Lagrangian perspectives will be used to describe the mixing process. Using the Lagrangian framework, the elementary mixing processes can be followed along the path of a fluid element: disintegration of eddies, engulfment, deformation, molecular diffusion, etc. Linking the Lagrangian framework to the Eulerian flow field permits the fluid element to move through the regions of varying concentration, velocity, flow rate and turbulence in the reactor.

### *1.5.1 Micromixing Model*

There are several mechanistic models available for simulating micromixing. These models are based on simple, idealized mechanisms that enable the mixing process to be simulated. Even though these models often do not describe the physics completely, they are valuable because they can provide insight into the relationship between turbulence and mixing.

Baldyga and Bourne (1989) proposed the engulfment model of micromixing which is based on the assumption that the viscous-convective process controls mixing at scales about equal to or less than the Kolmogorov scale $\lambda_K$. They showed that the effects of molecular diffusion are negligible when compared to the effects of viscous-convective process when Sc < 4000. The simplest case of mixing occurs when a small amount of reactant B is added to a relatively large amount of the second reactant A. For this situation the micromixed volume $V_m$ grows as

$$\frac{dV_m}{dt} = EV_m \qquad V_m(0) = V_{Bo} \tag{1.61}$$

where E is the engulfment parameter given in Equation ( 1.58 ). A mass balance on component i in the mixed volume gives

$$\frac{d(V_m c_i)}{dt} = EV_m\langle c_i\rangle + r_i V_m \tag{1.62}$$

where $\langle c_i\rangle$ is the concentration of component i in the surroundings and $r_i$ is the rate of formation of component i by reaction. Combining Equations ( 1.61 ) and ( 1.62 ) gives the evolution of concentration of component i in the mixed volume

$$\frac{dc_i}{dt} = E(\langle c_i\rangle - c_i) + r_i \tag{1.63}$$

In the more complicated case, the reactant B is added to a similar amount of the second reactant A. Since the reactant B is no longer highly dilute, some self-engulfment will occur and mixing will not be advanced. Baldyga and Bourne (1989) accounted for this by estimating the probability that self-engulfment will occur as

$$P = 1 - X_m \tag{1.64}$$

where $X_m$ is the volume fraction of the mixed volume in the total volume available for mixing. Using Equation ( 1.64 ) in Equations ( 1.61 ) and ( 1.63 ) gives the result

$$\frac{dV_m}{dt} = E\left(1 - X_m\right)V_m \qquad V_m(0) = V_{Bo} \qquad \textbf{( 1.65 )}$$

$$\frac{dc_i}{dt} = E\left(1 - X_m\right)\left(\langle c_i \rangle - c_i\right) + r_i \qquad \textbf{( 1.66 )}$$

Equations ( 1.61 ) and ( 1.65 ) show how the processes of micromixing and mesomixing interact. Mesomixing determines the local surrounding compositions and volume in which micromixing proceeds. Mesomixing controls the mixing process when $X_m \sim 1$, micromixing controls when $X_m \sim 0$ and both mechanisms must be considered when these conditions are not satisfied.

### *1.5.2 Mesomixing Models*

It is well known that microscale concentration inhomogeneity has a direct influence on the products of fast or instantaneous reactions. Likewise, inhomogeneity on larger scales involving macro- and mesomixing can also have an effect on the reaction products, although these effects are mainly indirect in nature. Macromixing deals with the overall bulk circulation in the reactor and is unimportant when the feed time is much greater than the blend time. However, mesomixing occurs at relatively smaller scales and may still be inhomogeneous relative to the microscale for high feed rates. Baldyga and Bourne (1999) identified two mesomixing mechanisms and proposed the following models to simulate the processes.

## Turbulent Dispersion Mesomixing

For a point source with homogenous turbulence, and $D_t$ and U being constant, the radial distribution of the volume fraction of B-rich feed sufficiently far downstream from the feed pipe exit is

$$X_f(r,t) = \frac{Q_f}{4\pi D_t x} \exp\left( - \frac{Ur^2}{4D_t x} \right) \qquad (1.67)$$

Micromixing proceeds within this volume fraction of B-rich fluid created by turbulent dispersion. This formulation neglects molecular diffusion relative to turbulent diffusion; the respective diffusivities are $10^{-9}$ and $10^{-4}$. The B-rich fluid is dispersed radially, transverse to the direction of fluid flow. The variance of the volume fraction distribution grows according to

$$\sigma^2 = \frac{4D_t x}{U} \qquad (1.68)$$

In the case of finite source with homogenous turbulence, and $D_t$ and $\bar{U}$ being constant, the following is given

$$X_f(r,t) = \frac{Q_f}{2\pi a^2 D_t x} \exp\left( - \frac{Ur^2}{4D_t x} \right) \times \int_0^a \exp\left( - \frac{Ur'^2}{4D_t x} \right) I_o \left( \frac{Urr'}{2D_t x} \right) r'dr' \qquad (1.69)$$

where $I_o$ is the modified Bessel function of the first kind of order zero.

## Inertial-Convective Mesomixing

Baldyga et al. (1997) used the eddies-in-eddies interpretation of inertial-convective mesomixing to develop a mathematical model based on the rate of decay of variance in the inertial-convective subrange of the concentration spectrum. They proposed the following

$$\frac{dX_u}{dt} = \frac{X_u(1 - X_u)}{t_s} \qquad X_u(0) = X_{Bo} \qquad (1.70)$$

where $X_u$ is the local volume fraction where B is present but not necessarily micromixed. Micromixing can only occur within the eddies of volume fraction $X_u$, therefore the micromixing equations must be modified to account for this effect. Now the micromixing Equations ( 1.65 ) and ( 1.66 ) become

$$\frac{dV_m}{dt} = E\left(1 - \frac{X_m}{X_u}\right)V_m \qquad V_m(0) = V_{Bo} \tag{1.71}$$

$$\frac{dc_i}{dt} = E\left(1 - \frac{X_m}{X_u}\right)\left(\langle c_i \rangle - c_i\right) + r_i \tag{1.72}$$

Equation ( 1.71 ) shows that the initial growth of the micromixed volume is zero since both $X_m$ and $X_u$ equal $X_{Bo}$. However, as eddy breakup increases $X_u$, the constraint of self-engulfment in Equation ( 1.71 ) is relaxed and micromixing is initiated.

Equation ( 1.71 ) also shows that mesomixing retards micromixing when mesomixing is incomplete ($X_u < 1$), and that when mesomixing is rapid relative to micromixing ($X_u \sim 1$) the equations reduce to the micromixing engulfment model with self-engulfment (Equations ( 1.65 ) and ( 1.66 )).

## 1.6 Stirred Tank Reactor

The stirred tank reactor is one of the most commonly used reactors for investigating mixing since the local mixing rate can be easily determined from the well known turbulence and flow fields. In the case of this study, the stirred tank was equipped with four baffles and a six-bladed Rushton turbine as a radial flow impeller (Figure 1.13). The vessel geometry was standard and the dimensions are given in Table 1.2. The impeller clearance is the distance from the bottom of tank to the center of the impeller. The tank diameter used in this study was 0.2 m.

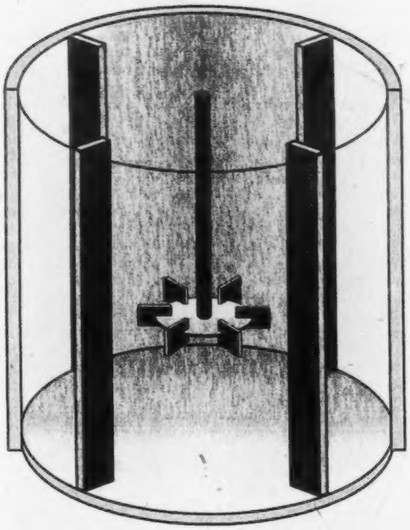

**Figure 1.13** The stirred tank reactor equipped with a radial pumping, six-bladed Rushton turbine.

**Table 1.2** Dimensions of the stirred tank reactor.

| Description | Symbol | Value |
|---|---|---|
| Tank diameter | T | T |
| Impeller diameter | D | T/4 or T/3 |
| Impeller blade height | $D_H$ | D/5 |
| Impeller blade width | $D_W$ | D/4 |
| Impeller clearance | C | T/4 |
| Baffle width | W | T/12 |
| Initial liquid height | $H_o$ | T/2 |
| Final Liquid height | $H_f$ | T |

The average flow properties in the stirred tank can be characterized by the impeller Reynolds number, which is based on the impeller tip speed (~ND) and diameter

$$Re = \frac{ND^2}{\nu} \qquad (1.73)$$

where N is the rotational speed. The flow is taken to be fully turbulent near the impeller for Reynolds numbers greater than $2 \times 10^4$, although Kresta et al. (2001) reported that much larger Reynolds numbers are required for the turbulence to penetrate throughout the tank. When the flow is fully turbulent, the impeller power number $N_P$ becomes independent of the Reynolds number, and the power injected into the system by shaft work is

$$P = \rho N_p N^3 D^5 \qquad (1.74)$$

where $N_P = 5.5$ for a six-bladed Rushton turbine.

The circulating flow in a stirred tank is driven by the primary pumping capacity of the turbine. The pumping capacity is given by

$$Q = N_Q N D^3 \qquad (1.75)$$

where $N_Q$ is the flow number and is equal to 0.76 for a six-bladed Rushton turbine. Figure 1.14 shows the circulation pattern in a fully baffled stirred tank at two different fill heights as determined by CFD using multiple reference frames. It should be noted that the circulation pattern in the lower portion of the tank remains constant with changes in the fill height, while the residence time in the upper portion of the tank increases as the tank fills. The flow from a Rushton turbine is a swirling radial jet that leaves the impeller blades at an angle of 45° to the radial direction (Kresta and Wood 1991). As the discharge travels towards the tank wall, the peak velocity decays as the inverse of the distance traveled and the spreading half-angle of the jet is taken to be 9.6° (Kresta and Wood 1991, Figure 1.15). As the flow impinges on the tank wall, the baffles remove the remaining angular component and redirect the flow to the top and bottom of the tank. Kresta et al. (2001) considered the flow at the tank wall to be an annular wall jet, and concluded that this wall jet drives the recirculating flow.

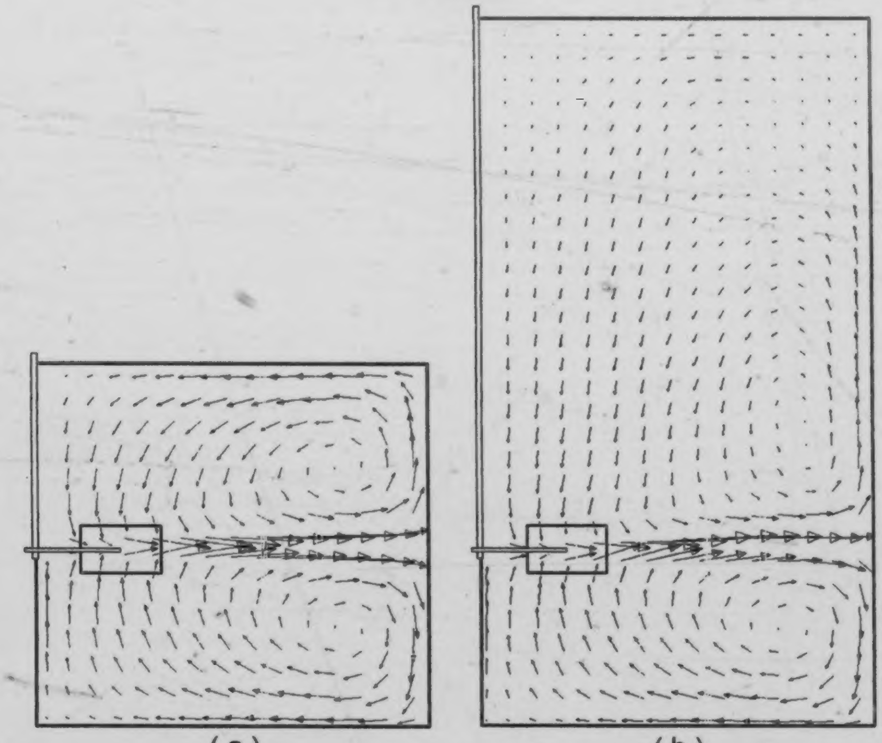

**Figure 1.14** CFD simulated flow field for a Ruston turbine with T = 2 m, D = T/3, C = T/4, and N = 10.5 rps. (a) $H_o$ = T/2, and (b) $H_f$ = T

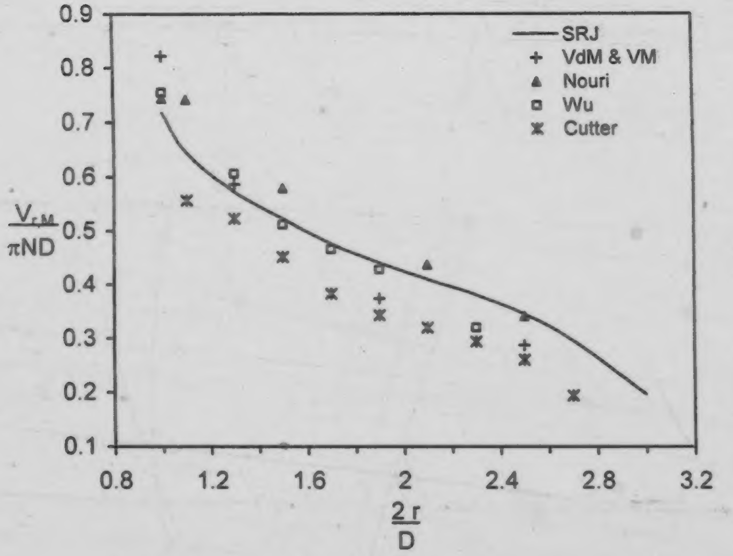

**Figure 1.15** Decay of dimensionless radial velocity on impeller centerline: for D = T/3. (data from Kresta and Wood, 1991)

In stirred tanks the turbulence energy is maintained by power injected through impeller rotation. Often the average power input per unit mass of fluid is used to characterize the turbulence conditions, although it is not sufficient to completely define the system. For instance, the same average power input per unit mass can result in very different distributions of turbulence energy dissipation when different impellers are used in the same tank. The distribution created by a Rushton turbine results in 15% of the total power injected being dissipated within the impeller swept volume (Zhou and Kresta 1996 a, D = T/2 at C = T/2), with the maximum dissipation at the impeller tip being 2.8 and 3.8 times greater for impeller diameters of D/4 and D/2, respectively (Zhou and Kresta 1996 b, C = T/4). Kresta and Wood (1991) recommend that the integral turbulent length scale should equal the characteristic diameter of the trailing vortices ($D_H/2$ or D/10) in this region. Kresta and Wood (1991) also reported that the maximum turbulent kinetic energy and dissipation decay with distance traveled from the impeller tip in proportion to $\left(2r/D\right)^{-2}$ and $\left(2r/D\right)^{-4}$, respectively (Figure 1.16 and

Figure 1.17). Kresta et al. (2001) suggest that the turbulent velocity fluctuations within the wall jet are 15% of the impeller tip speed, and that the integral turbulent length scale is equal to the baffle width (T/10). After integrating the dissipation over these zones, the remaining power is dissipated over the remaining tank volume. The integral turbulent length scale is approximated as T/10 in this region.

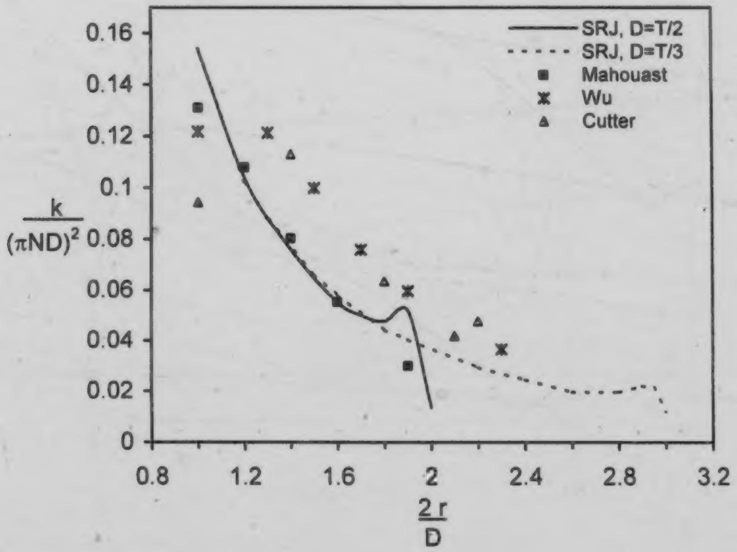

**Figure 1.16** Decay of dimensionless turbulence kinetic energy on impeller centerline. (data from Kresta and Wood, 1991)

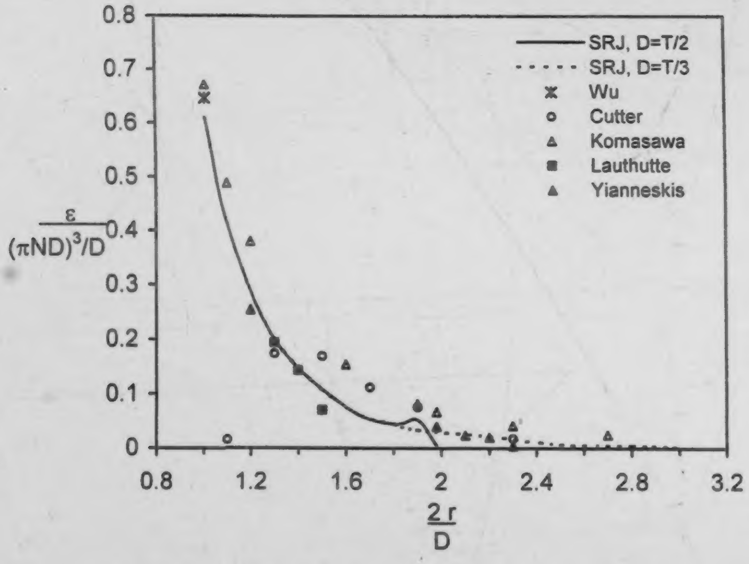

**Figure 1.17** Decay of dimensionless turbulence kinetic energy dissipation on impeller centerline. (data from Kresta and Wood, 1991)

## 1.7 Previous Models of Silver Halide Precipitation

The importance of silver halide precipitates in the photographic industry has led to extensive studies of how to improve the quality of photographic emulsions. However, very few studies have attempted to investigate the precipitation process using a numerical model. The first work of this kind was that of Margolis and Gutoff (1974) but their model was oversimplified and gave only qualitatively correct results. The model was based on the following assumptions:

i. the precipitation vessel was approximated as a well-mixed reactor;
ii. the size of the newly formed nuclei was taken to be 0.1 μm;
iii. the crystal growth rate was directly proportional to the supersaturation;

iv. McCabe's law applied, therefore the growth rate was only a direct function of supersaturation;

v. the solubility varied with size according to the Gibbs-Thompson effect, hence supersaturation (i.e. growth rate) varied with crystal size;

vi. the nucleation rate was proportional to a power of the supersaturation measured with respect to the nuclei size;

vii. the crystals were assumed to be spherical;

viii. the chemical complexes $AgBr_i^{1-i}$ were taken into consideration;

ix. the growth and nucleation constants were chosen to give reasonable results.

In light of the complexity associated with each of these simplifying assumptions, this model was able to qualitatively predict the increase in average crystal size with increased addition time, with increased temperature, and with increased halide levels.

Villermaux and co-workers (1988) began a series of studies into the numerical modeling of the precipitation process, which ultimately led to the modeling of silver bromide precipitation in a double-jet semi-batch reactor. Muhr et al. (1995) updated this model based on the significant amount of research conducted on silver halide precipitation since 1974. Using the now known kinetic and thermodynamic parameters, the model involved fewer approximations than the Margolis and Gutoff model. The Muhr et al. model is based on the following statements:

i. the precipitation vessel is approximated as a well-mixed reactor;

ii. the size of the newly formed nuclei is a function of the supersaturation;

iii. the crystal growth rate is controlled by both diffusion and integration of the species on the crystal surface;

iv. the solubility varies with size according to the Gibbs-Thompson effect;
v. the nucleation rate is a function of supersaturation according to classical nucleation theory (Volmer and Weber 1926);
vi. the crystal morphology is described through surface and volume shape factors;
vii. the chemical complexes $AgBr_i^{1-i}$ are taken into consideration;
viii. the growth rate constants were extracted from the literature and the nucleation rate constants were fitted to experimental results.

The trial results obtained by this model were satisfactory, and were particularly useful for pointing out the problems with the physical model and numerical methods. Muhr et al. (1996) examined these problems, established solutions, and concluded that this base model should be appropriate to introduce micromixing for assessing the effects of mixing on the precipitation process. However, their mixing model has not yet been published.

Leubner (2001) developed the Balanced Nucleation and Growth (BNG) model based on the observation that existing nucleation models and theories do not yield useful information to model the results of certain crystallization processes. For instance, classical nucleation theory predicts continuous nucleation during the precipitation of insoluble materials like silver halides, but in some experiments only a limited number of crystals are obtained. In contrast to this, the BNG model assumes that only the excess supersaturation remaining after maximum population growth can be converted to nuclei. Nucleation ends when the maximum population growth equals or exceeds the rate of newly added material. However, this formulation ignores the possibility of continuous unstable nuclei formation in the high supersaturation region near the feed point (Berry 1976). Using several adjustable parameters the BNG model predicts that increasing the initial nucleation rate or crystal growth rate reduces the time during which new crystals are formed, and that increasing the addition rate has the opposite effect. This model also correctly predicts the experimental result that in many crystallization processes a limited number of crystals are formed during the nucleation period. This model is, however, unable to quantitatively predict the required parameters and is fundamentally not suitable for use with mixing models.

In light of the progress made with previous precipitation models, the opportunity to incorporate a comprehensive mixing model still exists. Such a model could provide useful insights into the interactions between turbulence, feed rate, feed location, bulk blending, nucleation and subsequent crystal growth, in turn providing a better process understanding to improve precipitation scale-up protocol.

## 1.8 Conclusions

The use of silver halide crystals in photographic applications requires that average crystal characteristics such as shape, size, thickness and halide composition be tightly controlled. It is well known that both reactor design and mixing have a strong influence on product quality, and that successful prediction of the average characteristics under different mixing conditions, especially mesomixing, is frequently difficult. Very few attempts have been made to numerically model silver halide precipitations, and until now none have incorporated the effects of micromixing or mesomixing into the precipitation model.

The concepts introduced in this chapter have gone beyond the fundamentals describing crystallization and mixing, and into the theory used to model these processes. The improved precipitation model developed in Chapter 2 uses these ideas to establish a foundation for simulations. Specifically, this model is based on the three main processes of precipitation theory: nucleation, crystal growth and Ostwald ripening, as well as advancing to now include the influence of local mixing on these processes within a stirred tank reactor. The key model equations presented in this chapter are summarized in Table 1.3.

**Table 1.3** Summary: Key model equations.

| Description | Equation | Model Development |
|---|---|---|
| Supersaturation | ( 1.2 ) | Section 2.3.1 pp.74 |
| Nucleation | | Section 2.3.2 pp.80 |
| Crystal Growth | ( 1.24 ) | Section 2.3.3 pp.81 |
| Discretized Population Balance | ( 1.41 ) | Section 2.3.4 pp.82 |
| Micromixing | ( 1.65 ) and ( 1.66 ) | Section 2.2.3 pp.68 |
| Turbulent Dispersion Mesomixing | ( 1.67 ) | Section 2.2.3 pp.68 |
| Inertial-Convective Mesomixing | ( 1.70 ) | Section 2.2.3 pp.68 |

# Chapter 2

## Model Development

## 2.1 Model Overview

The significance of this model development arises from its uniqueness. Never before has a model been developed that incorporates nucleation, multiple species thermodynamic equilibria, size-dependent growth kinetics, discretized population balances and accurate modeling of turbulent flow. Others have previously modeled combinations of some of these aspects, but none have developed a model that incorporates all of them simultaneously. The uniqueness of the model also allows it to be used for modeling various other mixing problems. For instance, the model can be easily converted to use different thermodynamic data, growth kinetics, tank geometries or flow fields.

The program was written in Fortran 90 code as it supercedes previous versions of Fortran and is often encountered in industry. During all of the programming stages emphasis was placed on developing reliable and maintainable software. This demanded that the code be produced using three main criteria: first, the code was developed using a top-down design technique that broke the program into logical portions (procedures) that are independent and can be implemented or replaced separately. Second, the procedures were extensively tested before combining them into a finished product. Third, the combined model was validated using experimental data.

Specifically, the model under development tracks the consumption of silver within the silver feed stream as it mixes with and moves through the bulk kettle volume. The silver feed stream is discretized into $\Delta t_E$ time steps or discrete feed volumes (DFV) that travel through the kettle until the feed silver is completely consumed by nucleation or mixing has progressed as far as possible. At this point the remaining contents of the DFV are added to the bulk kettle volume and the concentration and population balances are updated for the kettle.

A brief outline of the logic used in developing the precipitation model is given in Figure 2.1. Refer to Appendix D for complete detailed logic diagrams.

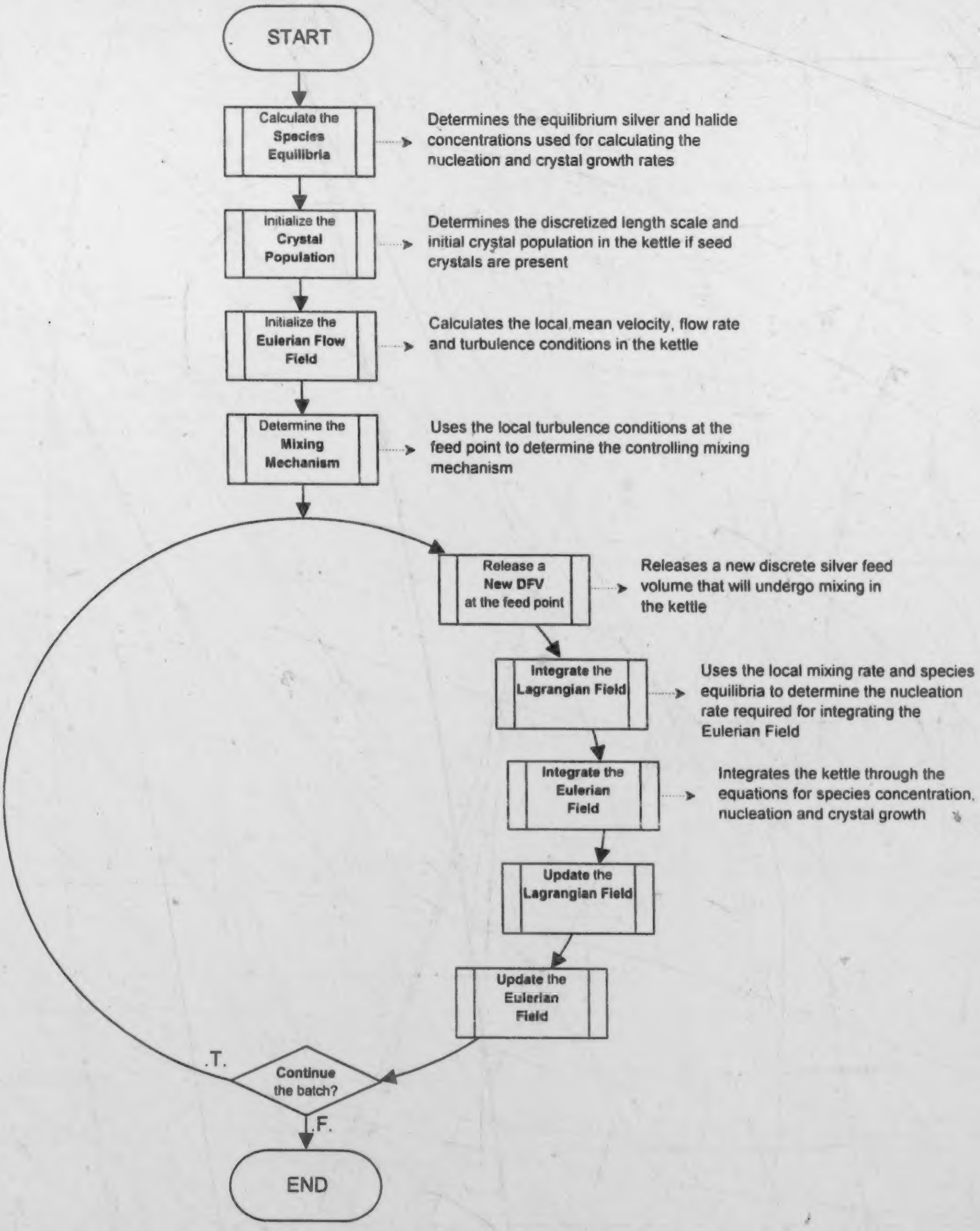
START
Calculate the Species Equilibria
Determines the equilibrium silver and halide concentrations used for calculating the nucleation and crystal growth rates
Initialize the Crystal Population
Determines the discretized length scale and initial crystal population in the kettle if seed crystals are present
Initialize the Eulerian Flow Field
Calculates the local mean velocity, flow rate and turbulence conditions in the kettle
Determine the Mixing Mechanism
Uses the local turbulence conditions at the feed point to determine the controlling mixing mechanism
Release a New DFV at the feed point
Releases a new discrete silver feed volume that will undergo mixing in the kettle
Integrate the Lagrangian Field
Uses the local mixing rate and species equilibria to determine the nucleation rate required for integrating the Eulerian Field
Integrate the Eulerian Field
Integrates the kettle through the equations for species concentration, nucleation and crystal growth
Update the Lagrangian Field
Update the Eulerian Field
.T.
Continue the batch?
.F.
END

**Figure 2.1** A brief outline of the logic used in the precipitation model.

## 2.2 Mixing Model

The model developed here uses the approach of coupling the Eulerian and Lagrangian perspectives to describe the mixing process. Within the Lagrangian framework the various mixing processes can be followed along the path of a discrete feed volume (DFV): micromixing, inertial-convective mesomixing and turbulent-dispersion mesomixing. Linking the Lagrangian framework to the Eulerian flow field allows the DFV to experience changes in the mixing process as it passes through zones of varying velocity, flow rate and turbulence in the tank. The main assumptions in the model are:

i. the silver reactant remains in the DFV and is segregated from the bulk of the precipitation kettle until it is completely consumed or mixing is complete;
ii. there is no self-mixing between DFVs because of the time discretization (i.e. DFVs cannot exist in the same space-time);
iii. the bulk of the precipitation is well mixed;
iv. the halide feed is located at 180° to the silver feed and is well mixed into the bulk before it encounters the silver feed stream;

Chapter 1 introduced general aspects of the stirred tank reactor and mixing models used in the following development.

### *2.2.1 Eulerian Flow Field Model (fixed frame)*

The Eulerian Flow Field Model (EFM) idea was originated by Bourne and Yu (1994), who fit the best available data at the time to an estimated velocity field. The approach used here takes advantage of a significant amount of data published since then by Kresta and Wood (1991), Zhou and Kresta (1996a & b), and Kresta et al. (2001) to model the circulation patterns and turbulence conditions in a fully baffled stirred tank with a Rushton turbine. The circulation pattern for this configuration is shown in Figure 1.14. The tank is divided into zones (Figure 2.2) where average properties can be applied such as the direction of flow, velocity, U, turbulent kinetic energy, k, and the rate of turbulent kinetic energy dissipation, $\varepsilon$. The following constraints were used in development of the model:

i. continuity must be satisfied at any radial or axial cross section of the tank;

ii. all of the power injected by the impeller is dissipated as turbulent kinetic energy;

iii. the minimum initial fill height is $H_o = T/2$, and the maximum final fill height is $H_f = T$;

iv. the impeller diameter is between $D = T/4$ and $D = T/2$, and the off-bottom clearance is $C = T/4$;

v. the flow is axisymmetric (i.e. no variation in the angular direction);

vi. the impeller flow number $N_Q$, the impeller power number $N_P$, and the fractional split at the wall $SF_W$ are known, and may be taken as 0.76, 5.5, and 0.5 if no better values are available.

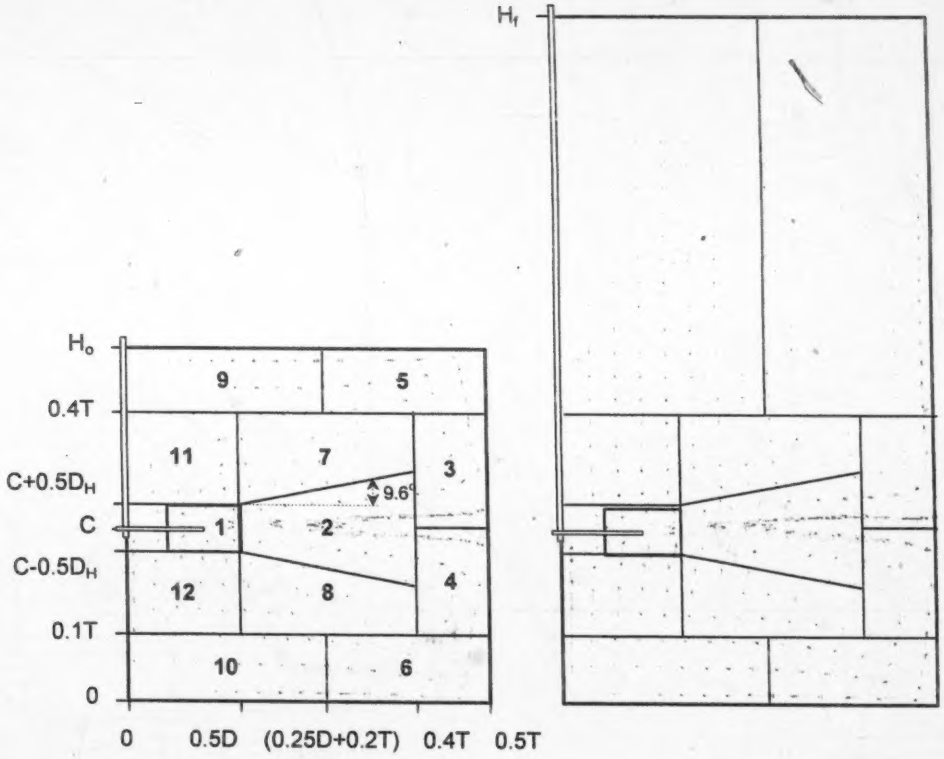

( a ) ( b )

**Figure 2.2** Circulation pattern for a fully baffled stirred tank reactor with a Rushton turbine divided into zones of similar hydrodynamic properties (D = T/3, C = T/4). a) Initial fill height of $H_o$ = T/2, b) Final fill height of $H_f$ = T.

The model development for each zone is now summarized in turn, with all of the final equations given in Table 2.1 and the values for the kettle geometry used in this study given in Table 2.2. In each case the turbulent kinetic energy is determined by estimating the turbulent fluctuating velocity u from the rate of turbulent kinetic energy dissipation and the local characteristic turbulent length scale ℓ according to Equation ( 1.42 ). This gives

$$u = (\varepsilon \ell)^{1/3} \qquad (2.1)$$

and the turbulent kinetic energy for isotropic turbulence as

$$k = \frac{3}{2}(\varepsilon\ell)^{2/3} \qquad (2.2)$$

***Zone 1: Impeller Swept Volume***

This volume is used to initialize the circulating flow with the primary pumping capacity of the impeller. The volumetric flow rate out of this volume is well defined by Equation ( 1.75 ) as $Q = N_QND^3$. Mean velocities in this volume are not modeled, and all DFVs entering this volume are immediately folded into the bulk as this volume is assumed to be well mixed.

The rate of turbulent energy dissipation is taken from Zhou and Kresta (1996a) for an impeller of diameter $D = T/2$ at an off-bottom clearance of $C = T/2$ as 15% of the total power inputted by shaft work, divided by the mass of fluid in the impeller swept volume. The characteristic turbulent length scale is taken as D/10 (Kresta and Wood 1991).

***Zone 2: Impeller Discharge Stream***

The impeller discharge stream forms the core of the model, as the changes occurring in this zone define the rest of the flow field. In this zone, the velocity profile exhibits self-similarity so that given the local maximum velocity; the local mean velocity and volumetric flow rate are known. The peak maximum velocity at the impeller tip is taken as 70% of the impeller tip speed ($\pi ND$). The decay of the local maximum velocity in the swirling radial jet is inversely related to the distance traveled, r (Figure 2.3). The mean velocity at the impeller tip is taken as the superficial velocity ($5N_QND/\pi$), which equals $0.725N_Q$ of the local maximum velocity. The jet spreading half-angle is 9.6° as taken from Kresta and Wood (1991).

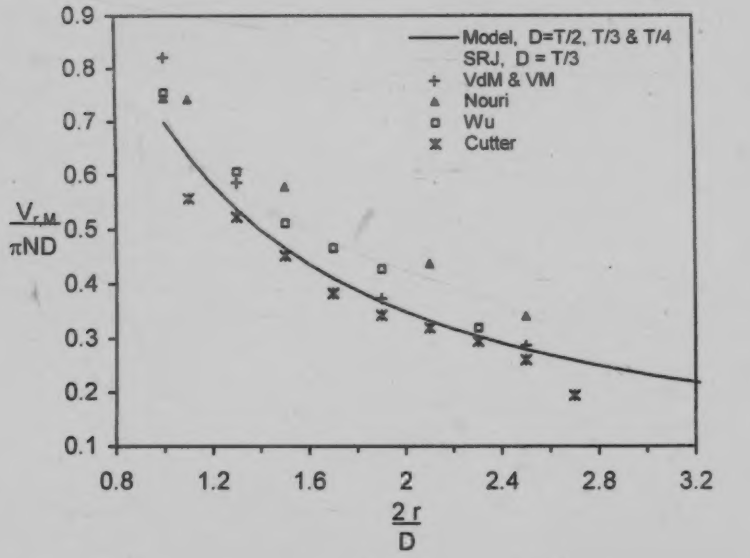

**Figure 2.3** Comparison of predicted and experimental decay of maximum dimensionless velocity on the impeller centerline (data taken from Kresta and Wood 1991).

The rate of turbulent kinetic energy dissipation decays as $1/r^4$ (Figure 2.4) and turbulent kinetic energy decays as $1/r^2$ (Figure 2.5), as taken from Kresta and Wood (1991). The maximum rate of turbulent kinetic energy dissipation at the impeller tip is $14.8N^3D^2$ and $19.9N^3D^2$ for impeller diameters of D = T/4 and D = T/2, respectively (Zhou and Kresta 1996b, C = T/4). Maximum rates of dissipation for intermediate impeller diameters can be estimated by linearly interpolating between these two limits. The mean rate of dissipation is estimated as 80% of the maximum as taken from Zhou and Kresta (1996b). The characteristic turbulent length scale is taken as D/10 (Kresta and Wood 1991).

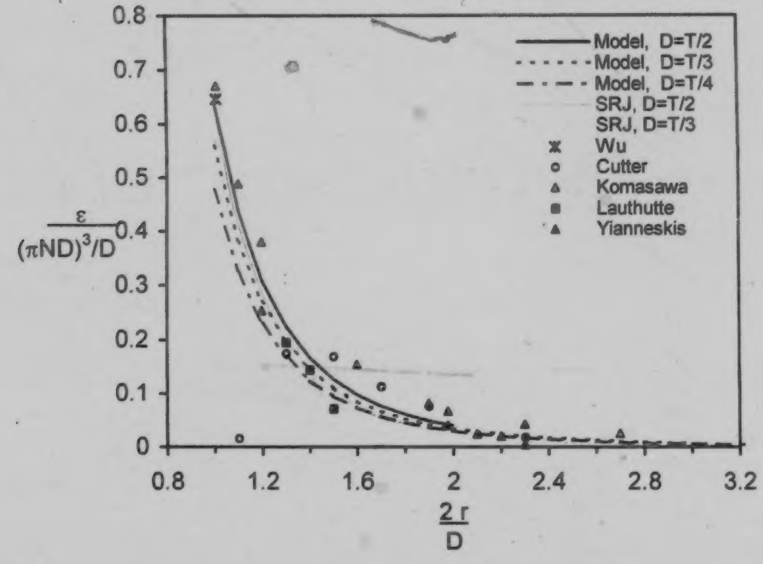

**Figure 2.4** Comparison of predicted and experimental decay of maximum dimensionless turbulent kinetic energy dissipation on the impeller centerline (data taken from Kresta and Wood 1991).

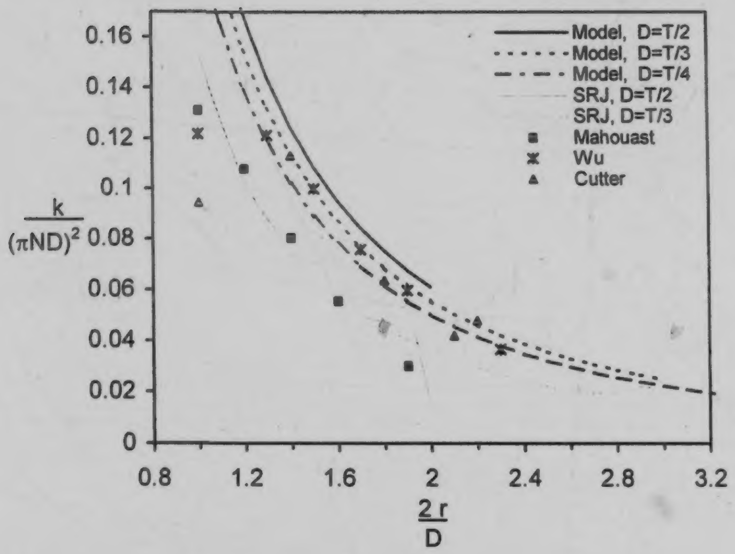

**Figure 2.5** Comparison of predicted and experimental decay of maximum dimensionless turbulent kinetic energy on the impeller centerline (data taken from Kresta and Wood 1991).

***Zones 3 and 4: Wall Jets***

These zones extend over a small portion of the tank height, from the point where the impeller discharge impinges on the wall, to the point where the return radial flow begins. This region only covers the constant velocity core of the wall jet where the turbulent fluctuating velocity u can be estimated as 50% of the local peak velocity (Kresta et al. 2001), or 145% of the local mean velocity. The dissipation is then estimated by Equation ( 1.42 ) as $u^3/\ell$, where the characteristic turbulent length scale is taken as the baffle width T/10 (Kresta et al. 2001).

The split fraction at the wall of the tank $SF_W$ appears in several equations throughout the model, and is defined as the fraction of the impeller discharge flow that enters the upper wall jet (zone 3). The fraction of the flow entering the lower wall jet (zone 4) is then $(1-SF_W)$.

### *Zones 5 and 9: Top Surface*

The volume at the top surface of the tank is divided into two portions to facilitate the movement of the Lagrangian DFV. This is not a physical hydrodynamic boundary. This boundary is positioned to have equal volumetric flow rates entering zone 7 from zones 5 and 9.

The mean velocity at the surface of the tank is a function of radius, as is the mean velocity in zone 2. The velocity at any radial position is determined by continuity, the wall split fraction and the cross sectional area available for flow. As the volume of fluid in the tank increases, all of the additional volume is contained in zones 5 and 9. This affects the cross sectional area available for flow, making the velocity in zones 5 and 9 a function of both radius and time.

After integration of the mean dissipation rates over zones 1, 2, 3 and 4, the remaining power is dissipated in the bulk volume. An average dissipation is determined for zones 5 through 12, based on the bulk volume of fluid in the tank at time zero. As the tank is filled, the total dissipation in zones 5 and 9 is held constant, therefore causing the average dissipation in these zones to decrease in proportion to the increase in their volume. The characteristic turbulent length scale is taken as the width of the wall baffle, T/10 (Kresta et al. 2001).

### *Zones 6 and 10: Bottom Surface*

The volume at the bottom surface of the tank is divided into two portions to facilitate the movement of the Lagrangian DFV, and is not a physical hydrodynamic boundary. This boundary is positioned to have equal volumetric flow rates entering zone 8 from zones 6 and 10.

The mean velocity at the bottom surface of the tank is a function of radius, as is the mean velocity in zone 2. The velocity at any radial position is determined by continuity, the wall split fraction and the cross sectional area available for flow.

The rates of turbulent kinetic energy dissipation and turbulent kinetic energy are the mean values for zones 6 through 10 (see zone 5).

### *Zones 7 and 8: Top and Bottom Returns to the Discharge Stream*

The flow in these zones is driven by the entrainment of the impeller discharge stream as it travels outwards to the wall of the tank. The velocity at any axial position is determined by continuity, the wall split fraction and the cross sectional area available for flow.

The rates of turbulent kinetic energy dissipation and turbulent kinetic energy are the mean values for zones 6 through 10 (see zone 5).

### *Zones 11 and 12: Top and Bottom Returns to the Impeller Volume*

The velocity at any axial position is completely defined by the primary pumping capacity of the impeller, the wall split fraction and the cross sectional area available for flow.

The rates of turbulent kinetic energy dissipation and turbulent kinetic energy are the mean values for zones 6 through 10 (see zone 5).

**Table 2.1** Definition and associated equations for the Eulerian Flow Field Model.

| Zone | **Dimensions** [a] **(m)** | **Volumetric Flow Rate ($m^3/s$)** | **Mean Velocity (m/s)** | **Mean Rate of Dissipation (W/kg)** | **Mean Turbulent Kinetic Energy (J/kg)** |
|---|---|---|---|---|---|
| **1: Impeller Swept Volume** | **$r = 0$ to $D/2$**<br>$\Delta z = D/5$ | $N_QND^3$ | $5\ N_QND/\pi$ | $3\ N_PN^3D^2/\pi$ | $1.5(\varepsilon_1 D/10)^{2/3}$ |
| **2: Impeller Discharge Stream** | **$r = D/2$ to $0.4T$**<br>$\Delta z = 0.024D+0.35r$ | $U_2(r)\Delta z(r)\pi r$ | $5Q_1/(2\pi Dr)$ | $\varepsilon_{peak}/(2r/D)^4$<br>see note b | $1.5(\varepsilon_2 D/10)^{2/3}$ |
| **3: Upper Wall Jet** | $r = 0.4T$ to $0.5T$<br>**$z = 0.25T$ to $0.4T$** | $SF_W\,Q_2(0.4T)$ | $Q_3/(0.09\pi T^2)$ | $(1.45U)^3/(T/10)$ | $1.5(\varepsilon_3 T/10)^{2/3}$ |
| **4: Lower Wall Jet** | $r = 0.4T$ to $0.5T$<br>**$z = 0.25T$ to $0.1T$** | $(1-SF_W)\,Q_2(0.4T)$ | $-Q_4/(0.09\pi T^2)$ | $(-1.45U)^3/(T/10)$ | $1.5(\varepsilon_4 T/10)^{2/3}$ |
| **5: Outer Top Surface** | **$r = 0.5T$ to $(D/4+T/5)$**<br>$\Delta z = 0.1T+\Sigma Q_{feed}t/(\pi T^2/4)$ | $SF_W\,Q_2(r)$ for $r < 0.4T$<br>$Q_3$ for $r > 0.4T$ | $-Q_5/(2\pi\Delta z_5 r)$ | $\varepsilon_{bulk}$<br>see note c | $k_{bulk}$<br>see note d |
| **6: Outer Bottom Surface** | **$r = 0.5T$ to $(D/4+T/5)$**<br>$\Delta z = 0.1T$ | $(1-SF_W)\,Q_2(r)$ for $r < 0.4T$<br>$Q_4$ for $r > 0.4T$ | $-Q_6/(0.2\pi Tr)$ | $\varepsilon_{bulk}$ | $k_{bulk}$ |
| **7: Upper Return** | $r = D/2$ to $0.4T$<br>**$z = 0.4T$ to $z_2(r)$** | $Q_3-Q_{11}$ | $-Q_7/(\pi(0.16T^2-D^2/4))$ | $\varepsilon_{bulk}$ | $k_{bulk}$ |
| **8: Lower Return** | $r = D/2$ to $0.4T$<br>**$z = 0.1T$ to $z_2(r)$** | $Q_4-Q_{12}$ | $Q_8/(\pi(0.16T^2-D^2/4))$ | $\varepsilon_{bulk}$ | $k_{bulk}$ |
| **9: Inner Top Surface** | **$r = (D/4+T/5)$ to $0$**<br>$\Delta z = 0.1T+\Sigma q_{feed}t/(\pi T^2/4)$ | $Q_{11}$ for $r < D/2$<br>$SF_W\,Q_2(r)$ for $r > D/2$ | $-Q_9/(2\pi\Delta z_9 r)$ | $\varepsilon_{bulk}$ | $k_{bulk}$ |

| | | | | | |
|---|---|---|---|---|---|
| **10: Inner Bottom Surface** | **$r = (D/4+T/5)$ to 0**<br>$\Delta z = 0.1T+\Sigma Q_{feed}t/(\pi T^2/4)$ | $Q_{12}$ for $r < D/2$<br>$(1-SF_W)\ Q_2(r)$ for $r > D/2$ | $-Q_{10}/(0.2\pi Tr)$ | $\varepsilon_{bulk}$ | $k_{bulk}$ |
| **11: Upper Impeller Suction** | $r = 0$ to $D/2$<br>**$z = 0.4T$ to $(0.25T+D/10)$** | $SF_W\ N_QND^3$ | $-Q_{11}/(\pi D^2/4)$ | $\varepsilon_{bulk}$ | $k_{bulk}$ |
| **12: Lower Impeller Suction** | $r = 0$ to $D/2$<br>**$z = 0.1T$ to $(0.25T-D/10)$** | $(1-SF_W)\ N_QND^3$ | $Q_{12}/(\pi D^2/4)$ | $\varepsilon_{bulk}$ | $k_{bulk}$ |

[a] direction of flow in bold

[b] peak rate of turbulent kinetic energy dissipation at the impeller tip

[c] bulk rate of turbulent kinetic energy dissipation obtained by difference

$$P_{total}/\rho = N_PN^3D^5$$

$$P_1/\rho = 0.15P_{total}$$

$$P_2/\rho = 80\% \text{ of } \int_{D/2}^{0.4T} \varepsilon_2 \Delta z_2 \pi r\, dr$$

$$P_3/\rho = \varepsilon_3 Vol_3$$

$$P_4/\rho = \varepsilon_4 Vol_4$$

$$P_{bulk} = P_{total}-P_1-P_2-P_3-P_4$$

$$Vol_{bulk} = \pi H_o T^2/4-Vol_1-Vol_2-Vol_3-Vol_4$$

$$\varepsilon_{bulk} = P_{bulk}/\rho/Vol_{bulk}$$

[d] bulk turbulent kinetic energy

$$k_{bulk} = 1.5(\varepsilon_{bulk}T/10)^{2/3}$$

**Table 2.2** Eulerian Flow Field Model for the kettle geometry used in this study (Rushton turbine, T = 0.2 m, $H_o$ = T/2, D = T/4, N = 16.7 rps).

| Zone | Dimensions (m) | Volumetric Flow Rate ($m^3/s$) | Mean Velocity (m/s) | Mean Rate of Dissipation (W/kg) | Mean Turbulent Kinetic Energy (J/kg) |
|---|---|---|---|---|---|
| **1: Impeller Swept Volume** | **r = 0 to 0.025**<br>$\Delta z = 0.01$ | $1.6\text{x}10^{-3}$ | 1.01 | 61.1 | 0.68 |
| **2: Impeller Discharge Stream** | **r = 0.025 to 0.08**<br>$\Delta z = 0.0012+0.35r$ | $U_2(r)\Delta z(r)\pi r$ | 0.0252/r | $6.7\text{x}10^{-5}/r^4$ | $1.5(0.005\varepsilon_2)^{2/3}$ |
| **3: Upper Wall Jet** | r = 0.08 to 0.1<br>**z = 0.05 to 0.08** | $2.3\text{x}10^{-3}$ | 0.21 | 1.3 | 0.13 |
| **4: Lower Wall Jet** | r = 0.08 to 0.1<br>**z = 0.05 to 0.02** | $2.3\text{x}10^{-3}$ | -0.21 | 1.3 | 0.13 |
| **5: Outer Top Surface** | **r = 0.1 to 0.0525**<br>$\Delta z = 0.02+\Sigma Q_{feed}t/(\pi 0.01)$ | $0.5\ Q_2(r)$ for $r < 0.08$<br>$2.3\text{x}10^{-3}$ for $r > 0.08$ | $-Q_5/(2\pi\Delta z_5 r)$ | 1.0 | 0.1 |
| **6: Outer Bottom surface** | **r = 0.1 to 0.0525**<br>$\Delta z = 0.02$ | $0.5\ Q_2(r)$ for $r < 0.08$<br>$2.3\text{x}10^{-3}$ for $r > 0.08$ | $-Q_6/(\pi 0.04r)$ | 1.0 | 0.1 |
| **7: Upper Return** | r = 0.08 to 0.025<br>**z = 0.08 to $z_2(r)$** | $1.6\text{x}10^{-3}$ | -0.085 | 1.0 | 0.1 |
| **8: Lower Return** | r = 0.08 to 0.025<br>**z = 0.02 to $z_2(r)$** | $1.6\text{x}10^{-3}$ | 0.085 | 1.0 | 0.1 |

| | | | | | |
|---|---|---|---|---|---|
| **9: Inner Top Surface** | **$r = 0.0525$ to 0**<br>$\Delta z = 0.02+\Sigma Q_{feed}t/(\pi 0.01)$ | $7.9\text{x}10^{-4}$ for $r < 0.025$<br>$0.5\ Q_2(r)$ for $r > 0.025$ | $-Q_9/(2\pi\Delta z_9 r)$ | 1.0 | 0.1 |
| **10: Inner Bottom Surface** | **$r = 0.0525$ to 0**<br>$\Delta z = 0.02$ | $7.9\text{x}10^{-4}$ for $r < 0.025$<br>$0.5\ Q_2(r)$ for $r > 0.025$ | $-Q_{10}/(\pi 0.04r)$ | 1.0 | 0.1 |
| **11: Upper Impeller Suction** | $r = 0$ to 0.025<br>**$z = 0.08$ to 0.055** | $7.9\text{x}10^{-4}$ | -0.40 | 1.0 | 0.1 |
| **12: Lower Impeller Suction** | $r = 0$ to 0.025<br>**$z = 0.02$ to 0.045** | $7.9\text{x}10^{-4}$ | 0.40 | 1.0 | 0.1 |

### 2.2.2 *Coupling the Eulerian and Lagrangian Fields*

As previously mentioned the model under development describes the mixing process by linking the Eulerian and Lagrangian fields. Implementing this approach requires that the feed stream be discretized into $\Delta t_E$ time steps or volumes (DFV) that move through the zones of varying conditions as described by the Eulerian Flow Field. It should be noted that these are not isolated drops of fluid, but discretized elements of the feed stream that progress through space-time, or Lagrangian time. Figure 2.6 displays the DFV movement for the impeller feed point and illustrates the following key points:

i. a new DFV being added at the feed point each time step $\Delta t_E$;
ii. the DFV mixing with the surroundings as it travels at exactly the local mean velocity through the varying conditions in the EFM;
iii. the DFV dividing according to the volumetric flow rate split at the entrances of zones 3 & 4, 7 & 9, and 8 & 10 (green arrows);
iv. discontinuities in the DFV path due to changes in direction of travel (arrows);
v. the DFV terminating due to the EFM constraints of entering the impeller swept volume or re-entering the impeller discharge stream (red arrows).

Figure 2.6 also illustrates the DFV trajectory for any other feed point by simply completing the remainder of the path after the feed point, except for surface additions where the DFV path is slightly modified as shown in Figure 2.7. In this case, the hydrodynamic properties of zone 7 are extended to the fluid surface, effectively bypassing zones 5 and 9.

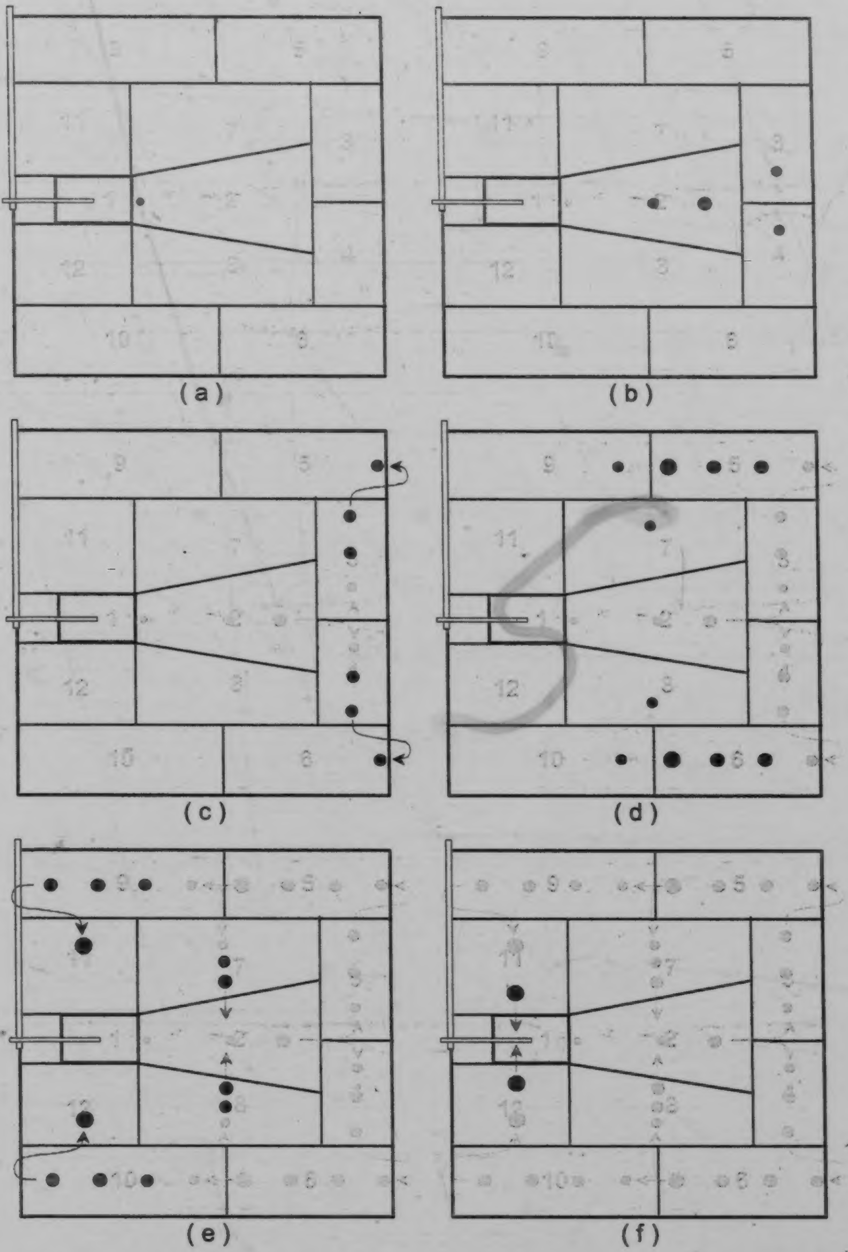

( a ) ( b )

( c ) ( d )

( e ) ( f )

**Figure 2.6** Lagrangian path of a discrete feed volume (DFV). a) Entering at the impeller tip, b) Dividing and entering the wall jets, c) Exiting the wall jets, d) Dividing and entering the return streams, d) Terminating due to re-entering the impeller discharge stream, e) Terminating due to entering the impeller swept volume.

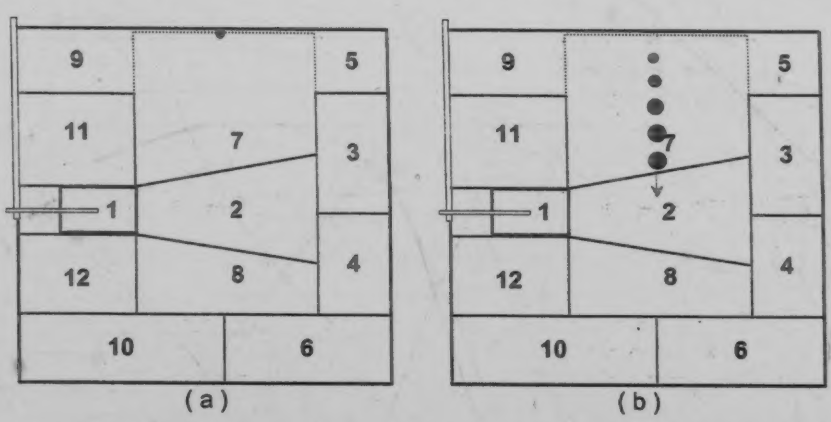

(a) (b)

**Figure 2.7** Modified Lagrangian path of a discrete feed volume (DFV). a) Entering at the top surface, b) Traveling downwards and then terminating due to entering the impeller discharge stream.

Implementing the Lagrangian approach within the EFM also implicitly constrains a DFV to only mix with the immediate local surrounding solution (shown as the dotted boundaries in Figure 2.8). This makes it appropriate to describe the size of the DFV as a volume fraction X of the immediate surroundings, defined as

$$X_{DFV} = \frac{V_{DFV}}{Q_{local} \Delta t_E} \tag{2.3}$$

where $V_{DFV}$ is the volume of the DFV and $Q_{local}$ is the volumetric flow rate of the EFM zone at the DFV position. When $X_{DFV}$ equals 1, mixing of the DFV with the local surroundings is complete and the DFV is terminated.

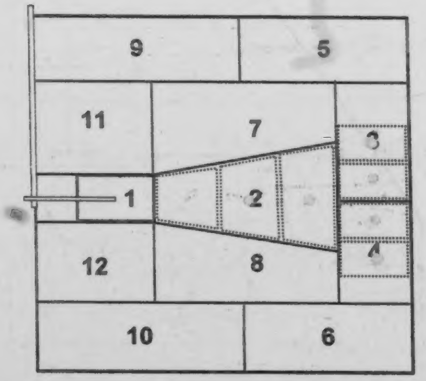

**Figure 2.8** Dotted boundaries illustrate the immediate local surrounding solution available to mix with each discrete feed volume (DFV).

### *2.2.3 Lagrangian Mixing Model (moving frame)*

The mixing model begins with two checkpoints to define the regime of operation. First, in order to use the simplified engulfment model (Section 1.4.1), engulfment of fluid into the eddies in the viscous subrange of the spectrum must be slower than molecular diffusion of the fluid through the individual layers of fluid in the eddies. This requires the characteristic micromixing time $t_M$ to be greater than characteristic diffusion time $t_{diffusion}$, which requires the Schmidt number to be less than 4000 (Baldyga and Bourne 1989).

$$t_M = 12\left(\frac{\nu}{\varepsilon}\right)^{1/2} \qquad (2.4)$$

$$t_{diffusion} = 2\left(\frac{\nu}{\varepsilon}\right)^{1/2} \operatorname{arcsinh}(0.05\,Sc) \qquad (2.5)$$

$$\frac{t_M}{t_{diffusion}} > 1 \quad \text{if} \quad Sc = \frac{\nu}{D_{mol}} < 4000 \qquad (2.6)$$

The diffusivity of silver ions in the gelatin solution is taken to be 2 to $5 \times 10^{-9}$ $m^2/s$ (Judd 1999), and the viscosity of the gelatin solution is taken as no more than twice that of water (< $2\times10^{-6}$ m$^2$/s). This gives a maximum Schmidt number of 1000 and indicates that engulfment will be the rate-limiting step, not diffusion.

Second, the relative importance of micromixing, inertial-convective mesomixing, and turbulent dispersion mesomixing is evaluated by comparing characteristic time constants. As first mentioned in Section 1.3.2, the largest characteristic mesomixing time constant indicates the rate-limiting mesomixing step, and is considered to be important in the mixing process if it is greater than 20% of the characteristic micromixing time constant. Therefore, the rate-limiting step is:

- Micromixing if $t_s < 0.2t_M$ and $t_D < 0.2t_M$
- Inertial-convective mesomixing if $t_s > t_D$ and $t_s > 0.2t_M$
- Turbulent dispersion mesomixing if $t_D > t_s$ and $t_D > 0.2t_M$

The remaining equations in the mixing model ultimately give the change in micromixed fluid volume of the DFV, $V_{DFV}$, and the accompanying change in concentration and crystal population as a function time, as given below.

$$\frac{dV_{DFV}}{dt} = E\left(1 - \frac{X_{DFV}}{X_u}\right)V_{DFV} \qquad V_{DFV}(0) = Q_f \Delta t_E \qquad (2.7)$$

$$\frac{dC_{DFV,i}}{dt} = E\left(1 - \frac{X_{DFV}}{X_u}\right)\left(C_{kettle,i} - C_{DFV,i}\right) \qquad (2.8)$$

$$\frac{dN_{DFV,i}}{dt} = E\left(1 - \frac{X_{DFV}}{X_u}\right)\left(N_{kettle,i} - N_{DFV,i}\right) \qquad (2.9)$$

where E is the micromixing engulfment parameter, $X_{DFV}$ is the local micromixed volume fraction, and $X_u$ is the local mesomixed volume fraction. When micromixing is the rate-limiting step, $X_u$ is unity and Equation ( 2.7 ) reduces to the simplified engulfment model of micromixing and is schematically shown in

Figure 2.8. When inertial-convective mesomixing is the rate-limiting step (Section 1.4.2), $X_u$ is given by

$$\frac{dX_u}{dt} = \frac{X_u(1-X_u)}{t_s} \qquad X_u(0) = X_{DFVo} \qquad (2.10)$$

In this case, $X_u$ is always less then or equal to 1 indicating that only a fraction of the local fluid volume is at a concentration scale relevant for micromixing to proceed; this effectively acts to slow the growth of the micromixed volume. This mixing process is schematically shown in Figure 2.9. When turbulent dispersion mesomixing is the rate-limiting step (Section 1.4.2), $X_u$ is given for each of the I radial integration rings up to a maximum value of 1 by

$$\begin{aligned} \frac{dX_{u,i}}{dt} &= \frac{4\pi D_t U}{Q_{local}} k_i \qquad X_{u,i}(0) = X_{DFVo,i} = \frac{Q_f \Delta t_E}{I} \\ \text{where} \quad k_i &= \ln\left(\frac{2I}{2(I-i)+1}\right) \end{aligned} \qquad (2.11)$$

as derived below.

The radial variation of the volume fraction of B-rich feed $X_f$ at any axial position in the plume will be expressed in discrete form by defining I rings in R-space (Figure 2.10). The radii will be chosen so that each ring contains the same amount of B, $Q_f/I$, which is independent of time and axial position. Defining $r_i$ and $r_{i+1}$ as the inner and outer radii of any ring i, then

$$\begin{aligned} 2\pi U \int_{r_i}^{r_{i+1}} r X_f \, dr &= \frac{Q_f}{I} \\ r_i^2 &= 4D_t t \ln\left(\frac{I}{I-i+1}\right) \\ r_{i+1}^2 &= 4D_t t \ln\left(\frac{I}{I-i}\right) \end{aligned} \qquad (2.12)$$

where $X_f$ is given by Equation ( 1.67 ). Equation ( 2.12 ) permits the radii to be determined for any value of I, and is schematically shown in Figure 2.10 for I equal to 3. Using the mean volume fraction radii to describe the rate of expansion for each ring gives

$$
\begin{aligned}
2\pi U \int_{r_i}^{r_{a,i}} r X_f \, dr &= \frac{Q_f}{2I} \\
r_{a,i}^{2} &= 4D_t t \ln\left(\frac{2I}{2(I-i)+1}\right) \qquad (2.13) \\
r_{a,i}^{2} &= 4D_t t \, k_i
\end{aligned}
$$

and

$$\frac{dr_{a,i}^{2}}{dt} = 4D_t \, k_i \quad \text{or} \quad \frac{dV_{u,i}}{dt} = 4\pi D_t U \Delta t_E \, k_i \qquad (2.14)$$

In this case, each $X_{u,i}$, is always less than or equal to 1 indicating that only a fraction of the local fluid volume is at a concentration scale relevant for micromixing to proceed; this effectively acts to slow the growth of the micromixed volume in each ring. The constraint of limiting each $X_{u,i}$ to a maximum value of 1 has the non-physical potential of giving $\Sigma X_{u,i} \geq 1$, however the micromixing constraint of $\Sigma X_{DFV,i} \leq 1$ is frequently invoked prior to this occurring and avoids this possibility of $\Sigma X_{u,i} \geq 1$ by terminating the outermost ring (Figure 2.11d).

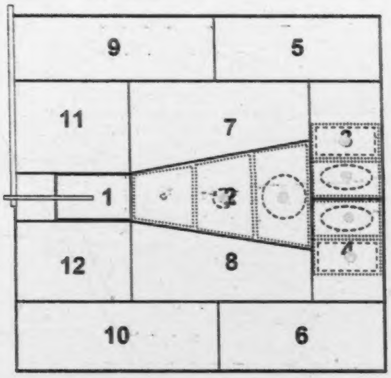
9
5
11
7
3
1
2
4
12
8
10
6

**Figure 2.9** Inertial-convective mesomixing process. Mesomixing limits the volume of fluid at a relevant concentration scale (dashed boundaries) to a fraction of the maximum potential volume (dotted boundaries) available for micromixing to proceed in.

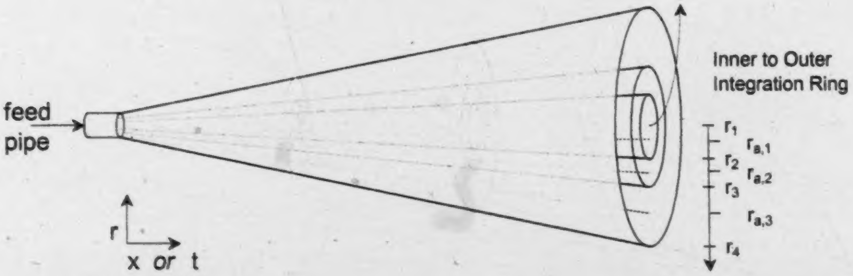
Inner to Outer
Integration Ring
feed
pipe
$r_1$
$r_{a,1}$
$r_2$
$r_{a,2}$
$r_3$
$r_{a,3}$
$r_4$
r
x or t

**Figure 2.10** Radial and axial discretization of the feed plume for turbulent dispersion mesomixing. Mean volume fraction radii ($r_{a,i}$) are used to describe the rate of expansion for each ring.

Micromixing, inertial-convective mesomixing and turbulent dispersion mesomixing models are available to describe the mixing process experienced by a discrete feed volume (DFV) as it travels through the varying conditions of the Eulerian Flow Field. Figure 2.11 illustrates growth of the local micro- and mesomixed volume fractions for each of the three mixing models when they are invoked under identical turbulence conditions.

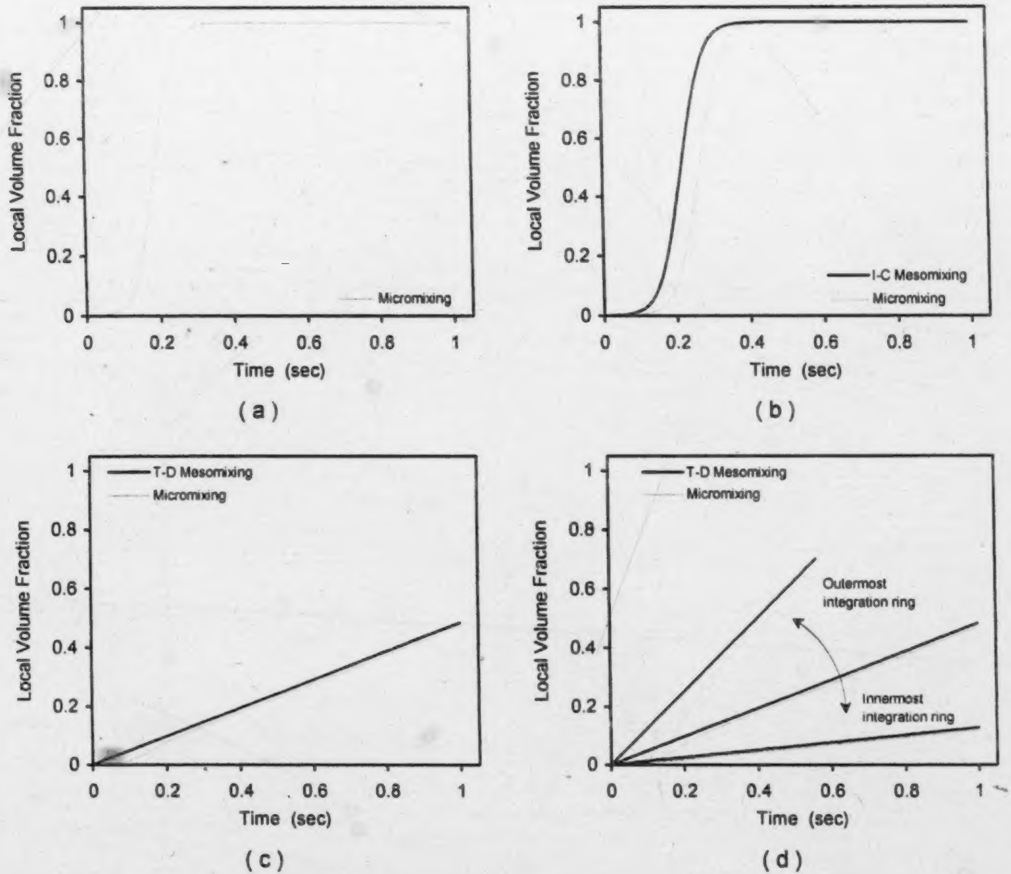

**Figure 2.11** Local micro- and mesomixed volume growth for each mixing model invoked under identical turbulence conditions ($Q_{feed} = 7.5x10^{-7}$ $m^3/s$, $Q_{zone} = 1.5x10^{-3}$ $m^3/s$, $U_{zone} = 0.085$ m/s, $\varepsilon = 1.0$ W/kg, k = 0.1 J/kg). a) Micromixing controlled, b) Micromixing limited by inertial-convective mesomixing, c) and d) Micromixing limited by turbulent dispersion mesomixing modeled using 1 and 3 integration rings, respectively.

## 2.3 Double-jet Addition Precipitation Model

The model developed here uses instantaneous primary homogeneous nucleation, multiple complex species equilibria, size-dependent crystal growth, and discretized population balances to simulate silver halide double-jet precipitations. The main assumptions in the model are:

i. isothermal process: the heat of reaction is negligible;
ii. no primary heterogeneous nucleation, secondary nucleation, crystal breakage or agglomeration;
iii. primary homogeneous nucleation is instantaneous and is limited by only mixing and the local excess supersaturation;
iv. all nuclei formed are cubic and are at the critical length in equilibrium with the critical supersaturation limit;
v. size-dependent growth kinetics measured by Wey and Strong are valid;
vi. crystal size solubility according to the Gibbs-Thompson relation is valid;

Chapter 1 introduced the crystallization fundamentals and population balance models used in the following development.

### 2.3.1 *Complex Species Equilibria*

The ionic speciation equations for total silver and halide ($C_{T,Ag}$, $C_{T,Br}$), including all complex ions appearing under the model conditions, in terms of molar concentrations are

$$\begin{aligned} C_{T,Ag} = {} & \left[Ag^{+}\right] + \left[AgX^{\circ}\right] + \left[AgX_2^{-}\right] + \left[AgX_3^{2-}\right] + \left[AgX_4^{3-}\right] + \left[Ag\cdot gel\right] + \left[AgX\cdot gel^{-}\right] + \\ & \left[AgX_2\cdot gel^{2-}\right] + 2\left[Ag_2X^{+}\right] + 3\left[Ag_3X^{2+}\right] + 4\left[Ag_4X^{3+}\right] + 2\left[Ag_2X\cdot gel\right] \end{aligned} \tag{2.15}$$

$$C_{T,X} = \left[X^{-}\right] + \left[AgX^{\circ}\right] + 2\left[AgX_2^{-}\right] + 3\left[AgX_3^{2-}\right] + 4\left[AgX_4^{3-}\right] + \left[AgX \cdot gel^{-}\right] + 2\left[AgX_2 \cdot gel^{2-}\right] + \left[Ag_2X^{+}\right] + \left[Ag_3X^{2+}\right] + \left[Ag_4X^{3+}\right] + \left[Ag_2X \cdot gel\right]$$

( 2.16 )

Using the following relationships, the ionic speciation equations can be rewritten in terms of silver, halide and gelatin activities ($a_{Ag}$, $a_X$, $a_{gel}$), activity coefficients ($\gamma_i$) and stability constants ($\beta_i$).

$$\gamma_i = \frac{a_i}{C_i} \qquad (2.17)$$

$$\beta_{Ag_mBr_n \cdot gel_g{}^{m-n}} = \frac{a^m_{Ag^+}\, a^n_{Br^-}\, a^g_{gel}}{a_{Ag_mBr_n \cdot gel_g}} \qquad (2.18)$$

And the rewritten ionic speciation equations are

$$C_{T,Ag} = \frac{a_{Ag}}{\gamma_{Ag}} + \frac{a_{Ag}a_X}{\gamma_{11}\beta_{11}} + \frac{a_{Ag}a_X^2}{\gamma_{12}\beta_{12}} + \frac{a_{Ag}a_X^3}{\gamma_{13}\beta_{13}} + \frac{a_{Ag}a_X^4}{\gamma_{14}\beta_{14}} + \frac{a_{Ag}a_{gel}}{\gamma_{15}\beta_{15}} + \frac{a_{Ag}a_X a_{gel}}{\gamma_{16}\beta_{16}} + \frac{a_{Ag}a_X^2 a_{gel}}{\gamma_{17}\beta_{17}} + 2\frac{a_{Ag}^2 a_X}{\gamma_{18}\beta_{18}} + 3\frac{a_{Ag}^3 a_X}{\gamma_{19}\beta_{19}} + 4\frac{a_{Ag}^4 a_X}{\gamma_{20}\beta_{20}} + 2\frac{a_{Ag}^2 a_X a_{gel}}{\gamma_{21}\beta_{21}}$$

( 2.19 )

$$C_{T,X} = \frac{a_X}{\gamma_X} + \frac{a_{Ag}a_X}{\gamma_{11}\beta_{11}} + 2\frac{a_{Ag}a_X^2}{\gamma_{12}\beta_{12}} + 3\frac{a_{Ag}a_X^3}{\gamma_{13}\beta_{13}} + 4\frac{a_{Ag}a_X^4}{\gamma_{14}\beta_{14}} + \frac{a_{Ag}a_X a_{gel}}{\gamma_{16}\beta_{16}} + 2\frac{a_{Ag}a_X^2 a_{gel}}{\gamma_{17}\beta_{17}} + \frac{a_{Ag}^2 a_X}{\gamma_{18}\beta_{18}} + \frac{a_{Ag}^3 a_X}{\gamma_{19}\beta_{19}} + \frac{a_{Ag}^4 a_X}{\gamma_{20}\beta_{20}} + \frac{a_{Ag}^2 a_X a_{gel}}{\gamma_{21}\beta_{21}}$$

( 2.20 )

where $\gamma_i$ and $\beta_i$ were measured at the Eastman Kodak Research laboratories.

In order to determine the concentration of silver and halide ions in equilibrium with an infinitely large crystal ($C_{e,Ag}$, $C_{e,X}$), the ionic speciation equations must be solved under the condition of an exactly saturated solution, meaning

$$\frac{a_{Ag}a_X}{K_{SP}} = 1.0 \qquad (2.21)$$

where the solubility product, $K_{SP}$, equals $10^{-10.46}$ mol$^2$/L$^2$ for silver bromide at 70°C. After substituting this condition into Equations ( 2.19 ) and ( 2.20 ), the equations are solved by applying a mass balance to the solution. It is known that the silver and the halide ions must "precipitate" out of solution in a 1:1 stoichiometric ratio, thus the difference between total ion concentrations must remain constant. Given the initial total silver and halide concentrations, $C_{T,Ag_o}$ and $C_{T,X_o}$, this difference in total ion concentrations is known. The resulting mass balance can be written as

$$C_{T,X_o} - C_{T,Ag_o} = C_{e,X} - C_{e,Ag} \qquad (2.22)$$

This equation is solved for the silver or halide activity by using the Newton-Raphson method. The silver or halide activity found is then used to determine the total silver and halide ion concentrations by Equations ( 2.15 ) and ( 2.16 ). The results of this model are in reasonable agreement with the published values of Harding 1979 as shown in Figure 2.12.

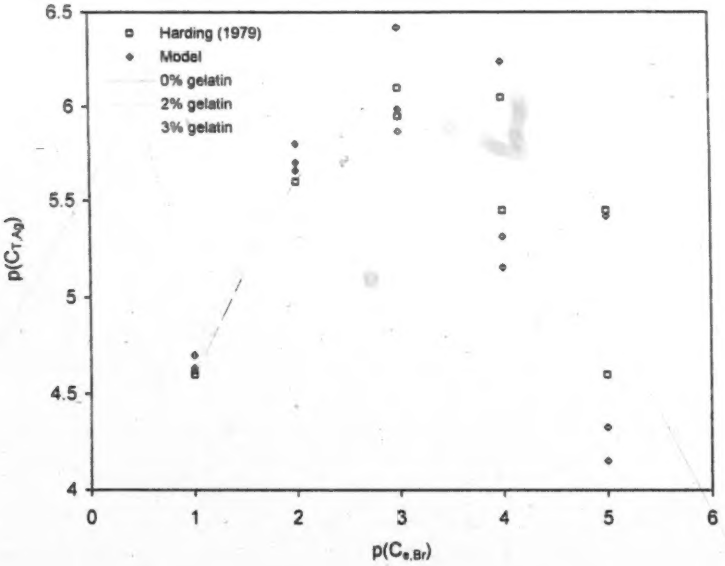

**Figure 2.12** Agreement of the thermodynamic equilibrium model with published data.

In the case of the size-dependent crystal growth rates, the total silver and halide ion concentrations in equilibrium with an infinitely large crystal are required ($C_{e,Ag}$, $C_{e,X}$). And in the case of the nucleation rates, the ion concentrations at the limiting supersaturation with an infinitely large crystal are required ($C_{Sc,Ag}$, $C_{Sc,X}$).

$$C_{Sc,Ag} = S_{critical} C_{e,Ag} \qquad (2.23)$$

$$C_{Sc,X} = S_{critical} C_{e,X} \qquad (2.24)$$

where $S_{critical}$ is the critical supersaturation required for instantaneous nucleation. These concentrations are then used to calculate the instantaneous rate of nucleation, or equivalently, the concentration of silver and halide relieved as nuclei ($C_{rel,AgX}$) by

$$C_{rel,AgX} = C_{T,Ag_0} - S_{critical} C_{T,Ag} \qquad (2.25)$$

or

$$C_{rel,AgX} = C_{T,X_0} - S_{critical} C_{T,X} \tag{2.26}$$

If the solution saturation was not initially above the limiting supersaturation $C_{rel,AgX}$ will be negative indicating that nuclei will not be formed, therefore $C_{rel,AgX}$ is set to zero.

## New Solution Strategy

In addition to the repeated use of the Newton-Raphson solver becoming computationally expensive, this method also requires an initial guess of the solution. The only approach for estimating the initial guess is to use the previous local solution, however this is problematic as the local conditions change rapidly with time in the feed plume (DFVs). The alternative solution strategy reduces the computational time required by the solver and eliminates the need for initial guesses by predetermining the silver and halide activities over the expected range of concentration conditions ($C_{T,Br}$ - $C_{T,Ag}$) in the model. As shown in Figure 2.13 the silver and halide activities are approximately linear with the local concentration conditions when total silver and total halide are in excess by greater than $2\text{x}10^{-4}$ mol/L, respectively. The least squares regression coefficients for this range are given in Table 2.3. Applying the linear fit when total silver and halide are in excess by less than $2\text{x}10^{-4}$ mol/L results in large, unacceptable error as shown in Figure 2.14 (b) and (d). Although this concentration condition does not occur in the bulk solution, it does occur at least once in each DFV as the conditions change from excess silver to excess halide. At that time, the linear-fit solution is used as an initial guess for the Newton-Raphson solver.

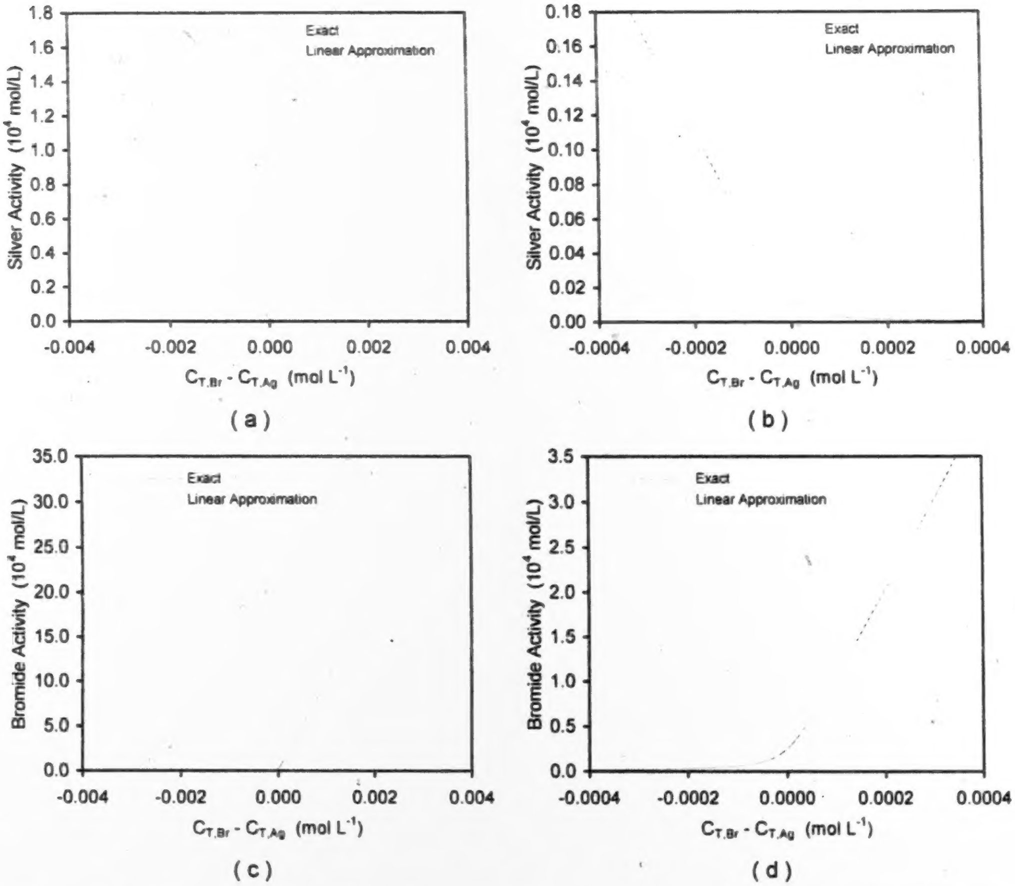

**Figure 2.13** Comparison of calculated and approximated activities showing the deviation when in excess by less than 0.0002 mol/L. a) and b) Silver activity, and c) and d) Bromide activity. (b) and (d) are expanded scales.

**Table 2.3** Least squares regression coefficients used to describe the silver and halide activities.

| Activity (mol L$^{-1}$) | $C_{T,Br} - C_{T,Ag}$ (mol L$^{-1}$) | Slope | Intercept (mol L$^{-1}$) |
|---|---|---|---|
| Silver | $\leq -2\times10^{-4}$ | $-5.4526\times10^{-2}$ | $1.7081\times10^{-7}$ |
| Bromide | $\geq 2\times10^{-4}$ | $9.9831\times10^{-1}$ | $3.1286\times10^{-6}$ |

general equation: $a_i = \text{Slope}(C_{T,Br} - C_{T,Ag}) + \text{Intercept}$

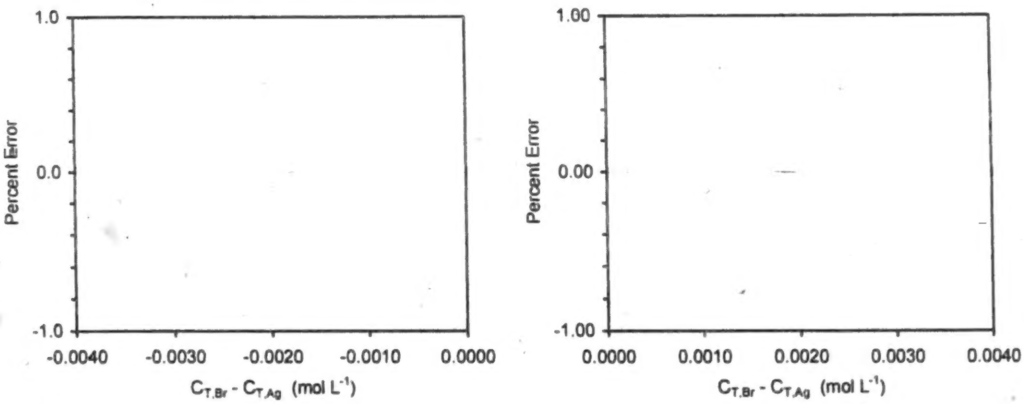

( a ) ( b )

**Figure 2.14** Percent error in the approximated activities becomes unacceptable when in excess by less than 0.0002mol/L. a) Excess silver, and b) Excess halide.

### *2.3.2 Nucleation Model*

The nucleation model is based on an instantaneous rate of primary homogenous nucleation that relieves excess supersaturation down to the critical supersaturation limit required for nucleation ($S_{critical}$). All nuclei formed are cubic and of size $L_{Pn}$. The size $L_{Pn}$ is held constant, and is equal to the critical size in equilibrium with the critical supersaturation limit as determined by the Gibbs-Thompson relation

$$L_{Pn} = \frac{4\sigma M}{\nu R_g T_k \rho \ln(S_{critical})} \qquad (2.27)$$

where $\sigma$ is the interfacial tension, $R_g$ is the universal gas constant and $T_k$ is the absolute temperature. The quantity $\nu$ represents the number of moles of ions formed from one mole of electrolyte.

### Implementing the Nucleation Model

The nucleation model is only applied in the discrete feed volumes (DFV) since the local excess supersaturation is the highest in the feed plume and is negligible in the well-mixed bulk of the kettle. Since the rate of nucleation is instantaneous whenever the local supersaturation exceeds the critical limit, and on nucleation the supersaturation drops to the critical limit, the maximum supersaturation for growth in each DFV equals the critical supersaturation limit. This in turn limits the maximum crystal growth rates within each DFV, as the rate is a function of local supersaturation. Once the critical limit ($S_{critical}$) is reached within the DFV and nucleation begins, the crystal growth rates, and therefore the consumption by crystal growth in that time step, are set. Thus, only the halide engulfed from the bulk exceeding the amount consumed by the crystal growth is available for nucleation, assuming that the high supersaturation is maintained during the time step. This gives the nucleation terms

$$B_{o,i} = 0 \quad \text{if } i \neq Pn$$
$$\text{and} \tag{2.28}$$
$$B_{o,Pn} = \frac{C_T - C_e}{L_{Pn}^3\left(\rho/M\right)} = \frac{C_{rel,AgX}}{L_{Pn}^3\left(\rho/M\right)}$$

where $C_T$ and $C_e$ are the total local concentration and total local equilibrium concentration of silver or halide at the end of the time step.

## 2.3.3 *Growth Model*

The crystal growth rate expression includes bulk diffusion and surface integration processes, and is modified to include size-dependent solubility based on the Gibbs-Thompson relation (Section 1.1.4). The size-dependent rate as given by Wey and Strong (1977b) is

$$G = \frac{K(C_T - C_L)}{1 + \xi L} \tag{2.29}$$

$$C_L = C_e \exp\left(\frac{4\sigma M}{\nu R_g T_k \rho L}\right) \qquad (2.30)$$

$$\xi = \frac{\rho K}{4D_{mol}M} \qquad (2.31)$$

where $C_T$ and $C_e$ are the total local concentration and total local equilibrium concentration of the limiting species (*i.e.* silver or halide), and $C_L$ is the concentration in equilibrium with the crystal size L. The kinetic parameters are given by Wey and Strong (1977a) for crystal sizes larger than 0.047 μm at high supersaturations, but should be used cautiously for crystal sizes smaller than 0.3 μm at low supersaturations. The measured ratio of relative resistance of diffusion to surface integration is

$$\xi = 16.3\text{x}10^{6}\ \text{m}^{-1}$$

which gives the rate constant for surface integration as

$$K = 3.85\text{x}10^{-6}\ \text{m}^{4}\ \text{mol}^{-1}\ \text{s}^{-1}$$

for the following values of interfacial tension, molar mass of the solute, absolute temperature, crystal density, molecular diffusivity and the number of moles of ions formed from one mole of electrolyte, respectively

$$\sigma = 0.14\ \text{N m}^{-1}$$
$$M = 0.187772\ \text{kg mol}^{-1}$$
$$T_k = 343\ \text{K}$$
$$\rho = 6473\ \text{kg m}^{-3}$$
$$D_{mol} = 2\text{x}10^{-9}\ \text{m}^{2}\ \text{s}^{-1}$$
$$\nu = 1$$

### 2.3.4 *Crystal Population Balance*

Population balances that simulate growth of the crystal distribution are applied in each discrete feed volume (DFV), as well as in the perfectly mixed bulk of the precipitation kettle. As mentioned in Section 1.2.1 and detailed in Appendix A, the discretized population balance method proposed by Hounslow et al. (1988) most accurately predicts the rates of change in the moments of the distribution due to growth and has been selected for this model. Implementing this approach first requires crystal length, the internal co-ordinate, to be discretized into geometrically increasing size intervals.

### Length Scale Discretization

The population balance method of Hounslow et al (1988) was developed specifically for a geometric length scale discretization to avoid problems inherent in a linear discretization. Specifically, geometric discretizations shift some of the resolution from larger crystal sizes to smaller crystals, therefore decreasing the number of size intervals required for adequate resolution over the entire length domain, relative to that required by linear discretizations (Figure 2.15a and b). However, to achieve the resolution needed for the dissolution of fine crystal sizes, too much resolution is shifted from large crystal sizes for a given number of size intervals. Moreover, the nature of geometric discretizations has the significant disadvantage of asymptotically approaching zero, thus dissolution of fine particles cannot be completely described with a finite number of size intervals.

### New Discretization Method

A novel discretization method was developed to resolve the issues with the resolution and dissolution of fine crystal sizes. This method consists of a symmetric geometric discretization, which uses appropriate resolution for all crystal sizes beginning at zero (Figure 2.15c). In addition, this method has the unique characteristic of placing the highest resolution at some intermediate size, and thus allowing the possibility for the highest resolution to follow the majority of the crystals. This length scale discretization method is derived in Appendix A.

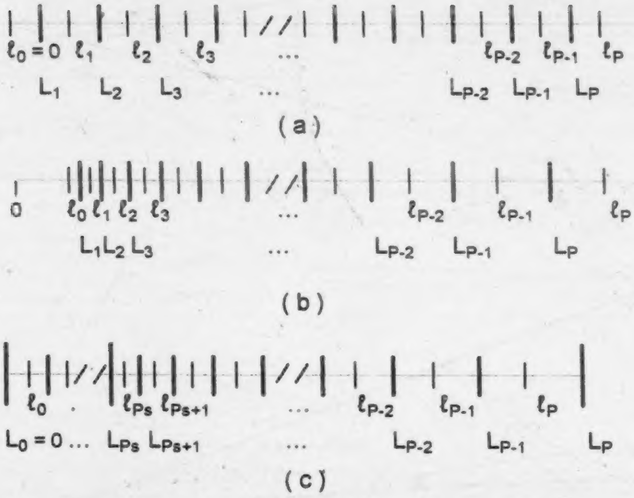
$\ell_0 = 0$ $\ell_1$ $\ell_2$ $\ell_3$ … $\ell_{P-2}$ $\ell_{P-1}$ $\ell_P$
$L_1$ $L_2$ $L_3$ … $L_{P-2}$ $L_{P-1}$ $L_P$
(a)
0 $\ell_0$ $\ell_1$ $\ell_2$ $\ell_3$ … $\ell_{P-2}$ $\ell_{P-1}$ $\ell_P$
$L_1$ $L_2$ $L_3$ … $L_{P-2}$ $L_{P-1}$ $L_P$
(b)
$\ell_0$ . $\ell_{Ps}$ $\ell_{Ps+1}$ … $\ell_{P-2}$ $\ell_{P-1}$ $\ell_P$
$L_0 = 0$ … $L_{Ps}$ $L_{Ps+1}$ … $L_{P-2}$ $L_{P-1}$ $L_P$
(c)

**Figure 2.15** Possible length scale discretization methods. a) Linear discretization illustrating low resolution of small crystal sizes and high resolution of large crystal sizes, b) Geometric discretization illustrating adequate resolution for all sizes but not extending to zero, and c) Symmetric geometric discretization illustrating adequate resolution for all sizes with the highest resolution at the point of symmetry ($L_{Ps}$) and extending to zero.

The required equations for the forward discretization are

$$\begin{aligned} L_{Ps+i} &= r^i L_{Ps} = r L_{Ps+i-1} \\ \ell_{Ps+i} &= \frac{2r^{i+1}}{r+1} L_{Ps} = \frac{2r}{r+1} L_{Ps+i} \\ \Delta L_i &= \ell_{Ps+i} - \ell_{Ps+i-1} = \frac{2(r-1)}{r+1} L_{Ps+i} = r \Delta L_{Ps+i-1} \end{aligned} \qquad (2.32)$$

And the required equations for the reverse discretization are

$$\begin{aligned} L_{Ps-i} &= \left(2 - r^{i}\right) L_{Ps} \\ \ell_{Ps-i} &= 2\left(1 - \frac{r^{i}}{r+1}\right) L_{Ps} \\ \Delta L_{PS-i} &= \ell_{Ps-i} - \ell_{Ps-i-1} = 2\left(\frac{r^{i-1} - r^{i}}{r+1}\right) L_{Ps} = r \Delta L_{Ps-i+1} \end{aligned} \qquad (2.33)$$

where Ps is the index of the symmetric size interval, i is the number of intervals below or above Ps, r is the common geometric ratio, $\ell$ is the interval limit and L is the characteristic length of the size interval. The index of the symmetric size interval is given by

$$Ps = \frac{\ln 2}{\ln\left(\frac{2L_P}{L_{Ps}}\right)} P \qquad (2.34)$$

where P is the total number of size intervals. To ensure that the length scale covers the required range, Ps should be rounded down to the nearest integer. In this work the point of symmetry, $L_{Ps}$, was fixed at the nuclei length $L_{Pn}$ to provide the highest possible resolution for nuclei growth during the nucleation event.

Test simulations where the point of symmetry was varied so that the highest resolution in the length scales remains near the majority of the crystals throughout the simulation showed very small improvements in the predictions (see Appendix A). The constraint which requires the length scale to coincide exactly with the nuclei length strongly restricts the variable range for the point of symmetry and the improvements in the predictions are outweighed by the added complexity in the model.

### Implementing the Population Balance

The population balance method proposed by Hounslow et al. (1988) adapted for use with the symmetric geometric length scale discretization for the forward progression from Appendix A is

$$\frac{dN_{Ps+i}}{dt} = \frac{1}{r^{i}L_{Ps}}\left(\frac{rG_{Ps+(i-1)}N_{Ps+(i-1)}}{r^{2}-1} + G_{Ps+i}N_{Ps+i} - \frac{rG_{Ps+(i+1)}N_{Ps+(i+1)}}{r^{2}-1}\right) \quad (2.35)$$

where i is the number of intervals above the symmetrical interval.

And for the reverse progression is

$$\frac{dN_{Ps-i}}{dt} = \frac{-1}{r^{i}L_{Ps}}\left(\frac{rG_{Ps-(i-1)}N_{Ps-(i-1)}}{r^{2}-1} + G_{Ps-i}N_{Ps-i} - \frac{rG_{Ps-(i+1)}N_{Ps-(i+1)}}{r^{2}-1}\right) \quad (2.36)$$

where i is the number of intervals below the symmetrical interval.

These equations were tested using a set of typical conditions taken from this study ($\mu$ = 0.117 $\mu$m, $\sigma$ = 0.021 $\mu$m, G = 4.0 Å/s), and were validated by comparing the model predictions to analytical solutions as shown in Figure 2.16. Analytical solutions using the method of characteristics are given in Appendix E. The symmetric geometric length scale used $L_{Ps}$ = 0.00435 $\mu$m, $L_P$ = 2.0 $\mu$m and P = 200.

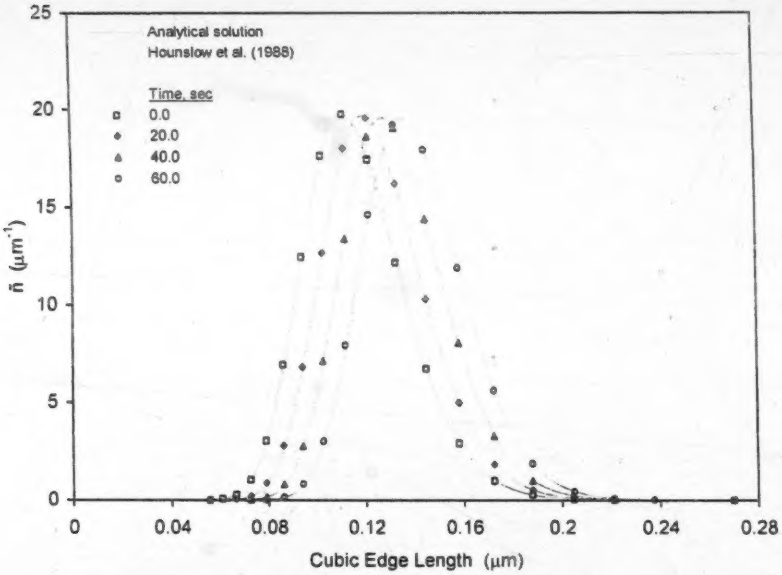

**Figure 2.16** Agreement of the population balance method of Hounslow et al. (1988) modified for use with a symmetric geometric length scale with analytical solutions for typical conditions ($\mu$ = 0.117 µm, $\sigma$ = 0.021 µm, G = 4.0 Å/s, $L_{Ps}$ = 0.00435 µm, $L_P$ = 2.0 µm, P = 200).

### 2.3.5 *Material Balances*

The complete mathematical expressions describing the exchange of material between the discrete feed volumes (DFV) and the bulk of the kettle, consumption of reactants by nucleation and crystal growth, and population balances are given.

In the *jth* DFV, the balances for concentration and crystal population are written as

$$\frac{dC_{DFV,i}}{dt} = E\left(1 - \frac{X_{DFV}}{X_u}\right)\left(C_{kettle,i} - C_{DFV,i}\right) - \frac{\rho}{M}\sum_{p}\left(\frac{dN_p}{dt}L_p^3\right) - B_o\left(L_{Pn}^3 \frac{\rho}{M}\right) \quad (2.37)$$

$$\frac{dN_{DFV,i}}{dt} = E\left(1 - \frac{X_{DFV}}{X_u}\right)\left(N_{kettle,i} - N_{DFV,i}\right) + \left.\frac{dN_{DFV,i}}{dt}\right|_{growth} + B_{o,i} \qquad (2.38)$$

The terms in Equation ( 2.37 ) from left to right represent the rate of change in concentration in the DFV, engulfment from the kettle at the micromixing scales, consumption by crystal growth, and consumption by nucleation. The rate of nucleation is taken to be infinite, so this term is a discrete term that is implemented at the end of the time step (Section 2.3.2). The terms in Equation ( 2.38 ) from left to right represent the accumulation of crystals in the DFV, growth of the crystal population, and nuclei formation. Again, the rate of nucleation is taken to be infinite, so this term is a discrete term that is implemented at the end of the time step (Section 2.3.2).

In the precipitation kettle, the balances are written as

$$\frac{dC_{k,i}}{dt} = \frac{Q_X}{V_k}\left(C_{f,i} - C_{k,i}\right) + \frac{1}{V_k \Delta t_E} \sum_{terminated} V_{DFV}\left(C_{DFV,i} - C_{k,i}\right) - \frac{\rho}{M}\sum_{p}\left(\frac{dN_{kettle,p}}{dt} L_p^3\right) \qquad (2.39)$$

$$\frac{dN_{k,i}}{dt} = \left.\frac{dN_{k,i}}{dt}\right|_{growth} + \frac{1}{V_k \Delta t_E} \sum_{terminated} V_{DFV}\left(N_{DFV,i} - N_{k,i}\right) \qquad (2.40)$$

$$\frac{dV_k}{dt} = Q_X + \frac{1}{\Delta t_E} \sum_{terminated} V_{DFV} - \sum_{j}\left(\frac{dV_{DFV,j}}{dt}\right) \qquad (2.41)$$

The terms in Equation ( 2.39 ) from left to right represent the rate of change in concentration in the kettle, addition from feed streams other than the silver feed stream, addition from DFVs terminated in the current time step, and consumption by crystal growth. The terms in Equation ( 2.40 ) from left to right represent the accumulation of crystals in the kettle, growth of the crystal population, and addition of crystals from DFVs terminated in the current time step.

### 2.3.6 *Equation Solving Technique*

The differential equations appearing in the precipitation model for mixing, material balances and population balances are solved using linear approximations with step size control. This solution method avoids the complexity of slow differential equation solvers, and takes advantage of the extremely small time discretization ($\Delta t_E$) required to minimize the effects of solving the equations for the Eulerian and Lagrangian fields in parallel. In this model the time step equals the lesser of 0.015 s or 1/10th the transit time of the feed zone.

The step size control begins by estimating the time step required to consume the excess silver halide by crystal growth

$$\Delta t = \left(C_T - C_e\right)\frac{M}{3\rho}\sum_i G_i L_i^2 N_i \qquad (2.42)$$

where $C_T$ and $C_e$ are the total local concentration and total local equilibrium concentration of the limiting species (*i.e.* silver or halide). For supersaturations greater than 1, the actual calculation time step is then calculated as

$$\Delta t_{step} = \frac{1}{S}\Delta t \qquad (2.43)$$

where S is the local supersaturation. Multiplying the initial time step by the fraction 1/S acts to decrease the actual time step when the supersaturation is greater than 1 and the crystal growth, or consumption, is the most rapid. In contrast, for supersaturations less than 1, the actual calculation time step is then calculated as

$$\Delta t_{step} = S\left|\Delta t\right| \qquad (2.44)$$

Multiplying the initial time step by S acts to decrease the actual time step when the supersaturation is less than 1 and the negative crystal growth, or dissolution, is the most rapid. If the calculation time step falls outside the allowable range set by the user ($\Delta t_{max}$ to $\Delta t_{max}/20$), the calculation time step is set to the closest limit.

In this model a maximum time step of $2 \times 10^{-4}$ s was used. If the time step is too large, the consumption by crystal growth will exceed the amount of the limiting species available. In this case, the integration is restarted using half of the previous maximum time step.

## 2.4 Conclusions

The precipitation model developed above combines Eulerian and Lagrangian modeling perspectives to accurately model the interactions between turbulent flow and reactant mixing in a stirred tank reactor. The precipitation model incorporates instantaneous nucleation, multiple species thermodynamic equilibria, size-dependent crystal growth, and discretized population balances to accurately predict the double-jet precipitation of silver bromide.

# Chapter 3

---

## [redacted] Precipitation Experiments

## 3.1 Introduction

Crystallization is an important unit operation in the photographic industry. In order to control the properties of the photographic materials it is necessary to produce silver halide crystals with a specific morphology and uniform final crystal size. The final crystal size is a function of four processes occurring simultaneously: nucleation, growth, Ostwald ripening and renucleation; all of which are influenced by mixing. It is the purpose of this study to model the effects of mixing on these processes, and ultimately the effects of mixing on the final crystal size.

The precipitation experiments were structured to validate the model by progressively increasing the complexity of the stages in the precipitation process. Under certain precipitation conditions combinations of the nucleation, growth, Ostwald ripening, renucleation and mixing processes may be minimized or eliminated. The initial experiments eliminated all processes except for crystal growth so that the size-dependent growth kinetics could be validated. The next experiments removed all processes except for nucleation and growth so that the nucleation model could be validated. Lastly, only Ostwald ripening and renucleation were eliminated so that the mixing effects on the remaining precipitation processes could be validated. This strategy of stepwise validation was essential for effective troubleshooting and problem recognition during model development.

## 3.2 Experimental Method and Conditions

### *3.2.1 Apparatus*

The precipitation experiments used balanced double-jet addition of $AgNO_3$ and NaBr solutions to an agitated reaction kettle immersed in a constant temperature bath (Figure 3.1). The reaction kettle was a stainless steel, flat-bottomed, right cylinder of diameter T = 0.2 m, with an initial fill height of $H_o$ =0.1 m and a final fill height of $H_f$ = 0.2 m, which gave a working tank volume of $V_T$ = 6 L. The kettle was fully baffled with four evenly spaced baffles of width W = T/12, at zero off wall spacing. The agitation was provided by a stainless steel, center mounted, radially pumping Rushton impeller of rotational speed N =10.5 or 16.7 rps, diameter D = T/3 or T/4, blade height $D_H$ = D/5, and an off bottom clearance of C = T/4, to limit the degree of compartmentalization in the kettle. In all instances, a standard geometry was used so that the hydrodynamic conditions were well defined.

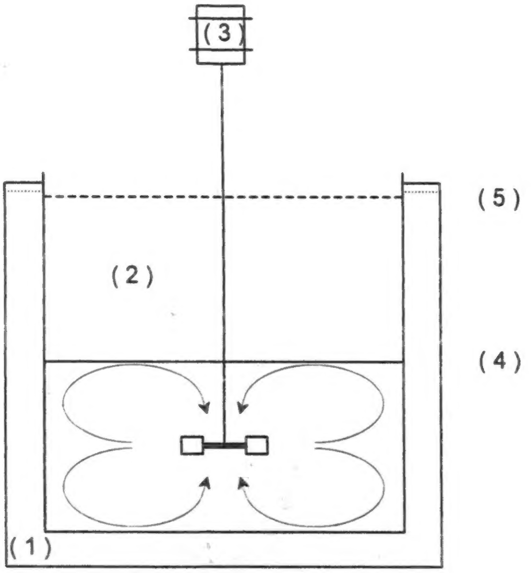

**Figure 3.1** Experimental apparatus used for the Balanced Double-Jet precipitation. (1) Constant temperature bath, (2) Reaction kettle, (3) Impeller and drive, (4) Initial fill height, (5) Final fill height.

The placement of the probes used to monitor and control the precipitation experiments was crucial to achieving reproducible results. The bromide ion concentration which determined the crystal morphology and indirectly affected the nucleation through the supersaturation was controlled potentiometrically using a Ag/AgBr electrode. It was essential that this probe was placed in a well mixed region of the kettle, such as just upstream of the baffle preceding the silver feed plume, as shown in Figure 3.2. Here it was found that the effects of the bromide feed plume were minimized, while avoiding the depleted bromide ion region of the silver feed plume. It was also essential to control the suspension temperature as this determines the solubility, and consequently the supersaturation of the system. To avoid stagnant regions in the kettle, both the Ag/AgBr electrode and the temperature probe were axially placed in the center of the radial impeller discharge (Figure 3.2).

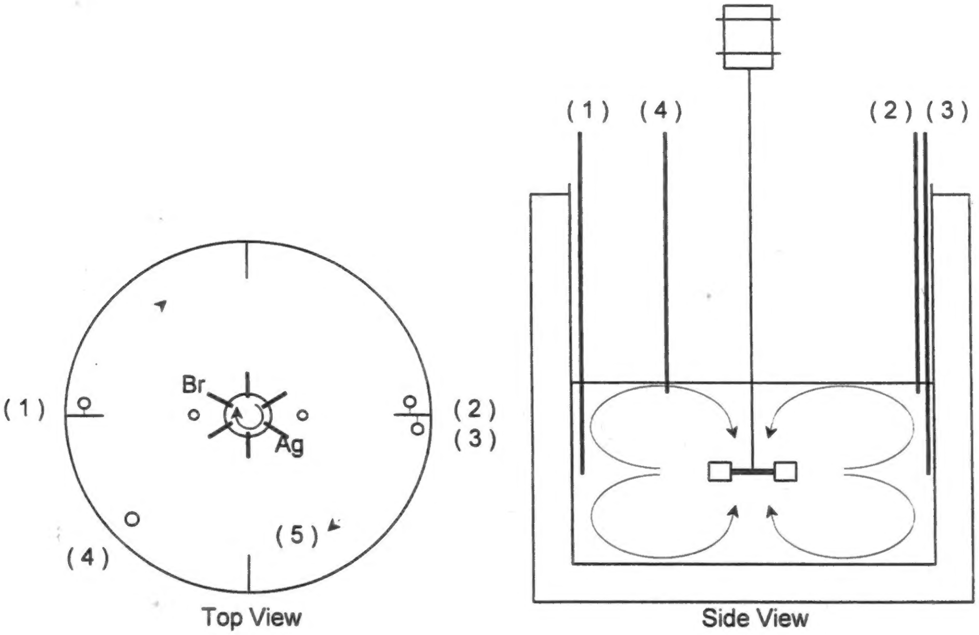

**Figure 3.2** Experimental apparatus used for monitoring and controlling the precipitation. (1) Temperature probe, (2) Ag/AgBr electrode, (3) Ag/AgCl reference electrode, (4) pH probe, (5) Feed plume path.

The reactant solutions were separately introduced using two peristaltic pumps and one of two feed modes. In both modes the $AgNO_3$ and NaBr solution introduction points were radially separated by 180° to isolate the two feed zones. The first mode, or impeller feed (Figure 3.3a), introduced both the $AgNO_3$ and NaBr solutions below the surface using tubes directed vertically downwards and ending at the impeller tip. The second mode, or surface feed (Figure 3.3b), introduced the $AgNO_3$ solution at the surface, midway between the impeller tip and the baffle. Again the NaBr solution was introduced below the surface using a tube directed vertically downwards and ending at the impeller tip. The sub-surface tubes were built with a hole in the tube wall. This provided a feed solution exit perpendicular to the tube axis and in the direction of surrounding fluid flow through an outlet diameter of $D_p$ = 0.8 or 1.6 mm. The outside diameter of the sub-surface tubes was restricted to 3 mm to minimize disturbances to the well defined hydrodynamic conditions.

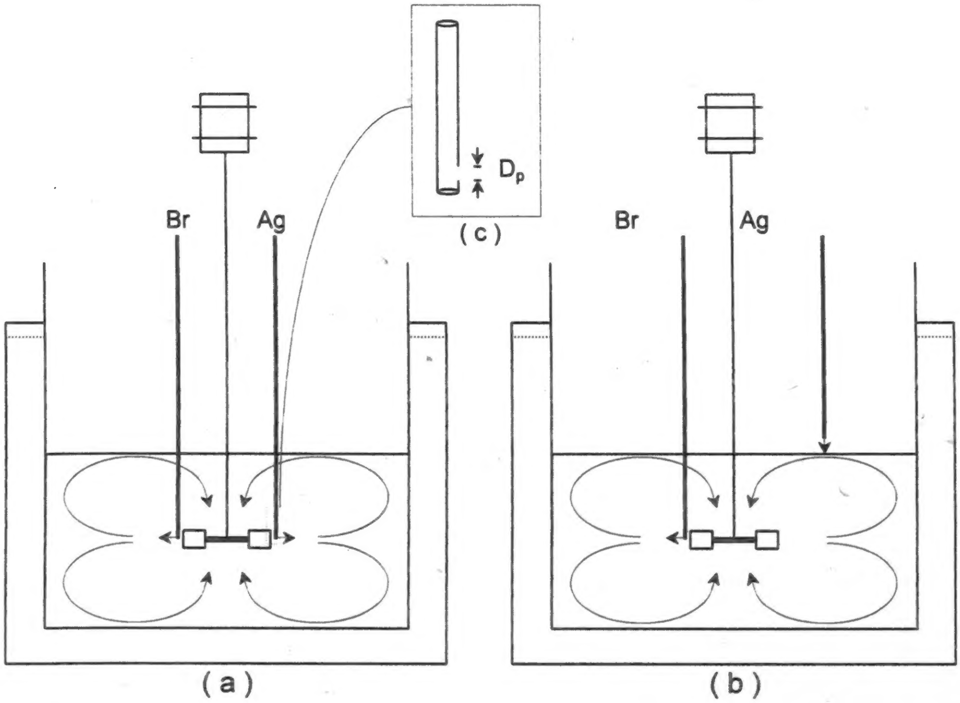

**Figure 3.3** Feed addition points for the precipitation. (a) Impeller feed, (b) Surface feed, and (c) Detail of feed pipe design.

## 3.3 Precipitation Conditions

The precipitation conditions were selected to allow the use of predetermined kinetic (Wey and Strong, 1977a), morphological (Leubner et al., 1980), and thermodynamic data. The precipitation took place at 70 °C, in an aqueous solution of deionized bone gelatin having a weight concentration of 3% in the initial 3 L kettle volume. Based on the definition provided by Antoniades and Wey (1998) this gave an estimated minimum gelatin to silver halide ratio of 500 g/mol at both feed points. The kettle was initially charged with $NaNO_3$ solution to give an initial kettle concentration of 1.0M to avoid changes in ionic strength due to reactant addition during the make. The $AgNO_3$ (2.0M) reactant solution was added at a constant flow rate $Q_f$, while the NaBr (2.0M) reactant solution was added at a regulated flow rate to maintain the initial bromide ion concentration of pBr = 2.55 (defined as: $pBr = -\log_{10}([Br^-])$), which was great enough to avoid kettle segregation due to halide consumption by crystal growth. This corresponds to a pAg of 7.9, and sets the morphology of the precipitates during primary nucleation to be cubic (Leubner et al. 1980).

The precipitation conditions were selected to minimize both secondary nucleation and agglomeration; thus ensuring that only the mixing effects on the precipitation process were investigated. Nielsen (1957) concluded that heterogeneous nucleation occurred when initial concentrations were less than 0.001M, while homogeneous nucleation occurred for initial concentrations greater than 0.01M, or 1000 times the solubility of the solute. Nielsen based his findings on the sudden rapid increase in the number of nuclei from $10^6$ to $10^{12}$ crystals per ml over the concentration range of 0.01 to 0.05M. After making comparisons to Nielsen's work and several other experiments, Berry and Skillman (1968) concluded that homogeneous nucleation is dominant in photographic emulsions as there are typically more than $10^{12}$ crystals per ml. Moreover, Berry and Skillman were unable to observe significant differences in crystal number, even with extremely high concentrations of added impurities, gross inefficiencies in mixing, and decreases in the initial concentrations by factors of 1/100. Wey (1981) found that no secondary nucleation should be expected due to the small nuclei size and the protective role of gelatin. Recently, Antoniades and Wey (1998) established the critical level of gelatin required to provide adequate protection against aggregation as a gelatin to silver halide ratio of 50 g/mol at the feed point. The ratio is defined as

$$R_{gs} = \frac{C_g Q_{surr}}{C_f Q_f} \qquad (3.1)$$

where $C_g$ is the gelatin mass concentration in the suspension, $C_f$ and $Q_f$ are the molar concentration and volumetric flow rate of the silver feed stream, and $Q_{surr}$ is the volumetric suspension flow rate local to the silver feed point. At ratios slightly greater than this (50 to150 g/mol) flocculation occurs, but unlike aggregation flocculation is reversible and does not interfere with the nucleation and growth of crystals.

### *3.3.1 Crystal Size Distribution*

**Sampling**

Leubner et al. (1980) developed a theoretical model ( 3.2 ) to describe the dependence of the stable number of nuclei, Z no./ml on reactant addition rate, R mol/s-ml based on a dynamic mass balance and a growth mechanism including bulk diffusion and the Gibbs-Thompson effect. Their derivation was based on the assumption that the added reactants were ideally mixed and uniformly distributed to all stable crystals in the precipitation kettle. The final expression derived by Leubner et al. (1980) results in the stable number of nuclei being proportional to the molar reactant addition rate. Leubner et al. (1980) then performed several balanced double-jet silver halide precipitations that validated their model. Similar models ( 3.3 ), ( 3.4 ), and ( 3.5 ) were developed by Klein and Moisar (1963), Kharitanova (1979), and Sugimoto (1990), respectively.

$$Z = K\frac{RR_gT}{\sigma D_{mol}V_mC_s} \quad \text{where:}$$

$$K = \frac{1}{8\pi(\bar{r}/r^* - 1)} \tag{3.2}$$

$$K = \frac{1}{8\pi} \tag{3.3}$$

$$K = \frac{3}{8\pi} \tag{3.4}$$

$$K = \frac{1}{5.9\pi} \tag{3.5}$$

Where, $R_g$ is the universal gas constant, T is the absolute temperature, $\sigma$ is the surface energy, $D_{mol}$ is the molecular diffusion coefficient, $V_m$ is the molar volume, $C_s$ is the solubility of the precipitate, and $\bar{r}/r^*$ is the ratio of average to critical crystal size.

Given that the stable number of nuclei formed is proportional to the molar reactant addition rate, under the assumption of ideal mixing it can be shown that average crystal size should be proportional to time. This can be done by incorporating the proportionality ( 3.6 ) into a simple mass balance ( 3.7 ) that assumes negligible accumulation of reactants in the kettle, which is reasonable for high yield precipitations.

$$Z \propto R \tag{3.6}$$

$$Z \cdot \bar{L}^3 \propto R \cdot t \quad \rightarrow \quad \bar{L}^3 \propto t \tag{3.7}$$

This conclusion suggests that the samples for each experiment should be taken at the same standard time intervals, regardless of the molar reactant addition rate. It is expected that any non-linearity in the proportionality between the stable number of nuclei formed and the addition rate, hence the average crystal size, should be attributed to non-ideal mixing. This is contrary to all previous authors (Baldyga et al., 1995) who evaluated the effects of non-ideal mixing under the assumption that the final crystal size should be constant regardless of addition rate. As shown in the following mass balance, this requires that the number of stable nuclei formed be proportional to the total moles fed, which is held constant for each addition rate. However, the number of stable nuclei formed during the nucleation event is completely unrelated to the total moles fed, making this method an inappropriate measure for non-ideal mixing.

$$Z \cdot \overline{L}^{3}_{final} \propto R \cdot t_{final} \quad \rightarrow \quad Z \propto R \cdot t_{final} = \text{mols fed} \qquad (3.8)$$

The standard sampling times in this work were chosen to coincide with the total precipitation time of the experiments conducted, (i.e. 6, 13, 23, 33, 66, 132, and 264 minutes). As well, the standard sampling time of 3 minutes was chosen to provide additional resolution of the crystal size distribution during the initial stages of the precipitation.

Each sample of 10 ml of suspension was obtained using a glass pipette without interrupting the precipitation process. The pipette inlet was several orders of magnitude greater than the typical crystal size. Further physical ripening of these samples was prevented by adding growth restrainer (Gilman *et al.*) and refrigerating the samples until analysis could be performed (see pp. 103 and Figure 3.6).

## Measurement and Analysis

The samples obtained during the course of the precipitation were analyzed using Ultrafine Electron Image Analysis (EIA). EIA uses specialized computer algorithms to digitally analyze crystal images captured by SEM. The equivalent circular diameter (ECD), mean ECD ($\mu_{ECD}$), standard deviation ($\sigma_{ECD}$) and normalized crystal size distribution (CSD) were found using approximately 2000 crystals grouped into at least 20 classes. Figure 3.4 shows a typical electron micrograph used in the EIA.

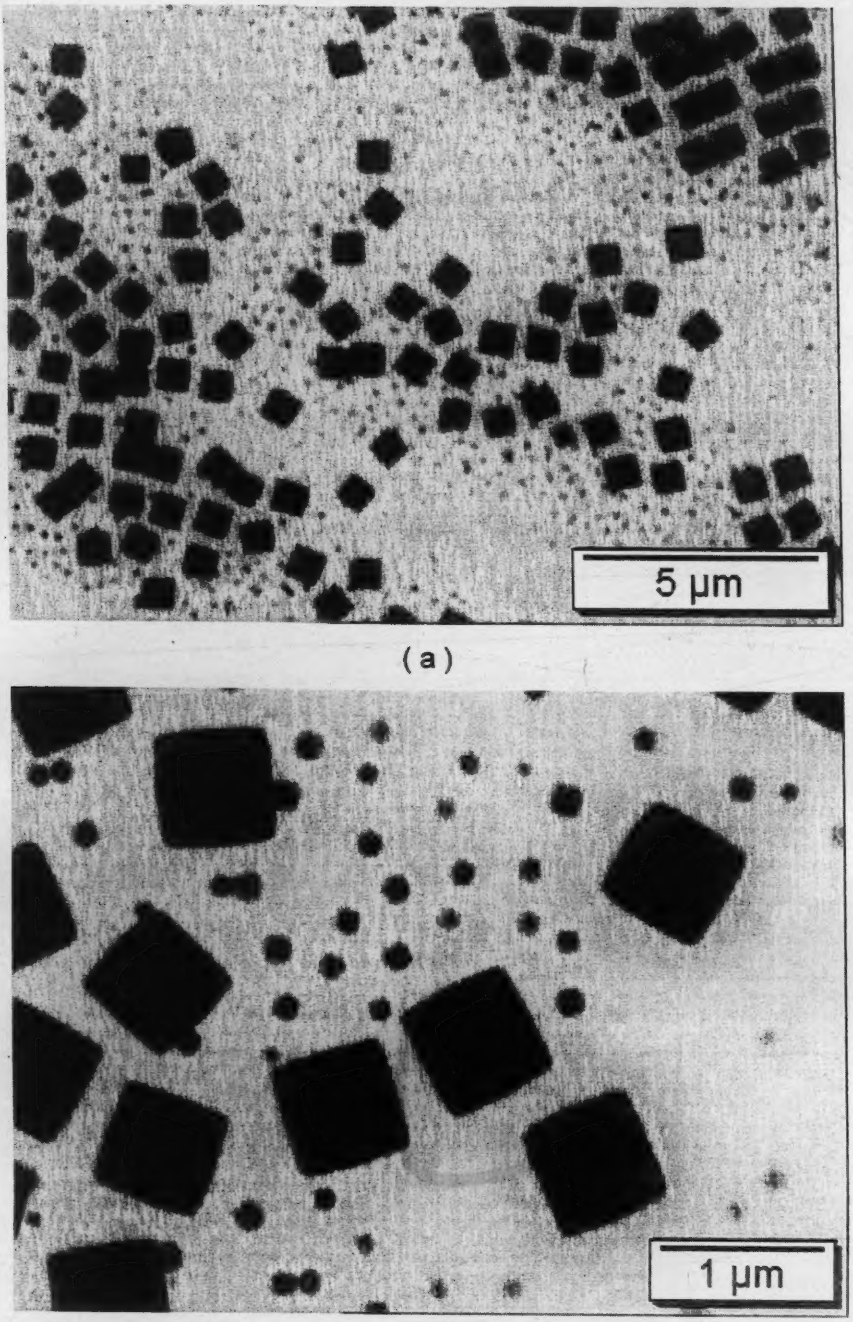

( a )

( b )

**Figure 3.4** Example electron micrographs used in the Ultrafine Electron Image Analysis (EIA). a) Magnification of 2000x, b) Magnification of 6700x.

The ECD of each crystal as measured by the EIA was based on its equivalent circular projected area, therefore the cubic edge length (CEL), mean CEL ($\mu$), standard deviation ($\sigma$), and coefficient of variation (CoV) can be found using the relations ( 3.9 ) through ( 3.12 ), respectively.

$$\text{CEL} = \sqrt{\frac{\pi}{4}}\,\text{ECD} \qquad (3.9)$$

$$\mu = \sqrt{\frac{\pi}{4}}\,\mu_{\text{ECD}} \qquad (3.10)$$

$$\sigma = \sqrt{\frac{\pi}{4}}\,\sigma_{\text{ECD}} \qquad (3.11)$$

$$\text{CoV} = \frac{\sigma}{\mu}100\% \qquad (3.12)$$

In order to enhance the visual information in the measured CSD data, it was vital for the proper normalizations to be made. For instance, Figure 3.5a displays the same CSD ($\mu$ = 0.10 μm, $\sigma$ = 0.01 μm), plotted for total crystal counts (sample sizes) of $N_T = 1 \times 10^9$, $2 \times 10^9$ and $2 \times 10^9$, with constant size intervals of $\Delta L$ = 2.5 and 5.0 nm, and a geometrically increasing interval ($\Delta L_{i+1} = 1.025\Delta L_i$), respectively. From Figure 3.5a, where $N_i$ is the crystal count per size interval, it is immediately obvious that both the total crystal count and the interval sizing have a visual impact on the CSD. The effects of total crystal count can be removed by normalizing the data with the total crystal count as shown in Figure 3.5b where $\tilde{N}_i$ is the relative crystal count per size interval $(N_i/N_T)$. However, Figure 3.5b still shows some variation in the CSDs due to the interval sizing method. The CSDs having constant size intervals of 2.5 and 5.0 nm are different by exactly a factor of two at every point in the distribution. The variation due to the geometrically increasing size intervals is more subtle. Specifically, the geometric CSD differs from the first two distributions by a geometrically decreasing factor. This difference manifests itself by slightly shifting the distribution to the right, which could be visually misinterpreted as an increase in the mean length. To remove the above effects it is necessary to further normalize each CSD with the interval size as shown in Figure 3.5c where $\tilde{n}$ is the relative crystal count per size interval per unit size $\left(\tilde{N}_i/\Delta L\right)$. The resulting function is an approximation to the true normalized crystal density function, which can be properly defined as

$$\lim_{\Delta L \to 0} \frac{\Delta \tilde{N}}{\Delta L} = \frac{d\tilde{N}}{dL} = \tilde{n} \qquad (3.13)$$

where $N$ is the cumulative under-size crystal count and $\Delta\tilde{N}$, or $N_i$, is the relative number of crystals appearing in the size interval $\Delta L$.

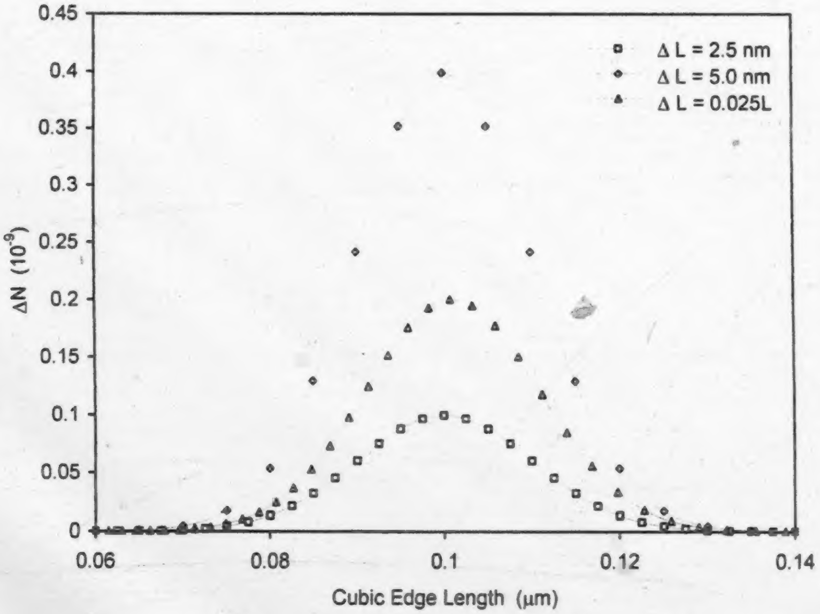

**Figure 3.5a** Comparison of identical crystal size distributions ($\mu$ = 0.10 μm, $\sigma$ = 0.01 μm), for total crystal counts of $1\times10^9$, $2\times10^9$ and $2\times10^9$, with size intervals of 2.5 and 5.0, and 0.025L nm, respectively.

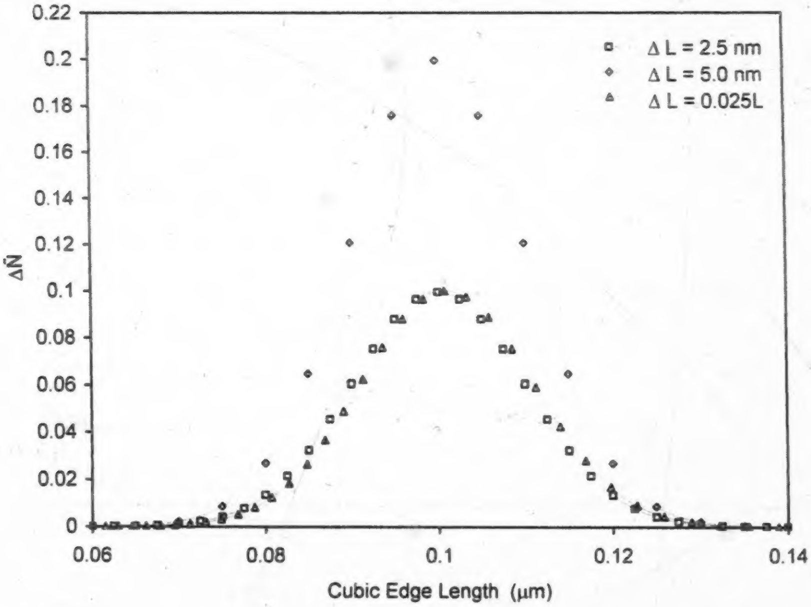

**Figure 3.5b** Comparison of identical normalized crystal size distributions ($\mu$ = 0.10 μm, $\sigma$ = 0.01 μm), for total crystal counts of $1\times10^9$, $2\times10^9$ and $2\times10^9$, with size intervals of 2.5 and 5.0, and 0.025L nm, respectively.

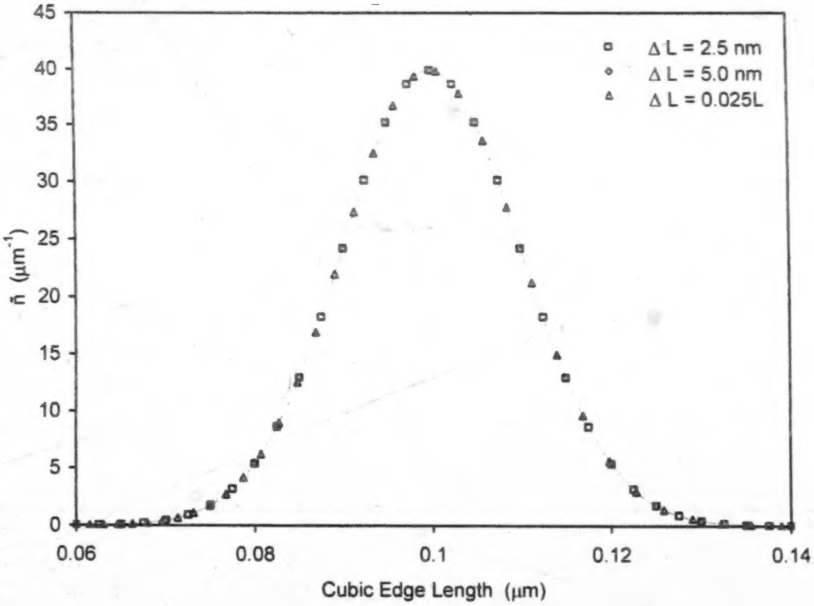

**Figure 3.5c** Comparison of identical normalized crystal density functions ($\mu$ = 0.10 μm, $\sigma$ = 0.01 μm), for total crystal counts of $1 \times 10^9$, $2 \times 10^9$ and $2 \times 10^9$, with size intervals of 2.5 and 5.0, and 0.025L nm, respectively.

For further information and examples of plotting the crystal size distributions refer to Appendix C.

The EIA calibration suggested less than 1% error in the measurements. Analyzing two identical samples more than a week apart demonstrated very high repeatability in the measurement of the samples and no measurable change in the sample over time (Figure 3.6).

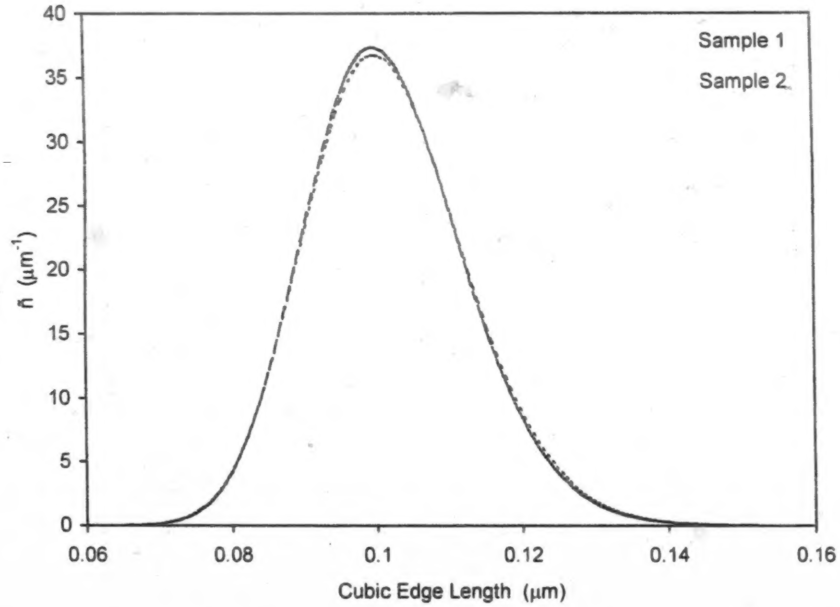

**Figure 3.6** Comparison of Electron Image Analysis Measurements for Two Identical Samples.

### *3.3.2 Mixing Conditions*

The nucleation process is an instantaneous chemical reaction that requires molecular scale homogeneity to proceed. Micromixing theory is used to explain small-scale processes such as the reduction in concentration scale by fluid breakage, deformation, and molecular diffusion. Micromixing effects can directly affect the course of fast or instantaneous chemical reactions and hence, their conversion or selectivity. As feed rates increase, micromixing may no longer be the limiting scale. The relevant scale is not the macro scale of the whole vessel, but an intermediate or mesoscale. This mesomixing scale creates the concentration field in which micromixing takes place. The relative importance of the micromixing and mesomixing processes can be quantified by the ratio of their characteristic time constants, which are functions of the local turbulence field (Equation 1.60). Thus, knowledge of the turbulence field is necessary to estimate the degree of mixing and consequently the problem of reaction kinetics to be studied.

To determine the turbulence field, the vessel's liquid properties, geometry, and operating conditions must be known. Then the circulation patterns and turbulence conditions can be estimated by applying the published data of Kresta and Wood (1991), Zhou and Kresta (1993 a and b), and Kresta et al. (2001) (Section 1.5). These data require that the vessel be operated under fully turbulent conditions. A Reynolds number of $2 \times 10^4$ describes the lower limit of fully developed turbulence at the impeller, but much larger Reynolds numbers are required for the turbulence to penetrate to the upper portion of the vessel (Kresta et al., 2001).

It is the primary objective of this work to study the effects of mixing on the precipitation process and particularly the effect of mesomixing on the product crystal size distribution. Therefore, experiments were performed at the limiting condition of micromixing and over the transition from micromixing to mesomixing. Initial estimates of the limiting micromixing conditions were made and targeted to begin the mesomixing analysis.

Using the above criteria of maintaining a turbulent impeller Reynolds number resulted in lower impeller rotational speed limits (Table 3.1). However, increasing the impeller rotational speed to create more turbulence caused significant roll over of the upper fluid surface and air entrainment into the fluid. The upper limits as determined by experimentation are shown in Table 3.1. The impeller rotational speeds selected were within these narrow limits.

**Table 3.1** Minimum, maximum and selected impeller rotational speeds.

| Impeller Diameter (m) | | $N_{low}$ (rps) | $N_{high}$ (rps) | $N_{expt}$ (rps) | $N_{expt}$ (rpm) |
|---|---|---|---|---|---|
| T/3 | 0.067 | 9.0 | 11.0 | 10.5 | 630 |
| T/4 | 0.050 | 16.0 | 17.0 | 16.7 | 1000 |

Fixing the impeller rotational speed fixed the remaining hydrodynamic quantities. The relevant quantities were mean velocity, U, turbulent kinetic energy, k, rate of dissipation of turbulent kinetic energy, $\varepsilon$, and the turbulent diffusivity, $D_t$, at the silver feed point (Table 3.2).

**Table 3.2** Hydrodynamic quantities.

| | Impeller Diameter | | | |
|---|---|---|---|---|
| | T/3 (0.067 m) | | T/4 (0.050 m) | |
| | Impeller feed | Surface feed | Impeller feed | Surface feed |
| U (m/s) | 1.54 | 0.088 | 1.83 | 0.085 |
| k (J/kg) | 1.03 | 0.098 | 1.35 | 0.11 |
| $\varepsilon$ (W/kg) | 84.89 | 0.83 | 171.40 | 0.99 |
| $D_t$ ($m^2$/s) | 0.00125 | 0.00115 | 0.00107 | 0.00122 |

The characteristic micromixing time constant, $t_M$, was then determined at both the impeller and the surface (Table 3.3) according to the definition given by Baldyga and Bourne (1992). From this, the minimum characteristic turbulent dispersion mesomixing time constant, $t_{D,min}$ (Table 3.3) was calculated using the relation $Q_m=t_D/t_M$, which is expected to equal 0.2 when mesomixing first becomes significant (Baldyga et al. 1993, Bourne and Yu 1994).

**Table 3.3** Characteristic mixing time constants.

| | Impeller Diameter | | | |
|---|---|---|---|---|
| | T/3 (0.067 m) | | T/4 (0.050 m) | |
| | Impeller feed | Surface feed | Impeller feed | Surface feed |
| $t_M$ (s) | 2.7E-3 | 2.7E-2 | 1.9E-3 | 2.5E-2 |
| $t_{D,min}$ (s) | 5.3E-4 | 5.3E-3 | 3.7E-4 | 5.0E-3 |

Applying this definition of the characteristic mesomixing time constant (Baldyga and Bourne 1992) allowed the minimum feed rate, $Q_{f,min}$ (Table 3.4) required for mesomixing to be determined.

**Table 3.4** Minimum required feed rate for turbulent dispersion mesomixing.

| | Impeller Diameter | | | |
|---|---|---|---|---|
| | T/3 (0.067 m) | | T/4 (0.050 m) | |
| | Impeller feed | Surface feed | Impeller feed | Surface feed |
| $Q_{f,min}$ ($m^3/s$) | 1.0E-6 | 5.4E-7 | 7.3E-7 | 5.1E-7 |
| $Q_{f,min}$ (ml/min) | 60.6 | 32.3 | 43.7 | 30.3 |

## 3.4 Micromixing Analysis

In order to validate the preliminary components of the precipitation model, it was necessary to remove as much uncertainty due to inadequate mixing as possible. Comparison of the feed locations in Table 3.3 shows that the impeller feed point gave micromixing times one order of magnitude smaller than the surface feed. Further inspection of Table 3.3 then shows that the T/4 impeller gave the most rapid micromixing time of the two impeller sizes used. Thus the initial experiments were conducted using the impeller feed point and the T/4 impeller, as this configuration resulted in the most ideal mixing possible.

### 3.4.1 Seeded Experiments

The objective of the initial seeded experiments was to directly validate the size-dependent growth kinetics used in the precipitation model, which would also indirectly validate the thermodynamic equilibrium and population balance models. It should be emphasized that these experiments were designed specifically to diminish nucleation by reducing the supersaturation through using an initial seed population and slow feed and rapid mixing, thus making crystal growth the dominant mechanism in the vessel.

To validate the effect of the size-dependent growth kinetics, the kettle was seeded with two distinct seed crystal distributions. Continuous reactant addition was required to keep the suspension supersaturated with respect to each of the seed distributions. This ensured that Ostwald ripening did not lead to the dissolution of the smaller distribution. However, the Gibbs-Thompson effect may have still influenced the growth of the distributions relative to each other. This consideration, however, does not exclude the possibility of continuous nucleation in the high supersaturation region near the feed point (Berry 1976). It is expected that the nuclei generated here spontaneously dissolve in the bulk acting primarily as material for the growth of the two stable distributions. These transient nuclei can therefore be neglected in the overall precipitation process since the effective nucleation rate is negligible.

## Precipitation Conditions

The experimental conditions were selected to nearly replicate the work of Wey and Strong (1977b). Monodisperse seed crystals with cubic edge lengths of 0.114 and 0.688 μm were used in the amount of 0.099 and 3.267 moles of silver halide, respectively. These amounts correspond to the small distribution having one-fifth the surface area of the larger distribution. According to the kinetic data of Wey and Strong (1977a) it was estimated that the maximum consumption rate of the seed crystals would be 0.0067 mol/s of silver halide at the point of renucleation (Table 3.5). To reduce the possibility of renucleation the molar reactant addition rate should be a fraction of this limit. The solution must also be supersaturated with respect to the seed crystals to avoid the dissolution of the smallest crystal sizes in the distribution. A ratio of the calculated consumption rate to molar addition rate of four was used, which corresponds to a 2 M feed at 45 ml/min. The 45 ml/min feed was placed at the impeller tip to minimize inhomogeneity and mesomixing effects (Table 3.3). To ensure that mixing had no effect on the product crystal size distribution, experiments were conducted for both the T/3 and T/4 impellers. The experimental conditions are summarized below (Table 3.6).

**Table 3.5** Estimated silver halide consumption by seed crystals at renucleation.

| $\mu$ (m) | $N_T$ | AgBr (mol) | Total Surface Area ($m^2$) | Growth Rate ($m\ s^{-1}$) | Consumption ($mol\ s^{-1}$) |
|---|---|---|---|---|---|
| $1.14 \times 10^{-7}$ | $1.9 \times 10^{15}$ | 0.099 | 151.1 | $5.29 \times 10^{-10}$ | 0.0028 |
| $6.88 \times 10^{-7}$ | $2.9 \times 10^{14}$ | 3.267 | 826.5 | $1.39 \times 10^{-10}$ | 0.0040 |
| Total | $2.19 \times 10^{15}$ | 3.366 | 977.6 | | 0.0067 |

**Table 3.6** Summary: Mixing Conditions - Seeded experiments.

| Label | Impeller Diameter | N (rps) | $D_p$ (mm) | $Q_f$ (ml min$^{-1}$) | $t_f$ (min) |
|---|---|---|---|---|---|
| MM11 | T/3 | 10.5 | 0.8 | 45 | 33.3 |
| MM12 | T/4 | 16.7 | 0.8 | 45 | 33.3 |

## Results and Discussion

The experimental results confirm the size-dependent growth presented by Wey and Strong (1977a). This is shown in Figure 3.7 where the smaller and larger distributions grew approximately 0.2 and 0.12 μm while in the same environment, respectively. This indicates a size-dependent growth rate where the smaller crystals grew more rapidly than the larger crystals indicating the influence of diffusional growth. Moreover, it can be seen from Figure 3.7 that the smaller distribution first grows broader then narrower indicating a transition from Gibbs-Thompson influenced growth to diffusional growth. Due to the absence of unusually small crystals (0 to 0.01 μm) and the absence of significantly rounded crystal corners, it was concluded that no net nucleation or dissolution (Ostwald ripening) occurred. Moreover, the total crystal count remained relatively constant during each precipitation as calculated by a mass balance (Appendix B), and it is a known effect of Ostwald ripening to produce rounded corners on cubic crystals (Berry and Skillman 1968).

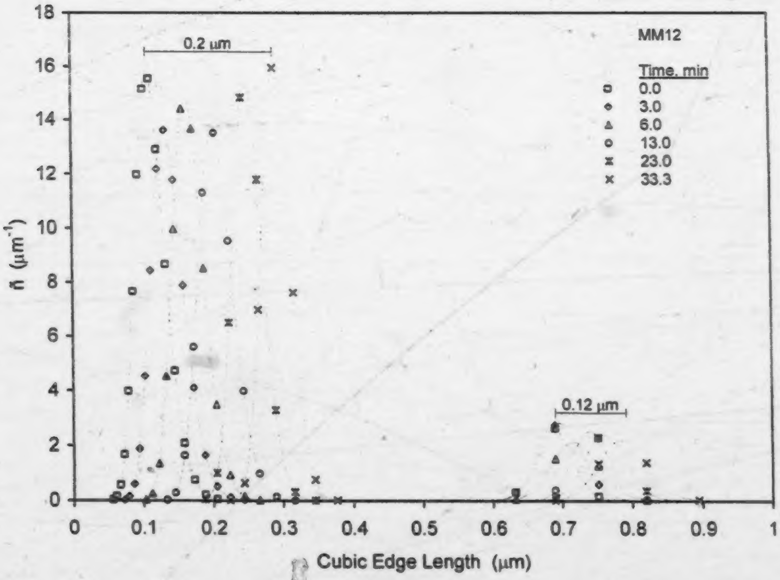

**Figure 3.7** CSD time evolution for Seeded Micromixing Analysis - MM12.

The precipitation conditions of MM12 were replicated and a comparison of the CSD results is shown in Figure 3.8. This figure shows very good repeatability between the experiments.

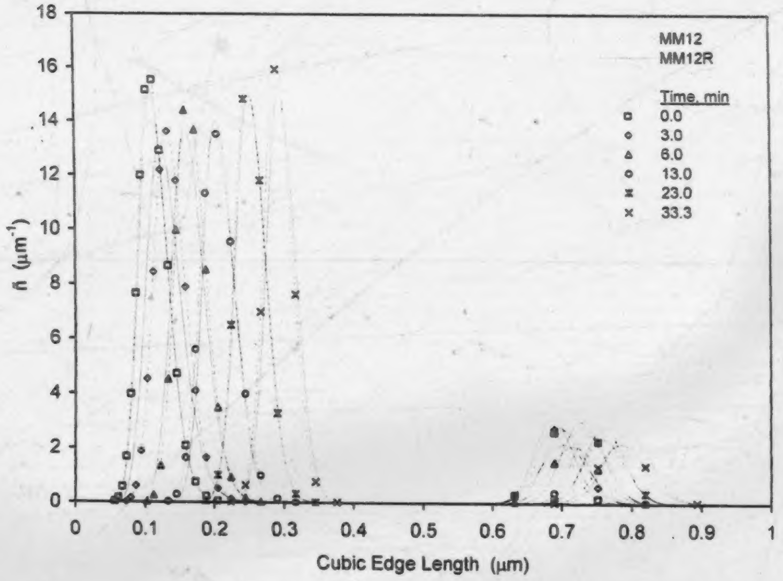

**Figure 3.8** Comparison of CSD time evolutions for the same seed distribution under identical mixing conditions.

Figure 3.9 compares the time evolution of the same seed distribution under different mixing conditions (MM11 vs. MM12). The slight variation between CSDs is comparable to the variation of results collected under the same mixing conditions (Figure 3.8). Thus, it was concluded that the selected mixing conditions did not have an effect on the time evolution of the CSD for the seeded experiments.

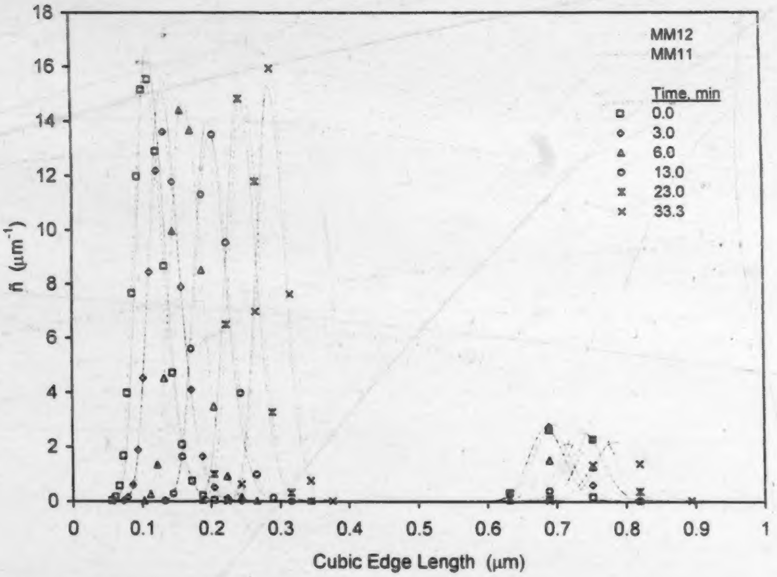

**Figure 3.9** Comparison of CSD time evolutions for the same seed distribution but under different mixing conditions.

### *3.4.2 Nucleation Experiments*

The objective of the initial nucleation experiments was to directly validate the instantaneous nucleation model. This would also indirectly validate the micromixing model used to generate the supersaturation required for nucleation. Finally, these experiments were used to validate the extrapolated size-dependent growth kinetics for crystal sizes on the order of the nuclei size. This validation is significant for the precipitation model since the size-dependent growth kinetics were only determined experimentally for crystal sizes much greater than the nuclei size (Wey and Strong 1977a).

To validate the nucleation model, the reactant solutions were simultaneously added to an unseeded reaction kettle. Initially, the function of the reactant addition was to generate the high supersaturation region required for nuclei formation. After a stable CSD had formed and nuclei survival ceased, the function of the reactant addition changed to keeping the suspension supersaturated with respect to the stable CSD. This ensured that Ostwald ripening did not lead to the dissolution of the smallest crystals in the CSD. However, the Gibbs-Thompson effect may have still influenced the relative growth of the crystals within the CSD. This consideration, however, does not exclude the possibility of continuous nuclei formation at the feed point (Berry 1976). It is expected that the nuclei generated after the stable CSD is formed are unstable and spontaneously dissolve, acting as a source of material for the growth of the CSD.

### Precipitation Conditions

The experimental conditions were exactly the same as in the preceding seeded experiments except for the absence of the initial seed distribution. To investigate the possible effects of mixing on the nucleation process, and hence the product crystal size distribution, the experiments were conducted for both the T/3 and T/4 diameter impellers. The experiments are summarized below (Table 3.7).

**Table 3.7** Summary: Mixing Conditions - Nucleation experiments.

| Label | Impeller Diameter | N (rps) | $D_p$ (mm) | $Q_f$ (ml min$^{-1}$) | $t_f$ (min) |
|---|---|---|---|---|---|
| MM14 | T/4 | 16.7 | 0.8 | 45 | 33.3 |
| MM16 | T/3 | 10.5 | 0.8 | 45 | 33.3 |

### Results and Discussion

The experimental results again confirm the size dependent growth presented by Wey and Strong (1977a). This is revealed in Figure 3.10 where the variance in the CSDs increases with mean length. This indicates that the smaller crystals grew more slowly than the larger crystals within the same distribution, a result of the Gibbs-Thompson effect. Again, due to the absence of unusually small crystals (0 to 0.01 μm) and the absence of significantly rounded crystal corners, it was concluded that no net nucleation or dissolution (Ostwald ripening) occurred once the stable population formed. In addition, the total crystal count remained relatively constant during each precipitation as calculated by a mass balance (Appendix B), with the exception of the sample taken at 13 minutes for MM14, which over estimates the total crystal count by approximately 20% relative to the other samples. This suggests the sample was taken too soon, therefore the crystal size was too small and caused an increase in the number of crystals required to equal the mass added to the reaction kettle.

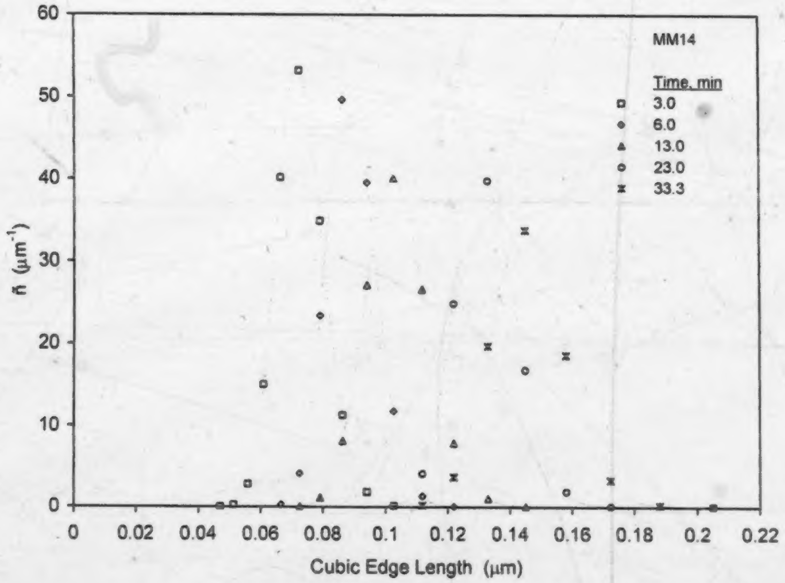

**Figure 3.10** CSD time evolution for Nucleated Micromixing Analysis - MM14.

Both MM14 and MM16 were replicated to establish the variability due to the nucleation process. The replicates are shown in Figure 3.11 and Figure 3.12, respectively. Both figures show excellent agreement between the replicated experimental results, with the exception of the sample taken at 13 minutes for the precipitation conditions of MM14. Examination of the total crystal counts for both samples suggests that MM14R is more accurate since its crystal count is in better agreement with the remaining samples of both replicates (Appendix B). Neglecting the samples taken at 13 minutes, the replicates demonstrate high reproducibility in the nucleation experiments.

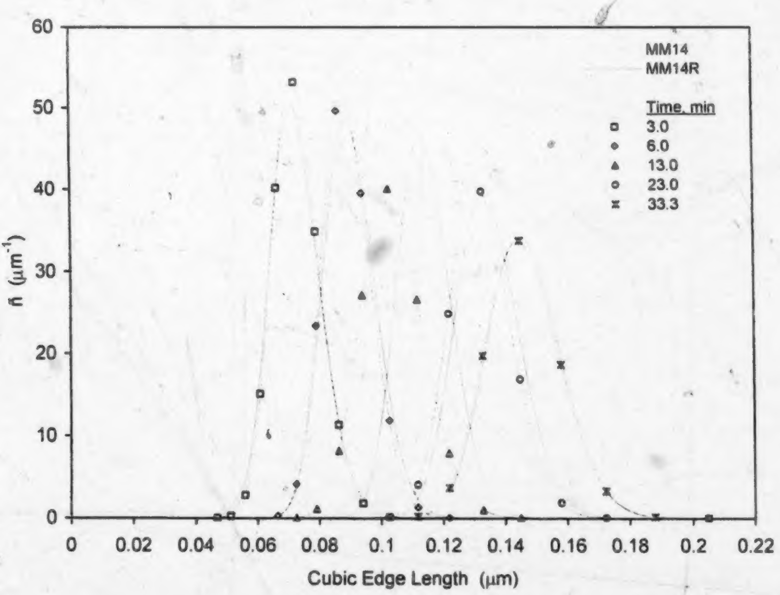

**Figure 3.11** Comparison of CSD time evolutions for the same nucleation conditions under identical mixing conditions.

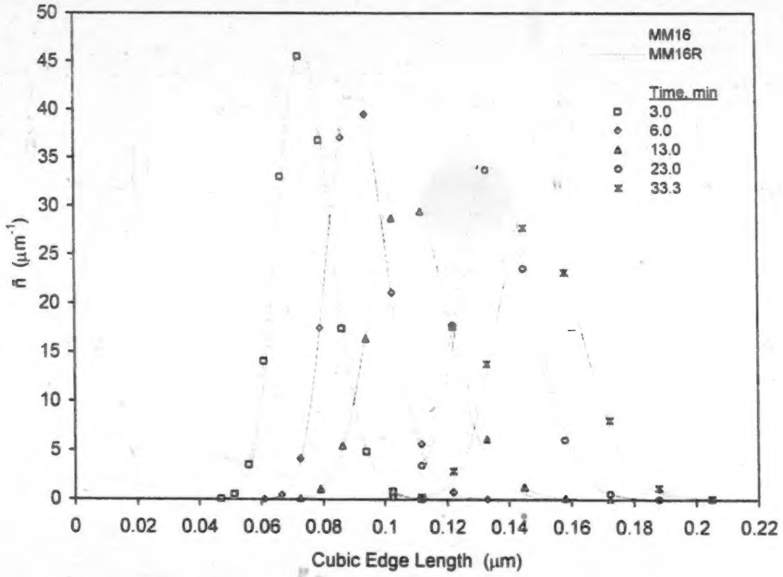

**Figure 3.12** Comparison of CSD time evolutions for the same nucleation conditions but under identical mixing conditions.

Figure 3.13 compares the time evolution for the same nucleation conditions but under different mixing conditions (MM14 vs. MM16). The variation between CSDs cannot be completely explained by the variability due to sampling, as it can be seen that this variation is generally greater than that of the replicated samples in Figure 3.11 and Figure 3.12. Therefore the additional variability must be attributed to the different mixing conditions of MM14 and MM16. Figure 3.13 indicates that the less ideal mixing conditions of MM16 caused a slight increase in both the variance and mean length of the product CSD. This suggests that less ideal mixing conditions have a lower nucleation efficiency since mean length and total crystal count are inversely related according to a mass balance on the reaction kettle.

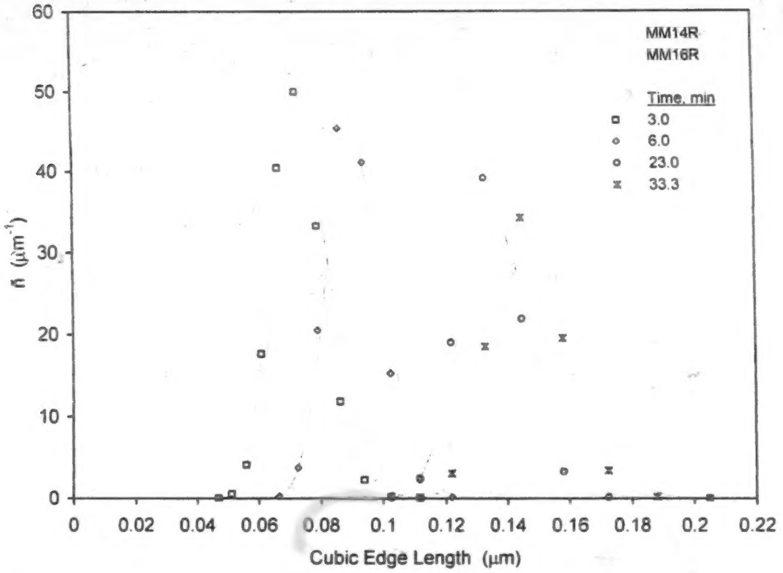

**Figure 3.13** Comparison of CSD time evolutions for nucleation under different mixing conditions.

## 3.5 Precipitation Model Validation

Initial validation of the precipitation model required removing as much uncertainty due to the nucleation event as possible. In the first set of conditions, the precipitation kettle was seeded with enough crystals to completely consume the added reactants by crystal growth, therefore keeping the supersaturation below the required limit for nucleation. Furthermore, the supersaturation within the feed plume was minimized through slow reactant addition and rapid mixing, thus making crystal growth the dominant mechanism in the vessel. In the second set of conditions the nucleation event was included, while still removing as much uncertainty due to the mixing model as possible. This required operating in the micromixing controlled regime as the most confidence and independent validation is available for the micromixing model.

The complete simulated results are given in Appendix B. Typical illustrative results are discussed below.

### 3.5.1 Seeded Precipitation Validation

To directly validate the size-dependent growth kinetics and confirm the thermodynamic equilibrium, material balances and crystal population balances, the precipitation kettle was seeded with a bimodal crystal distribution and operated under rapid micromixing conditions. These conditions did not exclude the possibility of continuous nucleation in the feed plume, but did maximize the likelihood of all nuclei spontaneously dissolving in the kettle. Therefore, these transient nuclei can be neglected in the overall precipitation process. Inaccuracies in the mixing model, which generates the excess supersaturation used for nucleation, will also have little effect on this validation.

The precipitation model prediction for the bimodal seed crystal distribution and the above conditions (*i.e.* replicating batch MM12) is shown in Figure 3.14. The small mode grows slightly too fast, and becomes narrower rather than broader. In accordance with the small mode growing too quickly, and thus consuming too much of the added reactant, the large mode consumes less and grows too slowly. The total crystal count ($N_T = 1.85 \times 10^{15}$) and kettle supersaturation ($S = 1.15$) remain relatively constant during the precipitation, in agreement with experimental measurements. The symmetric geometric length scale had the point of symmetry equal to the nuclei length ($L_{Pn} = 0.00435$ μm), a maximum crystal length of 2 μm, and required greater than 100 size intervals to converge on the solution. This result is satisfactory for confirming the validation of the thermodynamic equilibrium, material balance and population balance models, however it indicates that the kinetic parameters measured by Wey and Strong (1977a) are only approximate.

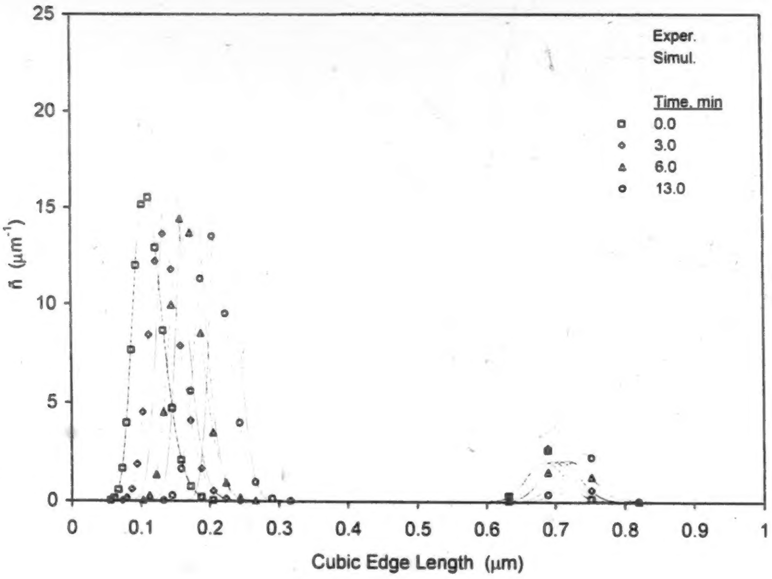

**Figure 3.14** Satisfactory agreement between the model predictions and experimental results for the bimodal seed crystal distribution (MM12) validates the thermodynamic equilibrium, material balances and population balances.

In addition to validating the precipitation model with the bimodal seed crystal distribution, the first sample distribution of the unseeded experiments was used as a pseudo-unimodal seed crystal distribution. This was done by starting the simulations with the measured CSD at 3 minutes, as a pseudo-seed population. This allowed validation of the size-dependent growth kinetics for both smaller crystal sizes and different supersaturations. The unseeded experimental batch MM14R was replicated since it used identical conditions to MM12 except for the seed crystal distribution and is more accurate than MM14. Figure 3.15 shows the increased accuracy of the kinetic parameters for this pseudo-unimodal seed crystal distribution. Again the experimental finding that total crystal count ($N_T = 2\text{x}10^{16}$) and supersaturation ($S = 1.10$) remain relatively constant during a precipitation was confirmed.

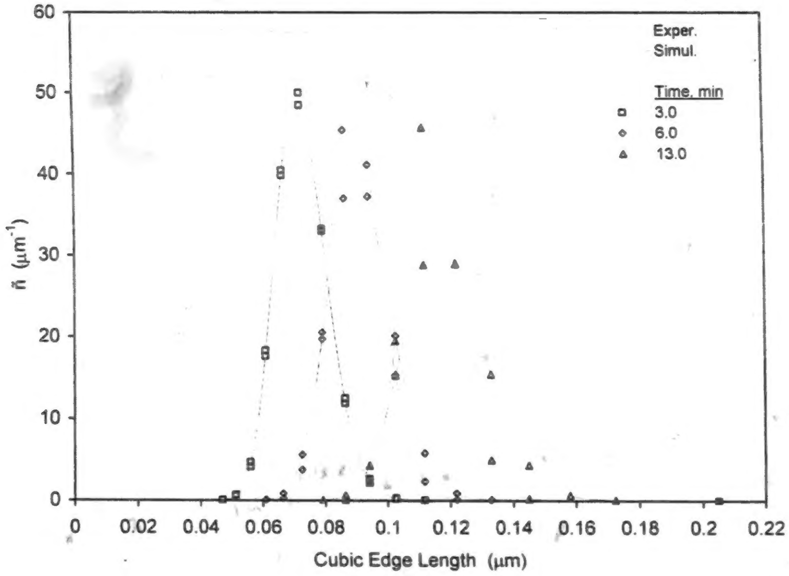

**Figure 3.15** Increased agreement between the model predictions and experimental results for the pseudo-unimodal seed crystal distribution (MM14R, t > 3 minutes) validates the growth kinetics measured by Wey and Strong (1977a) for unimodal distributions larger than 0.047 μm.

## Parameter Optimization: Sensitivity Analysis

In an attempt to find a set of optimized parameters that give satisfactory predictions for both the pseudo-unimodal and bimodal seed crystal distributions the relevant parameters were varied. Both the molecular diffusivity $D_{mol}$ and interfacial tension $\sigma$ were varied over the literature ranges of 1 to $5 \times 10^{-9}$ $m^2/s$ and 0.11 to 0.14 N/m, respectively, while the ratio of diffusion to surface integration resistance was varied over the range $\xi_o/10$ to $\xi_o$. The critical supersaturation limit required for nucleation and the mixing rate were not varied, as the nucleation event is negligible for seeded precipitations.

To evaluate the fit of the model predictions to the experimental data, the error in mean length and variance for each mode was summed over each sample according to

$$\text{Error} = \frac{\displaystyle\sum_{\text{Samples}}\sum_{\text{Modes}}\left[\left(\frac{\mu_{s,m} - \mu_{Ex,s,m}}{\mu_{Ex,1,m}}\right)^2 + \left(\frac{\sigma_{s,m} - \sigma_{Ex,s,m}}{\sigma_{Ex,1,m}}\right)^2\right]^{1/2}}{\text{Samples} \cdot \text{Modes}} \tag{3.14}$$

where each residual was normalized by the initial sample value to place the same emphasis on each error. The error plots for a surface tension of 0.11 N/m are shown below (Figure 3.16 and Figure 3.17) and are identical to the error plots for a surface tension of 0.14 N/m except for having slightly lower error values. As shown most clearly in the top-view plots, the combined error is a minimum at a molecular diffusivity of 4x10$^{-9}$ m$^2$/s and a ratio of relative resistance of $\xi_o/5$. The improved model predictions are shown in Figure 3.18 and Figure 3.19.

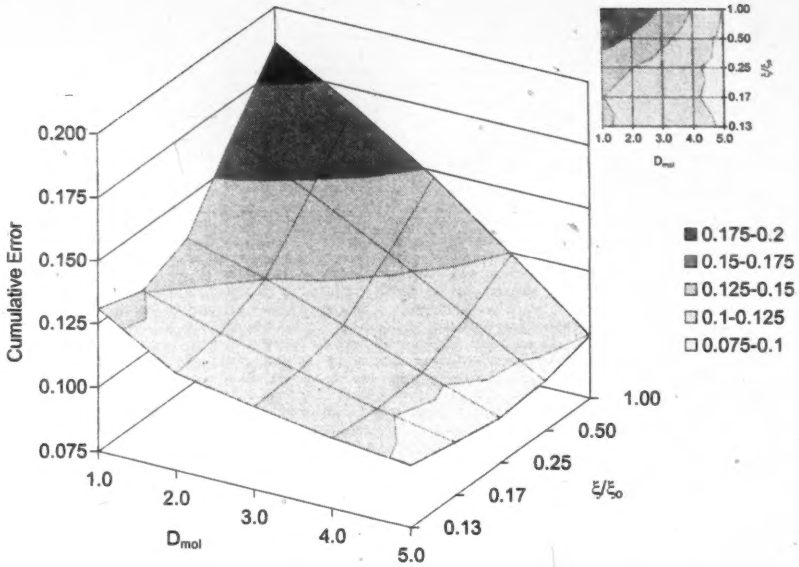

**Figure 3.16** Cumulative error in the model predictions for the bimodal seed distribution at an interfacial tension of 0.11 N/m.

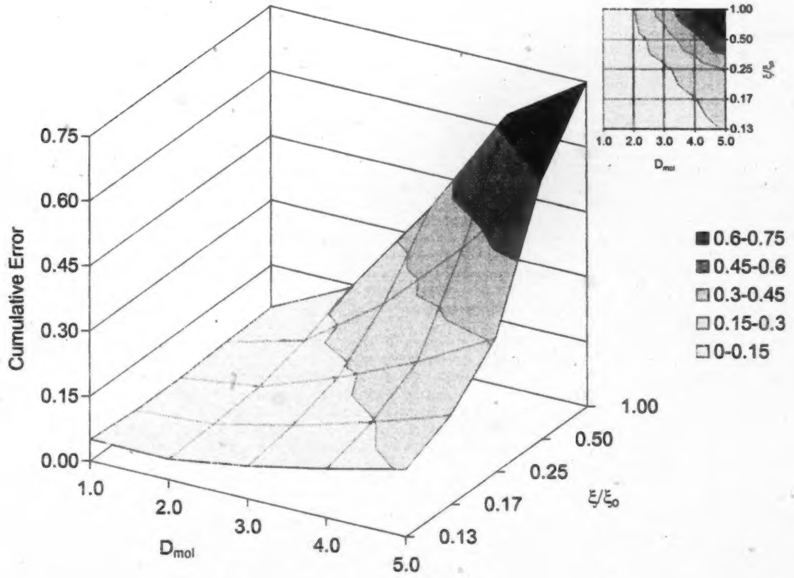

**Figure 3.17** Cumulative error in the model predictions for the pseudo-unimodal seed distribution at an interfacial tension of 0.11 N/m.

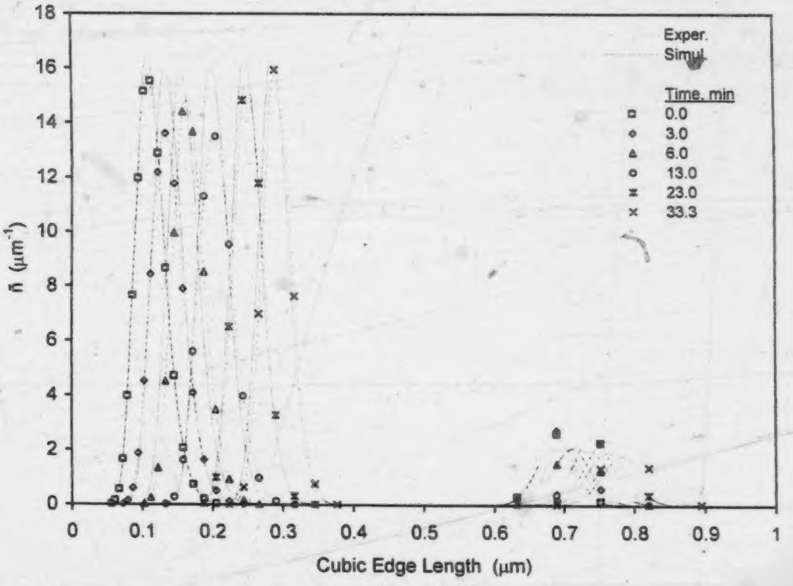

**Figure 3.18** Excellent agreement of the model predictions and experimental results using the optimized parameters.

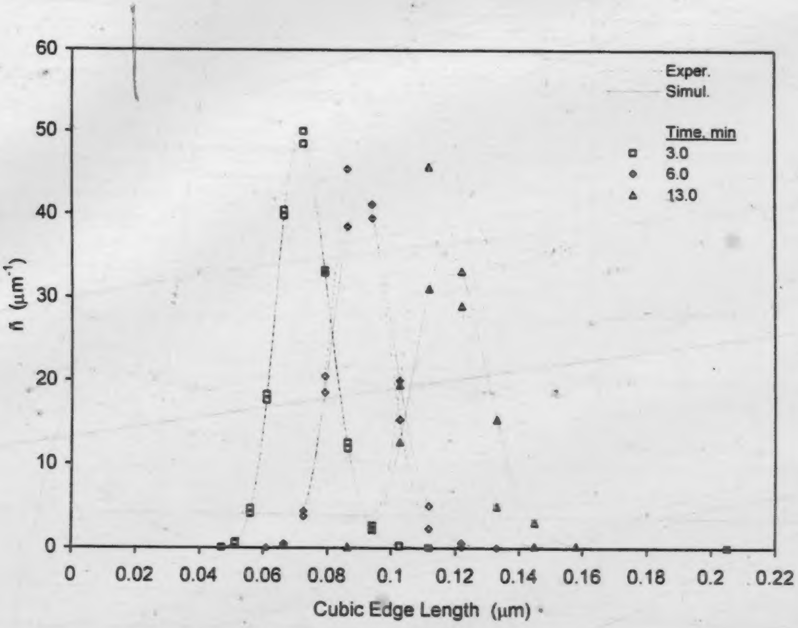

**Figure 3.19** Excellent agreement of the model predictions and experimental results using the optimized parameters.

### 3.5.2 *Unseeded Precipitation Validation: Nucleation Model*

To directly validate the instantaneous nucleation model, and indirectly confirm the micromixing model that generates the excess supersaturation required for nucleation, the reactants were added to an unseeded precipitation kettle operated under rapid mixing. These simulations were also used to validate the extrapolated size-dependent growth kinetics for crystal sizes on the order of the nuclei size. This validation was significant for the precipitation model since the kinetic parameters were only determined experimentally for crystal sizes much greater than the nuclei size (Wey and Strong 1977a).

Both the original kinetic parameters of Wey and Strong (1977a), and the optimized parameters determined in the previous section were used in the precipitation model to validate the nucleation model. In addition to these parameters, the nucleation model was optimized for a critical supersaturation limit required for nucleation between the literature values of 1.5 and 3.7 (Jagannathan and Wey 1985). The original parameters required a critical supersaturation limit of 3.7, while the optimized parameters required a limit of 2.1. The results of replicating the conditions of experimental batch MM14R are shown below in Figure 3.20 and Figure 3.21. Noting that both sets of parameters have been validated for unimodal crystal distributions having a mean length greater than 0.047 μm in the previous section, the evaluation of the nucleation model and growth kinetics should be based on the accuracy of the model for prediction of distributions having mean lengths less than 0.047 μm. Using this criterion, the nucleation model and extrapolated growth kinetics are satisfactorily validated for both sets of parameters, and are superior when the original parameters are used. This is based on the optimized parameters being slightly better at predicting the mean crystal length, while the original parameters are significantly better at predicting the variance of the crystal distribution. The total crystal count ($N_T = 1.85 \times 10^{15}$) and kettle supersaturation ($S = 1.15$) remained relatively constant after the nucleation event took place. The symmetric geometric length scale had the point of symmetry as the nuclei length ($L_{Pn}$ =

0.00435 μm), a maximum crystal length of 2 μm, and required greater than 200 size intervals to converge on the solution. The increased length scale resolution requirement can be explained by the need to accurately describe growth of much smaller crystals during and following the nucleation event.

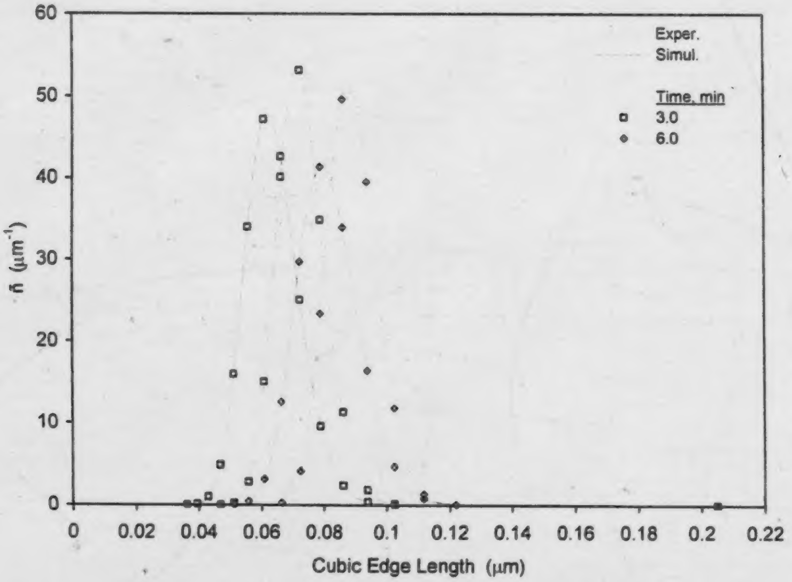

**Figure 3.20** Agreement of the model predictions and experimental results for the nucleation event using the original parameters and a critical supersaturation of 3.7 (first sample error = 0.13).

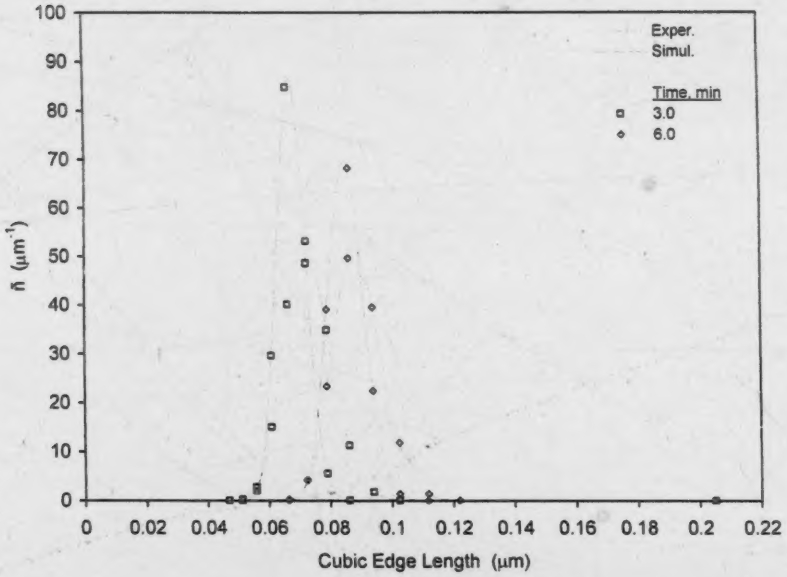

**Figure 3.21** Agreement of the model predictions and experimental results for the nucleation event using the optimized parameters and a critical supersaturation of 2.1 (first sample error = 0.44).

Further validation of the nucleation model and extrapolated growth kinetics is provided in Figure 3.22 and Figure 3.23. These figures demonstrate the ability of the precipitation model to predict mean crystal length, or total crystal count as determined by a mass balance, as a function of molar reactant addition rate. Again the original set of parameters greatly outperforms the ability of the optimized set of parameters to predict the nucleation event as shown by the close agreement with the experimental data. Figure 3.24 and Figure 3.25 demonstrate that the model does not predict the variance of the crystal distribution for other molar addition rates.

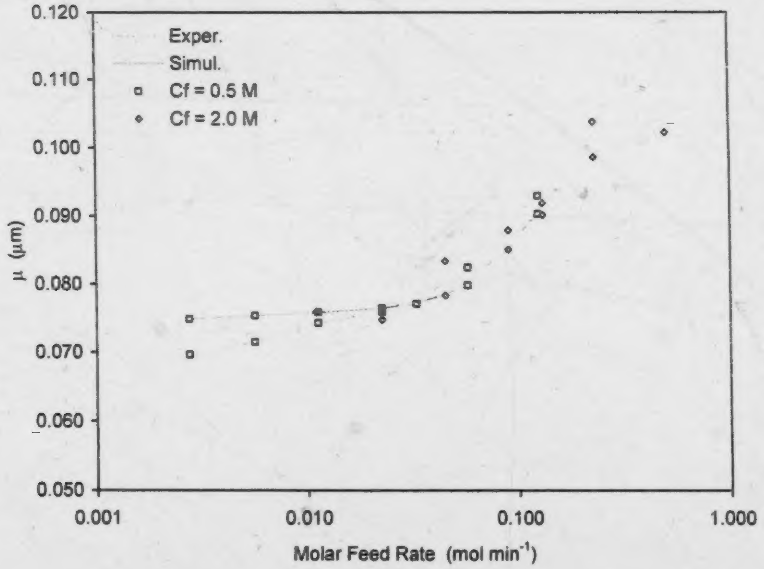

**Figure 3.22** Excellent agreement of the model predictions and mean crystal length at 6 minutes for various feed rates using the original parameters.

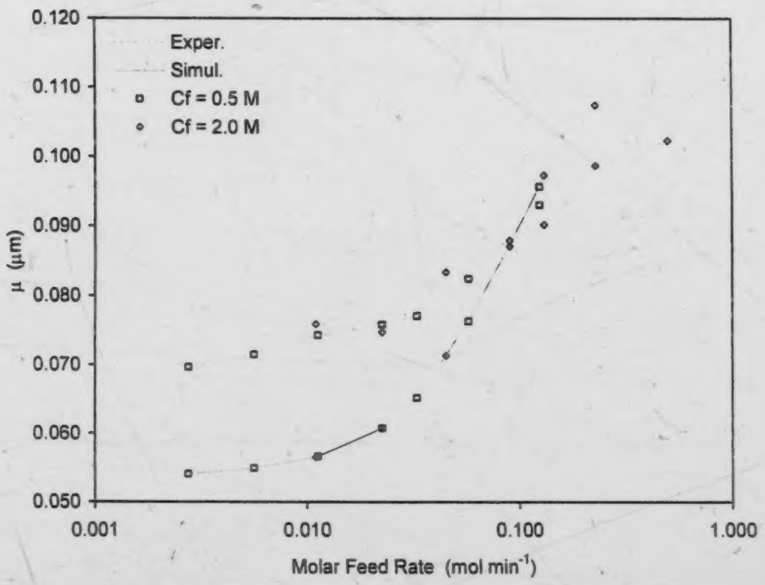

**Figure 3.23** Agreement of the model predictions and mean crystal length at 6 minutes for various feed rates using the optimized parameters.

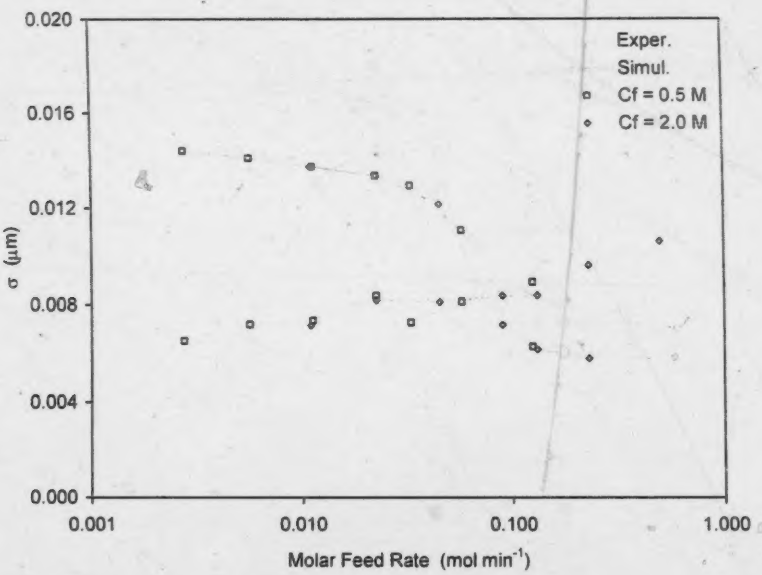

**Figure 3.24** Poor agreement of the model predictions and population variance at 6 minutes for various feed rates using the original parameters.

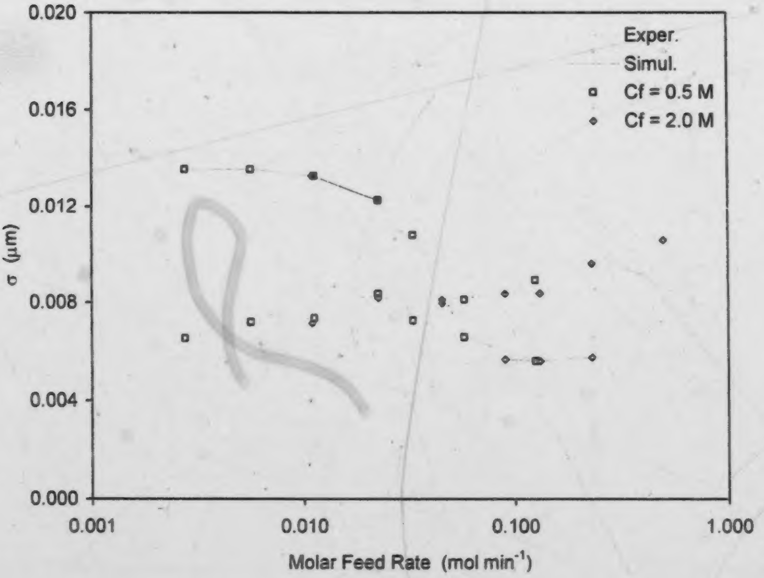

**Figure 3.25** Poor agreement of the model predictions and population variance at 6 minutes for various feed rates using the optimized parameters.

### 3.5.3 Validation Summary

The initial validation focused on the precipitation model and confirmed that the thermodynamic equilibrium, material balances and crystal population balances were functioning properly. In addition, the preliminary validation indicated that the parameters involved in the kinetic model given by Wey and Strong (1977a) are valid for unimodal seed crystal distributions, but are not valid for bimodal distributions. Optimizing the parameters, within the ranges found in the literature, to correctly predict growth of both seed crystal distributions gave the values in Table 3.8. The final validation of the precipitation model focused on the instantaneous nucleation model and the extrapolated size-dependent growth kinetics for small crystal sizes. This validation yielded the required critical supersaturation limits for each set of parameters (Table 3.8), and showed that the nucleation model is most accurate when the original set of parameters is used. Ultimately, this validation led to the conclusion that the model can accurately predict mean crystal length, and therefore total crystal count, but cannot accurately predict the variance of the crystal distributions. This is most likely due to the limitations of the kinetic model proposed by Wey and Strong (1977b) to properly describe growth of crystal sizes smaller than 0.047 μm.

**Table 3.8** Summary: Kinetic parameters and physical properties used in the precipitation model. Parameter sets are given in order of decreasing ability to predict unimodal crystal distributions.

| Parameter Set: | $\xi$ ($\mu m^{-1}$) | $D_{mol}$ ($m^2\ s^{-1}$) | $\sigma$ ($N\ m^{-1}$) | K ($m^4 mol^{-1} s^{-1}$) | $S_{critical}$ |
|---|---|---|---|---|---|
| Original [a] | 16.3 | $2 \times 10^{-9}$ | 0.14 | $3.85 \times 10^{-6}$ | 3.7 |
| Primary Optimized | 3.26 | $4 \times 10^{-9}$ | 0.11 | $1.54 \times 10^{-6}$ | 2.1 |
| Secondary Optimized | 3.26 | $4 \times 10^{-9}$ | 0.14 | $1.54 \times 10^{-6}$ | 2.4 |

[a] given by Wey and Strong (1977a)

## 3.6 Modifications Made to the Precipitation Model

Removing the crystal growth terms from the material and population balances in the discrete feed volumes (DFV) made a significant improvement in the computational time required by the precipitation model without making a noticeable change in the accuracy of its predictions. The decreased computational time was due to eliminating the need to solve the population balance in each DFV. Two points can explain the identical results obtained by each model:

i. after the nucleation event the mean crystal length is essentially given by a mass balance on the system (assuming no accumulation of the added reactants);

ii. possible changes in the variance of the crystal distribution due to growth occurring in both the high supersaturation feed plume versus the low supersaturation kettle are negligible since each crystal spends the same portion of time in each region (assuming an even distribution of the crystals in the kettle).

The modifications made to the precipitation model to implement this computational improvement were:

i. Ignoring entrainment of the crystal population at the micromixing scale by each DFV. The entire crystal population is grown within the well mixed bulk of the precipitation kettle. This eliminates the need for solving the population balance in each DFV.
ii. Immediately releasing the nuclei to the kettle following their formation in the DFVs, since nuclei no longer have the opportunity to grow inside the DFVs.

## 3.7 Conclusions

Several precipitation experiments were conducted under conditions that permitted the effects of crystal growth, nucleation and mixing on the final crystal size to be isolated. The stepwise strategy of increasing the complexity of the precipitation process was essential for effective troubleshooting and problem recognition during the model validation.

The first series of experiments was conducted to validate the size-dependent growth kinetics, and indirectly the thermodynamic and population balance models. This was achieved by operating under precipitation conditions dominated by crystal growth. Specifically, this was accomplished by seeding the reaction kettle with two distinct seed crystal distributions while operating within the micromixing regime. The results of the experiments confirmed the size-dependent growth kinetics of Wey and Strong (1977a). Two different impeller sizes were used to prove that the results were independent of mixing.

The second series of experiments was conducted to validate the instantaneous nucleation model, and indirectly the micromixing model. These results were also used to validate the extrapolated growth kinetics for crystal sizes on the order of the nuclei size. Again this was accomplished by operating in the micromixing regime as in the first series of experiments. The results of these experiments also confirmed the size-dependent growth kinetics of Wey and Strong (1977a). The smaller and larger crystals within the same distribution grew at different rates, thus the distribution became broader. These results also showed that less ideal mixing conditions led to an increase in both variance and mean length of the product distribution.

Validation of the model has shown that the model predictions are in excellent agreement with experimentally measured crystal counts and predict the growth of unimodal crystal distributions when the kinetic parameters measured by Wey and Strong (1977a) are used. The model predictions are also in excellent agreement with the experimentally measured growth of unimodal and bimodal crystal distributions when the kinetic parameters are optimized within acceptable ranges found in the literature. In addition, the precipitation model has shown that excluding crystal growth from the highly supersaturated feed plume is an acceptable simplification and greatly decreases the computational time required by the model.

# Chapter 4

## Mesomixing Analysis: Experiments and Simulations

This chapter begins with a comprehensive overview of the precipitation process and ~~its~~ dependence on the mixing process. Specifically, the primary precipitation quantity limited by mixing is identified. The experimental results of the variable feed rate mesomixing analysis are compared with the theoretical predictions made by the precipitation model. The precipitation model is then used to fully investigate how variable feed rates affect the precipitation products, to confirm methods of reducing the mixing limitations and to develop a scale-up protocol.

## 4.1 Features of the Precipitation and Mixing Processes

Prior to proceeding with discussion of the model results, the key features of the precipitation process are presented in the context of mixing effects. First, the rate of formation of nuclei can be taken as instantaneous relative to the rates of crystal growth and mixing. This implies that nucleation is the dominant process in the highly supersaturated region near the feed point and its rate is limited only by the rate of excess supersaturation generated by reactant mixing. Second, the solubility of the added reactant in the surrounding solution is negligible: therefore relieving the excess supersaturation in the highly supersaturated region requires removing essentially all of the added reactant from solution as nuclei. This in turn implies that nearly all of the added reactant enters the bulk of the kettle as nuclei as long as nucleation is not limited by the supply of the second reactant from the local surrounding solution. Third, the order of the nucleation step is so large that the nucleation process practically stops at low levels of the added reactant. This realization suggests that nucleation can only occur within the highly supersaturated region near the feed point. Fourth, growth of nuclei is governed by size-solubility according to the Gibbs-Thompson effect, which states that the critical crystal length is inversely proportional to local supersaturation. This feature implies that newly formed nuclei at the critical length require a supersaturation greater than the critical limit to survive, otherwise they become unstable and rapidly dissolve into solution to serve as material for growth of the stable crystal population. The last two features fundamentally distinguish precipitations from the classical competitive-consecutive chemical reactions. In these systems, both reactions can occur over the entire vessel, at any concentration, and are irreversible. In precipitation, nucleation is limited to the feed plume, and is reversible.

### *4.1.1 Application to Double-jet Precipitations*

These features of precipitation are now applied to the double-jet precipitation used in this study. The discussion which follows is summarized in Table 4.1 as the behavior of the key crystal size classes during the four stages of precipitation: dissolution ($<t_1$), nucleation ($t_1$ to $t_2$), transient ($t_2$ to $t_3$) and growth ($>t_3$). The supersaturation and crystal size distribution during the four stages are illustrated in Figure 4.1 and Figure 4.2, respectively. Initially, the precipitation kettle does not contain silver and the supersaturation in the kettle is less than the critical limit required for nuclei survival. All of the nuclei initially generated in the highly supersaturated mixing region become unstable and dissolve upon entering the bulk of the kettle. Newly formed nuclei continue to be unstable until dissolution has increased the bulk supersaturation above the critical limit required for nuclei survival. The period up to this point is the dissolution period as termed by this study. During the nucleation period, the dissolution of all newly formed nuclei ceases due to high supersaturation, while all of the nuclei previously deemed unstable continue to dissolve. This allows the newly formed nuclei to grow up to a stable crystal size at the expense of the dissolving unstable nuclei. Evidently, the growth of the newly formed nuclei during this period is limited by the amount of dissolved material available for growth, which is directly proportional to the number of nuclei remaining at the end of the dissolution period, as revealed by this model. Once the dissolved material is consumed and the stable crystal population has formed, the supersaturation remains just below the critical limit until the stable crystal population has completely consumed the excess nuclei formed during the nucleation period, a point that is characterized by a rapid decrease in the bulk supersaturation. This is the transient period. For the remainder of the precipitation the supersaturation throughout the kettle becomes relatively constant and the nuclei formed in the highly supersaturated region rapidly dissolve in the bulk of the kettle, serving only as material to grow the stable crystal population. This is the growth period.

**Table 4.1** Periods of the Double-jet Precipitation Process.

| | Newly Formed Nuclei Entering the Kettle ($L = L_{nuclei}$) | Unstable Crystals in the Kettle ($L < L_{critical}$) | Stable Crystals in the Kettle ($L > L_{critical}$) | Supersaturation in the Kettle |
|---|---|---|---|---|
| **Dissolution Period**<br>($t < t_1$)<br>All formed nuclei will eventually dissolve<br>(Figures 4.2a & 4.3a) | - Nucleation rate ramps up to steady state value as mixing plume grows<br>- All nuclei are unstable and rapidly dissolve<br>- $L_{nuclei} < L_{critical}$ | - All entering nuclei are unstable<br>- Therefore all crystals present are in the process of dissolving | - None at $t = 0$<br>- Do not form since all crystals are unstable<br>- Stable crystal count remains at zero | - Supersaturation is below the critical limit required for nuclei survival<br>- Increases rapidly due to dissolving nuclei |
| **Nucleation Period**<br>($t_1 < t < t_2$)<br>Newly entering nuclei have the potential to grow at the expense of nuclei captured in the process of dissolution<br>(Figures 4.2b & 4.3b) | - All entering nuclei are now stable<br>(i.e. none dissolve)<br>- All entering nuclei have the potential to be incorporated into the stable crystal population<br>- $L_{nuclei} > L_{critical}$ | - Consists of all nuclei formed during the dissolution period<br>- All remain unstable and must continue to dissolve<br>- Dissolution provides material for and drives growth of stable nuclei and crystals | - Formation begins due to existence of stable nuclei and the availability of material for growth<br>- Grow at expense of dissolving unstable crystals<br>- Stable crystal count rapidly increases | - Supersaturation is above the critical limit required for nuclei survival<br>- Will remain above the critical limit until the dissolving nuclei are completely consumed |

| | | | | |
|---|---|---|---|---|
| **Transient Period**<br>($t_2 < t < t_3$)<br>Stable crystals consume excess nuclei formed at the end of the nucleation period<br>(Figures 4.2c & 4.3c) | - All entering nuclei are unstable and dissolve slowly due to the relatively high supersaturation<br>- $L_{nuclei} < L_{critical}$ | - All crystal sizes less than that in equilibrium with the kettle supersaturation are unstable and slowly dissolve | - Stable crystals grow at the expense of the excess nuclei formed at the end of the nucleation period and of the nuclei currently being formed<br>- Stable crystal count is at final constant value | - Supersaturation is low enough for nuclei to be unstable, yet high enough for larger crystals to remain stable and grow<br>- Rapidly decreases once the excess nuclei formed at the end of the nucleation period are completely consumed |
| **Growth Period**<br>($t > t_3$)<br>Stable crystal population has completely formed and grows at the expense of the unstable nuclei entering the kettle<br>(Figures 4.2d & 4.3d) | - All entering nuclei are unstable and dissolve rapidly due to the relatively low supersaturation<br>- $L_{nuclei} < L_{critical}$ | - All crystal sizes less than that in equilibrium with the kettle supersaturation are unstable and rapidly dissolve | - Stable crystals grow at the expense of the nuclei currently being formed<br>- Stable crystal count remains at final constant value | - Supersaturation stabilizes at a level near equilibrium for the remainder of the precipitation<br>- Growth of the stable distribution continues at the expense of the unstable nuclei and consumption due to growth equals the feed rate |

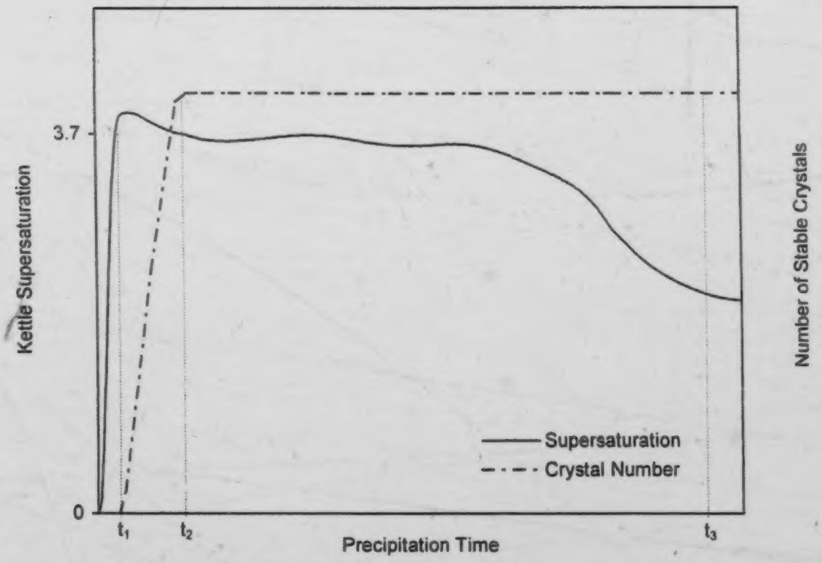

**Figure 4.1** Supersaturation and stable crystal count during the periods of the double-jet precipitation process. a) Dissolution period ($<t_1$), b) Nucleation period ($t_1$ to $t_2$), c) Transient period ($t_2$ to $t_3$), and d) Growth period ($>t_3$).

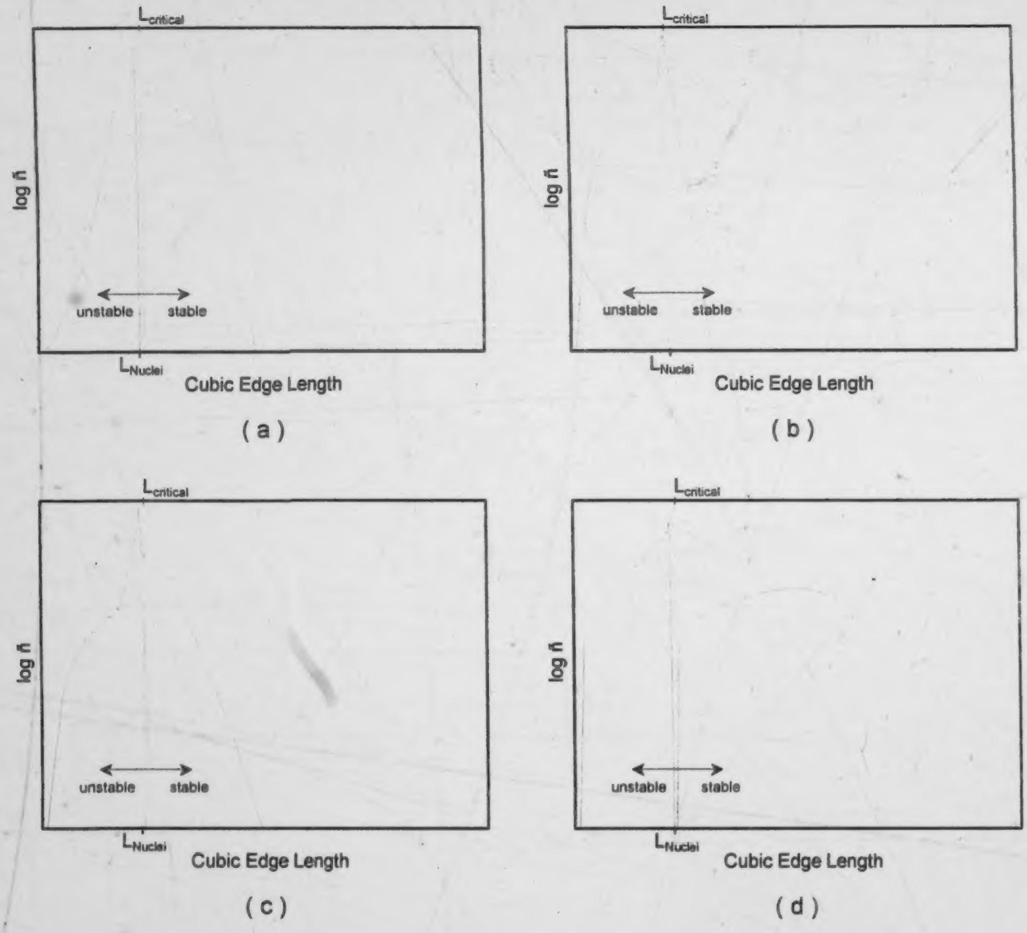
L_critical
log n̄
unstable
stable
L_Nuclei
Cubic Edge Length
(a)
L_critical
log n̄
unstable
stable
L_Nuclei
Cubic Edge Length
(b)
L_critical
log n̄
unstable
stable
L_Nuclei
Cubic Edge Length
(c)
L_critical
log n̄
unstable
stable
L_Nuclei
Cubic Edge Length
(d)

**Figure 4.2** Formation of the stable crystal population during the periods of the double-jet precipitation process. As the supersaturation in the kettle changes, the critical crystal length varies about the constant nuclei length. a) Dissolution period - all nuclei are unstable and dissolve ($L_N < L_C$), b) Nucleation period - newly formed nuclei are stable and grow, while all previously formed nuclei are unstable and continue to dissolve ($L_N > L_C$), c) Transient Period - excess nuclei previously formed become unstable and dissolve, while stable crystals continue to grow($L_N < L_C$), and d) Growth period - nuclei are unstable and dissolve rapidly, while stable crystals continue to grow ($L_N << L_C$).

This study revealed that of the four periods described in the double-jet precipitation process, only the outcome of the first stage, the dissolution period, is directly affected by mixing. The remaining periods are only indirectly affected by mixing through their dependence on the outcome of the dissolution period. Once the silver reactant addition is initiated, the mixing plume grows to its steady state size (Figure 4.3). During this period the nucleation rate, which is dictated by the mixing rate, also increases to its steady state value (Figure 4.3). It is here that mixing has a significant impact on the result of the precipitation. This study showed that different rates of mixing, and the consequently different rates of nucleation, result in different numbers of nuclei being captured in the process of dissolution at the end of the dissolution period for a given molar feed rate. Note, slow rates of mixing (Figure 4.3a) result in fewer nuclei being captured relative to fast rates of mixing (Figure 4.3b) as shown by the decreased area under the nucleation rate curve for slow mixing. Since the nuclei captured in the process of dissolution are unstable, they must continue to dissolve. This provides material for and drives the growth of nuclei formed during the nucleation period. Most importantly, the number of nuclei deemed unstable during the dissolution period is proportional to the amount of material to be dissolved. This in turn dictates the number of nuclei that grow and survive during the nucleation period. The growth of the stable crystal population during the transient and growth periods is not affected by mixing since all nuclei formed are unstable and rapidly dissolve in the low supersaturation environment of the stable crystal population.

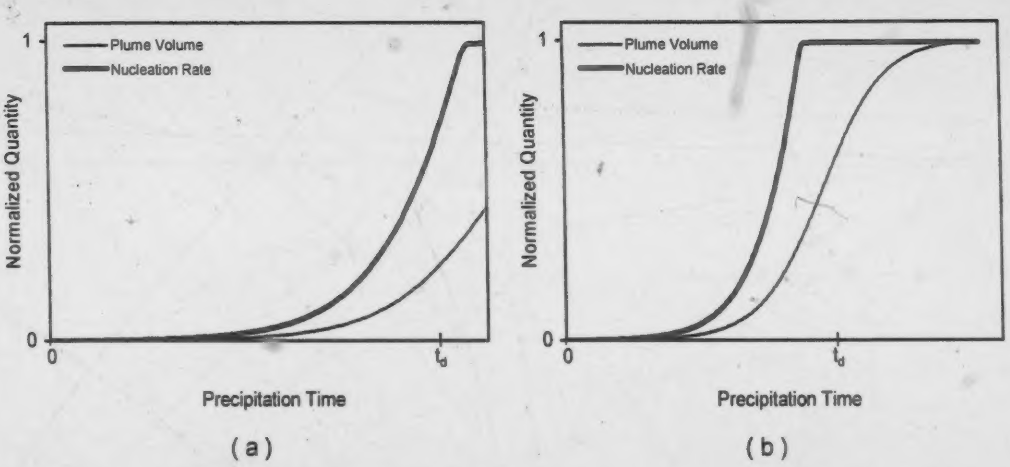

**Figure 4.3** Relationship between growth of the mixing plume volume fraction and the resulting nucleation rate normalized by the ideal nucleation rate. a) Slow mixing and b) Fast mixing. The end of the dissolution period is denoted $t_d$ and occurs later for slow mixing.

## 4.2 Ideal Double-jet Precipitations

In an ideal double-jet precipitation, there is no effect of mixing on the precipitation result. In contrast, for non-ideal conditions, mixing affects the outcome of the dissolution period by constraining the rate at which nucleation reaches its maximum steady state value, which in turn limits the number of nuclei captured in the process of dissolution prior to the beginning of the nucleation period. Under perfect mixing conditions, the number of nuclei captured in the process of dissolution is maximized. This situation requires an infinitely fast nucleation rate that is unlimited by mixing, which can be idealized by injecting the added reactants to the precipitation kettle as preformed nuclei. Implementing these ideal conditions yields the relationship between stable crystal number and molar feed rate shown in Figure 4.4. As expected, the number of nuclei captured in the process of dissolution prior to the nucleation period closely tracks the final number of stable crystals for low feed rates (Figure 4.4). This confirms that the stable number of crystals formed during a precipitation is related to the amount of material made available for nuclei growth during the dissolution period.

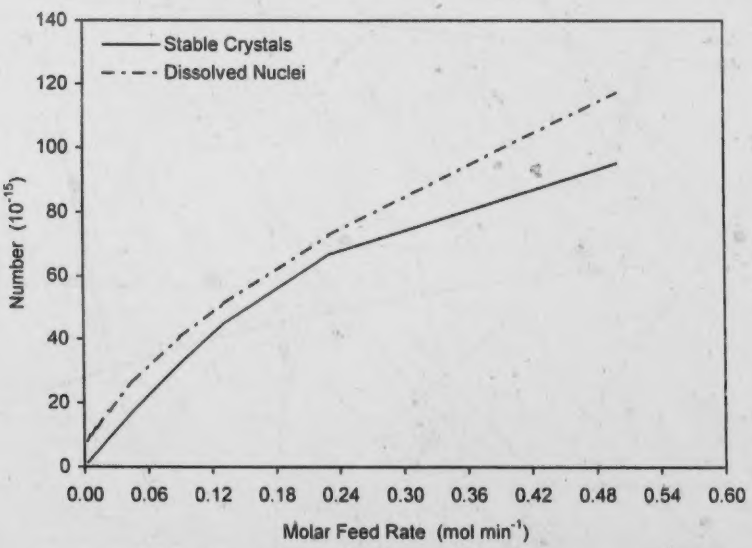

**Figure 4.4** Effect of molar addition rate on the stable number of crystals at the end of the nucleation period and on the number of dissolving nuclei at the end of the dissolution period for ideal mixing conditions.

Figure 4.4 also demonstrates that the number of stable crystals is not linearly related to the molar feed rate, as proposed by Leubner's theory for ideal mixing conditions (Section 3.3.1). Rather the slope of the stable crystal number curve in Figure 4.4 changes, demonstrating that the nucleation efficiency $X_N$ (proportionality constant) decreases as the molar feed rate increases. Leubner's theory requires that the mean crystal length be independent of molar feed rate when the precipitation time is held constant. Figure 4.5 clearly demonstrates that the model simulations do not predict this for ideal mixing conditions, and again contradicts the predictions of Leubner's theory. Based on the results of the model simulations shown in Figure 4.4, it is concluded that excluding the dissolution process is an oversimplification and weakness in Leubner's theory. The revised ideal mixing conditions are used as a baseline case to investigate the effect of mixing on the precipitation.

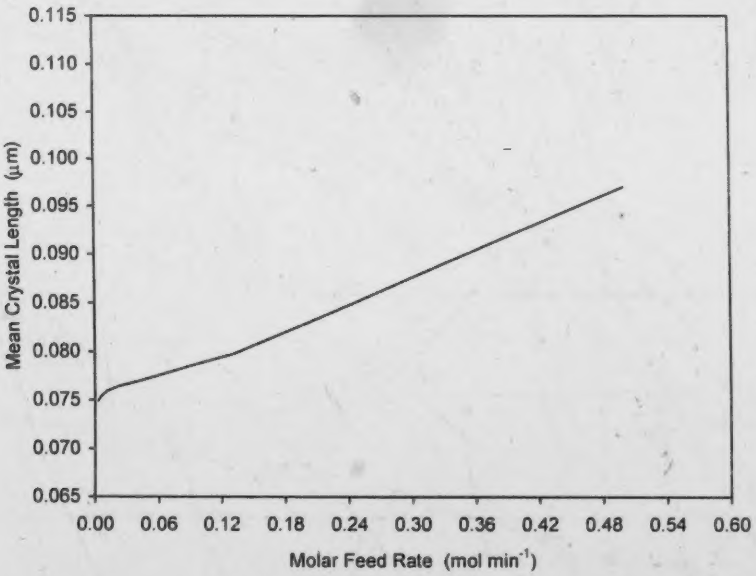

**Figure 4.5** Dependence of mean crystal length on molar feed rate for ideal double-jet precipitations at a precipitation time of 6 minutes.

## 4.3 Mesomixing Analysis

It is known that micromixing controls the practically instantaneous rate of nucleation by governing the development of supersaturation on a microscopic level. Additional inhomogeneity in the development of supersaturation can be caused by the interaction of the feed plume with its local surroundings. The main operating parameters affecting the rate of mesomixing for a given impeller type are rotational speed, feed pipe location, volumetric feed rate and feed pipe diameter. Since the range of impeller speeds for these experiments is limited by maintaining turbulent Reynolds numbers while avoiding air entrainment (Table

3.1), the feed rate was varied to attain mesomixing conditions. The surface feed for the T/4 impeller gives the most dominant mesomixing conditions and was used for all of the mesomixing experiments (Table 3.3).

### *4.3.1 Variable Feed Rate Experiments*

The first of the mesomixing variables investigated was the feed rate. This analysis gives the critical characteristic time constant ratio, $Q_m$, provided that the effects of feed pipe diameter are removed by using the smallest diameter possible (Baldyga et al. 1993). Use of a small diameter feed pipe was beneficial since the effects of back mixing are reduced for small feed pipe diameters (Baldyga et al. 1993). To allow a wide range of feed rates, a 1.6 mm diameter feed tube was selected.

#### Precipitation Conditions

The mesomixing analysis was conducted in the following order to maximize the possibility of finding the critical characteristic time ratio. First, the maximum effect of mesomixing was determined using the maximum feed rate possible (or equivalently, the shortest feed time) possible (QS4.01). The minimum feed time that still allowed sampling of the crystal size distribution was 360 seconds giving a maximum feed rate of 250 ml/min. Next, the effects of mesomixing were determined at the expected mesomixing limit of $Q_m = 0.2$ (QS4.02). Comparison of these results with those of the previous batch (QS4.01) showed significant differences in the crystal size distribution. Moreover, comparison of QS4.02 with the previous micromixed controlled regime (MM14 and MM16), resulted in negligible differences in the crystal size distribution. This indicated that the two mixing extremes, namely mesomixing and micromixing were found. Hence, the remainder of the variable feed rate mesomixing experiments were chosen to provide resolution between the batches QS4.01 (mesomixing controlled) and QS4.02 (mesomixing limit), as well as resolving the effects of mixing well below the expected mesomixing limit of $Q_m$=0.2. The variable feed rate mesomixing experiments were repeated using a feed concentration of 0.5 M; this corresponded to one quarter of the standard feed concentration used. These experiments were conducted to determine the effects of feed concentration, or equally the reactant molar addition rate.

**Table 4.2** Summary: Mesomixing Conditions - Variable feed rate experiments.

| $C_f$ 2 M | $C_f$ 0.5 M | $D_p$ (mm) | $t_f$ (min) | $Q_f$ (ml min$^{-1}$) | $u_f/U$ | $Q_m$ |
|---|---|---|---|---|---|---|
| QS4.01 | QS4.11 | 1.6 | 360 | 250.00 | 25.27 | 1.65 |
| QS4.02 | QS4.12 | 1.6 | 2000 | 45.00 | 4.55 | 0.30 |
| QS4.03 | QS4.13 | 1.6 | 780 | 115.38 | 11.66 | 0.76 |
| QS4.04 | QS4.14 | 1.6 | 4000 | 22.50 | 2.27 | 0.15 |
| QS4.05 | QS4.15 | 1.6 | 1380 | 65.22 | 6.59 | 0.43 |
| QS4.06 | QS4.16 | 1.6 | 8000 | 11.25 | 1.14 | 0.07 |
| QS4.07 | QS4.17 | 1.6 | 16000 | 5.63 | 0.57 | 0.04 |

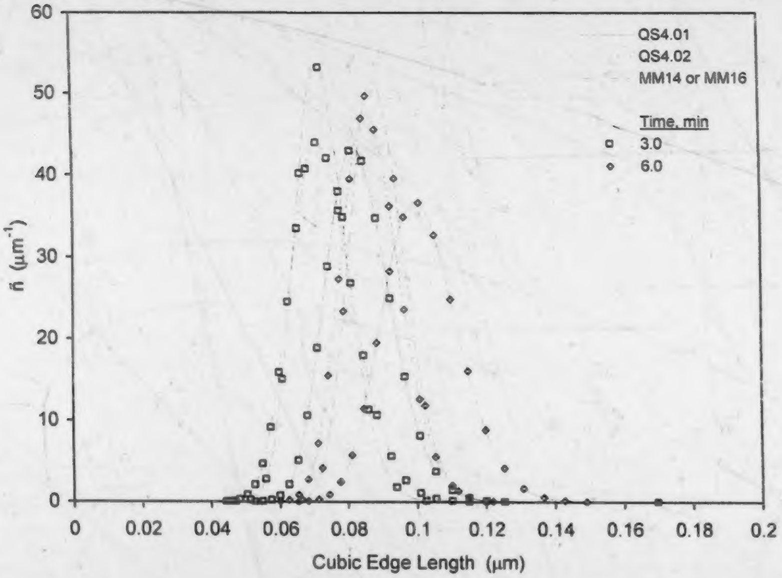

**Figure 4.6** Comparison of micromixing controlled (MM14, MM16, Qs4.02) and mesomixing controlled crystal size distributions.

## Repeatability

The precipitation conditions of QS4.01, QS4.02, QS4.03, and QS4.05 were replicated in triplicate. The mean sample values of crystal length and CoV for each condition are used in the following analysis. In each case the replicated crystal length and CoV varied less than 1.5 nm and 0.5% from their mean sample values, respectively.

## Results and Discussion

According to the theory presented in Section 3.3.1, the number of stable nuclei formed during an ideally mixed precipitation is proportional to the molar reactant addition rate. This leads directly to the conclusion that final crystal size is a function of total precipitation feed time even for ideal mixing. All previous authors (*e.g.* Baldyga et al., 1995) attributed variations in final crystal size solely to variable feed rate mesomixing; this analysis removed the expected variation due to feed rate and properly isolated the effects due to mixing by sampling each precipitation at 6 minutes. The experimental results from the variable feed rate analysis reveal that crystal length increased with both volumetric addition rate and feed concentration (Figure 4.7). As expected from the precipitation literature, the effects of volumetric addition rate and feed concentration can be combined by means of the molar reactant addition rate (Figure 4.8). This provides clear evidence that precipitation results should be plotted against molar feed rate not volumetric feed rate as usually done in the mixing literature.

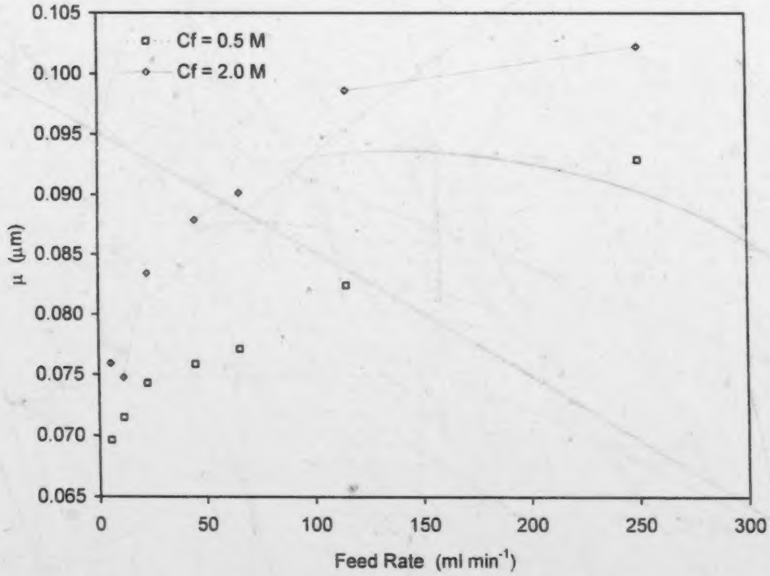

**Figure 4.7** Variation in mean crystal length for two feed concentrations over a range of volumetric feed rates at a sample time of 6 minutes.

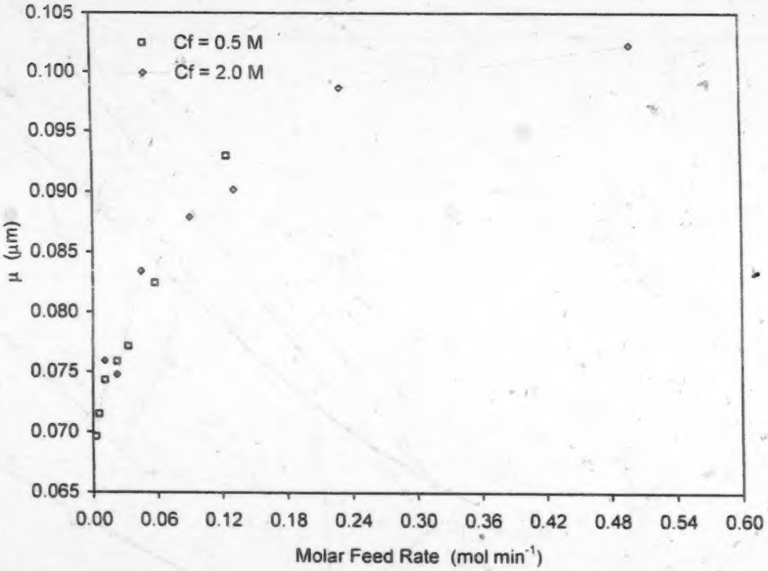

**Figure 4.8** Variation in mean crystal length for two feed concentrations over a range of molar feed rates at a sample time of 6 minutes.

The effects of molar addition rate on the mean crystal size are shown most clearly in Figure 4.9 where the molar addition rate is given on a log scale. This figure reveals that the minimum mean crystal length occurrs at low molar addition rates. Under these conditions, the largest fraction of the added material was converted to stable nuclei, or equivalently, the largest nucleation efficiency $X_N$ occurred at low molar addition rates. The nucleation efficiency is defined using Equations ( 3.6 ) and ( 3.7 ) as shown below

$$Z \propto X_N R \qquad (4.1)$$

$$Z \cdot \overline{L}^3 \propto R \cdot t \rightarrow X_N \propto \frac{t}{\overline{L}^3} \qquad (4.2)$$

Figure 4.9 illustrates the transition from high nucleation efficiency at low molar addition rates (< 0.033 mol/min), through the rapidly decreasing nucleation efficiency at moderate addition rates, to the minimum nucleation efficiency at high addition rates (> 0.23 mol/min). The decrease in nucleation efficiency from low to moderate addition rates suggests that mixing within the feed plume becomes limiting and results in a smaller fraction of the feed nucleating. At high addition rates the nucleation efficiency appears to be approaching a minimum value. This transition suggests that the feed plume mixing becomes so incomplete nucleation occurs in the bulk. In this case, the additional nucleation would be limited by the excess solubility of the diluted silver reactant in the relatively large volume of the reactor outside of the feed plume.

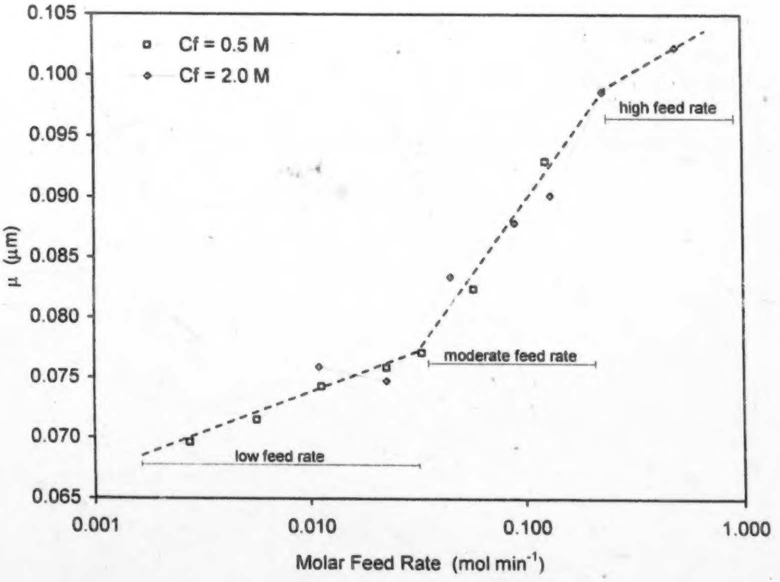

**Figure 4.9** Variation in mean crystal length for two feed concentrations over a range of molar feed rates at a sample time of 6 minutes (linear-log scale).

Figure 4.10 demonstrates that varying the molar addition rate had little effect on the variance of the crystal size distribution. The coefficient of variance remains relatively constant at a value of 10%. This finding suggests that the variance of the distribution is a function of the growth kinetics, rather than of nucleation efficiency.

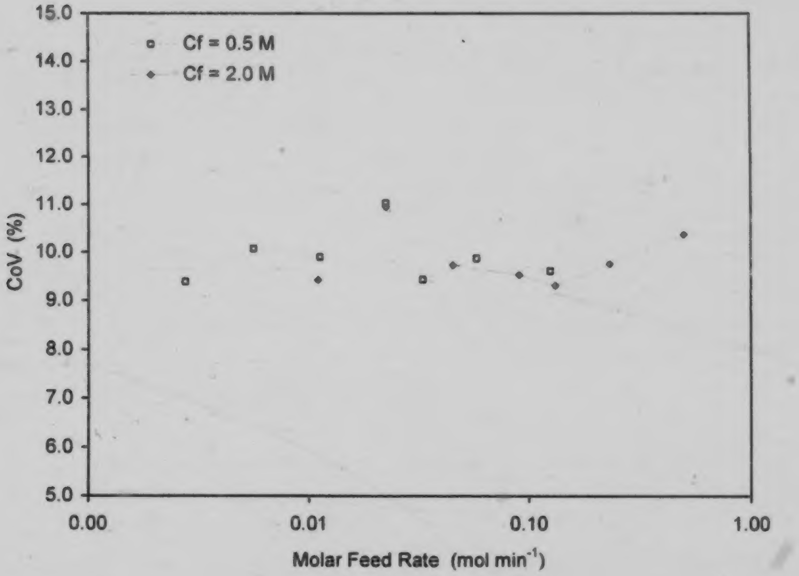

**Figure 4.10** Variation in coefficient of variation for two feed concentrations over a range of molar feed rates at a sample time of 6 minutes.

The current experimental results were compared to the published data of Leubner et al. (1980) and Leubner (1993) in Figure 4.11. These data sets were collected under similar conditions as this study with the main exception being that 4wt% gelatin was used in these precipitations. To facilitate the direct comparison of the data collected at various sampling times, the data is reported using total crystal count, which can be taken as constant once the stable distribution has formed.

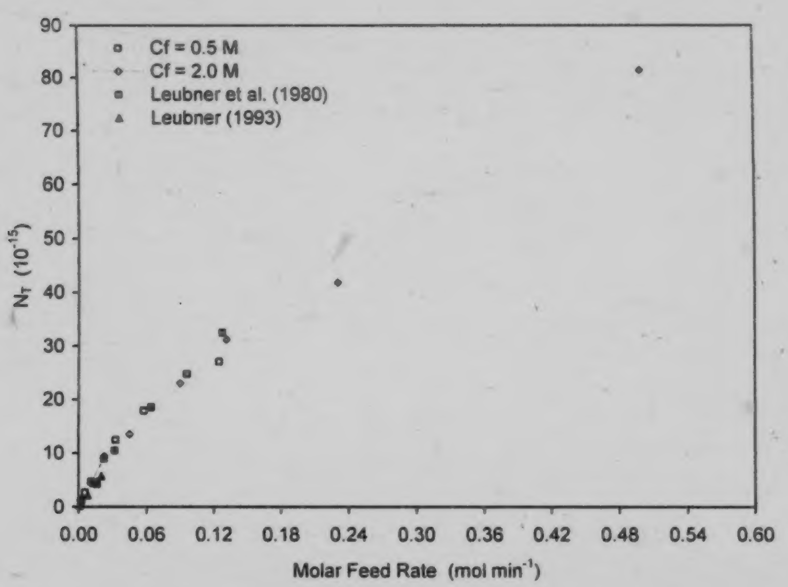

**Figure 4.11** Variation in total crystal count for two feed concentrations over a range of molar feed rates.

### *4.3.2 Variable Feed Pipe Diameter Experiments*

The last variable in the mesomixing experiments is the feed pipe diameter. The analysis of this variable required a balance of high feed rate to exaggerate the effects of mesomixing, with a feed rate low enough to allow some of the larger feed pipe diameters to become finite sources (Baldyga et al. 1993). Using the definitions of Baldyga et al. (1993) the feed pipe represented a point source if, $D_p/2 << L_D << T$, whereas it was a local finite source if $D_p << T$ and $D_p/2 \approx L_D$ or $D_p/2 > L_D$. $D_p$ is the feed pipe diameter, $L_D$ is the characteristic length scale for mesomixing

$$L_D = \sqrt{\frac{Q_f}{U}} \qquad (4.3)$$

and T is the tank diameter. In order to set the experimental conditions, an estimate of the critical characteristic time ratio was required since product distributions are independent of the feed pipe when micromixing controls (Baldyga et al. 1993). In the variable feed rate analysis the critical characteristic time ratio was 0.1 when the feed concentration was 2.0 M. To ensure that the experiments were in the mesomixing regime the characteristic time ratio was chosen to be 0.75 ($Q_f$ = 115.38 ml/min): this gave a range of $0.16 < D_p / L_D < 1.6$.

The maximum effects of mesomixing were determined by using the minimum feed pipe diameter possible (DS4.01). Due to the relatively high feed rate of 115.38 ml/min, the smallest feed pipe diameter was chosen to be 0.8 mm. Next, the minimum effects of mesomixing were determined by using the maximum feed pipe diameter possible (DS4.02). To maintain fully developed flow through the exit nozzle, the maximum feed pipe diameter was 4.8 mm. Comparison of these results with those of the previous batch (DS4.01) showed negligible differences in the crystal size distribution as shown in Figure 4.12. This suggests that that the feed rate was too large and did not allow the larger feed pipe diameters to become finite sources. This was expected as the ratio of feed velocity to surrounding fluid velocity (Table 4.3) exceeded the critical velocity ratio of 0.05 suggested by Baldyga et al. (1993). Velocity ratios above this critical value do not influence the final product distribution while in the mesomixing regime.

**Table 4.3** Summary: Mesomixing Conditions - Variable feed pipe diameter experiments I.

| Label | $D_p$ (mm) | $t_f$ (min) | $Q_f$ (ml min$^{-1}$) | $u_f/U$ | $Q_m$ | $D_p/L_D$ |
|---|---|---|---|---|---|---|
| DS4.01 | 0.8 | 780 | 115.38 | 11.66 | 0.76 | 0.33 |
| DS4.02 | 4.8 | 780 | 115.38 | 1.30 | 0.76 | 1.00 |

In a further attempt to establish the effects of feed pipe diameter, the feed rate was reduced to 65.22 ml/min ($Q_m$ = 0.43) and the above procedure was repeated. The constraint of maintaining fully developed flow through the 4.8 mm nozzle limited the feed rate to a minimum of 65.22 ml/min.

**Table 4.4** Summary: Mesomixing Conditions - Variable feed pipe diameter experiments II.

| Label | $D_p$ (mm) | $t_f$ (min) | $Q_f$ (ml min$^{-1}$) | $u_f/U$ | $Q_m$ | $D_p/L_D$ |
|---|---|---|---|---|---|---|
| DS4.03 | 0.8 | 1380 | 65.22 | 26.4 | 0.43 | 0.22 |
| DS4.04 | 4.8 | 1380 | 65.22 | 0.73 | 0.43 | 1.34 |

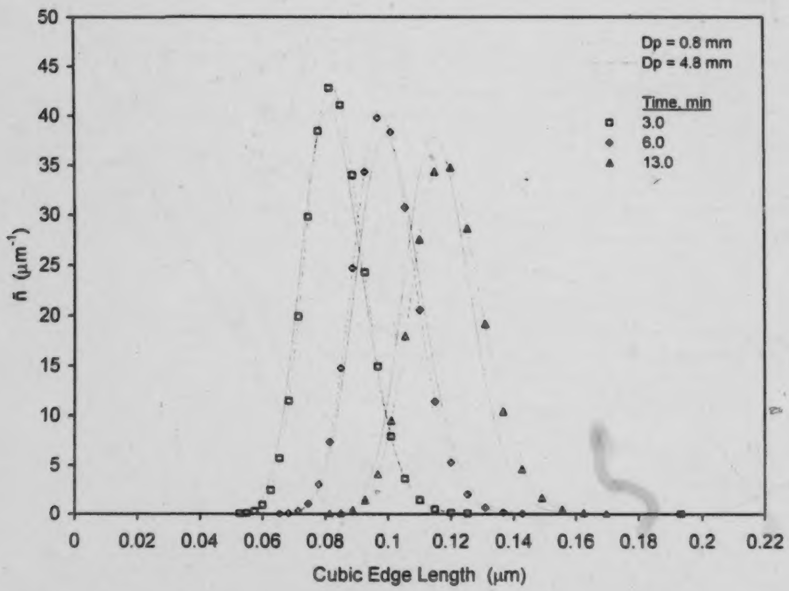

**Figure 4.12** Comparison of CSD time evolutions for feed pipe diameters of 0.8 and 4.8 mm, and a feed rate of 115.38 ml/min.

The experimental results showed negligible differences (Figure 4.13). Again, this can be attributed to the feed rate of 65.22 ml/min being too large, and therefore not allowing the 4.8 mm diameter feed pipe to become a finite source. And again this was expected as the ratio of feed velocity to surrounding fluid velocity (Table 4.4) still exceeded the critical velocity ratio suggested by Baldyga et al. (1993).

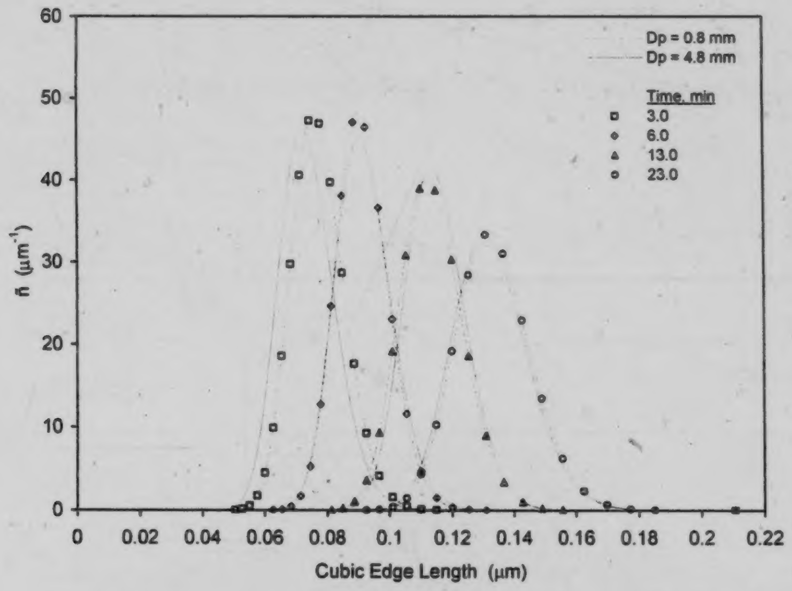

**Figure 4.13** Comparison of CSD time evolutions for feed pipe diameters of 0.8 and 4.8 mm, and a feed rate of 65.22 ml/min.

The above results indicate that extremely small velocity ratios, or unusually large feed pipe diameters, are required to affect the product CSD. Under the constraint of maintaining fully developed flow through the exit nozzle, these conditions were not attainable for the current analysis in the mesomixing regime.

## 4.4 Model Prediction

The precipitation model was described in Chapter 2 and validated in Chapter 3. In all experiments simulated, the inertial-convective disintegration of large concentration eddies controlled the turbulent mixing process as determined by comparing the characteristic mixing time constants. This is confirmed by the poor agreement of the turbulent dispersion model prediction with the experimental results (Figure 4.14 and Figure 4.15). The mixing models and Eulerian-Lagrangian framework employed in the model are outlined in Section 1.4. No fitted parameters were used in these simulations.

Comparisons between the model predictions and the experimental results are shown in Figure 4.14 (crystal number) and Figure 4.15 (crystal size). The model accurately predicts the deviations from ideal mixing conditions, with the single exception of the highest molar feed rate. In this case mixing significantly limits nucleation within the feed plume, and results in additional nucleation in the kettle. The model developed here lacks the ability to simulate this situation (Section 2.3.2) and therefore this molar feed rate has been excluded from this and following plots. The model predictions begin to deviate from the ideal precipitation results for moderate to high molar feed rates, and depend on the molar feed rate as observed for the experimental results. These findings will be discussed in further detail in the following sections.

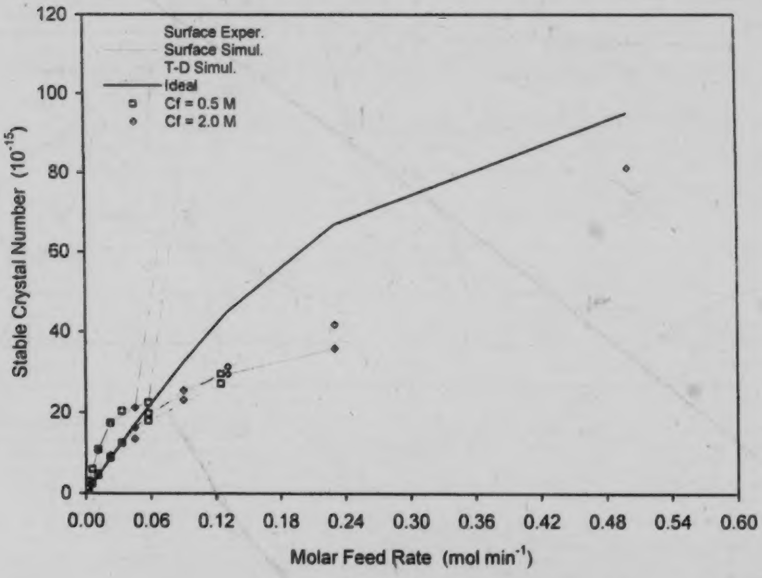

**Figure 4.14** Comparison of the theoretical model predictions and the experimental results of the variable feed rate mesomixing analysis.

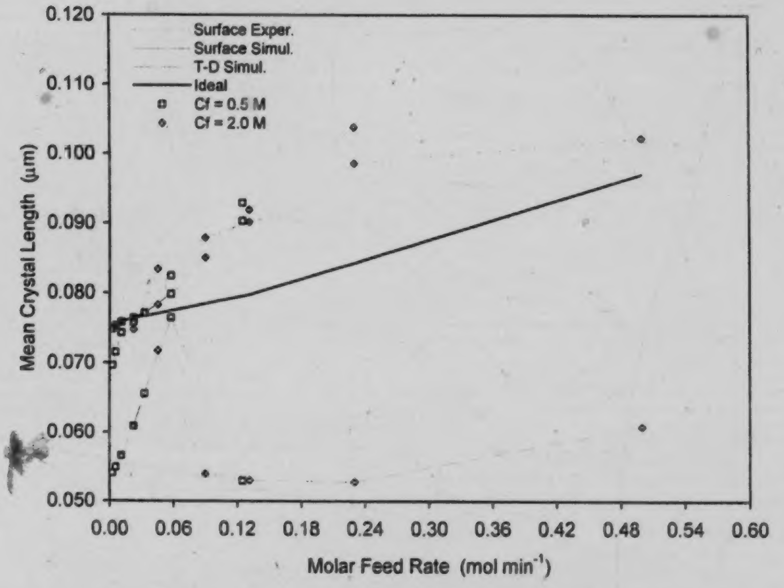

**Figure 4.15** Comparison of the theoretical model predictions and the experimental results of the variable feed rate mesomixing analysis at precipitation time of 6 minutes.

### 4.4.1 Deviation from Ideal Double-jet Precipitations

Understanding the deviation of the model prediction and experimental results from the ideal precipitation result is a key observation of the modeling work. The effect of mixing is most easily explained by analyzing the number of nuclei captured in the process of dissolution for each case (Figure 4.16). This figure displays the same departure from the ideal case as the number of stable crystals (Figure 4.14), and confirms that the amount of dissolving material limits the number of stable crystals formed during a precipitation. The underlying cause of the deviation from the ideal case is inadequate mixing during the dissolution period. Under these conditions, mixing limitations during the first instants of the precipitation retard the increase in nucleation rate. This mixing limitation reduces the number of nuclei generated, and therefore the number of nuclei entering the process of dissolution prior to the nucleation period. Figure 4.16 also shows that ideal precipitation conditions exist at low molar feed rates.

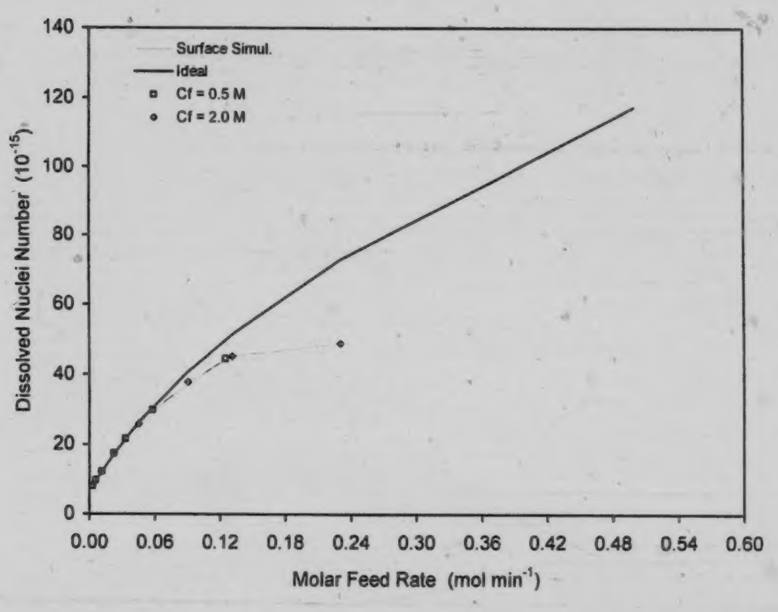

**Figure 4.16** Number of nuclei captured in the process of dissolution, as taken from the simulation results.

### 4.4.2 *Correlation with Molar Feed Rate*

The results depend on molar feed rate and varying the volumetric feed rate for the same molar feed rate has a negligible impact on the precipitation results. This is most clearly shown by comparing the initial increase in the nucleation rate for two different volumetric feed rates having the same molar feed rate (Figure 4.17). This figure demonstrates that the nucleation processes are identical except for a time lag of approximately 0.03 seconds for the concentrated feed, thus explaining the identical precipitation results. The time lag can be explained as the time required for the concentrated feed to be diluted to the same level as diluted feed. It should be noted that the mixing taking place during this short, initial period is insignificant when compared to the overall mixing process. A more detailed description of the mixing process follows.

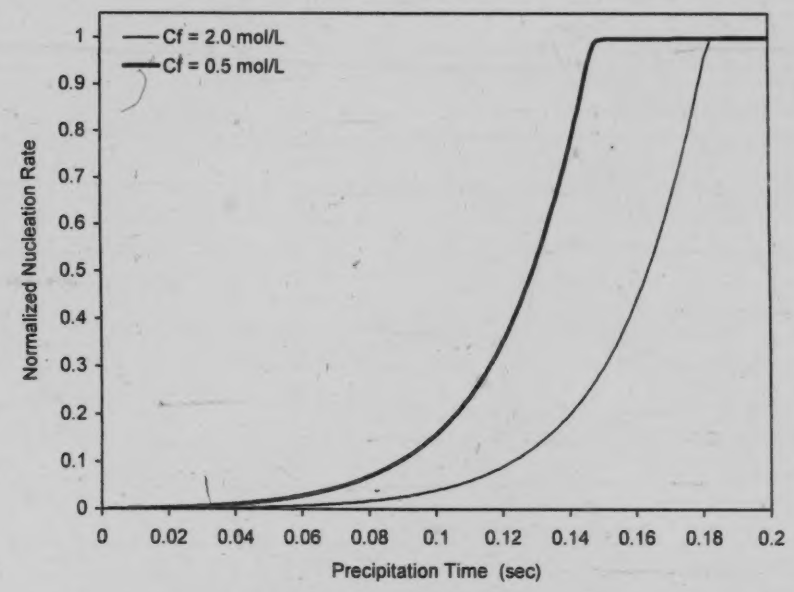

**Figure 4.17** Normalized nucleation rate for two different volumetric feed rates, both having a molar feed rate of 0.0225 mol/min.

## Lagrangian Mixing Description

The following description will be used to briefly introduce the Lagrangian mixing concept. Initially, a discrete feed volume enters the reaction kettle as pure silver reactant (Figure 4.18a). As the discrete feed volume becomes mixed with the surrounding halide reactant solution the supersaturation within the discrete feed volume rapidly increases and nucleation begins (Figure 4.18b). Since nucleation is considered to be instantaneous relative to mixing, any excess supersaturation is instantly removed as nuclei, which are placed in the bulk of the kettle (Figure 4.18c). Consequently, the maximum supersaturation attained within the discrete feed volume is always equal to the critical supersaturation limit. If mixing continues past this point, at some time nucleation and dilution due to mixing reduce the silver reactant concentration enough that the halide becomes in excess within the discrete feed volume. Soon after this, the silver reactant concentration is driven below the critical limit and nucleation ends. After this point, if mixing is still not complete, the concentrations within the discrete feed volume approach the surrounding level until its contents are rapidly dispersed by the highly turbulent impeller discharge stream (Figure 4.18d).

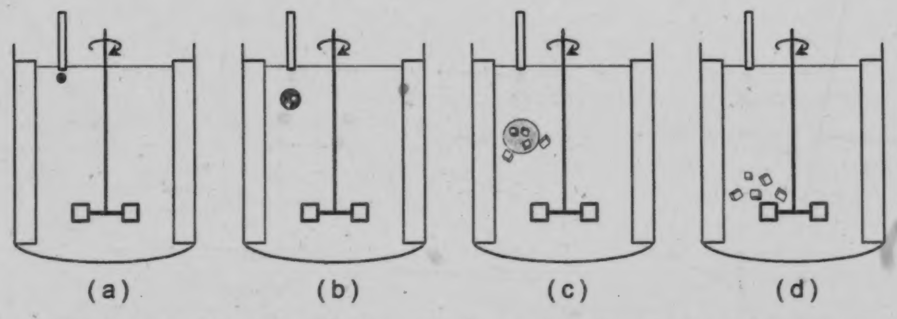

**Figure 4.18** Lagrangian description of the precipitation and mixing processes within a discrete feed volume. (a) Entering as pure reactant, (b) Mixing with the surrounding reactant and nucleating to relieve the high supersaturation, (c) Nuclei released into the kettle where crystal growth begins, and (d) Mixing and nucleation are completed.

Figure 4.19 displays detailed quantitative Lagrangian evolutions of the precipitation process and its dependence on the mixing process for two feed concentrations at a molar feed rate of 0.0225 mol/min. This figure confirms that the mixing and precipitation processes are identical for different feed concentrations at the same molar feed rate except for a time lag of 0.03 seconds. Moreover, Figure 4.19a confirms that insignificant amounts of nucleation take place during the initial dilution of the concentrated feed to the inlet level of the diluted feed. Therefore, the silver content remains practically constant during the dilution, and the case of the concentrated feed reduces exactly to the case of the diluted feed having the same molar feed rate.

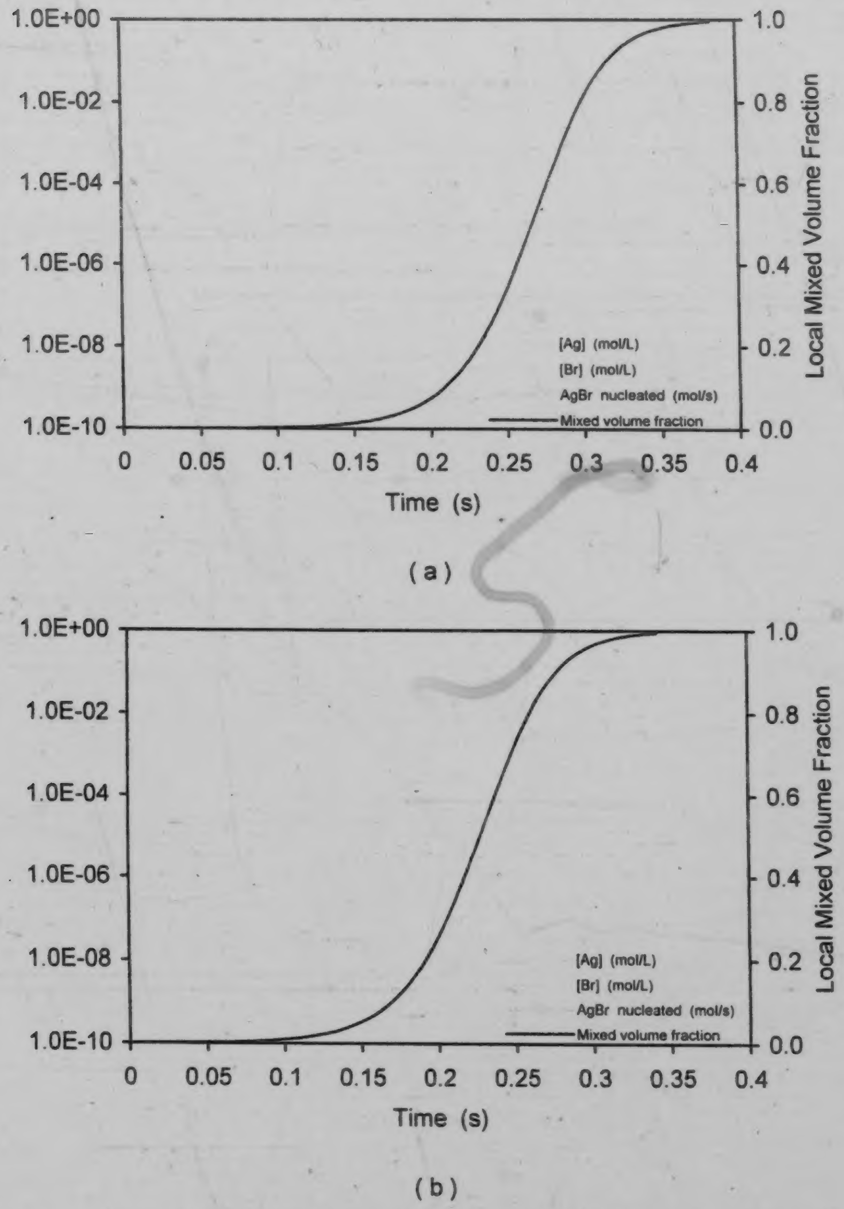

**Figure 4.19** Lagrangian evolution of the mixed reaction volume for a molar feed rate of 0.0028 mol/min. a) Concentrated feed, and b) Diluted feed. Units for each quantity are given in the legend.

## 4.5 Mixing Effects on Double-jet Precipitations

The preceding figures clearly show that local mixing dictates the rate at which nucleation reaches its maximum, steady state value during the precipitation start-up. From the mixing perspective there are two factors that can constrain the mixing process: the local mixing rate and the amount of the second reactant available in the local surroundings.

### *4.5.1 Mixing Rate*

The most obvious factor controlling the rate of increase in nucleation is the local mixing rate. Micromixing is the dominant mixing process since chemical reaction requires the reactants to be mixed on a molecular scale, however micromixing may be limited by mesomixing, which determines the local environment in which micromixing proceeds. In either case, increasing the local turbulence increases the overall mixing rate and thus reduces the effects of mixing on the precipitation product. The local turbulence can be increased in several different ways, but for a given impeller and kettle geometry there are only two methods. First, the local turbulence can be increased by moving the feed point to a region of higher turbulence such as near the impeller tip (Figure 4.20). Second, the local turbulence can be increased by increasing the power input to the kettle by an increase in the impeller rotational speed (Figure 4.21).

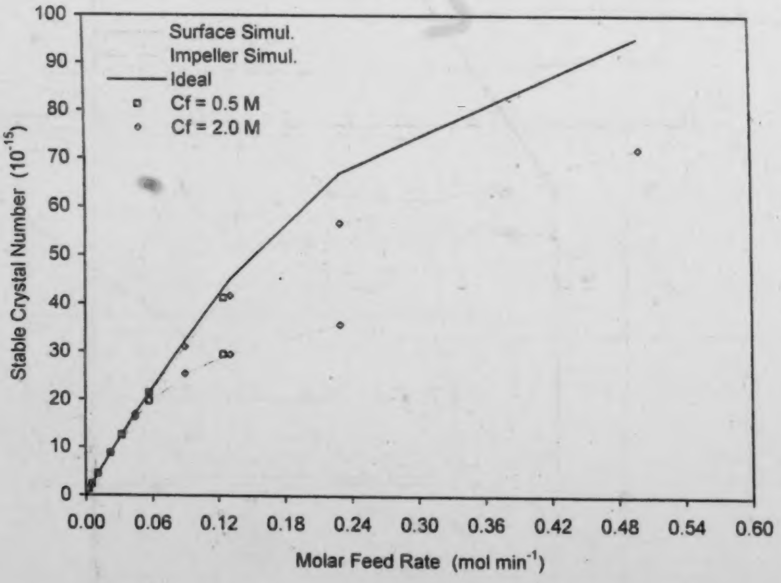

**Figure 4.20** Increasing the local turbulence by relocating the feed point to the impeller tip results in the precipitation approaching the ideal limit.

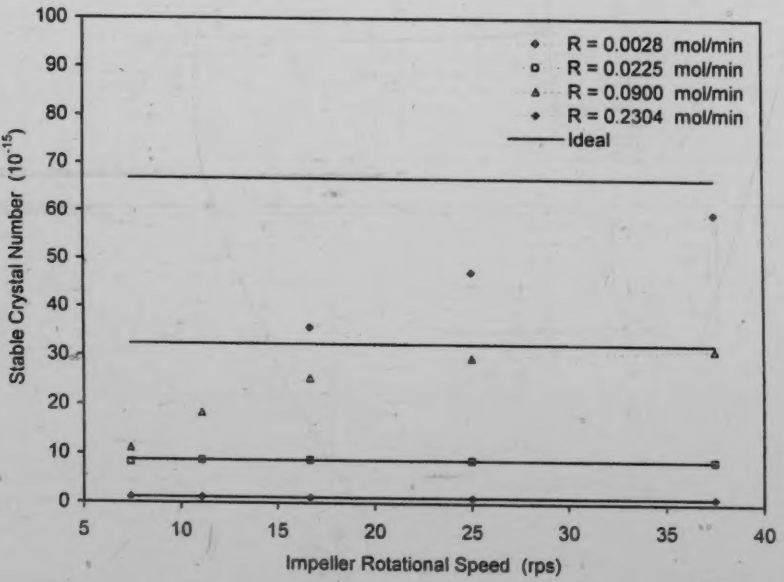

**Figure 4.21** Increasing the local turbulence by raising the impeller rotational speed results in each precipitation product approaching the respective ideal limit.

### 4.5.2 *Convective-Stoichiometric Limited Mixing*

Even in the presence of infinitely fast mixing, nucleation may be limited by the supply of the reactant from the local surrounding solution. In this study, this situation is termed convective-stoichiometric limited mixing (CSL). It is evident that complete nucleation of the feed requires a stoichiometric amount of the second reactant to be transported to the reaction zone, but in addition to this, nucleation requires a high supersaturation to occur and therefore requires a large excess amount of the second reactant to be locally available for mixing. For large molar feed rates, nucleation becomes limited by the amount of the second reactant transported to the local surroundings by the circulation pattern in the vessel and can not proceed to completion as shown in Figure 4.22 for the return stream to the impeller region. In this situation, the mixing is limited by the bounds of the recirculating flow. Once the feed plume has completely engulfed the recirculating flow, the supply of the second reactant is exhausted and the convective-stoichiometric limit is reached. This is shown in Figure 4.22c, and will occur for high molar feed rates. Under these convective-stoichiometric limited mixing conditions, the high level of unreacted feed leaving the feed plume causes nucleation to take place in the bulk of the kettle. This mixing limitation can be eliminated by increasing the availability of the second reactant in the convective flow either by relocating the feed point to region of intense circulation, or by increasing the entire circulation rate in the kettle by increasing the impeller rotational speed. Both situations have been previously shown in Figure 4.20 and Figure 4.21, respectively.

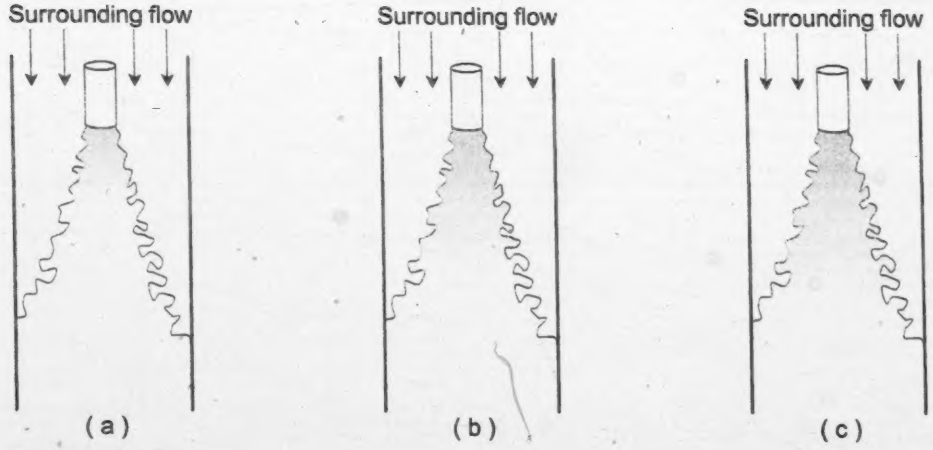

**Figure 4.22** Effect of reactant stoichiometric imbalance on nucleation near the feed point. Silver reactant concentration is proportional to the shading. a) At low molar feed rates there is rapid and complete nucleation within the feed plume, b) At moderate feed rates there is complete nucleation in the feed plume, and c) At high molar feed rates nucleation is incomplete due to limited amounts of the reactant in the surrounding solution.

## 4.6 Precipitation Scale-up Protocol

The precipitation product depends primarily on the local rate of mixing when nucleation is not limited by the local supply of the second reactant. In this case, an identical precipitation product will be obtained on different scales, under geometrically similar conditions (*i.e.* D, $D_H$, C, W, $H_o$, *etc.*, all change by the same scale-up factor as T), if both the local rate of turbulent dissipation (*i.e.* mixing) and precipitation time are held constant. This scale-up/down rule states that the power input to the system per unit volume must be held constant assuming there are no convective-stoichiometric limitations. However, if the same feed time is used for all scales the precipitation product is likely to become dominated by reactant circulation on scale-up, rather than by micromixing, and alternative choices to the current kettle geometry should be considered. For example, using an impeller with a higher pumping capacity for an equivalent power consumption or injecting the reactants using a completely different feed strategy such as an impinging jet premixer (Johnson 2003) or a side-arm loop reactor (Jézéquel 2001). The latter options allow the auxiliary units to be highly optimized, as well as allowing a linear scale-up by simply increasing the number of units by the volume scale-up factor.

The above protocol was applied to scaled-up simulations of the precipitation conditions used in this study. The kettle geometry scale-up factor was $S_F = 10$. In order to maintain a constant precipitation time, the volumetric feed rate was scaled by the same factor $S_F^3$ as kettle volume, while the feed concentrations remained at the original values. According to the scale-up rule of constant power per unit volume $\left(N_1^3D_1^2 = N_2^3D_2^2\right)$, the impeller rotational speed was scaled by a factor of $S_F^{-2/3}$. The results of the simulated scaling are shown in Figure 4.23. This figure shows that this scaling rule is appropriate when nucleation is not convective-stoichiometric limited. In fact, the convective-stoichiometric limit is of considerable importance when attempting to scale-up a precipitation, as shown in Table 4.5. The circulation rate per feed rate scales as $S_F^{-2/3}$, so the convective-stoichiometric limit becomes more constraining on scale-up. In an attempt to eliminate the increasing effect of the stoichiometric limit on scale-up, the circulation rate per unit of kettle volume was held constant by maintaining the small-scale impeller rotational speed (Figure 4.24). However, the accompanying increase in the power input per unit volume drastically increased the overall mixing rate, and shifted all of the precipitation products to the ideal limit except for the highest molar feed rate, which was dominated by the convective-stoichiometric limit. This molar addition rate exceeded the local molar flow rate as determined by the bulk halide concentration and flow field.

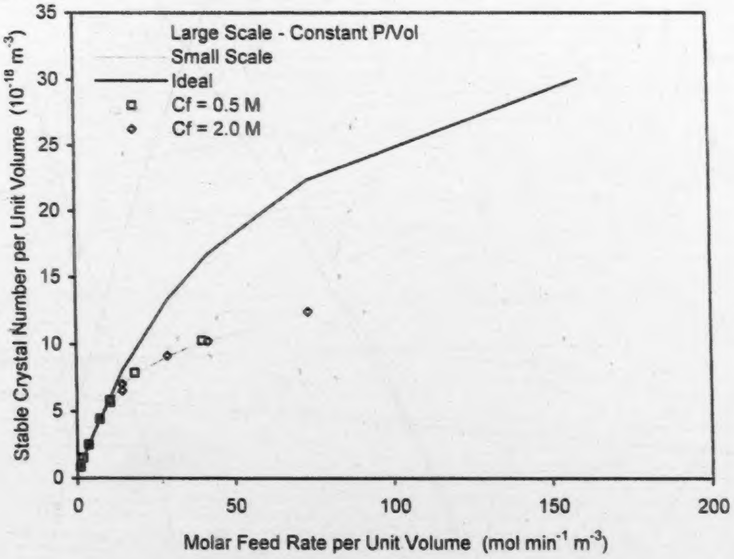

**Figure 4.23** Precipitation scale-up based on constant power input per unit volume. Predicted results for the small and large scale are identical. Large scale based on a scale-up factor of 10.

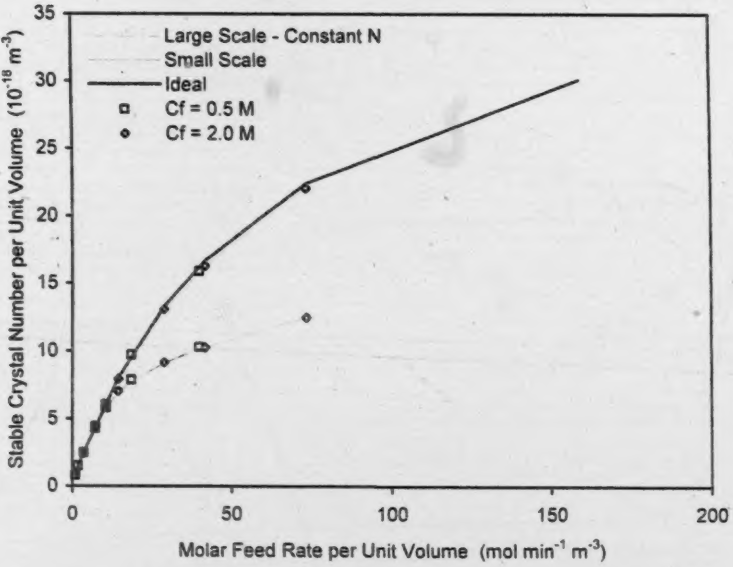

**Figure 4.24** Predicted precipitation scale-up based on constant impeller rotational speed. Large scale based on a scale-up factor of 10.

**Table 4.5** Index of mixing limitations on the precipitation products for various molar feed rates.

| Molar Feed Rate per Unit Volume (mol min$^{-1}$ m$^{-3}$) | Small Scale Surface Feed | Large Scale Surface Feed - Constant P/Vol | Large Scale Surface Feed - Constant N |
|---|---|---|---|
| $C_f$ = 0.5 M | | | |
| 0.9 | Ideal | Ideal | Ideal |
| 1.8 | Ideal | Ideal | Ideal |
| 3.6 | Ideal | Ideal | Ideal |
| 7.2 | ML | ML | Ideal |
| 10.4 | ML | ML | Ideal |
| 18.3 | ML | CSL | Ideal |
| 39.8 | ML | CSL | Ideal |
| $C_f$ = 2.0 M | | | |
| 3.5 | Ideal | Ideal | Ideal |
| 7.2 | Ideal | Ideal | Ideal |
| 14.3 | ML | ML | Ideal |
| 28.7 | ML | CSL | Ideal |
| 41.6 | ML | CSL | Ideal |
| 73.4 | ML | CSL | Ideal |
| 159.2 | CSL | CSL | CSL |

*Ideal - Ideal Precipitation Result

*CSL - Convective-Stoichiometric Limited Mixing

*ML - Mixing Rate Limited

## 4.7 Conclusions

Experiments were conducted to investigate the effects of variable feed rate and variable feed pipe diameter mesomixing on the precipitation process. The results of the variable feed rate experiments showed that mean crystal length increases with molar reactant addition rate, while the CoV of the distribution remains constant. The data also indicated that the nucleation efficiency was highest at low molar feed rates (< 0.033 mol/min), decreased through moderate feed rates, and approached a constant value at high feed rates (> 0.23 mol/min). These transitions suggest that nucleation was effectively unlimited by mixing for low feed rates, was partially limited for moderate feed rates and was significantly limited for high feed rates. The variable feed pipe diameter experiments showed that extremely small velocity ratios, or unusually large feed pipe diameters, would be required to affect the product distribution. Under the constraint of maintaining fully developed flow through the exit nozzle, these conditions were not attainable in this analysis. Therefore, it can be concluded that changes in feed pipe diameter had no effect on mixing in this study.

The model validated here permits the precipitation product to be predicted from the nucleation and crystal growth kinetics, and the flow field. In situations where nucleation was not limited by the local supply of the second reactant, comparisons between experimental results and the model predictions showed excellent agreement for the two feed concentrations and seven volumetric feed rates used. No fitted parameters were used in these simulations.

The modeling work revealed that the primary precipitation quantity affected by mixing is the number of nuclei captured in the process of dissolution prior to the nucleation period. High rates of mixing, and hence high rates of increase in nucleation, cause large numbers of nuclei to be captured in the process of dissolution, while low rates of mixing have the opposite effect. Since this dissolution provides material for and drives the growth of subsequent nuclei formed during the nucleation period, the amount of dissolving material limits the number of nuclei surviving during the nucleation period. This ultimately dictates the number of stable crystals produced during a precipitation, and equivalently the final crystal size. In addition, the model revealed that nucleation could be limited by the supply of the second reactant in the local recirculating flow; this situation was termed convective-stoichiometric limited mixing. This circumstance became evident for high molar feed rates and resulted in nucleation not completing within the feed plume. Since the model developed here lacks the ability to simulate this situation these cases were excluded from further analysis.

A precipitation scaling protocol based on constant power input per unit volume was used successfully, within the constraints of CSL mixing, to scale-up simulations of the precipitation conditions used in this study. However, convective-stoichiometric limitations become increasingly important on scale-up as this scaling rule decreases the circulation rate per unit of kettle volume. Attempting to avoid this limitation by increasing the circulation rate resulted in increased overall mixing rates and thus different precipitation products. This clearly illustrates the difficult balance that must be reached for successful scale-up: a balance that can be more closely defined and understood using predictive models.

# References

Antoniades M.G., and J.S. Wey, 1992, Precipitation of Fine AgBr Crystals in a Continuous Reactor: Effect *of Gelatin on Agglomeration*, J. Imaging Sci. Technol., **36**, 517-524.

Antoniades M.G., and J.S. Wey, 1998, *Aggregation Phenomena in AgX Precipitation in the Presence of Gelatin*, J. Imaging Sci. Technol., **42**, 393-398.

Baldyga J. and J.R. Bourne, 1999, *Turbulent Mixing and Chemical Reactions*, John Wiley and Sons, Chichester, U.K.

Baldyga J. and S. Rohani, 1987, *Micromixing Described in Terms of Inertial-Convective Disintegration of Large Eddies and Viscous-Convective Interactions Between Small Eddies*, Chem. Eng. Sci., **42**, 2611-2619.

Baldyga J., and J.R. Bourne, 1989, Simplification of Micromixing Calculations. I. Derivation and Application of New Model, Chem. Engng. Sci., **42**, 83-92.

Baldyga J., and J.R. Bourne, 1992, *Interactions Between Various Scales In Stirred Tank Reactors*, Chem. Engng. Sci., **47**, 1839-1848.

Baldyga J., and R. Pohorecki, 1995, *Turbulent Mixing In Chemical Reactors - A Review*, Chem. Engng. J., **58**, 183-195.

Baldyga J., J.R. Bourne and S.J. Hearn, 1997, *Interactions Between Chemical Reactions and Mixing On Various Scales*, Chem. Engng. Sci., **52**, 457-466.

Baldyga J., J.R. Bourne, and Yang Yang, 1993, *Influence Of Feed Pipe Diameter On Mesomixing In Stirred Tank Reactors*, Chem. Engng. Sci., **48**, 3383-3390.

Baldyga J., W. Podgorska and R. Pohorecki, 1995, *Mixing Precipitation Model With Application To Double Feed Semibatch Precipitation*, Chem. Engng. Sci., 50, 1281-1300.

Batchelor, 1959, *Small Scale Variation of Convected Quantities Like Temperature in a Turbulent Fluid: Part I: Discussion and the Case of Small Conductivity*, J. Fluid Mech., **5**, 113-133.

Berry C.R., 1976, *New Model For Double-Jet Precipitations*, Photogr. Sci. Eng., **20**, 1-4.

Berry C.R., and D.C. Skilman, 1968, *Fundamental Mechanisms in Silver Halide Precipitation*, J. Photographic Sci., **16**, 137-147.

Berthoud A., 1912, *Theorie de la formation des faces d'un crystal*, Journal de Chimique Physique, **10**, 624-635.

Bourne J.R. and S. Yu, 1994, *Investigation of Micromixing In Stirred Tank Reactors Using Parallel Reactions*, Ind. Engng. Chem. Res., **33**, 41-55.

Corrsin S., 1964, *The Isotropic Turbulent Mixer: Part II. Arbitrary Schmidt Number*, AIChE J., **10**, 870-877.

David R., J. Villermaux, P. Marchal and J.P. Klein, 1991, *Crystallization and Precipitation Engineering IV: Kinetic Model of Adipic Acid Crystallization*, Chem. Eng. Sci., **46**, 1129-1139.

Gibbs J.W., 1948, *Collected Works*, Thermodynamics, **Vol 1**, Yale University Press, New Haven.

Gilman et al., Benzothiazolium, 2-(3-(3-ethyl-2(3H)-benzothiazolylidene) || -2-methyl-1-propenyl)-3 -(3-sulfobutyl)-, inner salt, Dye B in US Patent 3, 730, 723, assigned to the Eastman Kodak Company

Harbury L., 1946, *Solubility and Melting Point as Functions of Particle Size*, Journal of Physical Chemistry, **50**, 190-199.

Harding M.J., 1979, *The Application of Calculations of Complex Solubility to the Interpretation of Crystal Growth Phenomena in Silver Halide Emulsions*, J. Photogr. Sci., **27**, 1-12.

Hounslow M.J., 1990, *A Discretized Population Balance for Continuous Systems at Steady State*, ALChE J, **36**, 106-116.

Hounslow M.J., R.L. Ryall and V.R. Marshall, 1988, *A Discretized Population Balance for Nucleation, Growth and Aggregation*, ALChE J, **34**, 1821-1832.

Jagannathan R., and J.S. Wey, 1985, *Nucleation Behavior in the precipitation of a Sparingly Soluble Salt - AgBr*, J. Crys. Growth, **73**, 226-232.

Jézéquel P.H., 2001, *The Concept of "Scaleable Reactor" in the Precipitation of Silver Halide Photographic Microcrystals*, Chem Eng Sci, **56**, 2399-2408.

Johnson B.K., 2003, *Flash NanoPrecipitation of Organic Actives via Confined Micromixing and Block Copolymer Stabilization*, Dissertation presented to the Faculty of Princeton University.

Judd G., 1999, *Personal Communication*, Eastman Kodak Company.

Kharitanova A.I., B.I. Shapiro, and K.S. Bogomolov, 1979, Z. Nauchn. Prikl. Fotogr. Kinematogr., **24**, 34-.

Klein E. and E. Moisar, 1963, Ber. Bunsenges. Phys. Chem., **67**, 349.

Knapp L.F., 1922, *The Solubility of Small Particles and the Stability of Colloids*, Transactions of the Faraday Society, **17**, 457-465.

Kresta S.M, K.J. Bittorf and D.J. Wilson, 2001, *Internal Annular Wall Jets: Radial Flow in a Stirred Tank*, AIChE Journal, **47**, 2390-2401.

Kresta S.M., and P.E. Wood, 1991, *Prediction of the Three Dimensional Turbulent Flow in Stirred Tanks*, AIChE Journal, **37**, 448-460.

Leubner I.H., 1993, *Number and Size of AgBr Crystals as a Function of Addition Rate: A Theoretical and Experimental Review*, J. Imaging Sci., **37**, 268-271.

Leubner I.H., 2001, *A Balanced Nucleation and Growth Model for Controlled Precipitations*, J. Dispersion Science and Technology, **22**, 125-138.

Leubner I.H., R. Jagannathan, and J.S. Wey, 1980, *Formation of Silver Bromide Crystals in Double-Jet Precipitation*, Photogr. Sci. Eng., **24**, 268-272.

Marchal P., R. David, J.P. Klein and J. Villermaux, 1988, *Crystallization and Precipitation Engineering I: An Efficient Method for Solving Population Balance in Crystallization with Agglomeration*, Chem. Eng. Sci., **43**, 59-67.

Margolis G. and E.B. Gutoff, 1974, *Simulation of the Precipitation of Silver Bromide Photographic Emulsions*, AIChE J., **20**, 467-474.

Muhr H., R. David and J. Villermaux, 1996, *Crystallization and Precipitation Engineering IV: Solving Population Balance in the Case of the Precipitation of Silver Bromide Crystals with High Primary Nucleation Rates by Using First Order Upwind Differentiation*, Chem. Eng. Sci., **51**, 309-319.

Muhr H., R. David J. Villermaux and P.H. Jezequel, 1995, *Crystallization and Precipitation Engineering V: Simulation of the Precipitation of Silver Bromide Octahedral Crystals in a Double-jet Semi-batch Reactor*, Chem. Eng. Sci., **50**, 345-355.

Mullin J.W., 2001, *Crystallization*, 4th ed., Butterworth-Heinemann Ltd., **Oxford**, Great Britain.

Nielsen A.E., 1957, *Nucleation in Barium Sulphate Precipitation*, Acta Chemica Scand., **11**, 1512.

Noyes A.A. and Whitney W.R., 1897, *Rate of Solution of Solid Substances in Their Own Solution*, Journal of the American Chemical Society, **19**, 930-934.

Ostwald W., 1896, *Lehrbuch der Algemeinen Chemie*, **2**, Englemann, Leipzig, 444.

Ostwald W., 1900, *Über die vermeintliche Isomeric des roten und gelben Quecksilberoxyds und die Oberfläschen spannung fester Körper*, Zeitschrift für Physikalische Chemie, **22**, 289-330.

Powers H.E.C., 1963, *Nucleation and Early Crystal Growth*, The Industrial Chemist, **39**, 351-353.

Ramkrishna D., 1985, *The Status of the Population Balance*, Rev. Chem. Eng., **3**, 49-95.

Randolph A.D. and M.A. Larson, 1971, *The Theory of Particulate Processes*, Academic Press, New York.

Strickland-Constable R.F., 1968, *Kinetics and Mechanism of Crystallization*, Academic Press, London.
Sugimoto T., 1990, *Proceedings: 11th Symposium On Industrial Crystallization*, Garmisch-Partenkirchen, Germany.

Thompson W., 1871, *On the Equilibrium of a Vapour at a Curved Surface of a Liquid*, Philosophical Magazine, **42**, 448-452. (First reported, 1869/70, *The Proceedings of the Royal Society of Edinburgh*, **7**, 63-68)

Valeton J.J.P., 1924, *Wachstum und Auflosung der Kristalle*, Zeitschrift für Kristallographie, **59**, 483.

Volmer M. and A. Weber, 1926, Zeitschrift für Physikalische Chemie, **119**, 277.

Volmer M., 1939, *Kinetic der Phasenbildung*, Steinkopff, Leipzig.

Wey J.S., 1981, *Precipitation and Properties of Solid State Materials*, Vol. 6 Chap. 2, (Edited by W.R. Wilcox). Marcel Dekker, New York.

Wey J.S., and R.W. Strong, 1977a, *Growth Mechanisms of AgBr Crystals in Gelatin Solution*, Photogr. Sci. Eng., **21**, 14-18.

Wey J.S., and R.W. Strong, 1977b, *Influence of the Gibbs-Thompson Effect on the Growth Behavior of AgBr Crystals*, Photogr. Sci. Eng., **21**, 248-252.

Zhou G., and S.M. Kresta, 1996a, *Distribution of Energy Between Convective and Turbulent Flow for Three Frequently Used Impellers*, Chem. Eng. Res. Des., **74A**, 379-389.

Zhou G., and S.M. Kresta, 1996b, *Impact of Geometry on the Maximum Turbulence Energy Dissipation Rate for Various Impellers*, AIChE Journal, **42**, 2476-2490.

# Appendix A

## Length Scale and Population Balance Discretization

# Appendix A

**Length Scale and Population Balance Discretization** 181

**A.1 Length Scale Discretization** 184

*A.1.1 Linear Discretization* 185

*A.1.2 Standard Geometric Discretization* 185

*A.1.3 Symmetric Geometric Discretization* 186

Imposing the constraints of $L_0$, $L_{Ps}$ and $L_P$ 189

Imposing the constraints of $L_0$, $L_{Pn}$, $L_{Ps}$ and $L_P$ 189

*Implementing Procedure* 190

**A.2 Population Balance Discretization** 191

*A.2.1 DPB Approach of Marchal et al. (1988)* 194

*A.2.2 DPB Approach of David et al. (1991)* 195

*A.2.3 DPB Approach of Muhr et al. (1995)* 195

*A.2.4 DPB Approach of Muhr et al. (1996)* 196

*A.2.5 DPB Approach of Hounslow (1990)* 197

**A.3 Adapting the DPB for Use With the Symmetric Geometric Discretization** 199

**A.4 Nomenclature** 201

**A.5 References** 202

## Table of Figures

Figure A.1 Schematic of the Linear Discretization method. 185

Figure A.2 Schematic of the Standard Geometric Discretization method. 186

Figure A.3 Schematic of the Symmetric Geometric Discretization method (constrained to $L_0$, $L_{Ps}$ and $L_P$). 187

Figure A.4 Schematic of the Symmetric Geometric Discretization method (constrained to $L_0$, $L_{Pn}$, $L_{Ps}$ and $L_P$). 188

Figure A.5 Discretization of the crystal size distribution for use in the population balance. 191

Figure A.6 Illustration of the symmetry in the Symmetric Geometric Discretization. 200

## A.1 Length Scale Discretization

The motivation for discretizing the population balance comes solely from the difficulty in solving the governing equation for any case other than the most ideal. For instance, in the case of constant growth (i.e. when McCabe's law holds) the mathematical transformation of the population balance into a set of ordinary differential equations describing the moments of the distribution is easy (Randolph and Larson 1971). However, when the growth rate is size-dependent this method can become complicated or even impossible (Randolph and Larson 1971). Analytic solutions may be found using the method of characteristics provided that the inverse of the growth rate is integratable with respect to length, and that the result can be solved explicitly for length (Appendix E).

Conventional methods for discretizing the length domain consist of either evenly sized or geometrically increasing intervals. Inherent to the method of evenly sized intervals, is the problem of requiring a very large number of intervals to cover a modest range of crystal sizes. Since there is usually a limit imposed on the number of intervals allowed, this can result in large interval sizes and therefore low resolution, if any, of small crystal sizes. On the other hand, geometrically increasing interval sizes shift some of the resolution from the larger crystal sizes to the smaller crystal sizes. However, to achieve the resolution needed for the dissolution of fine particles, too much resolution is shifted resulting in poor resolution of large sizes. A novel discretization method was developed to resolve the above issues. This method consists of a symmetric geometric discretization, which uses appropriate resolution for all crystal sizes beginning at zero. In addition, this method has the unique characteristic of placing the highest resolution at some intermediate size, and this allows the highest resolution to follow the majority of the crystals.

### A.1.1 Linear Discretization

The method of linear discretization is shown below in Figure A.1.

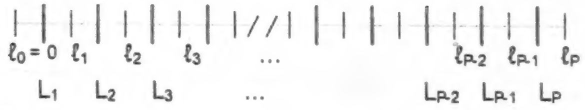

**Figure A.1** Schematic of the Linear Discretization method.

The required equations for the discretization are given below

$$\Delta L = \ell_i - \ell_{i-1} = \frac{\ell_P}{P}$$
$$\ell_i = i\,\Delta L \qquad (A.1)$$
$$L_i = (2i - 1)\Delta L$$

where $\ell_P$ is the maximum crystal size, $\ell_i$ is the upper limit and $L_i$ is the characteristic length of the *ith* size interval, and P is the total number of intervals.

### A.1.2 Standard Geometric Discretization

The method of standard geometric discretization is shown below in Figure A.2. It should be noted that the characteristic size $L_i$ appears in the arithmetic center of the *ith* interval $(\ell_{i-1} + \ell_i)/2$ not the geometric center $\sqrt{\ell_{i-1}\ell_i}$, and that the scale does not extend to zero.

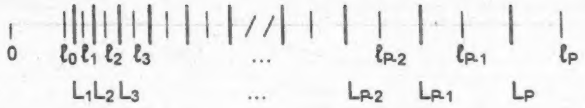

**Figure A.2** Schematic of the Standard Geometric Discretization method.

The required equations for the discretization are given below

$$\begin{aligned}
r &= \left(\frac{\ell_P}{\ell_o}\right)^{1/P} \\
\ell_i &= r^i \ell_o = r\ell_{i-1} \\
\Delta L_i &= \ell_i - \ell_{i-1} = \left(\frac{r-1}{r}\right)\ell_i = r\Delta L_{i-1} \\
L_i &= \frac{\ell_i + \ell_{i-1}}{2} = \left(\frac{r+1}{2r}\right)\ell_i = rL_{i-1}
\end{aligned} \qquad (\text{A.2})$$

where r is the common geometric ratio, $\ell_o$ is the minimum crystal size, $\ell_P$ is the maximum crystal size, $\ell_i$ is the upper limit and $L_i$ is the characteristic length of the *ith* size interval, and P is the total number of size intervals.

### *A.1.3 Symmetric Geometric Discretization*

The method of symmetric geometric discretization is shown below in Figure A.3. The method and implementation procedure are derived below. It should be noted that the characteristic size $L_i$ appears in the arithmetic center of the *ith* interval $(\ell_{i-1} + \ell_i)/2$ not the geometric center $\sqrt{\ell_{i-1}\ell_i}$, and that the scale does extend to zero.

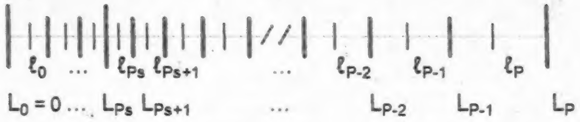
$\ell_0$ … $\ell_{Ps}$ $\ell_{Ps+1}$ … $\ell_{P-2}$ $\ell_{P-1}$ $\ell_P$
$L_0 = 0$ … $L_{Ps}$ $L_{Ps+1}$ … $L_{P-2}$ $L_{P-1}$ $L_P$

**Figure A.3** Schematic of the Symmetric Geometric Discretization method (constrained to $L_0$, $L_{Ps}$ and $L_P$).

To begin, the point of symmetry will be denoted as $L_{Ps}$. From the standard forward geometric progression ( A.2 ) the distance from $L_{Ps}$ to each *greater* characteristic length is

$$D_i = L_{Ps+i} - L_{Ps} = L_{Ps}\left(r^i - 1\right) \qquad \textbf{( A.3 )}$$

likewise the distance from $L_{Ps}$ to each *greater* upper size limit is

$$d_i = \left(\frac{2r}{r+1}\right)L_{Ps+i} - L_{Ps} = L_{Ps+i}\left(\frac{2r^{i+1}}{r+1} - 1\right) \qquad \textbf{( A.4 )}$$

Now, the following can be written for the characteristic crystal length in the reverse progression

$$L_{Ps-i} = L_{Ps} - D_i = L_{Ps} - L_{Ps}\left(r^i - 1\right) = L_{Ps}\left(2 - r^i\right) \qquad \textbf{( A.5 )}$$

and for the upper size limit, noting that $d_{i-1}$ is the distance to the upper size limit of the Ps-i *th* interval in the reverse progression

$$\ell_{Ps-i} = L_{Ps} - d_{i-1} = L_{Ps} - L_{Ps}\left(\frac{2r^i}{r+1} - 1\right) = 2L_{Ps}\left(1 - \frac{r^i}{r+1}\right) \qquad \textbf{( A.6 )}$$

The required equations for the forward discretization are

$$
\begin{aligned}
L_{Ps+i} &= r^{i} L_{Ps} = r L_{Ps+i-1} \\
\ell_{Ps+i} &= \frac{2r^{i+1}}{r+1} L_{Ps} = \frac{2r}{r+1} L_{Ps+i} \\
\Delta L_{i} &= \ell_{Ps+i} - \ell_{Ps+i-1} = \frac{2(r-1)}{r+1} L_{Ps+i} = r \Delta L_{Ps+i-1}
\end{aligned}
\qquad (\mathbf{A.7})
$$

And the required equations for the reverse discretization are

$$
\begin{aligned}
L_{Ps-i} &= \left(2 - r^{i}\right) L_{Ps} \\
\ell_{Ps-i} &= 2\left(1 - \frac{r^{i}}{r+1}\right) L_{Ps} \\
\Delta L_{PS-i} &= \ell_{Ps-i} - \ell_{Ps-i-1} = 2\left(\frac{r^{i-1} - r^{i}}{r+1}\right) L_{Ps} = r \Delta L_{Ps-i+1}
\end{aligned}
\qquad (\mathbf{A.8})
$$

where Ps is the index of the symmetric size interval, i is the number of intervals below or above Ps, r is the common geometric ratio, $\ell$ is the interval limit and L is the characteristic length of the size interval.

Several methods exist for determining the common geometric ratio, all of which depend on the constraints placed on the length scale discretization. For instance, in the simplest case the discretization would be constrained to having just $L_0$, $L_{Ps}$ and $L_P$ falling exactly on the characteristic lengths (Figure A.3). A more complex case would increase the number of constraints to include another characteristic length, such as the nuclei length $L_{Pn}$ (Figure A.4).

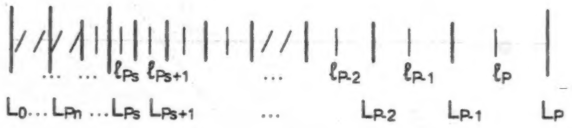

... ... $\ell_{Ps}$ $\ell_{Ps+1}$ ... $\ell_{P-2}$ $\ell_{P-1}$ $\ell_P$
$L_0$... $L_{Pn}$ ...$L_{Ps}$ $L_{Ps+1}$ ... $L_{P-2}$ $L_{P-1}$ $L_P$

**Figure A.4** Schematic of the Symmetric Geometric Discretization method (constrained to $L_0$, $L_{Pn}$, $L_{Ps}$ and $L_P$).

### Imposing the constraints of $L_0$, $L_{Ps}$ and $L_P$

From the constraint of having the scale begin at zero, Equation ( A.8 ) gives

$$r = \left(2 - \frac{L_{Ps-i}}{L_{Ps}}\right)^{1/i} = \left(2 - \frac{L_0}{L_{Ps}}\right)^{1/Ps} = 2^{1/Ps} \qquad \textbf{( A.9 )}$$

And then, from the constraint of having the scale end at a maximum length Equation ( A.7 ) gives

$$L_{Ps+i} = L_P = r^{P-Ps} L_{Ps} \qquad \textbf{( A.10 )}$$

And substituting this result into Equation ( A.9 ) gives the index of the symmetric size interval as

$$L_P = 2^{P-Ps/Ps} L_{Ps}$$
$$Ps = \frac{\ln 2}{\ln\left(\frac{2L_P}{L_{Ps}}\right)} P \qquad \textbf{( A.11 )}$$

To ensure that the length scale covers the required range, Ps should be rounded down to the nearest integer.

### Imposing the constraints of $L_0$, $L_{Pn}$, $L_{Ps}$ and $L_P$

Alternatively, an extra constraint may be placed on the length scale discretization to force another important length, such as the nuclei length $L_{Pn}$, to coincide with a characteristic length. This has been derived for the case where the nuclei length is less than the point of symmetry.

From the constraint of having the length scale begin at zero Equation ( A.8 ) gives

$$r = 2^{1/Ps} \qquad \textbf{( A.12 )}$$

From the constraint of having the length scale include $L_{Pn}$ Equation ( A.8 ) gives

$$L_{Pn} = L_{Ps}\left(2 - r^{Ps-Pn}\right) \qquad \textbf{( A.13 )}$$

And, from the constraint of having the scale end at a maximum length ( A.7 ) gives

$$L_{P} = L_{Ps} r^{P-Ps} \qquad \textbf{( A.14 )}$$

Combining Equations ( A.12 ) and ( A.13 ) gives the index of the size interval having a characteristic length $L_{Pn}$ as

$$Pn = \frac{\ln\left(\dfrac{2L_{Ps}}{2L_{Ps} - L_{Pn}}\right)}{\ln(2)} Ps \qquad \textbf{( A.15 )}$$

And combining Equations ( A.12 ) and ( A.14 ) gives the index of the symmetric interval as

$$Ps = \frac{\ln(2)}{\ln\left(\dfrac{2L_{P}}{L_{Ps}}\right)} P \qquad \textbf{( A.16 )}$$

***Implementing Procedure***

First solve Equations ( A.15 ) and ( A.16 ) for Pn and Ps. Then round both values down to the nearest integer after the calculations are completed to ensure that the scale covers the required range. Next, using Equation ( A.12 ) calculate the common geometric ratio. Since it is most imperative for both $L_0$ and $L_{Pn}$ to fall exactly on the scale, $L_{Ps}$ is recalculated according to Equation ( A.14 ) using the rounded numbers.

## A.2 Population Balance Discretization

To overcome the complexity of solving the continuous population balance equation, an approach has been developed that casts the population balance in terms of discrete size intervals. This discretized population balance (DPB) method transforms the integro-partial-differential equation into a set of ordinary first order differential equations. Several approaches exist in the literature for discretizing the population balance equation. Example discretization methods are derived below and their accuracy is given in terms of predicting the rate of change of the first, second and third moments of the distribution. Each discretization is given in terms of the length scale given in Figure A.5 below. Here $\ell_{i-1}$, $\ell_i$ and $L_i$ are the lower limit, upper limit and characteristic size of the *ith* interval.

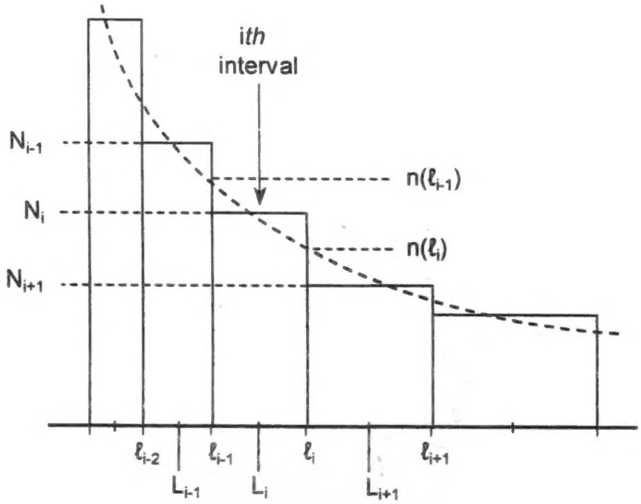

**Figure A.5** Discretization of the crystal size distribution for use in the population balance.

Integration of the continuous population balance equation between the limits of $\ell_{i-1}$ and $\ell_i$ yields the rate of change in particle number in the *ith* size interval.

$$\int_{\ell_{i-1}}^{\ell_i} \frac{\partial n}{\partial t} \partial \ell = - \int_{\ell_{i-1}}^{\ell_i} \frac{\partial (Gn)}{\partial \ell} \partial \ell$$

$$\frac{\partial \int_{\ell_{i-1}}^{\ell_i} n \partial \ell}{\partial t} = - Gn\Big|_{\ell_{i-1}}^{\ell_i} \qquad \textbf{( A.17 )}$$

$$\frac{\partial N_i}{\partial t} = - Gn\Big|_{\ell_{i-1}}^{\ell_i}$$

where $N_i$ is the crystal count per size interval, n is the crystal count per size interval per unit size and G is the crystal growth rate. Using the simple approximation of

$$n(\ell_i) = \frac{N_i}{\ell_i - \ell_{i-1}} = \frac{N_i}{\Delta L_i} \qquad \textbf{( A.18 )}$$

where $\Delta L_i$ is the size of the i*th* interval, Equation ( A.17 ) gives the rate of change in the i*th* interval as

$$\begin{aligned} \frac{\partial N_i}{\partial t} &= G(\ell_{i-1}) \frac{N_{i-1}}{\Delta L_{i-1}} - G(\ell_i) \frac{N_i}{\Delta L_i} \\ &= \frac{r}{\ell_i (r-1)} \left( r\, G(\ell_{i-1}) N_{i-1} - G(\ell_i) N_i \right) \end{aligned} \qquad \textbf{( A.19 )}$$

Hounslow et al. (1988) derived a method for evaluating the accuracy of a discretization method for the case of size-independent growth. The method is re-derived here for the length scale discretization given in Figure A.5.

The j*th* moment of a distribution is defined as

$$m_j = \int_0^\infty \ell^j n(\ell)\, d\ell \qquad \textbf{( A.20 )}$$

The zeroth, first, second, and third moments correspond to the total crystal number, length, area and volume. The discrete form of Equation ( A.20 ) is given by

$$
\begin{aligned}
m_j &= \sum_i L_i^j N_i \\
&= \sum_i \left(\frac{r+1}{2r}\ell_i\right)^j N_i
\end{aligned}
\qquad (\text{A.21})
$$

where $L_i$ is the mean or characteristic size of the *ith* interval. Therefore, the rate of change of the *jth* moment is

$$
\frac{dm_j}{dt} = \sum_i \left(\frac{r+1}{2r}\ell_i\right)^j \frac{dN_i}{dt} \qquad (\text{A.22})
$$

Now the predicted rate of change in the *jth* moment can be determined for the discretized population balance given by Equation ( A.19 ) assuming a size-independent growth rate.

$$
\begin{aligned}
\frac{dm_j}{dt} &= \sum_i \left(\frac{r+1}{2r}\ell_i\right)^j \frac{rG}{\ell_i(r-1)}\left(rN_{i-1} - N_i\right) \\
&= \cdots + \left(\frac{r+1}{2r}\ell_i\right)^j \frac{rG}{\ell_i(r-1)}\left(rN_{i-1} - N_i\right) + \left(\frac{r+1}{2r}\ell_{i+1}\right)^j \frac{rG}{\ell_{i+1}(r-1)}\left(rN_i - N_{i+1}\right) + \cdots \\
&= \sum_i \left(\frac{r+1}{2r}\ell_i\right)^j \frac{rG}{\ell_i(r-1)}\left(-N_i\right) + \left(\frac{r+1}{2r}\ell_{i+1}\right)^j \frac{rG}{\ell_{i+1}(r-1)}\left(rN_i\right) \\
&= \left(\frac{r+1}{2}\right)\left(\frac{r^j-1}{r-1}\right) G \sum_i N_i \left(\frac{r+1}{2r}\ell_i\right)^{j-1} \\
&= \left(\frac{r+1}{2}\right)\left(\frac{r^j-1}{r-1}\right) G m_{j-1}
\end{aligned}
\qquad (\text{A.23})
$$

Randolph and Larson (1971) showed that the moments of a distribution evolving under only nucleation and growth could be represented by the ordinary differential equation

$$
\frac{dm_j}{dt} = 0^j B_o + jGm_{j-1} \qquad (\text{A.24})
$$

Comparing the Equation ( A.23 ) to the expression derived by Randolph and Larson (1971) for pure growth yields results that are too high by a factor of

$$\begin{aligned}\left(\frac{r+1}{2}\right)\left(\frac{r^j-1}{r-1}\right)\frac{1}{j} &= 1.130\,(j=1)\\ &= 1.277\,(j=2)\\ &= 1.449\,(j=3)\end{aligned}$$

Thus, Equation ( A.19 ) over predicts the rate of change of the third moment by 45%.

### A.2.1 *DPB Approach of Marchal et al. (1988)*

Marchal et al. (1988) used the method of classes to formulate the rate of change in the population due to growth. They proposed the following approximation for the crystal number density function

$$n(\ell_i) = \frac{\dfrac{N_{i+1}}{\Delta L_{i+1}} + \dfrac{N_i}{\Delta L_i}}{2} = \frac{r}{2\ell_i(r-1)}\left(\frac{N_{i+1}}{r} + N_i\right) \qquad \text{( A.25 )}$$

Substituting this approximation into Equation ( A.17 ) gives the rate of change as

$$\frac{dN_i}{dt} = \frac{r}{2\ell_i(r-1)}\left(r\,G(\ell_{i-1})N_{i-1} + (G(\ell_{i-1}) - G(\ell_i))N_i - \frac{G(\ell_i)N_{i+1}}{r}\right) \qquad \text{( A.26 )}$$

Following an analogous method as that in Equations ( A.23 ) the error is

$$\begin{aligned}\left(\frac{r+1}{r-1}\right)\left(r^j - \frac{1}{r^j}\right)\frac{1}{4j} &= 1.013\,(j=1)\\ &= 1.041\,(j=2)\\ &= 1.087\,(j=3)\end{aligned} \qquad \text{( A.27 )}$$

thus, the rate of change of the third moment is too high by 9%.

### *A.2.2 DPB Approach of David et al. (1991)*

David et al. (1991) continued with the method of classes from Marchal et al. (1988), but modified the expression for approximating the density function. This modification accounted for non-constant interval sizing by interpolating between the number density function at the interval centers, $L_i$ and $L_{i+1}$, for number density function at $\ell_i$. They proposed the following approximation for the crystal number density function

$$n(\ell_i) = \frac{\frac{\Delta L_i}{\Delta L_{i+1}} N_{i+1} + \frac{\Delta L_{i+1}}{\Delta L_i} N_i}{\Delta L_{i+1} + \Delta L_i} = \frac{r}{\ell_i (r^2 - 1)} \left( \frac{N_{i+1}}{r} + r N_i \right) \qquad \text{( A.28 )}$$

Substituting this approximation into Equation ( A.17 ) gives the rate of change as

$$\frac{dN_i}{dt} = \frac{r}{\ell_i (r^2 - 1)} \left( r^2 G(\ell_{i-1}) N_{i-1} + (G(\ell_{i-1}) - r G(\ell_i)) N_i - \frac{G(\ell_i) N_{i+1}}{r} \right) \qquad \text{( A.29 )}$$

Following an analogous method as that in Equations ( A.23 ) the error is

$$\begin{aligned} \left(\frac{1}{r-1}\right)\left(r^{j+1} + 1 - r - \frac{1}{r^j}\right)\frac{1}{2j} &= 1.027\,(j=1) \\ &= 1.068\,(j=2) \qquad \text{( A.30 )} \\ &= 1.128\,(j=3) \end{aligned}$$

thus, the rate of change of the third moment is over predicted by 13%. Therefore, the expected increase in accuracy due to accounting for variable sized intervals, actually increased the error in predicting the rate of change of the moments relative to Equation ( A.26 ).

### *A.2.3 DPB Approach of Muhr et al. (1995)*

Muhr et al. (1995) used the method of finite differences, which transforms the population balance equation into a set of ordinary differential equations after discretizing the number density function. Using a central difference estimation they proposed

$$\frac{dn(\ell_i)}{dt} = G(\ell_i)\frac{n(\ell_{i+1}) - n(\ell_{i-1})}{\ell_{i-1} - \ell_{i+1}} + n(\ell_i)\frac{G(\ell_{i+1}) - G(\ell_{i-1})}{\ell_{i-1} - \ell_{i+1}} \qquad \textbf{( A.31 )}$$

Muhr et al. (1996) points out that Equations ( A.29 ) and ( A.31 ) can be quite similar depending on the choice of the above finite difference approximation or of the approximation for $n(\ell_i)$.

### *A.2.4 DPB Approach of Muhr et al. (1996)*

The previous DPB methods of Marchal et al. (1988), David et al. (1991), and Muhr et al. (1995) all have the potential of producing negative values for the crystal size distribution, which is physically impossible. Muhr et al. (1996) proposed using the method of first order upwind differentiation to circumvent this problem. The first order finite difference scheme is

$$\begin{aligned} \frac{dn_i}{dt} &= \frac{G(\ell_{i-1})n_{i-1} - G(\ell_i)n_i}{\ell_i - \ell_{i-1}} && \text{if} \quad G(\ell) > 0 \\ \frac{dn_i}{dt} &= \frac{G(\ell_i)n_i - G(\ell_{i+1})n_{i+1}}{\ell_{i+1} - \ell_i} && \text{if} \quad G(\ell) < 0 \end{aligned} \qquad \textbf{( A.32 )}$$

And where the growth rates on each side of the zero growth rate point are expressed as

$$G_L\big|_0 = \frac{G(\ell_{-1}) + G(\ell_0)}{2} \quad \text{and} \quad G_R\big|_0 = \frac{G(\ell_0) + G(\ell_1)}{2} \qquad \textbf{( A.33 )}$$

along with

$$\begin{aligned} &\text{if} \quad G_L \geq 0 \quad n_L = n_{-1} \\ &\text{if} \quad G_L < 0 \quad n_L = n_0 \\ &\text{if} \quad G_R \geq 0 \quad n_R = n_0 \\ &\text{if} \quad G_R < 0 \quad n_R = n_1 \end{aligned} \qquad \textbf{( A.34 )}$$

and, the rate of change

$$\left.\frac{dn}{dt}\right|_0 = \frac{G_L n_L - G_R n_R}{\ell_0 - \ell_{-1}} \qquad \textbf{( A.35 )}$$

For the case of selecting the simple approximation of the number density function given in Equation ( A.18 ), the DPB in Equation ( A.32 ) becomes similar to that given in Equation ( A.19 ). The DPB equations are

$$\begin{aligned} \frac{dN_i}{dt} &= \frac{1}{\ell_i(r-1)}\left(r\,G(\ell_{i-1})N_{i-1} - G(\ell_i)N_i\right) \qquad \text{if} \quad G(\ell) > 0 \\ \frac{dN_i}{dt} &= \frac{1}{\ell_i(r^2-r)}\left(G(\ell_i)N_i - \frac{G(\ell_{i+1})N_{i+1}}{r}\right) \qquad \text{if} \quad G(\ell) < 0 \end{aligned} \qquad \textbf{( A.36 )}$$

Following the approach given in Equation ( A.23 ) the errors in predicting the rate of change in the *jth* moments are

$$\begin{aligned} \left(\frac{r+1}{2}\right)\left(\frac{r^j-1}{r-1}\right)\frac{1}{j} &= 1.130\,(j=1) \\ &= 1.277\,(j=2) \qquad \text{if} \quad G(\ell) > 0 \\ &= 1.449\,(j=3) \end{aligned} \qquad \textbf{( A.37 )}$$

$$\begin{aligned} \left(\frac{r+1}{2}\right)\left(\frac{r^j-1}{r-1}\right)\frac{1}{r^{j+1}j} &= 0.712\,(j=1) \\ &= 0.638\,(j=2) \qquad \text{if} \quad G(\ell) < 0 \\ &= 0.575\,(j=3) \end{aligned} \qquad \textbf{( A.38 )}$$

Therefore, the errors associated with the rate of change of the third moment are 45 and -42.5%.

### *A.2.5 DPB Approach of Hounslow (1990)*

Hounslow et al. (1988) originally derived the DPB method for size-independent growth, and was later modified by Hounslow (1990) for size-dependent growth rates. The DPB method was developed under the constraints of correctly predicting the rates of change of the zeroth, first and second moments of the size distribution. To do so, the following form of the DPB was considered

$$\frac{dN_i}{dt} = \frac{1}{\ell_i}\left(a\,G(\ell_{i-1})N_{i-1} + b\,G(\ell_i)N_i + c\,G(\ell_{i+1})N_{i+1}\right) \qquad \textbf{( A.39 )}$$

where a, b and c are constants that were chosen in order to correctly predict the moments. Applying the method in Equation ( A.23 ) gives the predicted rates of change as

$$\frac{dm_j}{dt} = \left(\frac{r+1}{2r}\right)\left(a r^{j-1} + b + c r^{1-j}\right)G m_{j-1} \qquad \textbf{( A.40 )}$$

Comparison of this result with Equation ( A.24 ) reveals that the rate of change of the *jth* moment will be correctly predicted if

$$\left(\frac{r+1}{2r}\right)\left(a r^{j-1} + b + c r^{1-j}\right) = j \qquad \textbf{( A.41 )}$$

Solving the three linear equations generated by setting j = 0, 1 and 2, gives the constants

$$a = \frac{2r^2}{(r+1)(r^2-1)} \qquad b = \frac{2r}{(r+1)} \qquad c = \frac{-2r^2}{(r+1)(r^2-1)} \qquad \textbf{( A.42 )}$$

Now the DPB becomes

$$\frac{dN_i}{dt} = \frac{2r}{\ell_i(r+1)}\left(\frac{r\,G(\ell_{i-1})N_{i-1}}{r^2-1} + G(\ell_i)N_i - \frac{r\,G(\ell_{i+1})N_{i+1}}{r^2-1}\right) \qquad \textbf{( A.43 )}$$

This DPB is guaranteed to correctly predict the zeroth, first and second moments, and the rate of change of the third moment is only high by 1.8%.

Hounslow et al. (1988) mention that this DPB has the potential to produce negative crystal size distributions and indicated that meaningful results can be obtained by simply setting the negative values to zero.

## A.3 Adapting the DPB for Use With the Symmetric Geometric Discretization

First of all, to facilitate the use of the DPB with the mass balance equations, which are in terms of the interval characteristic length, the DPB will be rewritten in terms of characteristic length. From Equations ( A.7 ) and ( A.43 ) the DPB for the forward progression can be written as

$$\frac{dN_{Ps+i}}{dt} = \frac{1}{r^i L_{Ps}} \left( \frac{r\,G_{Ps+(i-1)} N_{Ps+(i-1)}}{r^2-1} + G_{Ps+i} N_{Ps+i} - \frac{r\,G_{Ps+(i+1)} N_{Ps+(i+1)}}{r^2-1} \right) \qquad \textbf{( A.44 )}$$

where i is the number of intervals above the symmetrical interval.

Section A.1.3 defined the reverse geometric progression as the mirror image of the forward geometric progression about some reference length $L_{Ps}$. In order to convert the DPB for the reverse progression, it must be realized that the process of growth in the forward progression is analogous to the process of dissolution in the reverse progression with respect to the scale discretization (Figure A.6). It should also be realized that the reverse progression must use an effective characteristic length that is equal in magnitude to characteristic length of its mirror image, thus

$$L_{Ps-i,eff} = r^i L_{Ps} \qquad \textbf{( A.45 )}$$

Applying the symmetry shown in Figure A.6 the DPB can be written for the reverse progression as

$$\frac{dN_{Ps-i}}{dt} = \frac{-1}{r^i L_{Ps}} \left( \frac{r\,G_{Ps-(i-1)} N_{Ps-(i-1)}}{r^2-1} + G_{Ps-i} N_{Ps-i} - \frac{r\,G_{Ps-(i+1)} N_{Ps-(i+1)}}{r^2-1} \right) \qquad \textbf{( A.46 )}$$

where i is the number of intervals below the symmetrical interval.

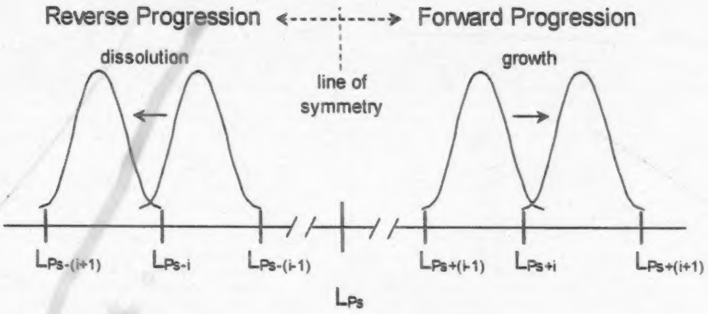
Reverse Progression
Forward Progression
dissolution
growth
line of symmetry
$L_{Ps-(i+1)}$
$L_{Ps-i}$
$L_{Ps-(i-1)}$
$L_{Ps}$
$L_{Ps+(i-1)}$
$L_{Ps+i}$
$L_{Ps+(i+1)}$

**Figure A.6** Illustration of the symmetry in the Symmetric Geometric Discretization.

## A.4 Nomenclature

| | |
|---|---|
| $D_i$ | distance from $L_{Ps}$ to $L_{Ps+i}$, m |
| $d_i$ | distance from $\ell_{Ps}$ to $\ell_{Ps+i}$, m |
| $\Delta L_i$ | spacing of *ith* size interval, m |
| $i$ | interval index (relative to zero or the symmetric interval) |
| $L_i$ | characteristic length of *ith* size interval, m |
| $\ell_i$ | upper length limit of *ith* size interval, m |
| $L_{Ps\text{-}i,\ eff}$ | effective characteristic length of *ith* size interval ($r^i L_{Ps}$), m |
| $m_j$ | *jth* moment of the distribution |
| $n$ | crystal count per size interval per unit size, $m^{-3}\ m^{-1}$ |
| $N_i$ | crystal count per size interval ($\Delta N$), $m^{-3}$ |
| $P$ | total number of size intervals |
| $Pn$ | nucleation interval index |
| $Ps$ | symmetric interval index |
| $r$ | common geometric factor |

## A.5 References

David R., J. Villermaux, P. Marchal and J.P. Klein, 1991, *Crystallization and Precipitation Engineering IV: Kinetic Model of Adipic Acid Crystallization*, Chem. Eng. Sci., **46**, 1129-1139.

Hounslow M.J., 1990, *A Discretized Population Balance for Continuous Systems at Steady State*, ALChE J, **36**, 106-116.

Hounslow M.J., R.L. Ryall and V.R. Marshall, 1988, *A Discretized Population Balance for Nucleation, Growth and Aggregation*, ALChE J, **34**, 1821-1832.

Marchal P., R. David, J.P. Klein and J. Villermaux, 1988, *Crystallization and Precipitation Engineering I: An Efficient Method for Solving Population Balance in Crystallization with Agglomeration*, Chem. Eng. Sci., **43**, 59-67.

Muhr H., R. David and J. Villermaux, 1996, *Crystallization and Precipitation Engineering IV: Solving Population Balance in the Case of the Precipitation of Silver Bromide Crystals with High Primary Nucleation Rates by Using First Order Upwind Differentiation*, Chem. Eng. Sci., **51**, 309-319.

Muhr H., R. David J. Villermaux and P.H. Jezequel, 1995, *Crystallization and Precipitation Engineering V: Simulation of the Precipitation of Silver Bromide Octahedral Crystals in a Double-jet Semi-batch Reactor*, Chem. Eng. Sci., **50**, 345-355.

Ramkrishna D., 1985, *The Status of the Population Balance*, Rev. Chem. Eng., **3**, 49-95.

Randolph A.D. and M.A. Larson, 1971, *The Theory of Particulate Processes*, Academic Press, New York.

# Appendix B

## Complete Experimental and Simulated Results

# Appendix B

**Complete Experimental and Simulated Results** 204

**B.1 Seeded Micromixing Analysis** 211
  *B.1.1 MM11* 212
  *B.1.2 MM12* 214
  *B.1.3 MM12R* 216
**B.2 Nucleated Micromixing Analysis** 218
  *B.2.1 MM14* 219
  *B.2.2 MM14R* 221
  *B.2.3 MM16* 223
  *B.2.4 MM16R* 225
**B.3 Variable Feed Rate Mesomixing Analysis I** 227
  *B.3.1 QS4.01* 228
  *B.3.2 QS4.02* 230
  *B.3.3 QS4.03* 232
  *B.3.4 QS4.04* 234
  *B.3.5 QS4.05* 236
  *B.3.6 QS4.06* 238
  *B.3.7 QS4.07* 240
**B.4 Variable Feed Pipe Diameter Mesomixing Analysis I** 242
  *B.4.1 DS4.01* 243
  *B.4.2 DS4.02* 245
**B.5 Variable Feed Pipe Diameter Mesomixing Analysis II** 247
  *B.5.1 DS4.11* 248
  *B.5.2 DS4.12* 250

## Table of Tables

Table B.1 Descriptive statistics for Seeded Micromixing Analysis - MM11. a) Small population, b) Large population. 213

Table B.2 Experimental conditions for Seeded Micromixing Analysis - MM11. 213

Table B.3 Descriptive statistics for Seeded Micromixing Analysis - MM12. a) Small population, b) Large population. 215

Table B.4 Experimental conditions for Seeded Micromixing Analysis - MM12. 215

Table B.5 Descriptive statistics for Seeded Micromixing Analysis - MM12R. a) Small population, b) Large population. 217

Table B.6 Experimental conditions for Seeded Micromixing Analysis - MM12R. 217

Table B.7 Descriptive statistics for Nucleated Micromixing Analysis - MM14. 220

Table B.8 Experimental conditions for Nucleated Micromixing Analysis - MM14. 220

Table B.9 Descriptive statistics for Nucleated Micromixing Analysis - MM14R. 222

Table B.10 Experimental conditions for Nucleated Micromixing Analysis - MM14R. 222

Table B.11 Descriptive statistics for Nucleated Micromixing Analysis - MM16. 224

Table B.12 Experimental conditions for Nucleated Micromixing Analysis - MM16. 224

Table B.13 Descriptive statistics for Nucleated Micromixing Analysis - MM16R. 226

Table B.14 Experimental conditions for Nucleated Micromixing Analysis - MM16R. 226

Table B.15 Descriptive statistics for Variable Feed Rate Analysis I - QS4.01. 229
Table B.16 Experimental conditions for Variable Feed Rate Analysis I - QS4.01. 229
Table B.17 Descriptive statistics for Variable Feed Rate Analysis I - QS4.02. 231
Table B.18 Experimental conditions for Variable Feed Rate Analysis I - QS4.02. 231
Table B.19 Descriptive statistics for Variable Feed Rate Analysis I - QS4.03. 233
Table B.20 Experimental conditions for Variable Feed Rate Analysis I - QS4.03. 233
Table B.21 Descriptive statistics for Variable Feed Rate Analysis I - QS4.04. 235
Table B.22 Experimental conditions for Variable Feed Rate Analysis I - QS4.04. 235
Table B.23 Descriptive statistics for Variable Feed Rate Analysis I - QS4.05. 237
Table B.24 Experimental conditions for Variable Feed Rate Analysis I - QS4.05. 237
Table B.25 Descriptive statistics for Variable Feed Rate Analysis I - QS4.06. 239
Table B.26 Experimental conditions for Variable Feed Rate Analysis I - QS4.06. 239
Table B.27 Descriptive statistics for Variable Feed Rate Analysis I - QS4.07. 241
Table B.28 Experimental conditions for Variable Feed Rate Analysis I - QS4.07. 241
Table B.29 Descriptive statistics for Variable Feed Pipe Diameter Analysis I - DS4.01. 244

Table B.30 Experimental conditions for Variable Feed Pipe Diameter Analysis I - DS4.01. 244

Table B.31 Descriptive statistics for Variable Feed Pipe Diameter Analysis I - DS4.02. 246

Table B.32 Experimental conditions for Variable Feed Pipe Diameter Analysis I - DS4.02. 246

Table B.33 Descriptive statistics for Variable Feed Pipe Diameter Analysis II - DS4.11. 249

Table B.34 Experimental conditions for Variable Feed Pipe Diameter Analysis II - DS4.11. 249

Table B.35 Descriptive statistics for Variable Feed Pipe Diameter Analysis II - DS4.12. 251

Table B.36 Experimental conditions for Variable Feed Pipe Diameter Analysis II - DS4.12. 251

## Table of Figures

Figure B.1 CSD time evolution for Seeded Micromixing Analysis - MM11. 212
Figure B.2 Simulated CSD time evolution for Seeded Micromixing Analysis - MM11. Optimized kinetic parameters were used. 212
Figure B.3 CSD time evolution for Seeded Micromixing Analysis - MM12. 214
Figure B.4 Simulated CSD time evolution for Seeded Micromixing Analysis - MM12. Optimized kinetic parameters were used. 214
Figure B.5 CSD time evolution for Seeded Micromixing Analysis - MM12R. 216
Figure B.6 CSD time evolution for Nucleated Micromixing Analysis - MM14. 219
Figure B.7 Simulated CSD time evolution for Nucleated Micromixing Analysis - MM14. Original kinetic parameters were used. 219
Figure B.8 CSD time evolution for Nucleated Micromixing Analysis - MM14R. 221
Figure B.9 CSD time evolution for Nucleated Micromixing Analysis - MM16. 223
Figure B.10 Simulated CSD time evolution for Nucleated Micromixing Analysis - MM16. Original kinetic parameters were used. 223
Figure B.11 CSD time evolution for Nucleated Micromixing Analysis - MM16R. 225
Figure B.12 CSD time evolution for Variable Feed Rate Analysis I - QS4.01. 228
Figure B.13 Simulated CSD time evolution for Variable Feed Rate Analysis I - QS4.01. Original kinetic parameters were used. 228
Figure B.14 CSD time evolution for Variable Feed Rate Analysis I - QS4.02. 230
Figure B.15 Simulated CSD time evolution for Variable Feed Rate Analysis I - QS4.02. Original kinetic parameters were used. 230
Figure B.16 CSD time evolution for Variable Feed Rate Analysis I - QS4.03. 232
Figure B.17 Simulated CSD time evolution for Variable Feed Rate Analysis I - QS4.03. Original kinetic parameters were used. 232

Figure B.18 CSD time evolution for Variable Feed Rate Analysis I - QS4.04. 234
Figure B.19 Simulated CSD time evolution for Variable Feed Rate Analysis I - QS4.04. Original kinetic parameters were used. 234
Figure B.20 CSD time evolution for Variable Feed Rate Analysis I - QS4.05. 236
Figure B.21 Simulated CSD time evolution for Variable Feed Rate Analysis I - QS4.05. Original kinetic parameters were used. 236
Figure B.22 CSD time evolution for Variable Feed Rate Analysis I - QS4.06. 238
Figure B.23 Simulated CSD time evolution for Variable Feed Rate Analysis I - QS4.06. Original kinetic parameters were used. 238
Figure B.24 CSD time evolution for Variable Feed Rate Analysis I - QS4.07. 240
Figure B.25 Simulated CSD time evolution for Variable Feed Rate Analysis I - QS4.07. Original kinetic parameters were used. 240
Figure B.26 CSD time evolution for Variable Feed Pipe Diameter Analysis I - DS4.01. 243
Figure B.27 CSD time evolution for Variable Feed Pipe Diameter Analysis I - DS4.02. 245
Figure B.28 CSD time evolution for Variable Feed Pipe Diameter Analysis II - DS4.11. 248
Figure B.29 CSD time evolution for Variable Feed Pipe Diameter Analysis II - DS4.12. 250

## B.1 Seeded Micromixing Analysis

The following model predictions were based on the kinetic parameters measured by Wey and Strong (1977a). See Section 3.5.1.

### *B.1.1 MM11*

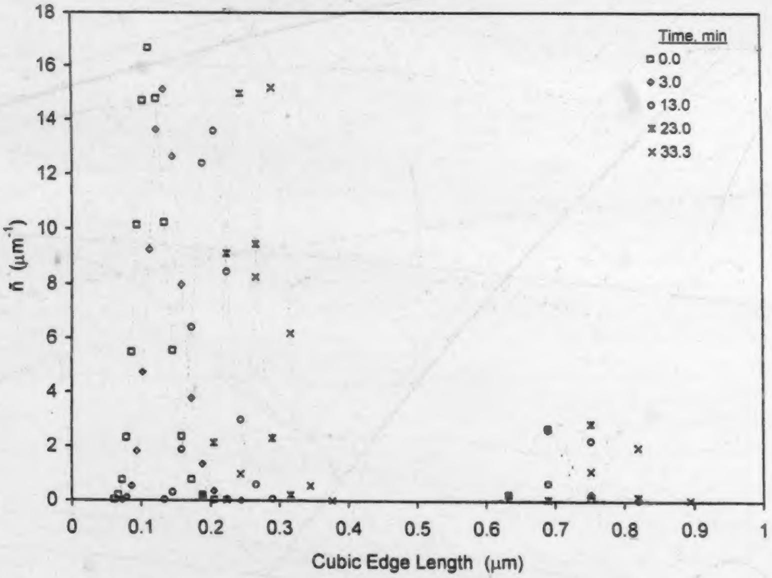

**Figure B.1** CSD time evolution for Seeded Micromixing Analysis - MM11.

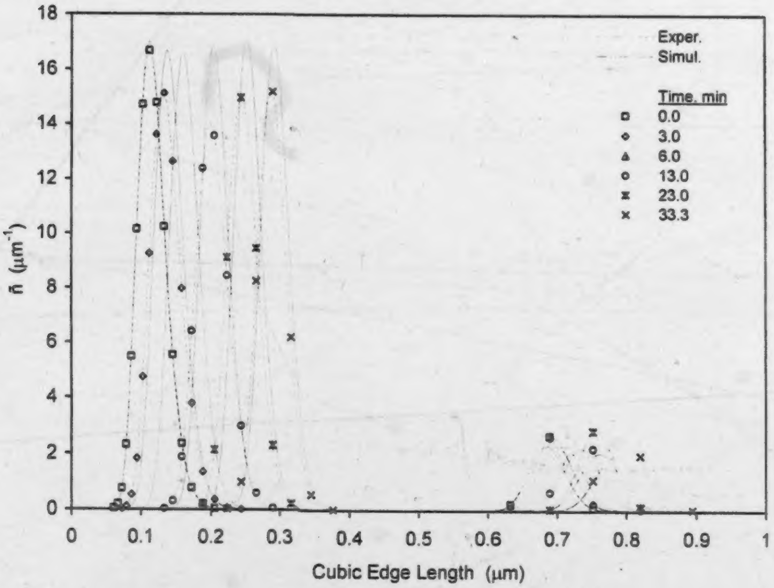

**Figure B.2** Simulated CSD time evolution for Seeded Micromixing Analysis - MM11. Optimized kinetic parameters were used.

**Table B.1** Descriptive statistics for Seeded Micromixing Analysis - MM11. a) Small population, b) Large population.

a)

| Time (min) | $\mu$ ($\mu$m) | $\sigma$ ($\mu$m) | $\mu_g$ ($\mu$m) | $\sigma_g$ | $N_T$ | AgBr (mol) |
|---|---|---|---|---|---|---|
| 0.0 | 0.117 | 0.021 | 0.115 | 1.191 | 1.8E+15 | 0.099 |
| 3.0 | 0.137 | 0.022 | 0.135 | 1.177 | 2.9E+15 | 0.256 |
| 6.0 | | | | | | |
| 13.0 | 0.203 | 0.023 | 0.202 | 1.122 | 1.7E+15 | 0.499 |
| 23.0 | 0.247 | 0.022 | 0.246 | 1.093 | 2.0E+15 | 1.047 |
| 33.3 | 0.290 | 0.020 | 0.289 | 1.073 | 1.5E+15 | 1.266 |

b)

| Time (min) | $\mu$ ($\mu$m) | $\sigma$ ($\mu$m) | $\mu_g$ ($\mu$m) | $\sigma_g$ | $N_T$ | AgBr (mol) |
|---|---|---|---|---|---|---|
| 0.0 | 0.687 | 0.025 | 0.686 | 1.037 | 2.9E+14 | 3.267 |
| 3.0 | 0.695 | 0.027 | 0.694 | 1.039 | 2.9E+14 | 3.380 |
| 6.0 | | | | | | |
| 13.0 | 0.737 | 0.029 | 0.736 | 1.039 | 2.9E+14 | 4.037 |
| 23.0 | 0.758 | 0.025 | 0.757 | 1.034 | 2.9E+14 | 4.389 |
| 33.3 | 0.797 | 0.033 | 0.796 | 1.043 | 2.9E+14 | 5.100 |

**Table B.2** Experimental conditions for Seeded Micromixing Analysis - MM11.

| Reaction Kettle Geometry | |
|---|---|
| T (m) | 0.2 |
| H (m) | 0.2 |
| D (m) | 0.067 |
| N (rps) | 630 |
| $D_P$ (mm) | 0.8 |

| Precipitation Conditions | |
|---|---|
| pBr | 2.55 |
| gel (wt%) | 3.0 |
| $C_f$ (M) | 2.0 |
| $Q_f$ ($m^3$ $s^{-1}$) | 7.5E-07 |
| Impeller feed point | |

### *B.1.2 MM12*

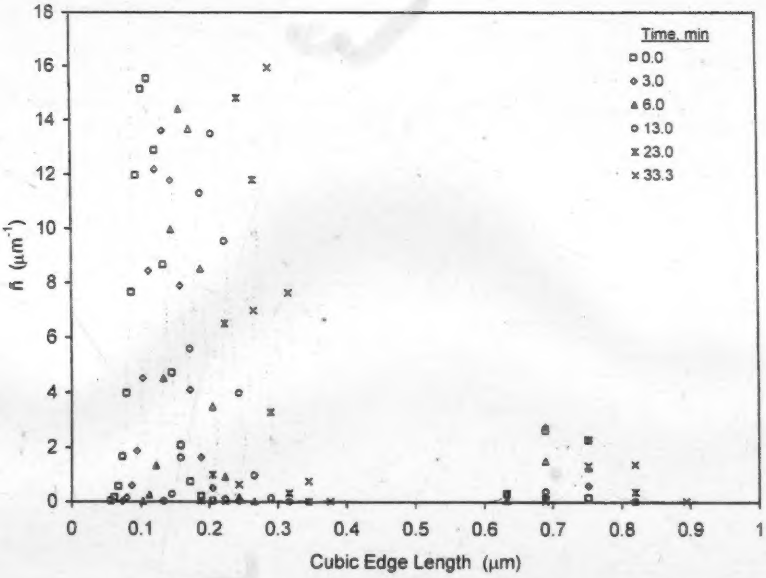

**Figure B.3** CSD time evolution for Seeded Micromixing Analysis - MM12.

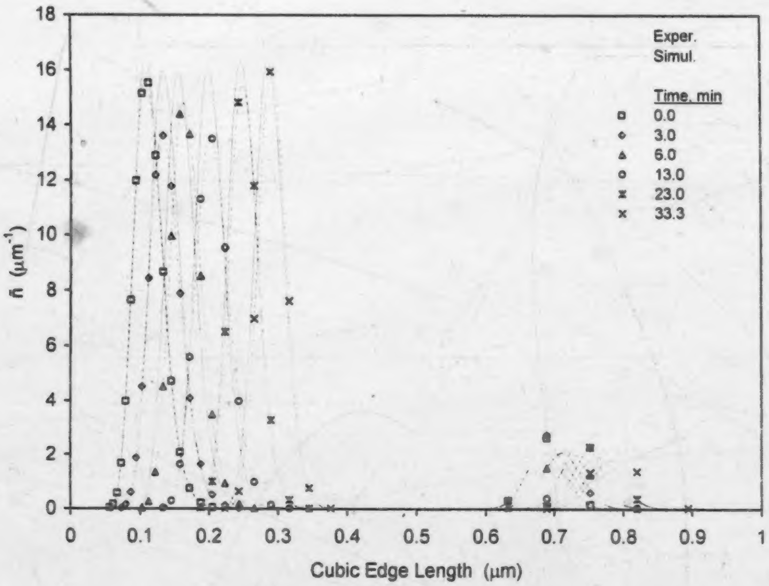

**Figure B.4** Simulated CSD time evolution for Seeded Micromixing Analysis - MM12. Optimized kinetic parameters were used.

**Table B.3** Descriptive statistics for Seeded Micromixing Analysis - MM12. a) Small population, b) Large population.

| Time (min) | $\mu$ ($\mu$m) | $\sigma$ ($\mu$m) | $\mu_g$ ($\mu$m) | $\sigma_g$ | $N_T$ | AgBr (mol) |
|---|---|---|---|---|---|---|
| 0.0 | 0.114 | 0.022 | 0.112 | 1.208 | 1.9E+15 | 0.099 |
| 3.0 | 0.138 | 0.024 | 0.136 | 1.187 | 2.3E+15 | 0.208 |
| 6.0 | 0.168 | 0.022 | 0.166 | 1.143 | 9.9E+14 | 0.161 |
| 13.0 | 0.207 | 0.025 | 0.205 | 1.127 | 1.4E+15 | 0.438 |
| 23.0 | 0.253 | 0.021 | 0.252 | 1.088 | 1.8E+15 | 0.993 |
| 33.3 | 0.293 | 0.020 | 0.292 | 1.072 | 1.7E+15 | 1.440 |

| Time (min) | $\mu$ ($\mu$m) | $\sigma$ ($\mu$m) | $\mu_g$ ($\mu$m) | $\sigma_g$ | $N_T$ | AgBr (mol) |
|---|---|---|---|---|---|---|
| 0.0 | 0.687 | 0.027 | 0.687 | 1.040 | 2.9E+14 | 3.267 |
| 3.0 | 0.699 | 0.031 | 0.698 | 1.045 | 2.9E+14 | 3.428 |
| 6.0 | 0.719 | 0.034 | 0.719 | 1.049 | 2.9E+14 | 3.745 |
| 13.0 | 0.741 | 0.027 | 0.741 | 1.037 | 2.9E+14 | 4.098 |
| 23.0 | 0.762 | 0.030 | 0.761 | 1.040 | 2.9E+14 | 4.443 |
| 33.3 | 0.788 | 0.035 | 0.787 | 1.045 | 2.9E+14 | 4.926 |

**Table B.4** Experimental conditions for Seeded Micromixing Analysis - MM12.

| Reaction Kettle Geometry | |
|---|---|
| T (m) | 0.2 |
| H (m) | 0.2 |
| D (m) | 0.05 |
| N (rps) | 16.7 |
| $D_P$ (mm) | 0.8 |

| Precipitation Conditions | |
|---|---|
| pBr | 2.55 |
| gel (wt%) | 3.0 |
| $C_f$ (M) | 2.0 |
| $Q_f$ ($m^3$ $s^{-1}$) | 7.5E-07 |
| Impeller feed point | |

### B.1.3 MM12R

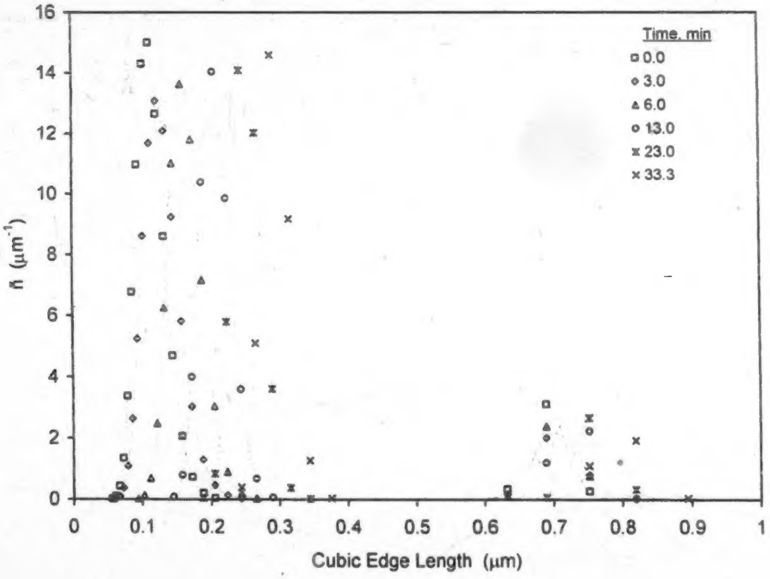

**Figure B.5** CSD time evolution for Seeded Micromixing Analysis - MM12R.

**Table B.5** Descriptive statistics for Seeded Micromixing Analysis - MM12R. a) Small population, b) Large population.

| Time (min) | $\mu$ ($\mu$m) | $\sigma$ ($\mu$m) | $\mu_g$ ($\mu$m) | $\sigma_g$ | $N_T$ | AgBr (mol) |
|---|---|---|---|---|---|---|
| 0.0 | 0.115 | 0.022 | 0.113 | 1.204 | 1.9E+15 | 0.099 |
| 3.0 | 0.130 | 0.026 | 0.128 | 1.219 | 1.9E+15 | 0.144 |
| 6.0 | 0.165 | 0.024 | 0.163 | 1.156 | 2.6E+15 | 0.406 |
| 13.0 | 0.208 | 0.022 | 0.207 | 1.113 | 2.1E+15 | 0.653 |
| 23.0 | 0.254 | 0.022 | 0.253 | 1.088 | 1.8E+15 | 1.030 |
| 33.3 | 0.297 | 0.021 | 0.296 | 1.073 | 1.5E+15 | 1.344 |

| Time (min) | $\mu$ ($\mu$m) | $\sigma$ ($\mu$m) | $\mu_g$ ($\mu$m) | $\sigma_g$ | $N_T$ | AgBr (mol) |
|---|---|---|---|---|---|---|
| 0.0 | 0.690 | 0.028 | 0.689 | 1.041 | 2.9E+14 | 3.267 |
| 3.0 | 0.705 | 0.034 | 0.705 | 1.049 | 2.9E+14 | 3.492 |
| 6.0 | 0.706 | 0.029 | 0.705 | 1.042 | 2.9E+14 | 3.500 |
| 13.0 | 0.731 | 0.030 | 0.730 | 1.042 | 2.9E+14 | 3.883 |
| 23.0 | 0.762 | 0.028 | 0.762 | 1.037 | 2.9E+14 | 4.406 |
| 33.3 | 0.796 | 0.033 | 0.796 | 1.042 | 2.9E+14 | 5.022 |

**Table B.6** Experimental conditions for Seeded Micromixing Analysis - MM12R.

| Reaction Kettle Geometry | |
|---|---|
| T (m) | 0.2 |
| H (m) | 0.2 |
| D (m) | 0.05 |
| N (rps) | 16.7 |
| $D_P$ (mm) | 0.8 |

| Precipitation Conditions | |
|---|---|
| pBr | 2.55 |
| gel (wt%) | 3.0 |
| $C_f$ (M) | 2.0 |
| $Q_f$ ($m^3 s^{-1}$) | 7.5E-07 |
| Impeller feed point | |

## B.2 Nucleated Micromixing Analysis

The following model predictions were based on the kinetic parameters measured by Wey and Strong (1977a). See Section 3.5.2.

### *B.2.1 MM14*

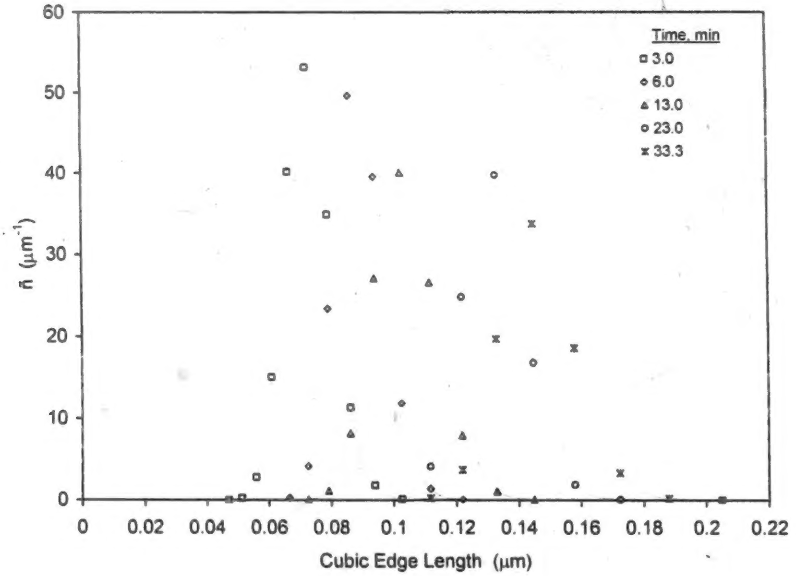

**Figure B.6** CSD time evolution for Nucleated Micromixing Analysis - MM14.

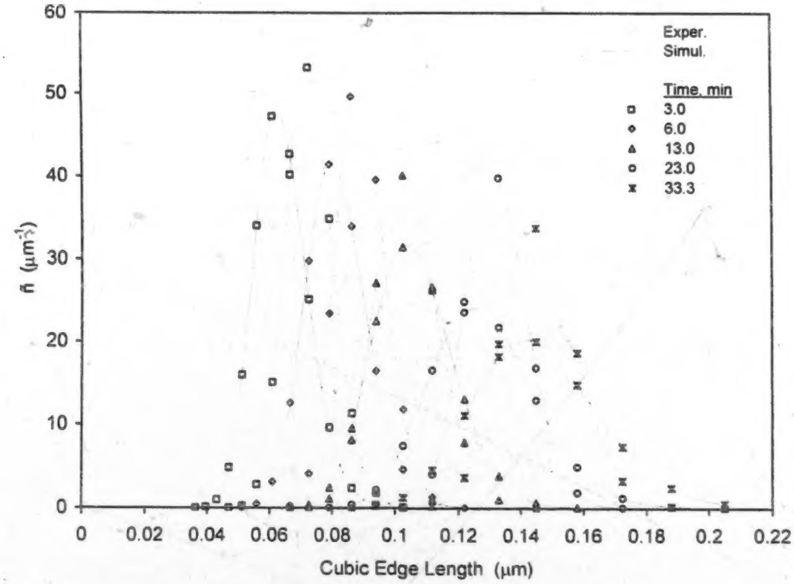

**Figure B.7** Simulated CSD time evolution for Nucleated Micromixing Analysis - MM14. Original kinetic parameters were used.

**Table B.7** Descriptive statistics for Nucleated Micromixing Analysis - MM14.

| Time (min) | $\mu$ ($\mu$m) | $\sigma$ ($\mu$m) | $\mu_g$ ($\mu$m) | $\sigma_g$ | $N_T$ | AgBr (mol) |
|---|---|---|---|---|---|---|
| 3.0 | 0.073 | 0.008 | 0.073 | 1.109 | 2.0E+16 | 0.270 |
| 6.0 | 0.089 | 0.008 | 0.089 | 1.092 | 2.2E+16 | 0.540 |
| 13.0 | 0.104 | 0.010 | 0.103 | 1.101 | 3.0E+16 | 1.170 |
| 23.0 | 0.132 | 0.010 | 0.132 | 1.078 | 2.6E+16 | 2.070 |
| 33.3 | 0.146 | 0.012 | 0.146 | 1.085 | 2.8E+16 | 3.000 |

**Table B.8** Experimental conditions for Nucleated Micromixing Analysis - MM14.

| Reaction Kettle Geometry | |
|---|---|
| T (m) | 0.2 |
| H (m) | 0.2 |
| D (m) | 0.05 |
| N (rps) | 16.7 |
| $D_P$ (mm) | 0.8 |

| Precipitation Conditions | |
|---|---|
| pBr | 2.55 |
| gel (wt%) | 3.0 |
| $C_f$ (M) | 2.0 |
| $Q_f$ ($m^3 s^{-1}$) | 7.5E-07 |
| Impeller feed point | |

### *B.2.2 MM14R*

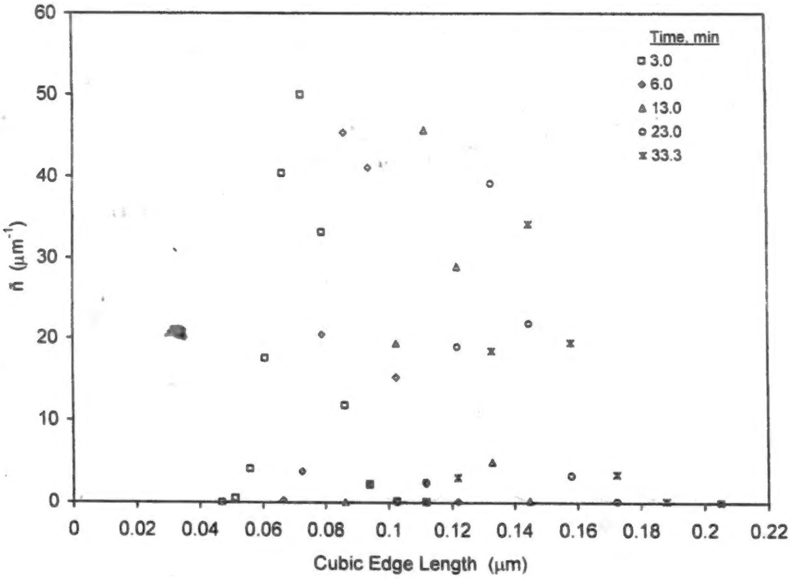

**Figure B.8** CSD time evolution for Nucleated Micromixing Analysis - MM14R.

**Table B.9** Descriptive statistics for Nucleated Micromixing Analysis - MM14R.

| Time (min) | $\mu$ ($\mu$m) | $\sigma$ ($\mu$m) | $\mu_g$ ($\mu$m) | $\sigma_g$ | $N_T$ | AgBr (mol) |
|---|---|---|---|---|---|---|
| 3.0 | 0.073 | 0.008 | 0.072 | 1.116 | 2.0E+16 | 0.270 |
| 6.0 | 0.090 | 0.008 | 0.090 | 1.096 | 2.1E+16 | 0.540 |
| 13.0 | 0.114 | 0.009 | 0.114 | 1.079 | 2.3E+16 | 1.170 |
| 23.0 | 0.135 | 0.010 | 0.134 | 1.079 | 2.5E+16 | 2.070 |
| 33.3 | 0.147 | 0.012 | 0.146 | 1.083 | 2.8E+16 | 3.000 |

**Table B.10** Experimental conditions for Nucleated Micromixing Analysis - MM14R.

| Reaction Kettle Geometry | |
|---|---|
| T (m) | 0.2 |
| H (m) | 0.2 |
| D (m) | 0.05 |
| N (rps) | 16.7 |
| $D_P$ (mm) | 0.8 |

| Precipitation Conditions | |
|---|---|
| pBr | 2.55 |
| gel (wt%) | 3.0 |
| $C_f$ (M) | 2.0 |
| $Q_f$ ($m^3 s^{-1}$) | 7.5E-07 |
| Impeller feed point | |

### B.2.3 MM16

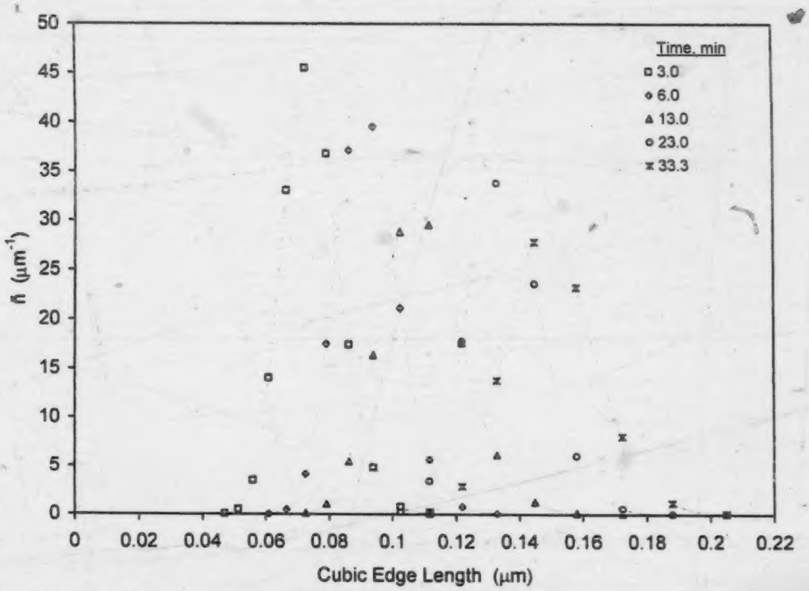

**Figure B.9** CSD time evolution for Nucleated Micromixing Analysis - MM16.

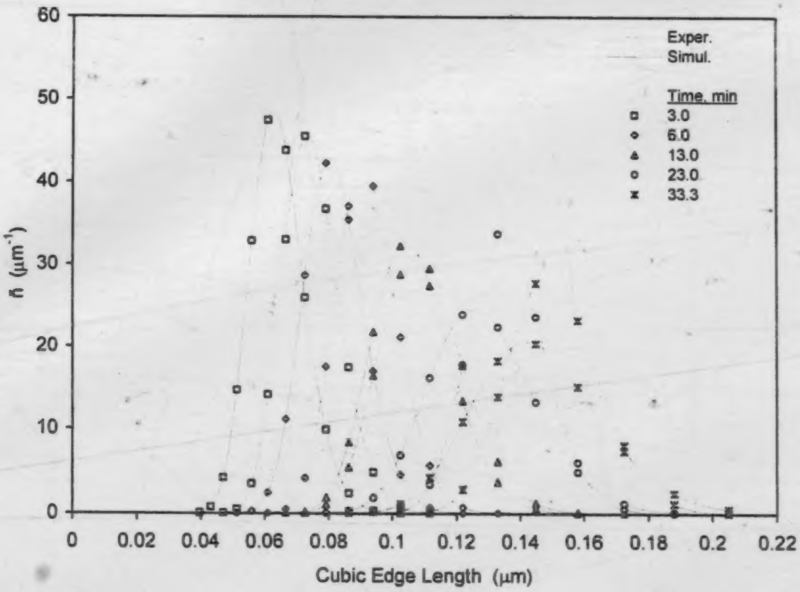

**Figure B.10** Simulated CSD time evolution for Nucleated Micromixing Analysis - MM16. Original kinetic parameters were used.

**Table B.11** Descriptive statistics for Nucleated Micromixing Analysis - MM16.

| Time (min) | $\mu$ ($\mu$m) | $\sigma$ ($\mu$m) | $\mu_g$ ($\mu$m) | $\sigma_g$ | $N_T$ | AgBr (mol) |
|---|---|---|---|---|---|---|
| 3.0 | 0.075 | 0.009 | 0.074 | 1.126 | 1.9E+16 | 0.270 |
| 6.0 | 0.092 | 0.010 | 0.092 | 1.110 | 2.0E+16 | 0.540 |
| 13.0 | 0.110 | 0.013 | 0.109 | 1.125 | 2.6E+16 | 1.170 |
| 23.0 | 0.136 | 0.012 | 0.136 | 1.090 | 2.4E+16 | 2.070 |
| 33.3 | 0.151 | 0.014 | 0.150 | 1.097 | 2.5E+16 | 3.000 |

**Table B.12** Experimental conditions for Nucleated Micromixing Analysis - MM16.

| Reaction Kettle Geometry | |
|---|---|
| T (m) | 0.2 |
| H (m) | 0.2 |
| D (m) | 0.067 |
| N (rps) | 10.5 |
| $D_P$ (mm) | 0.8 |

| Precipitation Conditions | |
|---|---|
| pBr | 2.55 |
| gel (wt%) | 3.0 |
| $C_f$ (M) | 2.0 |
| $Q_f$ ($m^3 s^{-1}$) | 7.5E-07 |
| Impeller feed point | |

### *B.2.4 MM16R*

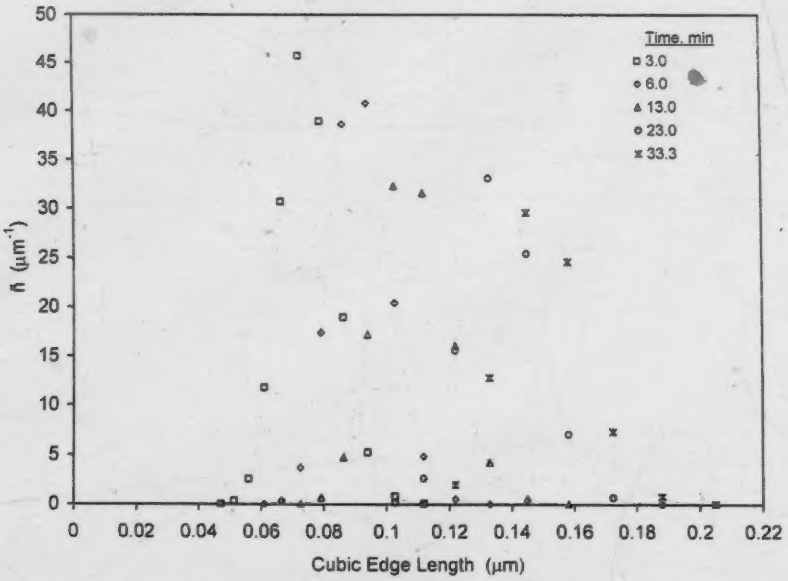

**Figure B.11** CSD time evolution for Nucleated Micromixing Analysis - MM16R.

**Table B.13** Descriptive statistics for Nucleated Micromixing Analysis - MM16R.

| Time (min) | $\mu$ ($\mu$m) | $\sigma$ ($\mu$m) | $\mu_g$ ($\mu$m) | $\sigma_g$ | $N_T$ | AgBr (mol) |
|---|---|---|---|---|---|---|
| 3.0 | 0.075 | 0.009 | 0.075 | 1.123 | 1.8E+16 | 0.270 |
| 6.0 | 0.092 | 0.009 | 0.092 | 1.106 | 2.0E+16 | 0.540 |
| 13.0 | 0.109 | 0.012 | 0.108 | 1.113 | 2.7E+16 | 1.170 |
| 23.0 | 0.137 | 0.012 | 0.137 | 1.090 | 2.3E+16 | 2.070 |
| 33.3 | 0.151 | 0.013 | 0.150 | 1.089 | 2.5E+16 | 3.000 |

**Table B.14** Experimental conditions for Nucleated Micromixing Analysis - MM16R.

| Reaction Kettle Geometry | |
|---|---|
| T (m) | 0.2 |
| H (m) | 0.2 |
| D (m) | 0.067 |
| N (rps) | 10.5 |
| $D_P$ (mm) | 0.8 |

| Precipitation Conditions | |
|---|---|
| pBr | 2.55 |
| gel (wt%) | 3.0 |
| $C_f$ (M) | 2.0 |
| $Q_f$ ($m^3$ $s^{-1}$) | 7.5E-07 |
| Impeller feed point | |

## B.3 Variable Feed Rate Mesomixing Analysis I

The following model predictions were based on the kinetic parameters measured by Wey and Strong (1977a). See Section 3.5.2.

### *B.3.1 QS4.01*

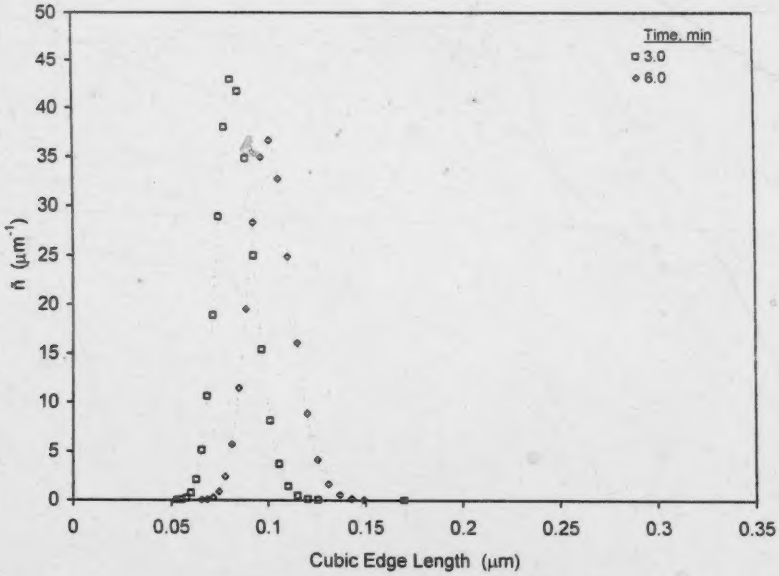

**Figure B.12** CSD time evolution for Variable Feed Rate Analysis I - QS4.01.

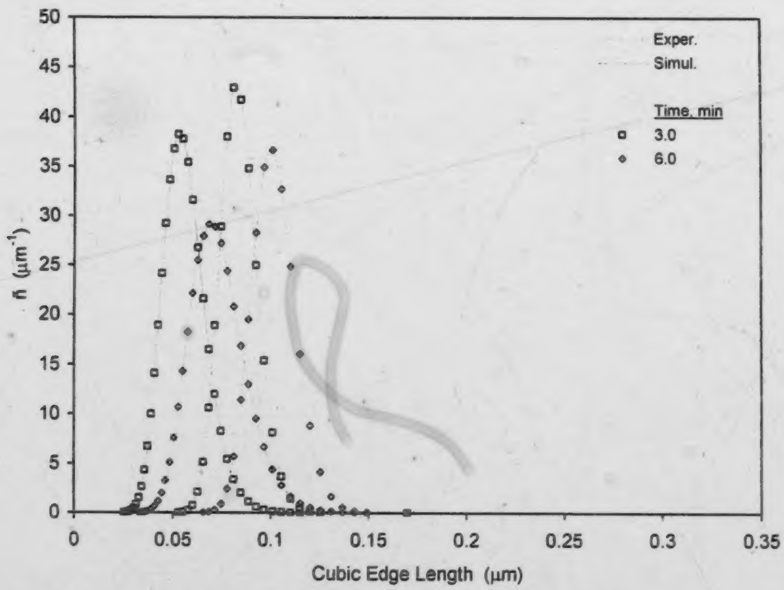

**Figure B.13** Simulated CSD time evolution for Variable Feed Rate Analysis I - QS4.01. Original kinetic parameters were used.

**Table B.15** Descriptive statistics for Variable Feed Rate Analysis I - QS4.01.

| Time (min) | $\mu$ ($\mu$m) | $\sigma$ ($\mu$m) | $\mu_g$ ($\mu$m) | $\sigma_g$ | $N_T$ | AgBr (mol) |
|---|---|---|---|---|---|---|
| 3.0 | 0.084 | 0.009 | 0.083 | 1.118 | 7.4E+16 | 1.501 |
| 6.0 | 0.102 | 0.011 | 0.101 | 1.114 | 8.3E+16 | 3.002 |

**Table B.16** Experimental conditions for Variable Feed Rate Analysis I - QS4.01.

| Reaction Kettle Geometry | |
|---|---|
| T (m) | 0.2 |
| H (m) | 0.2 |
| D (m) | 0.05 |
| N (rps) | 16.7 |
| $D_P$ (mm) | 1.6 |

| Precipitation Conditions | |
|---|---|
| pBr | 2.55 |
| gel (wt%) | 3.0 |
| $C_f$ (M) | 2.0 |
| $Q_f$ ($m^3 s^{-1}$) | 4.2E-06 |
| Surface feed point | |

### *B.3.2 QS4.02*

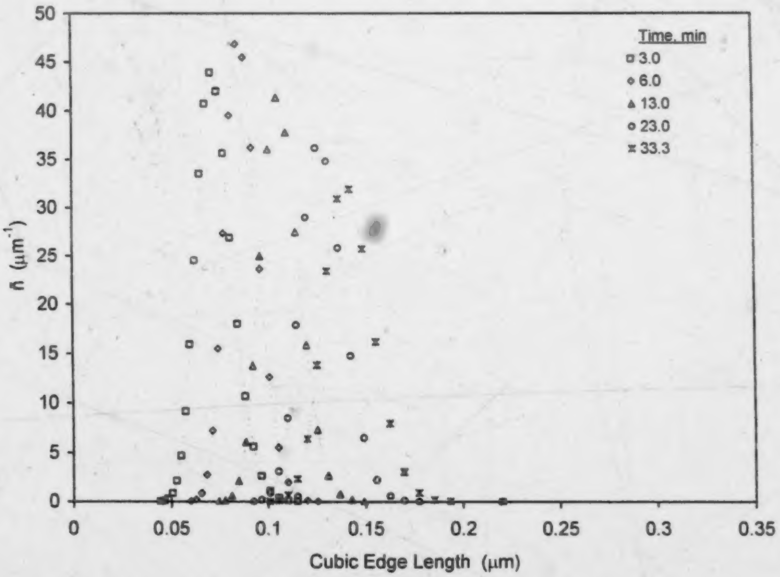

**Figure B.14** CSD time evolution for Variable Feed Rate Analysis I - QS4.02.

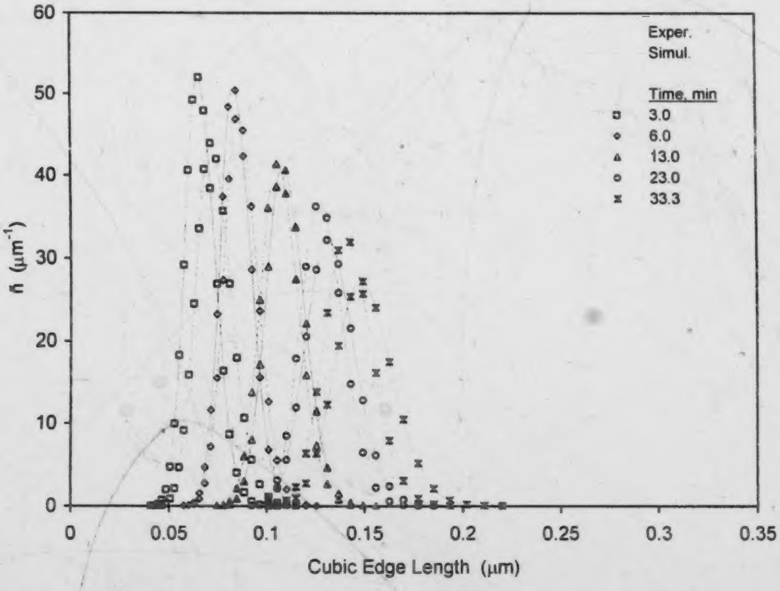

**Figure B.15** Simulated CSD time evolution for Variable Feed Rate Analysis I - QS4.02. Original kinetic parameters were used.

**Table B.17** Descriptive statistics for Variable Feed Rate Analysis I - QS4.02.

| Time (min) | $\mu$ ($\mu$m) | $\sigma$ ($\mu$m) | $\mu_g$ ($\mu$m) | $\sigma_g$ | $N_T$ | AgBr (mol) |
|---|---|---|---|---|---|---|
| 3.0 | 0.073 | 0.009 | 0.073 | 1.134 | 2.0E+16 | 0.270 |
| 6.0 | 0.087 | 0.009 | 0.087 | 1.102 | 2.3E+16 | 0.540 |
| 13.0 | 0.107 | 0.010 | 0.107 | 1.095 | 2.8E+16 | 1.170 |
| 23.0 | 0.129 | 0.011 | 0.128 | 1.089 | 2.8E+16 | 2.070 |
| 33.3 | 0.142 | 0.012 | 0.142 | 1.091 | 3.0E+16 | 3.000 |

**Table B.18** Experimental conditions for Variable Feed Rate Analysis I - QS4.02.

| Reaction Kettle Geometry | |
|---|---|
| T (m) | 0.2 |
| H (m) | 0.2 |
| D (m) | 0.05 |
| N (rps) | 16.7 |
| $D_P$ (mm) | 0.8 |

| Precipitation Conditions | |
|---|---|
| pBr | 2.55 |
| gel (wt%) | 3.0 |
| $C_f$ (M) | 2.0 |
| $Q_f$ ($m^3$ $s^{-1}$) | 7.5E-07 |
| Surface feed point | |

### *B.3.3 QS4.03*

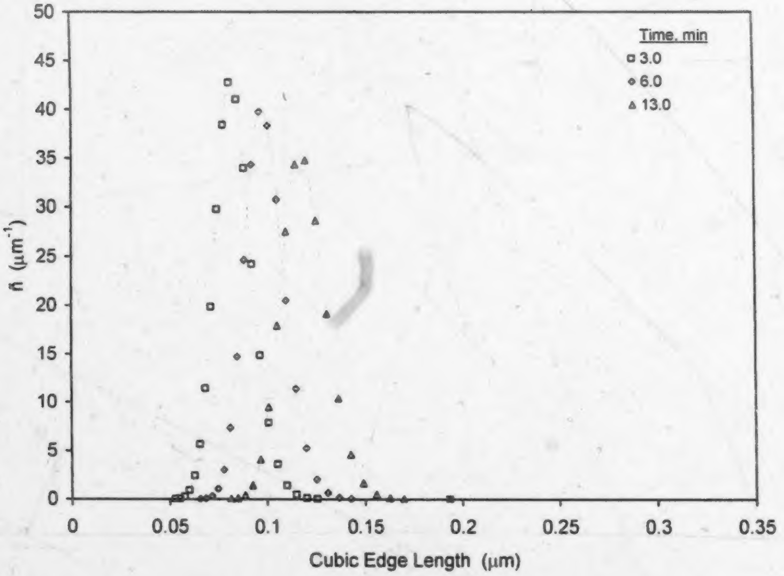

**Figure B.16** CSD time evolution for Variable Feed Rate Analysis I - QS4.03.

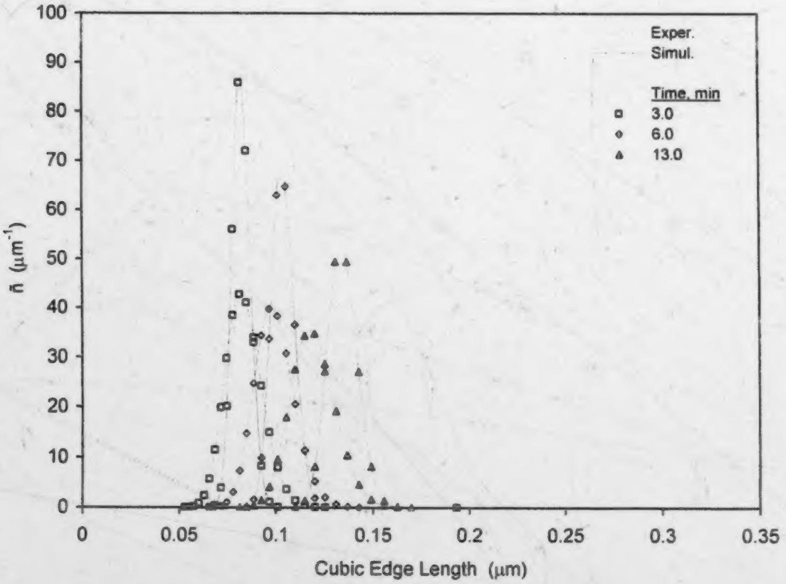

**Figure B.17** Simulated CSD time evolution for Variable Feed Rate Analysis I - QS4.03. Original kinetic parameters were used.

**Table B.19** Descriptive statistics for Variable Feed Rate Analysis I - QS4.03.

| Time (min) | $\mu$ ($\mu$m) | $\sigma$ ($\mu$m) | $\mu_g$ ($\mu$m) | $\sigma_g$ | $N_T$ | AgBr (mol) |
|---|---|---|---|---|---|---|
| 3.0 | 0.084 | 0.009 | 0.083 | 1.119 | 3.4E+16 | 0.691 |
| 6.0 | 0.099 | 0.010 | 0.099 | 1.106 | 4.1E+16 | 1.382 |
| 13.0 | 0.119 | 0.011 | 0.119 | 1.100 | 5.1E+16 | 2.995 |

**Table B.20** Experimental conditions for Variable Feed Rate Analysis I - QS4.03.

| Reaction Kettle Geometry | |
|---|---|
| T (m) | 0.2 |
| H (m) | 0.2 |
| D (m) | 0.05 |
| N (rps) | 16.7 |
| $D_P$ (mm) | 0.8 |

| Precipitation Conditions | |
|---|---|
| pBr | 2.55 |
| gel (wt%) | 3.0 |
| $C_f$ (M) | 2.0 |
| $Q_f$ ($m^3 s^{-1}$) | 1.9E-06 |
| Surface feed point | |

### B.3.4 QS4.04

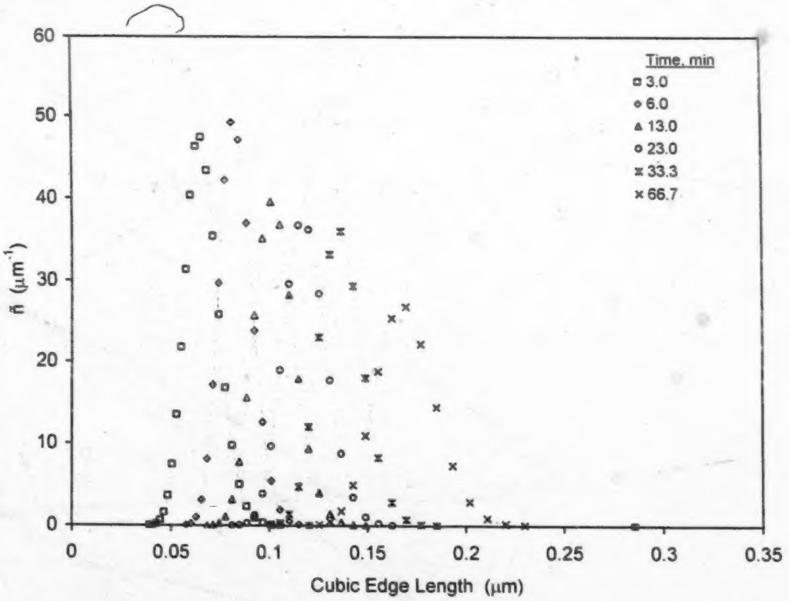

**Figure B.18** CSD time evolution for Variable Feed Rate Analysis I - QS4.04.

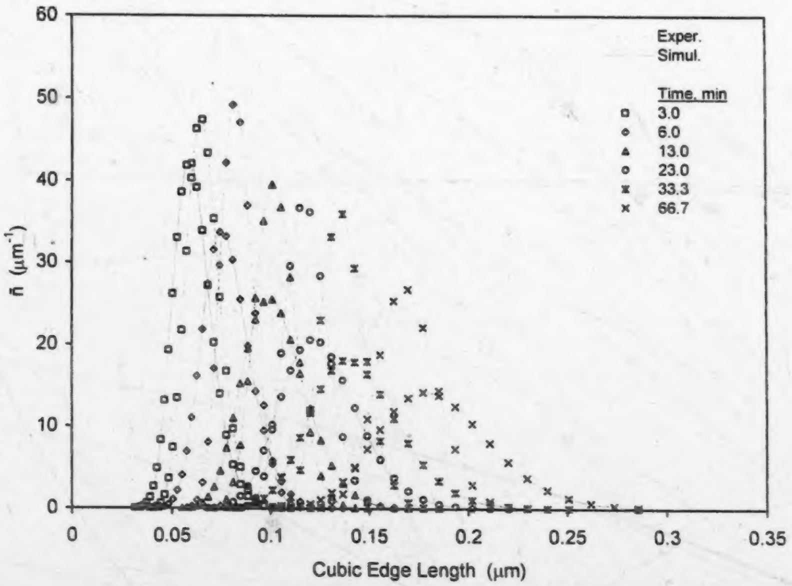

**Figure B.19** Simulated CSD time evolution for Variable Feed Rate Analysis I - QS4.04. Original kinetic parameters were used.

**Table B.21** Descriptive statistics for Variable Feed Rate Analysis I - QS4.04.

| Time (min) | $\mu$ ($\mu$m) | $\sigma$ ($\mu$m) | $\mu_g$ ($\mu$m) | $\sigma_g$ | $N_T$ | AgBr (mol) |
|---|---|---|---|---|---|---|
| 3.0 | 0.066 | 0.009 | 0.066 | 1.137 | 1.3E+16 | 0.135 |
| 6.0 | 0.083 | 0.008 | 0.083 | 1.102 | 1.3E+16 | 0.270 |
| 13.0 | 0.103 | 0.010 | 0.102 | 1.104 | 1.6E+16 | 0.585 |
| 23.0 | 0.119 | 0.011 | 0.118 | 1.095 | 1.8E+16 | 1.035 |
| 33.3 | 0.137 | 0.011 | 0.136 | 1.084 | 1.7E+16 | 1.500 |
| 66.7 | 0.170 | 0.015 | 0.169 | 1.092 | 1.8E+16 | 3.000 |

**Table B.22** Experimental conditions for Variable Feed Rate Analysis I - QS4.04.

| Reaction Kettle Geometry | |
|---|---|
| T (m) | 0.2 |
| H (m) | 0.2 |
| D (m) | 0.05 |
| N (rps) | 16.7 |
| $D_P$ (mm) | 0.8 |

| Precipitation Conditions | |
|---|---|
| pBr | 2.55 |
| gel (wt%) | 3.0 |
| $C_f$ (M) | 2.0 |
| $Q_f$ ($m^3 s^{-1}$) | 3.8E-07 |
| Surface feed point | |

### B.3.5 QS4.05

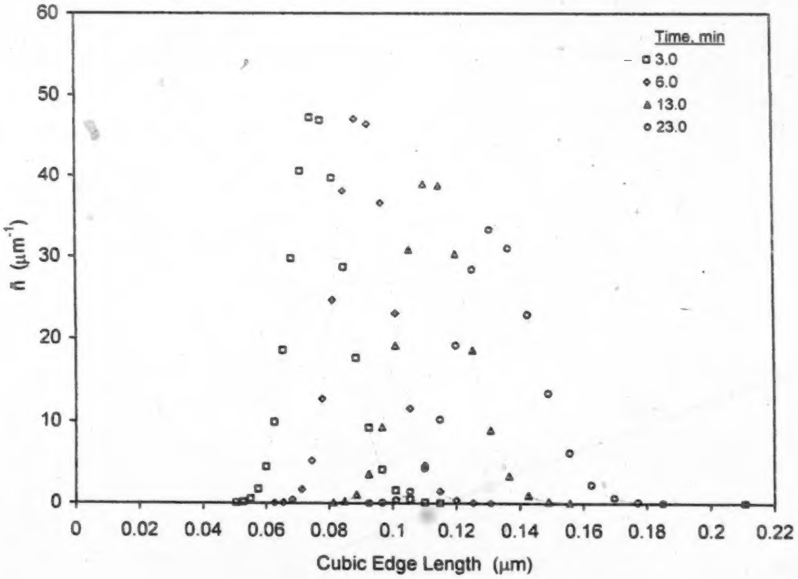

**Figure B.20** CSD time evolution for Variable Feed Rate Analysis I - QS4.05.

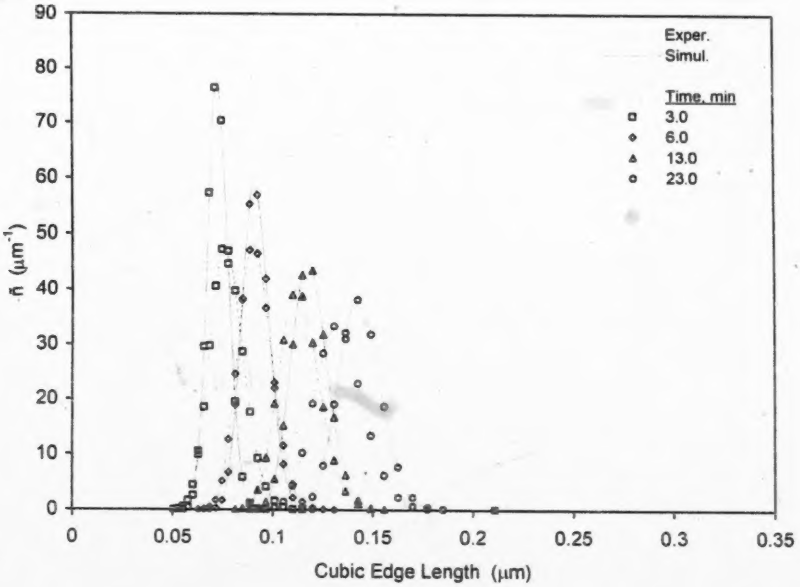

**Figure B.21** Simulated CSD time evolution for Variable Feed Rate Analysis I - QS4.05. Original kinetic parameters were used.

**Table B.23** Descriptive statistics for Variable Feed Rate Analysis I - QS4.05.

| Time (min) | $\mu$ ($\mu$m) | $\sigma$ ($\mu$m) | $\mu_g$ ($\mu$m) | $\sigma_g$ | $N_T$ | AgBr (mol) |
|---|---|---|---|---|---|---|
| 3.0 | 0.077 | 0.008 | 0.077 | 1.115 | 2.5E+16 | 0.392 |
| 6.0 | 0.091 | 0.008 | 0.091 | 1.096 | 3.0E+16 | 0.785 |
| 13.0 | 0.114 | 0.010 | 0.113 | 1.092 | 3.4E+16 | 1.700 |
| 23.0 | 0.134 | 0.012 | 0.133 | 1.094 | 3.7E+16 | 3.008 |

**Table B.24** Experimental conditions for Variable Feed Rate Analysis I - QS4.05.

| Reaction Kettle Geometry | |
|---|---|
| T (m) | 0.2 |
| H (m) | 0.2 |
| D (m) | 0.05 |
| N (rps) | 16.7 |
| $D_P$ (mm) | 0.8 |

| Precipitation Conditions | |
|---|---|
| pBr | 2.55 |
| gel (wt%) | 3.0 |
| $C_f$ (M) | 2.0 |
| $Q_f$ ($m^3\ s^{-1}$) | 1.1E-06 |
| Surface feed point | |

### B.3.6 QS4.06

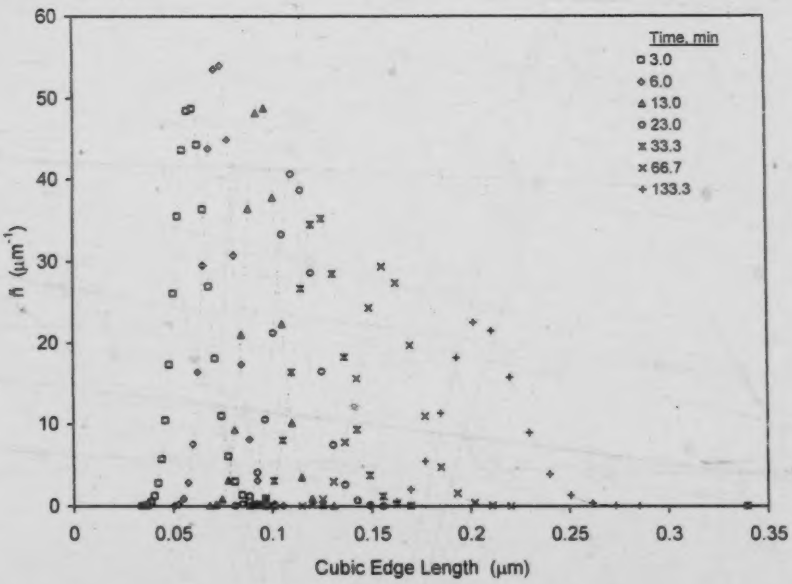

**Figure B.22** CSD time evolution for Variable Feed Rate Analysis I - QS4.06.

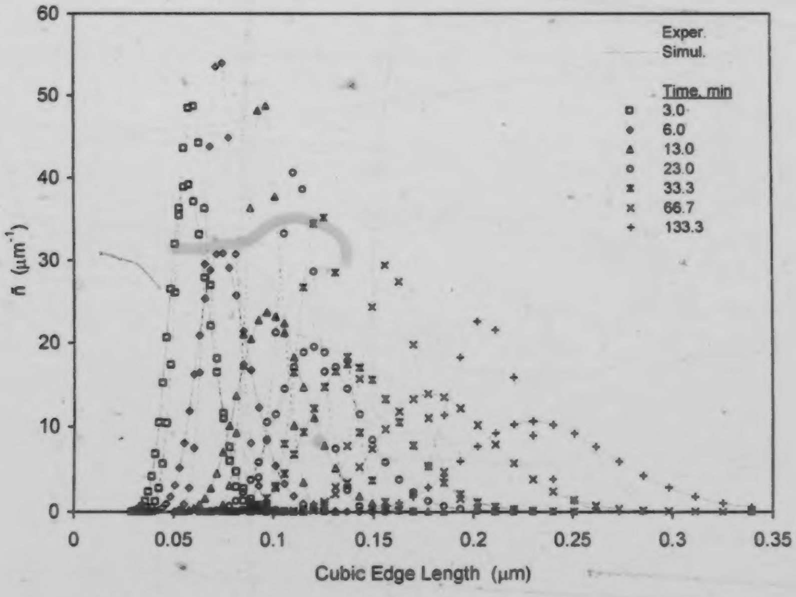

**Figure B.23** Simulated CSD time evolution for Variable Feed Rate Analysis I - QS4.06. Original kinetic parameters were used.

**Table B.25** Descriptive statistics for Variable Feed Rate Analysis I - QS4.06.

| Time (min) | $\mu$ ($\mu$m) | $\sigma$ ($\mu$m) | $\mu_g$ ($\mu$m) | $\sigma_g$ | $N_T$ | AgBr (mol) |
|---|---|---|---|---|---|---|
| 3.0 | 0.061 | 0.008 | 0.060 | 1.146 | 8.9E+15 | 0.068 |
| 6.0 | 0.074 | 0.007 | 0.074 | 1.104 | 9.6E+15 | 0.135 |
| 13.0 | 0.096 | 0.008 | 0.095 | 1.087 | 9.7E+15 | 0.293 |
| 23.0 | 0.113 | 0.010 | 0.112 | 1.091 | 1.0E+16 | 0.519 |
| 33.3 | 0.125 | 0.011 | 0.124 | 1.094 | 1.1E+16 | 0.752 |
| 66.7 | 0.159 | 0.014 | 0.158 | 1.089 | 1.1E+16 | 1.504 |
| 133.3 | 0.207 | 0.018 | 0.206 | 1.089 | 9.9E+15 | 3.008 |

**Table B.26** Experimental conditions for Variable Feed Rate Analysis I - QS4.06.

| Reaction Kettle Geometry | |
|---|---|
| T (m) | 0.2 |
| H (m) | 0.2 |
| D (m) | 0.05 |
| N (rps) | 16.7 |
| $D_P$ (mm) | 0.8 |

| Precipitation Conditions | |
|---|---|
| pBr | 2.55 |
| gel (wt%) | 3.0 |
| $C_f$ (M) | 2.0 |
| $Q_f$ ($m^3\ s^{-1}$) | 1.9E-07 |
| Surface feed point | |

### *B.3.7 QS4.07*

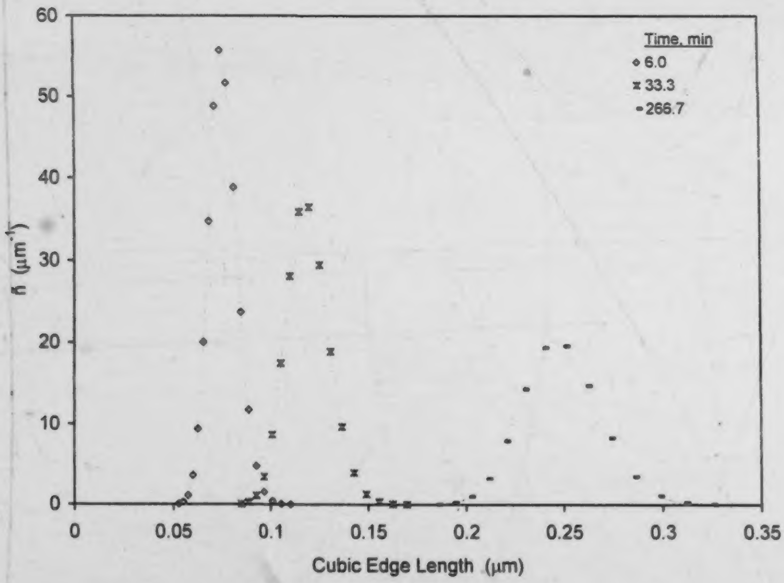

**Figure B.24** CSD time evolution for Variable Feed Rate Analysis I - QS4.07.

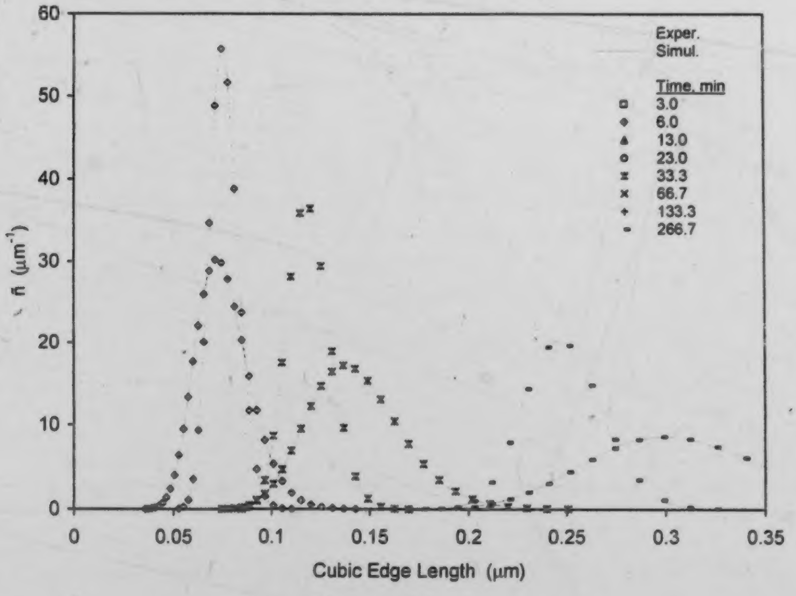

**Figure B.25** Simulated CSD time evolution for Variable Feed Rate Analysis I - QS4.07. Original kinetic parameters were used.

**Table B.27** Descriptive statistics for Variable Feed Rate Analysis I - QS4.07.

| Time (min) | $\mu$ ($\mu$m) | $\sigma$ ($\mu$m) | $\mu_g$ ($\mu$m) | $\sigma_g$ | $N_T$ | AgBr (mol) |
|---|---|---|---|---|---|---|
| 3.0 | | | | | | |
| 6.0 | 0.076 | 0.007 | 0.076 | 1.100 | 4.4E+15 | 0.066 |
| 13.0 | | | | | | |
| 23.0 | | | | | | |
| 33.3 | 0.119 | 0.011 | 0.119 | 1.095 | 6.3E+15 | 0.367 |
| 66.7 | | | | | | |
| 133.3 | | | | | | |
| 266.7 | 0.248 | 0.020 | 0.247 | 1.083 | 5.6E+15 | 2.934 |

**Table B.28** Experimental conditions for Variable Feed Rate Analysis I - QS4.07.

| Reaction Kettle Geometry | |
|---|---|
| T (m) | 0.2 |
| H (m) | 0.2 |
| D (m) | 0.05 |
| N (rps) | 16.7 |
| $D_P$ (mm) | 0.8 |

| Precipitation Conditions | |
|---|---|
| pBr | 2.55 |
| gel (wt%) | 3.0 |
| $C_f$ (M) | 2.0 |
| $Q_f$ ($m^3\ s^{-1}$) | 9.2E-08 |
| Surface feed point | |

## B.4 Variable Feed Pipe Diameter Mesomixing Analysis I

### B.4.1 DS4.01

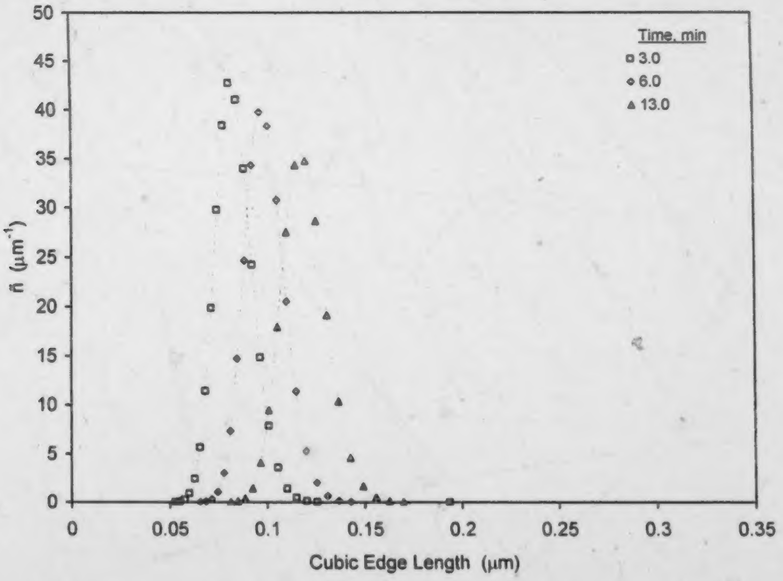

**Figure B.26** CSD time evolution for Variable Feed Pipe Diameter Analysis I - DS4.01.

**Table B.29** Descriptive statistics for Variable Feed Pipe Diameter Analysis I - DS4.01.

| Time (min) | $\mu$ ($\mu$m) | $\sigma$ ($\mu$m) | $\mu_g$ ($\mu$m) | $\sigma_g$ | $N_T$ | AgBr (mol) |
|---|---|---|---|---|---|---|
| 3.0 | 0.084 | 0.009 | 0.083 | 1.119 | 3.4E+16 | 0.691 |
| 6.0 | 0.099 | 0.010 | 0.099 | 1.106 | 4.1E+16 | 1.382 |
| 13.0 | 0.119 | 0.011 | 0.119 | 1.100 | 5.1E+16 | 2.995 |

**Table B.30** Experimental conditions for Variable Feed Pipe Diameter Analysis I - DS4.01.

| Reaction Kettle Geometry | |
|---|---|
| T (m) | 0.2 |
| H (m) | 0.2 |
| D (m) | 0.05 |
| N (rps) | 16.7 |
| $D_P$ (mm) | 0.8 |

| Precipitation Conditions | |
|---|---|
| pBr | 2.55 |
| gel (wt%) | 3.0 |
| $C_f$ (M) | 2.0 |
| $Q_f$ ($m^3$ $s^{-1}$) | 1.9E-06 |
| Surface feed point | |

## *B.4.2 DS4.02*

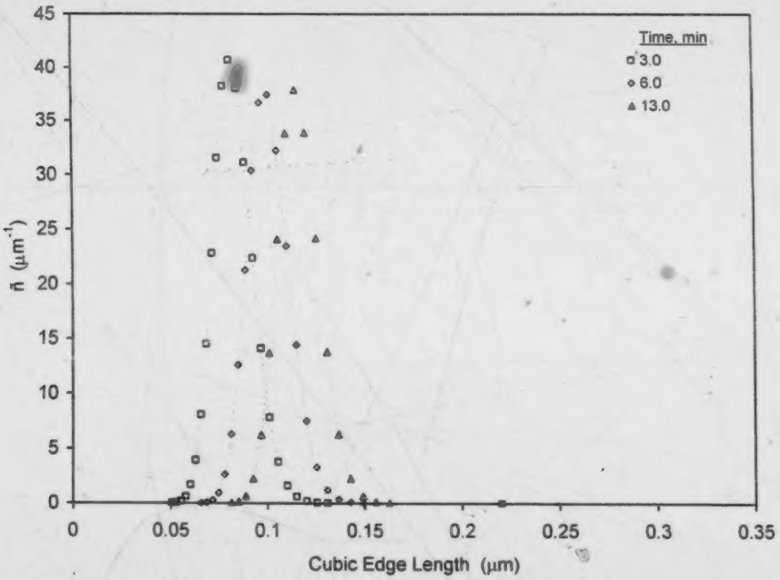

**Figure B.27** CSD time evolution for Variable Feed Pipe Diameter Analysis I - DS4.02.

**Table B.31** Descriptive statistics for Variable Feed Pipe Diameter Analysis I - DS4.02.

| Time (min) | $\mu$ ($\mu$m) | $\sigma$ ($\mu$m) | $\mu_g$ ($\mu$m) | $\sigma_g$ | $N_T$ | AgBr (mol) |
|---|---|---|---|---|---|---|
| 3.0 | 0.083 | 0.010 | 0.082 | 1.127 | 3.5E+16 | 0.691 |
| 6.0 | 0.101 | 0.011 | 0.100 | 1.111 | 3.9E+16 | 1.382 |
| 13.0 | 0.116 | 0.011 | 0.116 | 1.096 | 5.5E+16 | 2.995 |

**Table B.32** Experimental conditions for Variable Feed Pipe Diameter Analysis I - DS4.02.

| Reaction Kettle Geometry | |
|---|---|
| T (m) | 0.2 |
| H (m) | 0.2 |
| D (m) | 0.05 |
| N (rps) | 16.7 |
| $D_P$ (mm) | 4.8 |

| Precipitation Conditions | |
|---|---|
| pBr | 2.55 |
| gel (wt%) | 3.0 |
| $C_f$ (M) | 2.0 |
| $Q_f$ ($m^3 s^{-1}$) | 1.9E-06 |
| Surface feed point | |

## B.5 Variable Feed Pipe Diameter Mesomixing Analysis II

### B.5.1 DS4.11

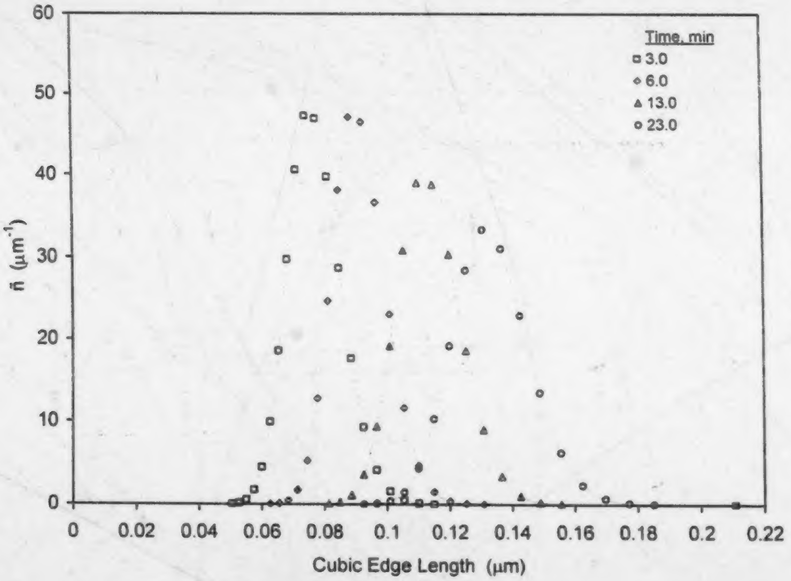

**Figure B.28** CSD time evolution for Variable Feed Pipe Diameter Analysis II - DS4.11.

**Table B.33** Descriptive statistics for Variable Feed Pipe Diameter Analysis II - DS4.11.

| Time (min) | $\mu$ ($\mu$m) | $\sigma$ ($\mu$m) | $\mu_g$ ($\mu$m) | $\sigma_g$ | $N_T$ | AgBr (mol) |
|---|---|---|---|---|---|---|
| 3.0 | 0.077 | 0.008 | 0.077 | 1.115 | 2.5E+16 | 0.392 |
| 6.0 | 0.091 | 0.008 | 0.091 | 1.096 | 3.0E+16 | 0.785 |
| 13.0 | 0.114 | 0.010 | 0.113 | 1.092 | 3.4E+16 | 1.700 |
| 23.0 | 0.134 | 0.012 | 0.133 | 1.094 | 3.7E+16 | 3.008 |

**Table B.34** Experimental conditions for Variable Feed Pipe Diameter Analysis II - DS4.11.

| Reaction Kettle Geometry | |
|---|---|
| T (m) | 0.2 |
| H (m) | 0.2 |
| D (m) | 0.05 |
| N (rps) | 16.7 |
| $D_P$ (mm) | 0.8 |

| Precipitation Conditions | |
|---|---|
| pBr | 2.55 |
| gel (wt%) | 3.0 |
| $C_f$ (M) | 2.0 |
| $Q_f$ ($m^3$ $s^{-1}$) | 1.1E-06 |
| Surface feed point | |

## B.5.2 DS4.12

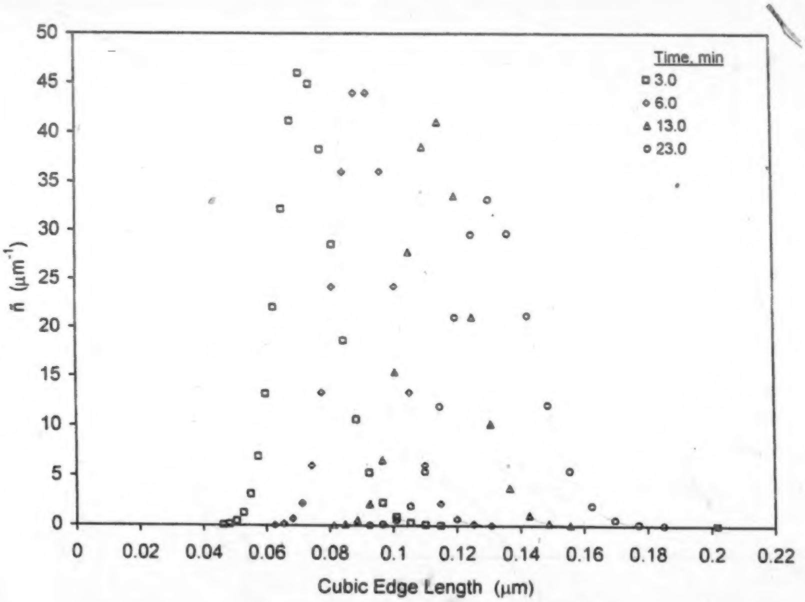

**Figure B.29** CSD time evolution for Variable Feed Pipe Diameter Analysis II - DS4.12.

**Table B.35** Descriptive statistics for Variable Feed Pipe Diameter Analysis II - DS4.12.

| Time (min) | $\mu$ ($\mu$m) | $\sigma$ ($\mu$m) | $\mu_g$ ($\mu$m) | $\sigma_g$ | $N_T$ | AgBr (mol) |
|---|---|---|---|---|---|---|
| 3.0 | 0.074 | 0.009 | 0.073 | 1.126 | 2.8E+16 | 0.392 |
| 6.0 | 0.092 | 0.009 | 0.091 | 1.102 | 2.9E+16 | 0.785 |
| 13.0 | 0.115 | 0.010 | 0.114 | 1.088 | 3.3E+16 | 1.700 |
| 23.0 | 0.133 | 0.012 | 0.132 | 1.096 | 3.7E+16 | 3.008 |

**Table B.36** Experimental conditions for Variable Feed Pipe Diameter Analysis II - DS4.12.

| Reaction Kettle Geometry | |
|---|---|
| T (m) | 0.2 |
| H (m) | 0.2 |
| D (m) | 0.05 |
| N (rps) | 16.7 |
| $D_P$ (mm) | 3.2 |

| Precipitation Conditions | |
|---|---|
| pBr | 2.55 |
| gel (wt%) | 3.0 |
| $C_f$ (M) | 2.0 |
| $Q_f$ ($m^3$ $s^{-1}$) | 1.1E-06 |
| Surface feed point | |

# Appendix C

## Data Treatment and Statistical Transformations

# Appendix C

**Data Treatment and Statistical Transformations** 252

**C.1 Data Treatment** 255
- *C.1.1 Representing the Empirical Distribution* 255
  - The Normal Density Distribution 255
  - The Log-Normal Density Distribution 256
- *C.1.2 Replicating the Empirical Distribution* 257
- *C.1.3 A Special Case - Multimodal Distributions* 257
  - *Example 1: Multimodal Data Treatment* 258

**C.2 Statistical Transformations** 263

**C.3 Nomenclature** 265

## Table of Tables

| | | |
|---|---|---|
| Table C.1 | Empirical size distribution data for micromixing experiment MM12. a) Small mode, b) Large mode. | 258 |
| Table C.2 | Adjustable Parameters used to represent the empirical sub-distributions. | 259 |
| Table C.3 | Calculation of the Empirical, Normal and Log-Normal density distributions. | 260 |
| Table C.4 | Replication of the Empirical size distribution using both the Normal and Log-Normal composite density distributions. | 262 |

## Table of Figures

| | | |
|---|---|---|
| Figure C.1 | Graphical representation of the Empirical, Normal and Log-Normal composite density distributions. | 261 |
| Figure C.2 | Graphical comparison of the replicated Empirical size distribution as determined by the Normal and Log-Normal composite density distributions. | 263 |

## C.1 Data Treatment

Often crystal sizing techniques, such as Ultrafine Electron Image Analysis, measure the frequency of crystals ($N_i$) appearing within each increment of the length scale ($\Delta L_i$). Typically, the measured frequencies are related to the midpoint of each increment ($L_i$). In principle, once this size distribution is obtained all remaining properties of interest are known or can be readily obtained.

### *C.1.1 Representing the Empirical Distribution*

A variety of one-dimensional unimodal density distribution functions are known that can be used to represent the empirical crystal size distribution. Such functions require a minimum of two independent adjustable parameters to describe both the mean ($\mu$) and variance ($\sigma^2$) of the distribution. Usually if the function has more than two parameters, they are difficult to determine from the experimental data. In the following description the data treatment will be given for the commonly used normal and log-normal density distributions.

**The Normal Density Distribution**

The normal density distribution provides a simple description of the relative frequency associated with a given length. Specifically, this distribution is used to calculate an area that represents the normalized frequency of crystals appearing in some length interval. This distribution can be given as

$$\tilde{n}(L) = \frac{1}{\sigma\sqrt{2\pi}} \exp\left[-\left(\frac{L-\mu}{\sigma\sqrt{2}}\right)^2\right] \tag{C.1}$$

$$\sigma = \sqrt{\frac{\sum_{i=0}^{\infty} N_i (L_i - \mu)^2}{\sum_{i=0}^{\infty} N_i - 1}} \tag{C.2}$$

$$\mu = \frac{\sum_{i=0}^{\infty} N_i L_i}{\sum_{i=0}^{\infty} N_i} \qquad (\text{C.3})$$

where σ and μ, respectively are the standard deviation and mean, which are measures of the uniformity and absolute size of the distribution.

## The Log-Normal Density Distribution

The log-normal density distribution is merely a normal density distribution in terms of ln L. Again, this distribution provides a simple description of the relative frequency associated with a given length. And again, this distribution is used to calculate an area that represents the normalized frequency of crystals appearing in some length interval. This distribution can be given as

$$\tilde{n}(L) = \frac{1}{L\sqrt{2\pi}\ln\sigma_g}\exp\left[-\left(\frac{\ln L/\mu_g}{\sqrt{2}\ln\sigma_g}\right)^2\right] \qquad (\text{C.4})$$

$$\sigma_g = \exp\left(\sqrt{\frac{\sum_{i=0}^{\infty} N_i\left(\ln L_i/\mu_g\right)^2}{\sum_{i=0}^{\infty} N_i - 1}}\right) \qquad (\text{C.5})$$

$$\mu_g = \exp\left(\frac{\sum_{i=0}^{\infty} N_i \ln L_i}{\sum_{i=0}^{\infty} N_i}\right) \qquad (\text{C.6})$$

where $\sigma_g$ and $\mu_g$, respectively are the geometric standard deviation and geometric mean, which are measures of the uniformity and absolute size of the distribution.

### C.1.2 Replicating the Empirical Distribution

Often in modeling it is desirable to identically replicate or reconstruct the empirical distribution on various length scales based on the variance and mean of the distribution. To begin, the normalized frequency of crystals ($\tilde{N}_i$) appearing within a given interval ($\Delta L_i$) is found by integrating the appropriate size density distribution over the interval

$$\tilde{N}_i = \int_{L_i-\Delta L_i/2}^{L_i+\Delta L_i/2} \tilde{n}\,dL \qquad (C.7)$$

where $L_i$ is the midpoint of $\Delta L_i$. Then the absolute frequency of crystals ($N_i$) appearing in the interval is found by multiplying the relative frequency and the absolute crystal count ($N_T$).

$$N_i = \tilde{N}_i N_T \qquad (C.8)$$

Refer to Appendix A for further details on the possible length scale discretizations.

### C.1.3 A Special Case - Multimodal Distributions

In the preceding description of data treatment it is assumed that the crystal size distribution is unimodal. To account for multimodal size distributions a third parameter is required to properly represent the entire data. This parameter is a weighting function that effectively renormalizes the individual density distributions according to their respective relative crystal counts. The multimodal density distribution is defined as

$$\tilde{n}(L) = \sum_{j=1}^{J} w_j \tilde{n}_j(L) \qquad (C.9)$$

where $w_j$ is the weighting function given by

$$w_j = \frac{N_{T,j}}{\sum_{j=1}^{J} N_{T,j}} \qquad (C.10)$$

### *Example 1: Multimodal Data Treatment*

Consider the bimodal size distribution data for the seed crystals used the micromixing experiment MM12.

**Table C.1** Empirical size distribution data for micromixing experiment MM12. a) Small mode, b) Large mode.

a)

| $L_i$ (μm) | $N_i$ ($10^{-10}$) |
|---|---|
| 0.05590 | 0.00263 |
| 0.06096 | 0.01975 |
| 0.06648 | 0.03028 |
| 0.07250 | 0.06846 |
| 0.07906 | 0.10137 |
| 0.08621 | 0.20800 |
| 0.09402 | 0.32385 |
| 0.10252 | 0.46076 |
| 0.11180 | 0.49104 |
| 0.12192 | 0.50420 |
| 0.13296 | 0.35808 |
| 0.14499 | 0.20010 |
| 0.15811 | 0.06977 |
| 0.17242 | 0.01053 |
| 0.18803 | 0 |
| 0.20505 | 0 |
| 0.22361 | 0 |
| 0.24384 | 0 |
| 0.26591 | 0 |
| 0.28998 | 0 |
| 0.31623 | 0 |
| 0.34485 | 0 |
| Total | 2.84880 |

b)

| CEL (μm) | $N_i$ ($10^{-10}$) |
|---|---|
| 0.37606 | 0 |
| 0.41010 | 0 |
| 0.44721 | 0 |
| 0.48769 | 0 |
| 0.53183 | 0.00263 |
| 0.57996 | 0.01316 |
| 0.63246 | 0.07767 |
| 0.68970 | 0.48840 |
| 0.75212 | 0.04871 |
| 0.82019 | 0 |
| 0.89443 | 0 |
| Total | 0.63058 |

The adjustable parameters used to represent the empirical sub-distributions can be determined using the definitions ( C.2 ), ( C.3 ), ( C.5 ) and ( C.6).

**Table C.2** Adjustable Parameters used to represent the empirical sub-distributions.

| Mode | $\mu$ (µm) | $\sigma$ (µm) | $\mu_g$ (µm) | $\sigma_g$ |
|---|---|---|---|---|
| Small | 0.11156 | 0.02082 | 0.10966 | 1.20325 |
| Large | 0.68452 | 0.03214 | 0.68377 | 1.04805 |

Given the adjustable parameters, the respective density sub-distributions can be determined according to Equations ( C.1 ) or ( C.4 ), and the composite density distribution according to Equation ( C.9 ).

$$\tilde{n}(L) = w_s \tilde{n}_s(L) + w_L \tilde{n}_L(L)$$

where the weighting function ( C.10 ) for the small and large modes is found to be

$$w_S = \frac{2.85\text{x}10^{10}}{2.85\text{x}10^{10} + 0.63\text{x}10^{10}} = 0.82$$

$$w_L = 1 - w_S = 0.18$$

This composite density distribution can then be compared to the normalized density distribution obtained directly from the data according to Equation ( C.7 ).

$$\tilde{n} = \frac{\tilde{N}_i}{\Delta L_i}$$

Where $\Delta L_i = 2\frac{r-1}{r+1}L_i$, and r is the common geometric factor (see Appendix A).

**Table C.3** Calculation of the Empirical, Normal and Log-Normal density distributions.

| $L_i$ (μm) | $\Delta L_i$ (μm) | $N_i$ ($10^{-10}$) | $\tilde{N}_i$ ($\Delta N_i/N_T$) | Experiment $\tilde{n}_i$ (μm$^{-1}$) | Normal $\tilde{n}_i$ (μm$^{-1}$) | Log-Normal $\tilde{n}_i$ (μm$^{-1}$) |
|---|---|---|---|---|---|---|
| 0.05590 | 0.00484 | 0.00263 | 0.00076 | 0.15633 | 0.44037 | 0.04165 |
| 0.06096 | 0.00528 | 0.01975 | 0.00568 | 1.07517 | 0.81873 | 0.18836 |
| 0.06648 | 0.00576 | 0.03028 | 0.00870 | 1.51176 | 1.50523 | 0.68410 |
| 0.07250 | 0.00628 | 0.06846 | 0.01967 | 3.13423 | 2.69918 | 1.99532 |
| 0.07906 | 0.00685 | 0.10137 | 0.02913 | 4.25588 | 4.63946 | 4.67386 |
| 0.08621 | 0.00747 | 0.20800 | 0.05978 | 8.00806 | 7.47863 | 8.79238 |
| 0.09402 | 0.00814 | 0.32385 | 0.09308 | 11.43343 | 11.00191 | 13.28328 |
| 0.10252 | 0.00888 | 0.46076 | 0.13243 | 14.91697 | 14.28066 | 16.11657 |
| 0.11180 | 0.00968 | 0.49104 | 0.14113 | 14.57783 | 15.68859 | 15.70390 |
| 0.12192 | 0.01056 | 0.50420 | 0.14491 | 13.72631 | 13.86026 | 12.28884 |
| 0.13296 | 0.01151 | 0.35808 | 0.10291 | 8.93913 | 9.24991 | 7.72293 |
| 0.14499 | 0.01255 | 0.20010 | 0.05751 | 4.58080 | 4.32044 | 3.89781 |
| 0.15811 | 0.01369 | 0.06977 | 0.02005 | 1.46469 | 1.28707 | 1.57989 |
| 0.17242 | 0.01493 | 0.01053 | 0.00303 | 0.20274 | 0.21847 | 0.51428 |
| 0.18803 | 0.01628 | 0 | 0 | 0 | 0.01843 | 0.13445 |
| 0.20505 | 0.01775 | 0 | 0 | 0 | 0.00066 | 0.02823 |
| 0.22361 | 0.01936 | 0 | 0 | 0 | 0.00001 | 0.00476 |
| 0.24384 | 0.02111 | 0 | 0 | 0 | 0 | 0.00064 |
| 0.26591 | 0.02303 | 0 | 0 | 0 | 0 | 0.00007 |
| 0.28998 | 0.02511 | 0 | 0 | 0 | 0 | 0.00001 |
| 0.31623 | 0.02738 | 0 | 0 | 0 | 0 | 0 |
| 0.34485 | 0.02986 | 0 | 0 | 0 | 0 | 0 |
| 0.37606 | 0.03256 | 0 | 0 | 0 | 0 | 0 |
| 0.41010 | 0.03551 | 0 | 0 | 0 | 0 | 0 |
| 0.44721 | 0.03872 | 0 | 0 | 0 | 0 | 0 |
| 0.48769 | 0.04223 | 0 | 0 | 0 | 0 | 0 |
| 0.53183 | 0.04605 | 0.00263 | 0.00076 | 0.01643 | 0.00003 | 0.00000 |
| 0.57996 | 0.05022 | 0.01316 | 0.00378 | 0.07534 | 0.01134 | 0.00565 |
| 0.63246 | 0.05476 | 0.07767 | 0.02232 | 0.40763 | 0.60587 | 0.61204 |
| 0.68970 | 0.05972 | 0.48840 | 0.14037 | 2.35047 | 2.22032 | 2.19615 |
| 0.75212 | 0.06513 | 0.04871 | 0.01400 | 0.21496 | 0.24637 | 0.26083 |
| 0.82019 | 0.07102 | 0 | 0 | 0 | 0.00030 | 0.00103 |
| 0.89443 | 0.07745 | 0 | 0 | 0 | 0 | 0 |
| Total |  | 3.47938 | 1.00000 |  |  |  |

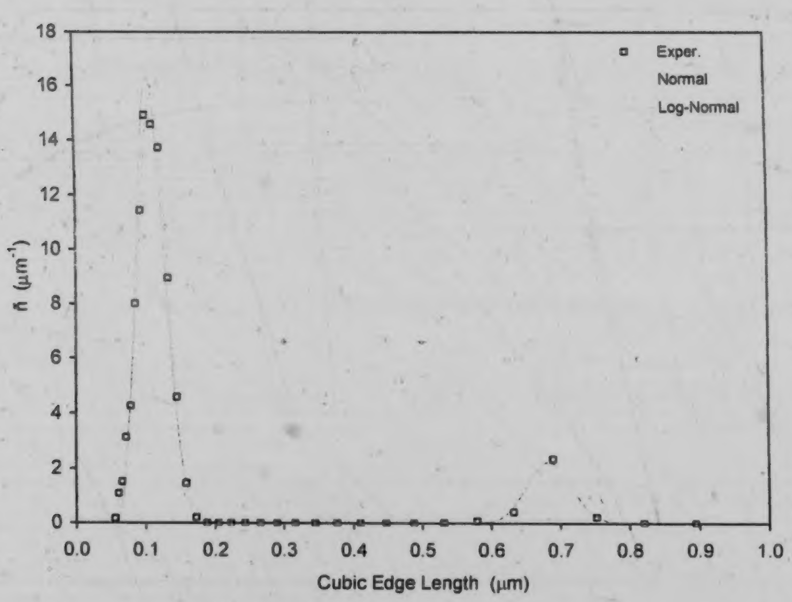

**Figure C.1** Graphical representation of the Empirical, Normal and Log-Normal composite density distributions.

The empirical crystal size distribution can be replicated from either the normal or log-normal composite density distributions by Equation ( C.7 ), where ñ is given by Equation ( C.9 ).

**Table C.4** Replication of the Empirical size distribution using both the Normal and Log-Normal composite density distributions.

| $L_i$ ($\mu$m) | $\Delta L_i$ ($\mu$m) | Experiment $N_i$ ($10^{-10}$) | Normal $N_i$ ($10^{-10}$) | Log-Normal $N_i$ ($10^{-10}$) |
|---|---|---|---|---|
| 0.05590 | 0.00484 | 0.00263 | 0.00742 | 0.00070 |
| 0.06096 | 0.00528 | 0.01975 | 0.01504 | 0.00346 |
| 0.06648 | 0.00576 | 0.03028 | 0.03015 | 0.01370 |
| 0.07250 | 0.00628 | 0.06846 | 0.05895 | 0.04358 |
| 0.07906 | 0.00685 | 0.10137 | 0.11050 | 0.11132 |
| 0.08621 | 0.00747 | 0.20800 | 0.19425 | 0.22837 |
| 0.09402 | 0.00814 | 0.32385 | 0.31162 | 0.37624 |
| 0.10252 | 0.00888 | 0.46076 | 0.44110 | 0.49781 |
| 0.11180 | 0.00968 | 0.49104 | 0.52845 | 0.52897 |
| 0.12192 | 0.01056 | 0.50420 | 0.50912 | 0.45140 |
| 0.13296 | 0.01151 | 0.35808 | 0.37052 | 0.30936 |
| 0.14499 | 0.01255 | 0.20010 | 0.18873 | 0.17027 |
| 0.15811 | 0.01369 | 0.06977 | 0.06131 | 0.07526 |
| 0.17242 | 0.01493 | 0.01053 | 0.01135 | 0.02672 |
| 0.18803 | 0.01628 | 0 | 0.00104 | 0.00762 |
| 0.20505 | 0.01775 | 0 | 0.00004 | 0.00174 |
| 0.22361 | 0.01936 | 0 | 0 | 0.00032 |
| 0.24384 | 0.02111 | 0 | 0 | 0.00005 |
| 0.26591 | 0.02303 | 0 | 0 | 0.00001 |
| 0.28998 | 0.02511 | 0 | 0 | 0 |
| 0.31623 | 0.02738 | 0 | 0 | 0 |
| 0.34485 | 0.02986 | 0 | 0 | 0 |
| 0.37606 | 0.03256 | 0 | 0 | 0 |
| 0.41010 | 0.03551 | 0 | 0 | 0 |
| 0.44721 | 0.03872 | 0 | 0 | 0 |
| 0.48769 | 0.04223 | 0 | 0 | 0 |
| 0.53183 | 0.04605 | 0.00263 | 0 | 0 |
| 0.57996 | 0.05022 | 0.01316 | 0.00198 | 0.00099 |
| 0.63246 | 0.05476 | 0.07767 | 0.11545 | 0.11662 |
| 0.68970 | 0.05972 | 0.48840 | 0.46136 | 0.45634 |
| 0.75212 | 0.06513 | 0.04871 | 0.05583 | 0.05910 |
| 0.82019 | 0.07102 | 0 | 0.00008 | 0.00025 |
| 0.89443 | 0.07745 | 0 | 0 | 0 |
| Total | | 3.47938 | 3.47430 | 3.48020 |

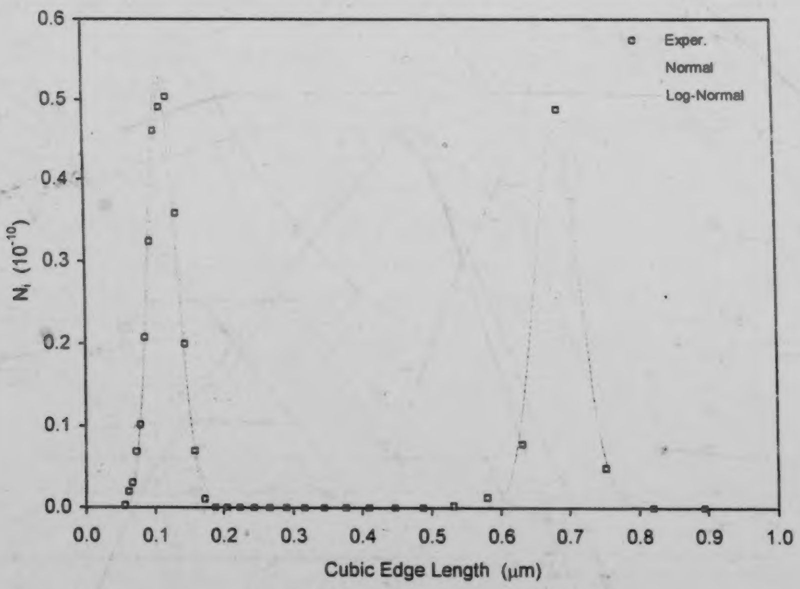

**Figure C.2** Graphical comparison of the replicated Empirical size distribution as determined by the Normal and Log-Normal composite density distributions.

## C.2 Statistical Transformations

Of the two density distributions presented above, it is likely that one form will be more suitable for representing the empirical data. Typically, plotting the various distributions is the easiest method for evaluating the goodness of fit for the given data. However, often only one set of parameters is reported. The relations ( C.11 ) through ( C.14 ) provide the necessary parameter transformations for converting between the normal and log-normal density distributions.

$$\mu = \mu_g \exp\left[\frac{1}{2}(\ln \sigma_g)^2\right] \qquad \text{( C.11 )}$$

$$\sigma = \sqrt{\mu_g^{\,2} \sigma_g^{\ln \sigma_g}\left(\sigma_g^{\ln \sigma_g} - 1\right)} \qquad \text{( C.12 )}$$

$$\mu_g = \frac{\mu}{\sqrt{\left(\sigma/\mu\right)^2 + 1}} \qquad (C.13)$$

$$\sigma_g = \exp\left[\sqrt{\ln\left(\left(\sigma/\mu\right)^2 + 1\right)}\right] \qquad (C.14)$$

## C.3 Nomenclature

| | |
|---|---|
| $\Delta L_i$ | spacing of *ith* size interval, m |
| $L_i$ | characteristic length of *ith* size interval, m |
| $\tilde{n}$ | relative crystal count per size interval per unit size, $(\tilde{N}/\Delta L)$, $m^{-3}$ |
| $N_i$ | crystal count per size interval $(\Delta N)$, $m^{-3}$ |
| $\tilde{N}_i$ | relative crystal count per size interval, $(\Delta N/N_T)$, $m^{-3}$ |
| $N_T$ | total crystal count, $m^{-3}$ |
| $r$ | common geometric factor |
| $w_j$ | weighting function for the *jth* sub-distribution |

***Greek***

| | |
|---|---|
| $\mu$ | mean crystal length, m |
| $\mu_g$ | geometric mean crystal length, m |
| $\sigma$ | standard deviation, m |
| $\sigma_g$ | geometric standard deviation, m |

# Appendix D

## Logic Diagrams for PreSim.V50 Source Code

# Appendix D

## Logic Diagrams for PreSim.V50 Source Code 266

**D.1 PreSim.V50** 269
**D.2 Global Variables** 270
**D.3 Read Input** 271
**D.4 Physical Properties** 272
**D.5 Thermodynamic Equilibrium** 273
  *D.5.1 Equilibrium Fit* 273
  *D.5.2 Equilibrium Solver* 274
  *D.5.3 Equilibrium Calculation* 275
  *D.5.4 Equilibrium Output* 276
**D.6 Population Distribution** 277
  *D.6.1 Seed Population* 277
  *D.6.2 Calculate Length Scale* 278
  *D.6.3 Calculate Frequency Distribution* 279
  *D.6.4 Population Solver* 280
**D.7 Eulerian Flow Model** 281
  *D.7.1 EFM Initialization* 281
  *D.7.2 Calculate Feed Flow Rate* 282
  *D.7.3 Calculate Feed Concentration* 283
  *D.7.4 Calculate Zone Flow Rate* 284
  *D.7.5 Calculate Zone Velocity* 285
  *D.7.6 Calculate Zone Dissipation* 286
  *D.7.7 Calculate Zone Turbulent Kinetic Energy* 287
  *D.7.8 Calculate DFV Position* 288
  *D.7.9 Calculate DFV Transit Time* 289
  *D.7.10 Calculate DFV Feed Zone* 290
  *D.7.11 EFM Update* 291
**D.8 Mixing Limit** 292

**D.9 Write Input** 293
**D.10 Initial Conditions** 294
**D.11 DFV Initial Conditions** 295
**D.12 DFV Trajectory** 296
**D.13 DFV Integration** 297
  *D.13.1 DFV Loop* 297
  *D.13.2 DFV Integration* 298
  *D.13.3 DFV Update* 299
  *D.13.4 DFV Tracking Output* 300
**D.14 Kettle Integration** 301
  *D.14.1 Kettle Integration* 301
  *D.14.2 Kettle Output* 302
**D.15 Integrator** 303
  *D.15.1 Integrate* 303
  *D.15.2 Calculate Nucleation Rate* 304
  *D.15.3 Calculate Growth Rate* 305
  *D.15.4 Population Balance* 306
  *D.15.5 Check Population Balance* 307
  *D.15.6 Calculate Consumption Rate* 308
**D.16 Write Output** 309
**D.17 Mass Balance** 310
**D.18 Population Statistics** 311
**D.19 Array Update** 312
**D.20 Statistics** 313
  *D.20.1 Statistics Transformations* 313
  *D.20.2 Calculate Probability* 314
  *D.20.3 Probability Density Function* 315
  *D.20.4 Smooth Function* 316

## D.1 PreSim.V50

- *An Eulerian-Lagrangian model of precipitation, crystal growth, complex species equilibria and turbulent mixing.*

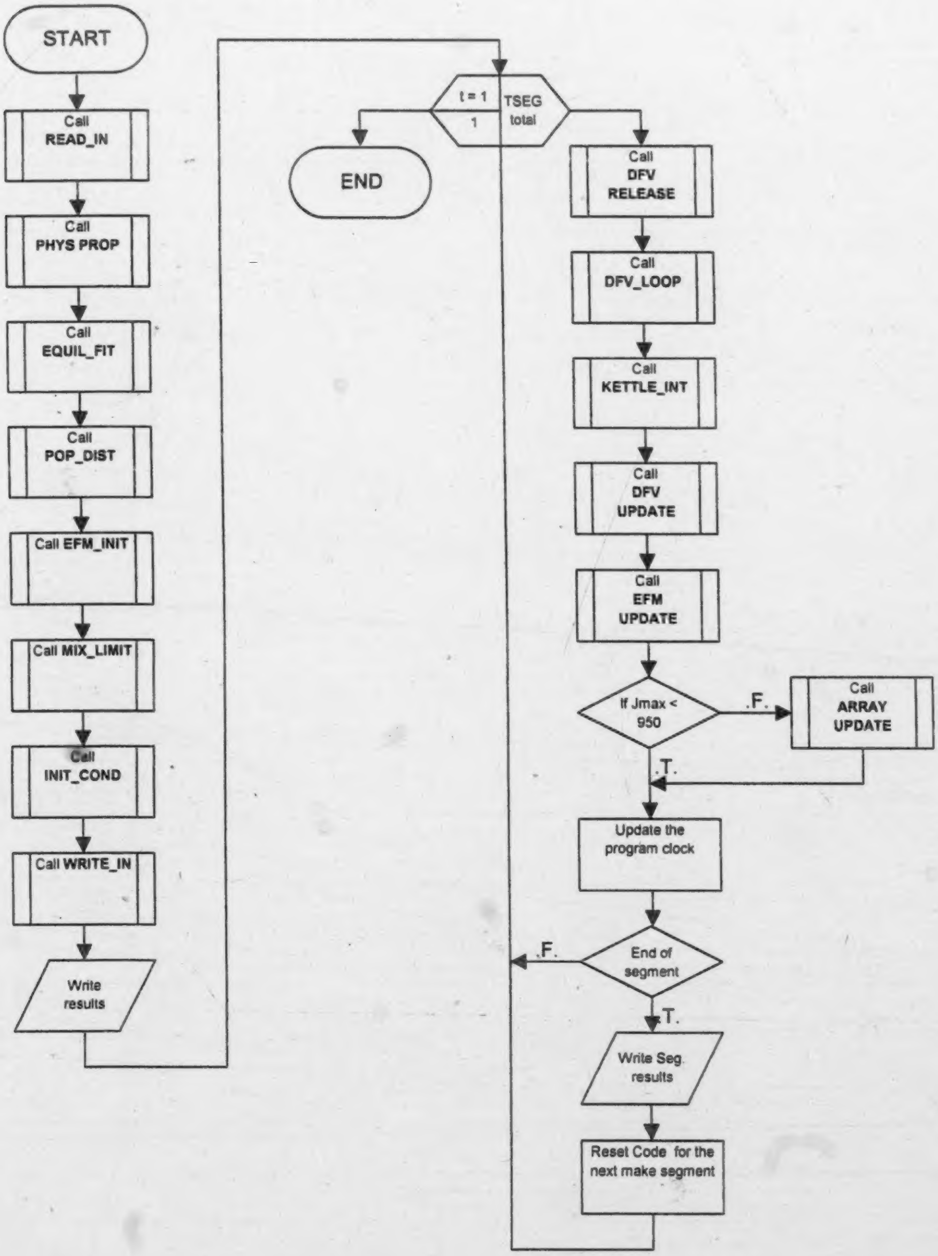
START
Call READ_IN
Call PHYS PROP
Call EQUIL_FIT
Call POP_DIST
Call EFM_INIT
Call MIX_LIMIT
Call INIT_COND
Call WRITE_IN
Write results
t = 1
1
TSEG
total
END
Call DFV RELEASE
Call DFV_LOOP
Call KETTLE_INT
Call DFV UPDATE
Call EFM UPDATE
If Jmax < 950
.F.
Call ARRAY UPDATE
.T.
Update the program clock
End of segment
.F.
.T.
Write Seg. results
Reset Code for the next make segment

## D.2 Global Variables

- *Contains and initializes all global variables for the source code PreSim.V50.*

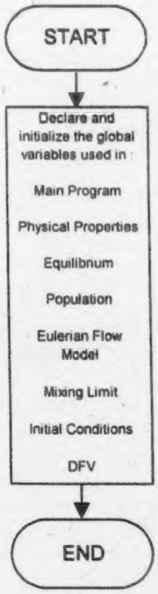
START
Declare and initialize the global variables used in :
Main Program
Physical Properties
Equilibrium
Population
Eulerian Flow Model
Mixing Limit
Initial Conditions
DFV
END

## D.3 Read Input

- *Reads in all necessary information from the user specified input files.*

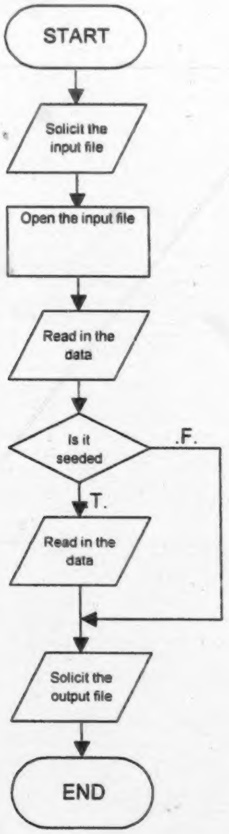
START
Solicit the input file
Open the input file
Read in the data
Is it seeded
.F.
.T.
Read in the data
Solicit the output file
END

## D.4 Physical Properties

- *Determines the constants used in future growth rate calculations, as well as the remaining equilibrium constants.*

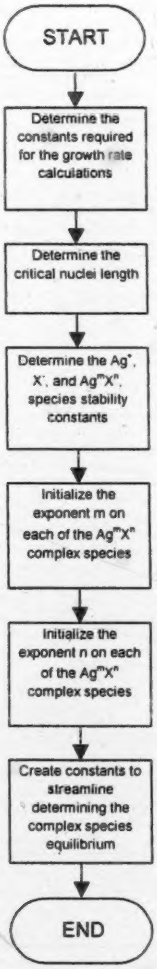
START
Determine the constants required for the growth rate calculations
Determine the critical nuclei length
Determine the $Ag^+$, $X^-$, and $Ag^mX^n$, species stability constants
Initialize the exponent m on each of the $Ag^mX^n$ complex species
Initialize the exponent n on each of the $Ag^mX^n$ complex species
Create constants to streamline determining the complex species equilibrium
END

## D.5 Thermodynamic Equilibrium

### *D.5.1 Equilibrium Fit*

- *Determines the equilibrium silver and halide activities for all possible initial conditions. The calculated data is then compressed by using linear regression.*

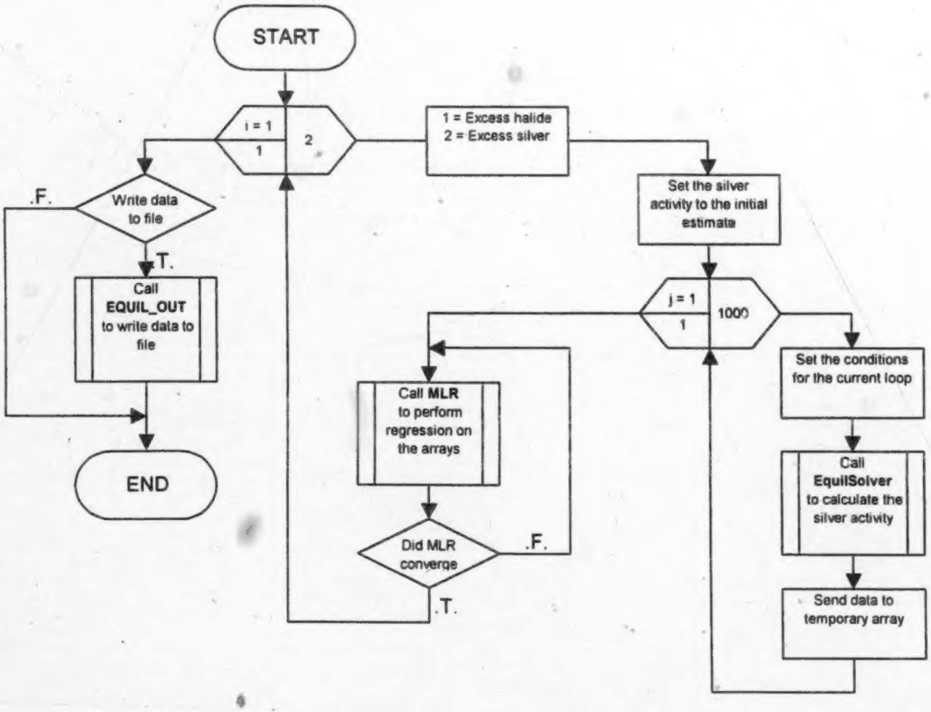
START
i = 1
1
2
1 = Excess halide
2 = Excess silver
Write data to file
.F.
.T.
Call **EQUIL_OUT** to write data to file
END
Set the silver activity to the initial estimate
j = 1
1
1000
Set the conditions for the current loop
Call **EquilSolver** to calculate the silver activity
Send data to temporary array
Call **MLR** to perform regression on the arrays
Did MLR converge
.F.
.T.

### D.5.2 Equilibrium Solver

- *Solves the silver and halide speciation equations for silver activity by using the Newton-Raphson technique.*

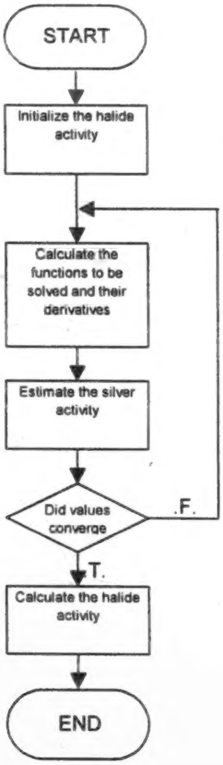
START
Initialize the halide activity
Calculate the functions to be solved and their derivatives
Estimate the silver activity
Did values converge
.F.
.T.
Calculate the halide activity
END

### D.5.3 Equilibrium Calculation

- *Determine all of the species concentrations at equilibrium by using the equilibrium solver if necessary.*

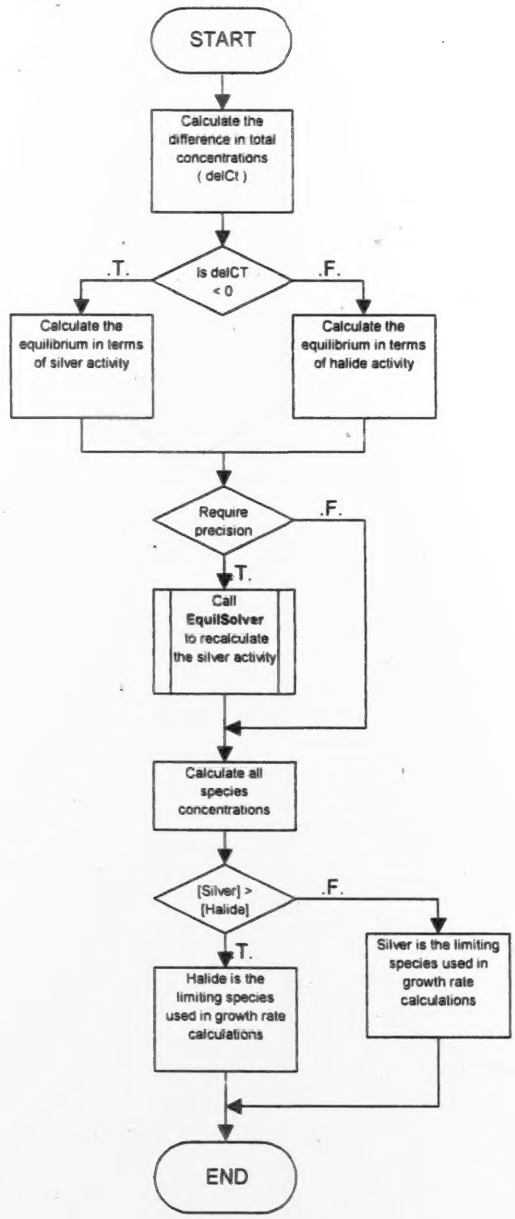
START
Calculate the difference in total concentrations ( delCt )
Is delCT < 0
.T.
.F.
Calculate the equilibrium in terms of silver activity
Calculate the equilibrium in terms of halide activity
Require precision
.F.
.T.
Call **EquilSolver** to recalculate the silver activity
Calculate all species concentrations
[Silver] > [Halide]
.F.
.T.
Halide is the limiting species used in growth rate calculations
Silver is the limiting species used in growth rate calculations
END

### D.5.4 Equilibrium Output

- *Writes the raw and approximated equilibrium data and the maximum error to file, if user requested.*

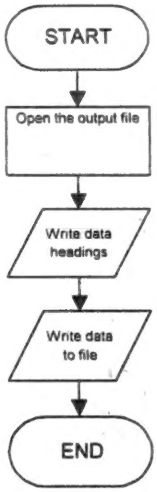
START
Open the output file
Write data headings
Write data to file
END

## D.6 Population Distribution

### *D.6.1 Seed Population*

- *Creates the length scale to be used in describing the crystal size distribution and if necessary creates the seed population.*

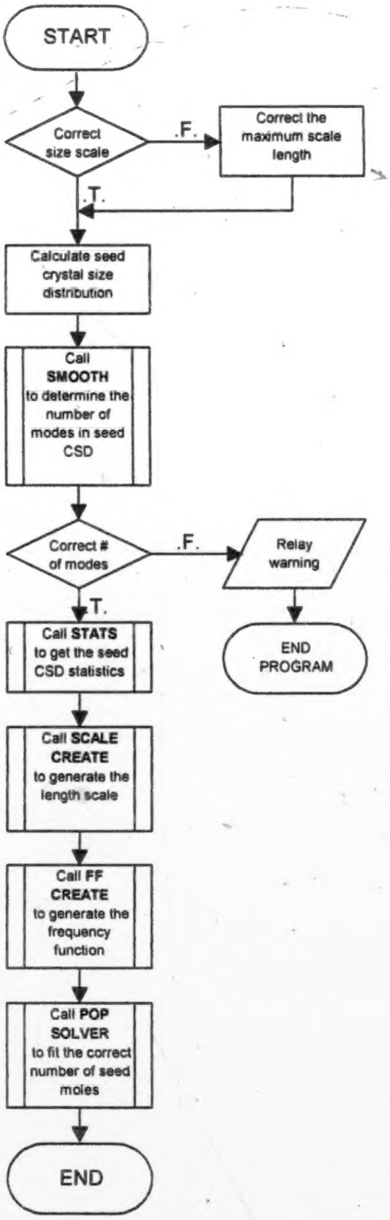
START
Correct size scale
.F.
Correct the maximum scale length
.T.
Calculate seed crystal size distribution
Call **SMOOTH** to determine the number of modes in seed CSD
Correct # of modes
.F.
Relay warning
END PROGRAM
.T.
Call **STATS** to get the seed CSD statistics
Call **SCALE CREATE** to generate the length scale
Call **FF CREATE** to generate the frequency function
Call **POP SOLVER** to fit the correct number of seed moles
END

## D.6.2 Calculate Length Scale

- *Creates a symmetrical geometric length scale about the nucleation bin. The lower extreme of the scale will also fall exactly on zero, and the upper extreme will fall slightly from the maximum length*

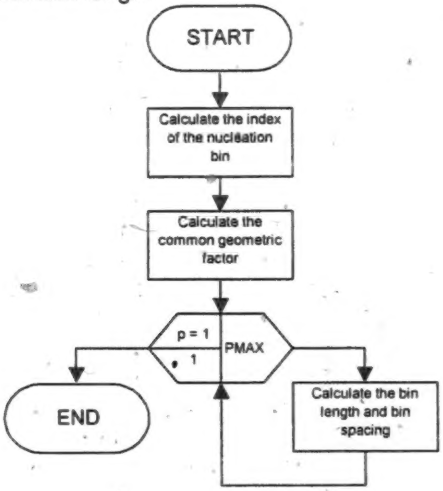
START
Calculate the index of the nucleation bin
Calculate the common geometric factor
p = 1
PMAX
1
Calculate the bin length and bin spacing
END

## D.6.3 Calculate Frequency Distribution

- *Creates a crystal frequency function for the given length scale, with predetermined scale divisions, mode standard deviations and means.*

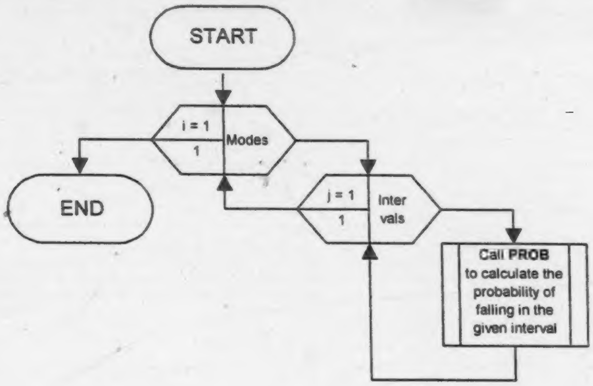
START
i = 1
1
Modes
END
j = 1
1
Inter
vals
Call **PROB** to calculate the probability of falling in the given interval

### D.6.4 Population Solver

- *Determines the number of crystals required in each CSD mode to produce the specified number of silver halide moles.*

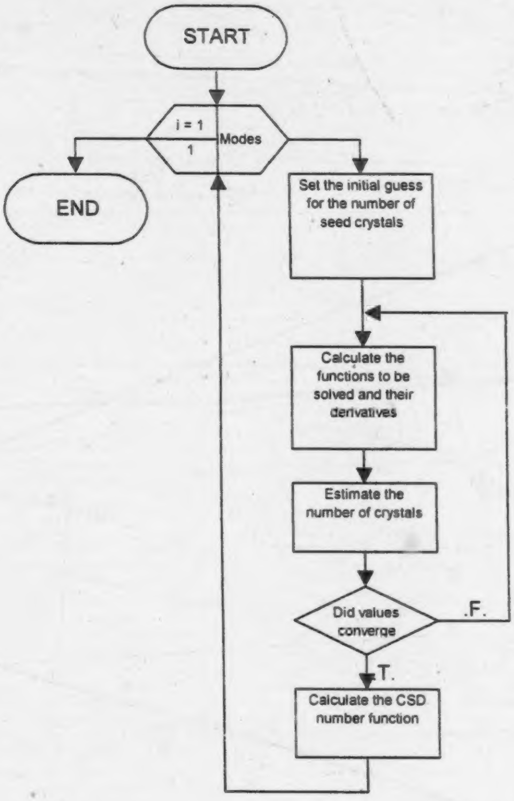
START
i = 1
1
Modes
END
Set the initial guess for the number of seed crystals
Calculate the functions to be solved and their derivatives
Estimate the number of crystals
Did values converge
.F.
.T.
Calculate the CSD number function

## D.7 Eulerian Flow Model

### D.7.1 *EFM Initialization*

- *Define the Eulerian Flow Field and initialize all relevant quantities on a feed free basis.*

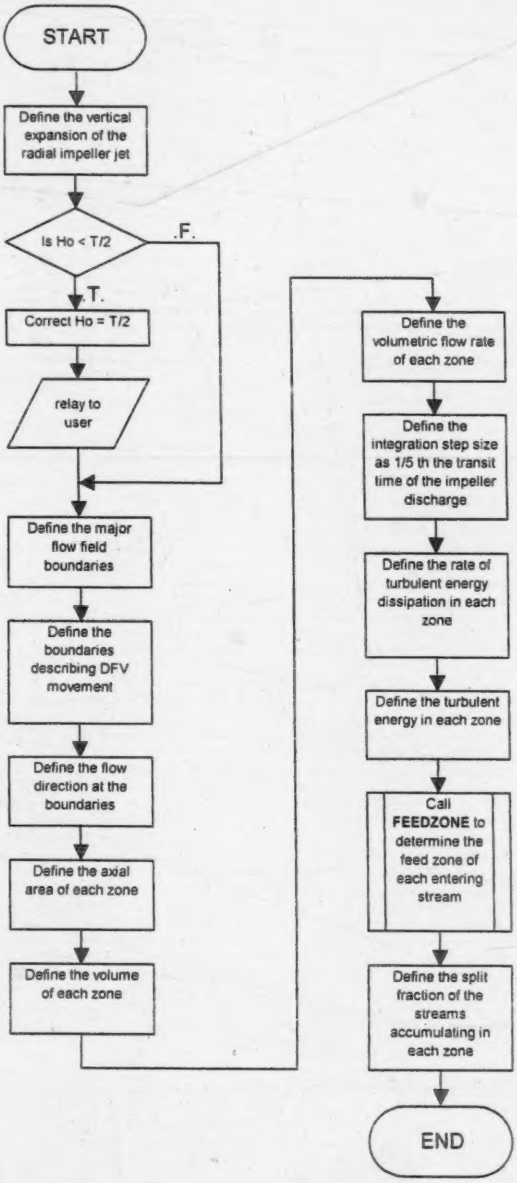
START
Define the vertical expansion of the radial impeller jet
Is Ho < T/2
.F.
.T.
Correct Ho = T/2
relay to user
Define the major flow field boundaries
Define the boundaries describing DFV movement
Define the flow direction at the boundaries
Define the axial area of each zone
Define the volume of each zone
Define the volumetric flow rate of each zone
Define the integration step size as 1/5 th the transit time of the impeller discharge
Define the rate of turbulent energy dissipation in each zone
Define the turbulent energy in each zone
Call FEEDZONE to determine the feed zone of each entering stream
Define the split fraction of the streams accumulating in each zone
END

## D.7.2 Calculate Feed Flow Rate

- *Calculates the volumetric flow rate of each feed stream as a function of time using linear interpolation.*

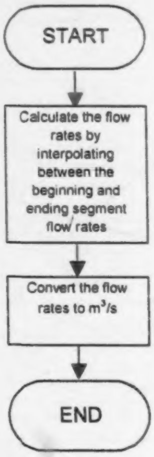
START
Calculate the flow rates by interpolating between the beginning and ending segment flow rates
Convert the flow rates to m³/s
END

### D.7.3 Calculate Feed Concentration

- *Calculates the concentration of each feed stream as a function of time using linear interpolation.*

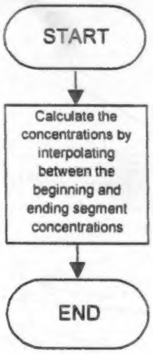
START
Calculate the concentrations by interpolating between the beginning and ending segment concentrations
END

### D.7.4 Calculate Zone Flow Rate

- *Calculates the volumetric flow rate in each EFM zone as a function of position if necessary.*

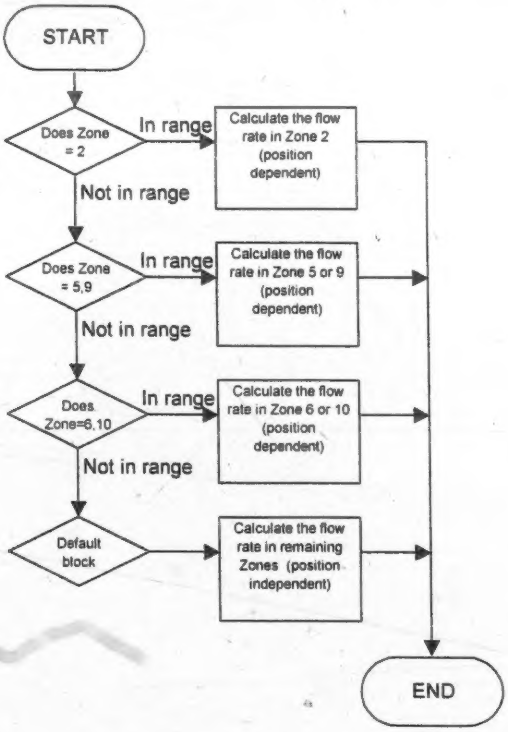
START
Does Zone = 2
In range
Calculate the flow rate in Zone 2 (position dependent)
Not in range
Does Zone = 5,9
In range
Calculate the flow rate in Zone 5 or 9 (position dependent)
Not in range
Does Zone=6,10
In range
Calculate the flow rate in Zone 6 or 10 (position dependent)
Not in range
Default block
Calculate the flow rate in remaining Zones (position independent)
END

## D.7.5 Calculate Zone Velocity

- *Calculates the superficial velocity in each EFM zone as a function of position if necessary.*

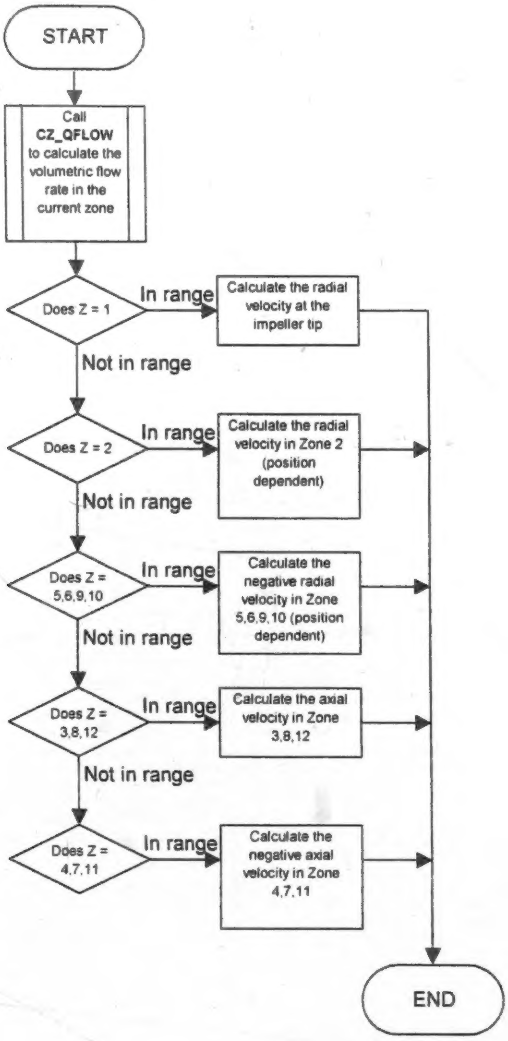
START
Call
CZ_QFLOW
to calculate the volumetric flow rate in the current zone
Does Z = 1
In range
Calculate the radial velocity at the impeller tip
Not in range
Does Z = 2
In range
Calculate the radial velocity in Zone 2 (position dependent)
Not in range
Does Z = 5,6,9,10
In range
Calculate the negative radial velocity in Zone 5,6,9,10 (position dependent)
Not in range
Does Z = 3,8,12
In range
Calculate the axial velocity in Zone 3,8,12
Not in range
Does Z = 4,7,11
In range
Calculate the negative axial velocity in Zone 4,7,11
END

### *D.7.6 Calculate Zone Dissipation*

- *Calculates the rate of turbulent kinetic energy dissipation in each EFM zone as a function of position if necessary.*

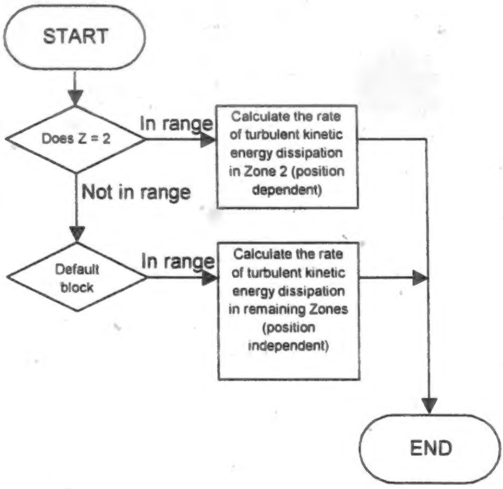
START
Does Z = 2
In range
Calculate the rate of turbulent kinetic energy dissipation in Zone 2 (position dependent)
Not in range
Default block
In range
Calculate the rate of turbulent kinetic energy dissipation in remaining Zones (position independent)
END

### D.7.7 Calculate Zone Turbulent Kinetic Energy

- *Calculates the turbulent kinetic energy in each EFM zone as a function of position if necessary.*

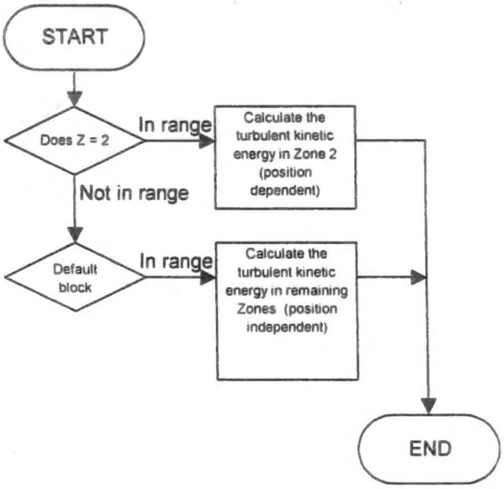
START
Does Z = 2
In range
Calculate the turbulent kinetic energy in Zone 2 (position dependent)
Not in range
Default block
In range
Calculate the turbulent kinetic energy in remaining Zones (position independent)
END

## D.7.8 Calculate DFV Position

- *Calculates the DFV's position after the timestep dt, by performing a numerical integration if necessary.*

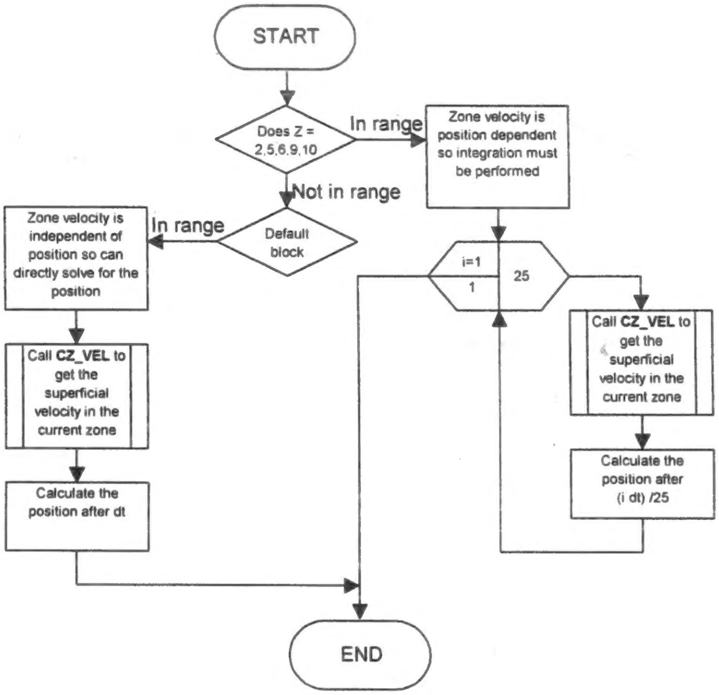
START
Does Z = 2,5,6,9,10
In range
Zone velocity is position dependent so integration must be performed
Not in range
Default block
In range
Zone velocity is independent of position so can directly solve for the position
i=1
1
25
Call **CZ_VEL** to get the superficial velocity in the current zone
Call **CZ_VEL** to get the superficial velocity in the current zone
Calculate the position after (i dt) /25
Calculate the position after dt
END

### D.7.9 Calculate DFV Transit Time

- *Calculates the DFV's transit time to travel the distance dx, by performing a numerical integration if necessary.*

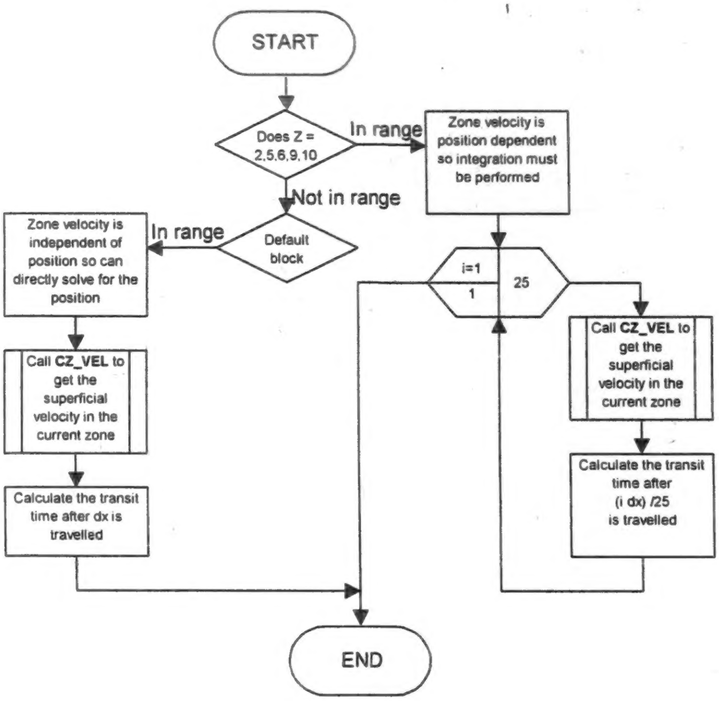
START
Does Z = 2,5,6,9,10
In range
Zone velocity is position dependent so integration must be performed
Not in range
Default block
In range
Zone velocity is independent of position so can directly solve for the position
i=1
1
25
Call **CZ_VEL** to get the superficial velocity in the current zone
Call **CZ_VEL** to get the superficial velocity in the current zone
Calculate the transit time after dx is travelled
Calculate the transit time after (i dx) /25 is travelled
END

## D.7.10 Calculate DFV Feed Zone

- *Determine the feed point of the given stream.*

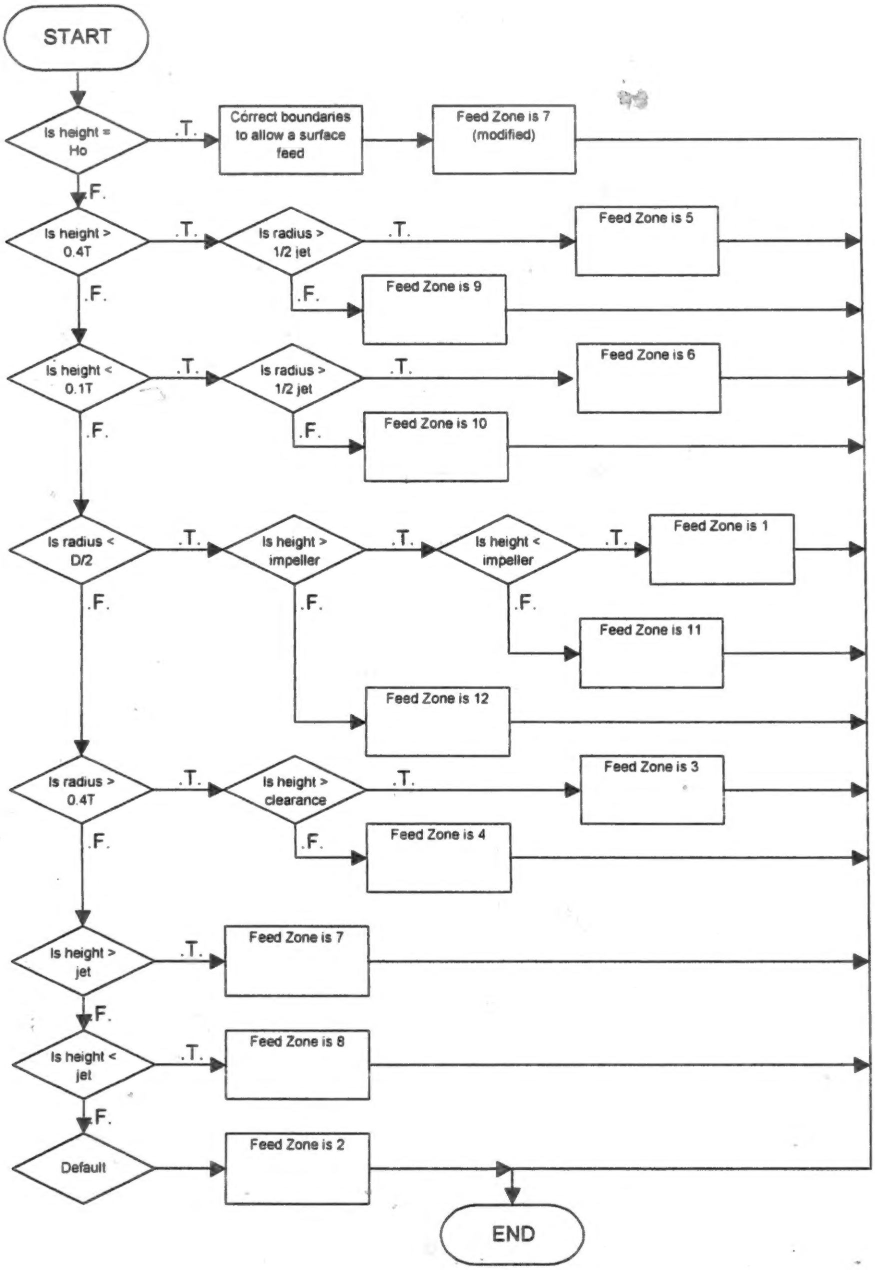
START
Is height = Ho
.T.
Correct boundaries to allow a surface feed
Feed Zone is 7 (modified)
.F.
Is height > 0.4T
.T.
Is radius > 1/2 jet
.T.
Feed Zone is 5
.F.
Feed Zone is 9
.F.
Is height < 0.1T
.T.
Is radius > 1/2 jet
.T.
Feed Zone is 6
.F.
Feed Zone is 10
.F.
Is radius < D/2
.T.
Is height > impeller
.T.
Is height < impeller
.T.
Feed Zone is 1
.F.
Feed Zone is 11
.F.
Feed Zone is 12
.F.
Is radius > 0.4T
.T.
Is height > clearance
.T.
Feed Zone is 3
.F.
Feed Zone is 4
.F.
Is height > jet
.T.
Feed Zone is 7
.F.
Is height < jet
.T.
Feed Zone is 8
.F.
Default
Feed Zone is 2
END

### D.7.11 EFM Update

- *Updates all EFM zone quantities that are affected by feed stream accumulation.*

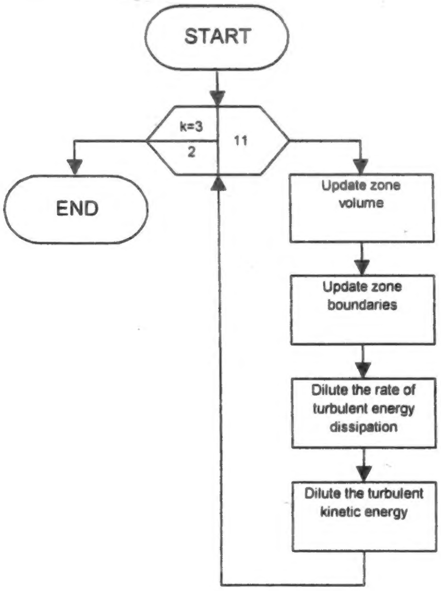
START
k=3
2
11
END
Update zone volume
Update zone boundaries
Dilute the rate of turbulent energy dissipation
Dilute the turbulent kinetic energy

## D.8 Mixing Limit

- *Determines the local mixing conditions for the silver feed stream, and configures the remaining code for the appropriate mixing type.*

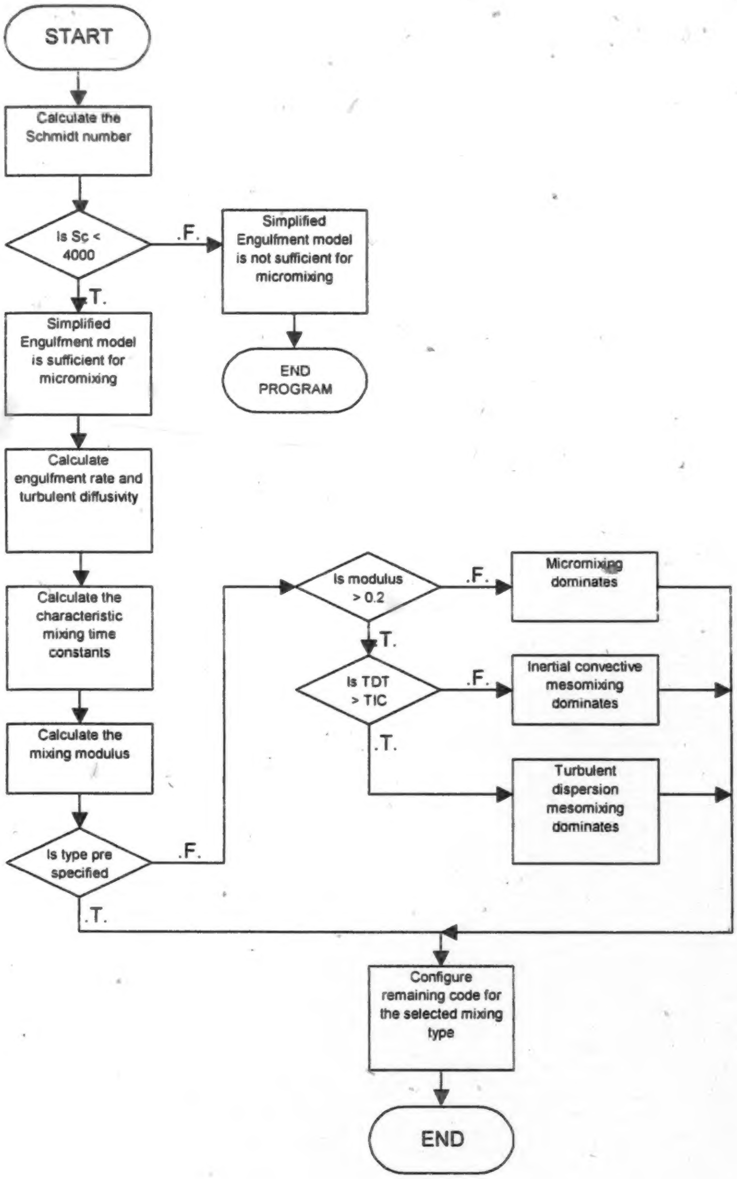
START
Calculate the Schmidt number
Is Sc < 4000
.F.
Simplified Engulfment model is not sufficient for micromixing
END PROGRAM
.T.
Simplified Engulfment model is sufficient for micromixing
Calculate engulfment rate and turbulent diffusivity
Calculate the characteristic mixing time constants
Calculate the mixing modulus
Is type pre specified
.F.
.T.
Is modulus > 0.2
.F.
Micromixing dominates
.T.
Is TDT > TIC
.F.
Inertial convective mesomixing dominates
.T.
Turbulent dispersion mesomixing dominates
Configure remaining code for the selected mixing type
END

## D.9 Write Input

- *Relays all of the user specified data and the initially calculated quantities and configurations to file.*

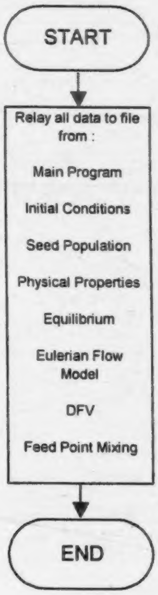
START
Relay all data to file from :
Main Program
Initial Conditions
Seed Population
Physical Properties
Equilibrium
Eulerian Flow Model
DFV
Feed Point Mixing
END

## D.10 Initial Conditions

- *Initializes the kettle's species concentration, equilibrium and crystal population.*

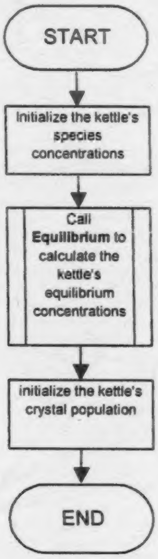
START
Initialize the kettle's species concentrations
Call **Equilibrium** to calculate the kettle's equilibrium concentrations
initialize the kettle's crystal population
END

## D.11 DFV Initial Conditions

- *Assigns the initial conditions to the most currently released DFV.*

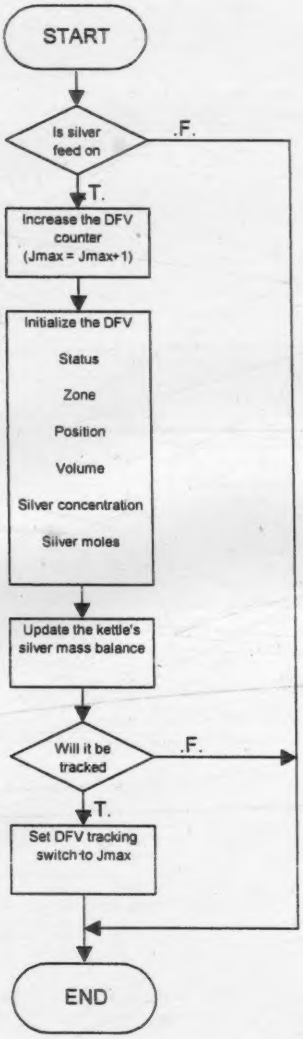
START
Is silver feed on
.F.
.T.
Increase the DFV counter (Jmax = Jmax+1)
Initialize the DFV
Status
Zone
Position
Volume
Silver concentration
Silver moles
Update the kettle's silver mass balance
Will it be tracked
.F.
.T.
Set DFV tracking switch to Jmax
END

## D.12 DFV Trajectory

- *Determines the trajectory of the DFV over the given time step, and if necessary two daughter DFVs are created at the EFM zone boundary.*

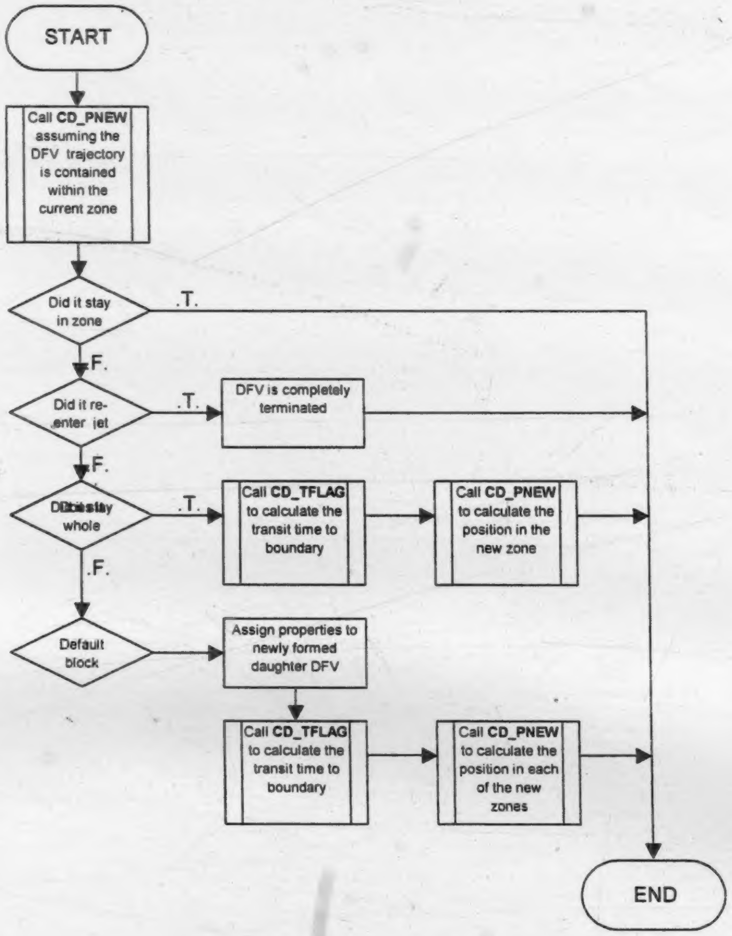
START
Call **CD_PNEW** assuming the DFV trajectory is contained within the current zone
Did it stay in zone
.T.
.F.
Did it re-enter jet
.T.
DFV is completely terminated
.F.
Does it stay whole
.T.
Call **CD_TFLAG** to calculate the transit time to boundary
Call **CD_PNEW** to calculate the position in the new zone
.F.
Default block
Assign properties to newly formed daughter DFV
Call **CD_TFLAG** to calculate the transit time to boundary
Call **CD_PNEW** to calculate the position in each of the new zones
END

## D.13 DFV Integration

### *D.13.1 DFV Loop*

- *Loop to integrate each DFV through the equations for mixing, concentration, ionic strength and nucleation.*

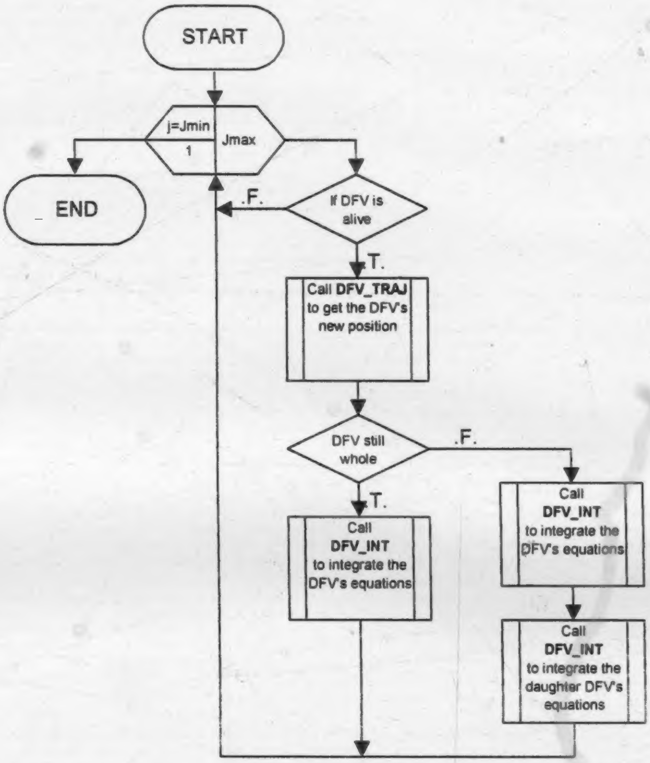

START
j=Jmin
1
Jmax
END
If DFV is alive
.F.
.T.
Call DFV_TRAJ to get the DFV's new position
DFV still whole
.F.
.T.
Call DFV_INT to integrate the DFV's equations
Call DFV_INT to integrate the DFV's equations
Call DFV_INT to integrate the daughter DFV's equations

## D.13.2 DFV Integration

- *Integrate each DFV through the equations for mixing, concentration, ionic strength and nucleation.*

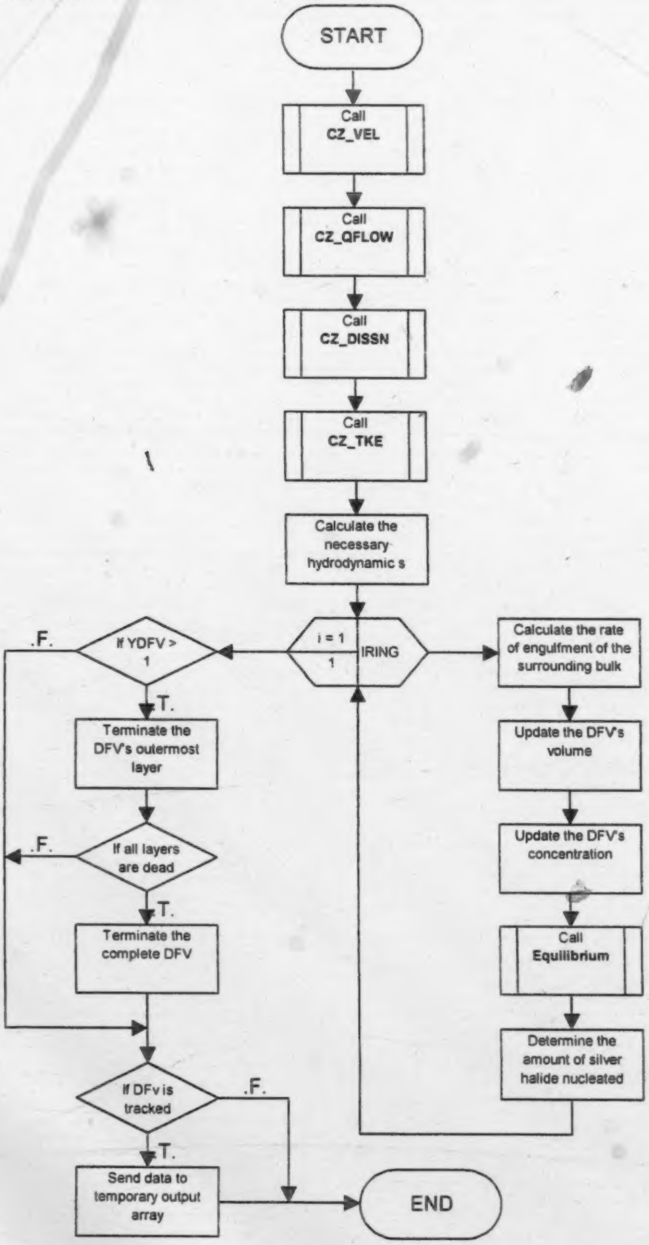
START
Call
CZ_VEL
Call
CZ_QFLOW
Call
CZ_DISSN
Call
CZ_TKE
Calculate the necessary hydrodynamic s
i = 1
1
IRING
Calculate the rate of engulfment of the surrounding bulk
Update the DFV's volume
Update the DFV's concentration
Call
Equilibrium
Determine the amount of silver halide nucleated
.F.
If YDFV > 1
.T.
Terminate the DFV's outermost layer
.F.
If all layers are dead
.T.
Terminate the complete DFV
If DFv is tracked
.F.
.T.
Send data to temporary output array
END

### *D.13.3 DFV Update*

- *Updates the status of a DFV.*

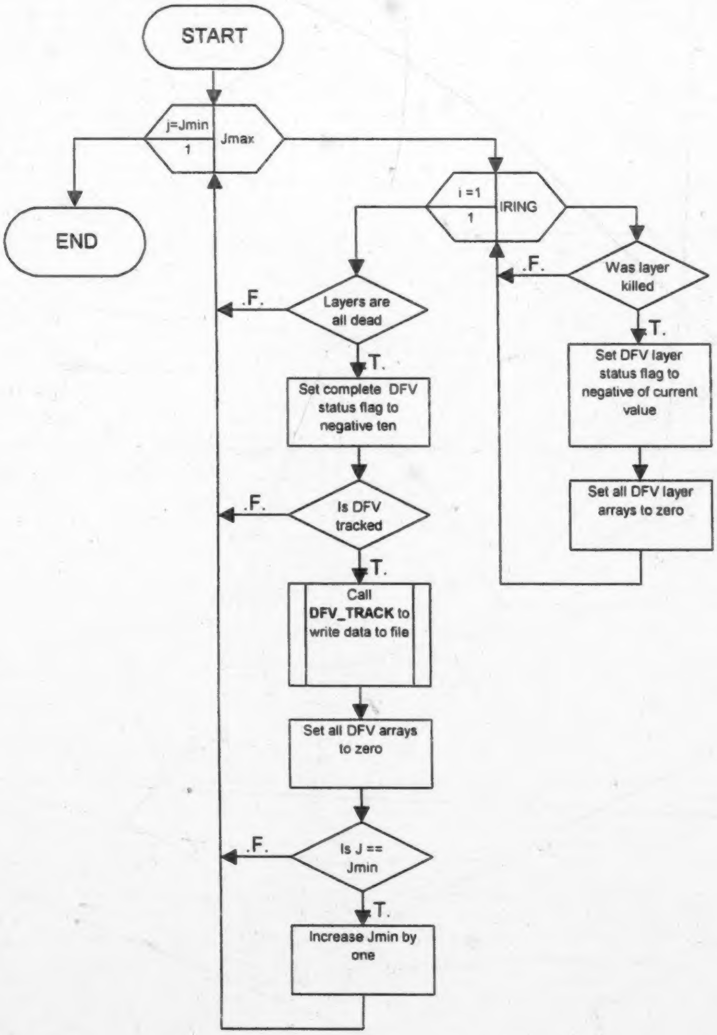
START
j=Jmin
Jmax
1
END
i =1
IRING
1
Was layer killed
.F.
.T.
Set DFV layer status flag to negative of current value
Set all DFV layer arrays to zero
Layers are all dead
.F.
.T.
Set complete DFV status flag to negative ten
Is DFV tracked
.F.
.T.
Call DFV_TRACK to write data to file
Set all DFV arrays to zero
Is J == Jmin
.F.
.T.
Increase Jmin by one

## D. 13.4 DFV Tracking Output

- *Writes the DFV tracking data to the output file.*

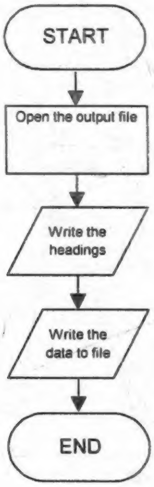
START
Open the output file
Write the headings
Write the data to file
END

# D.14 Kettle Integration

## *D.14.1 Kettle Integration*

- *Updates the kettle's species concentration, ionic strength, nucleation and growth.*

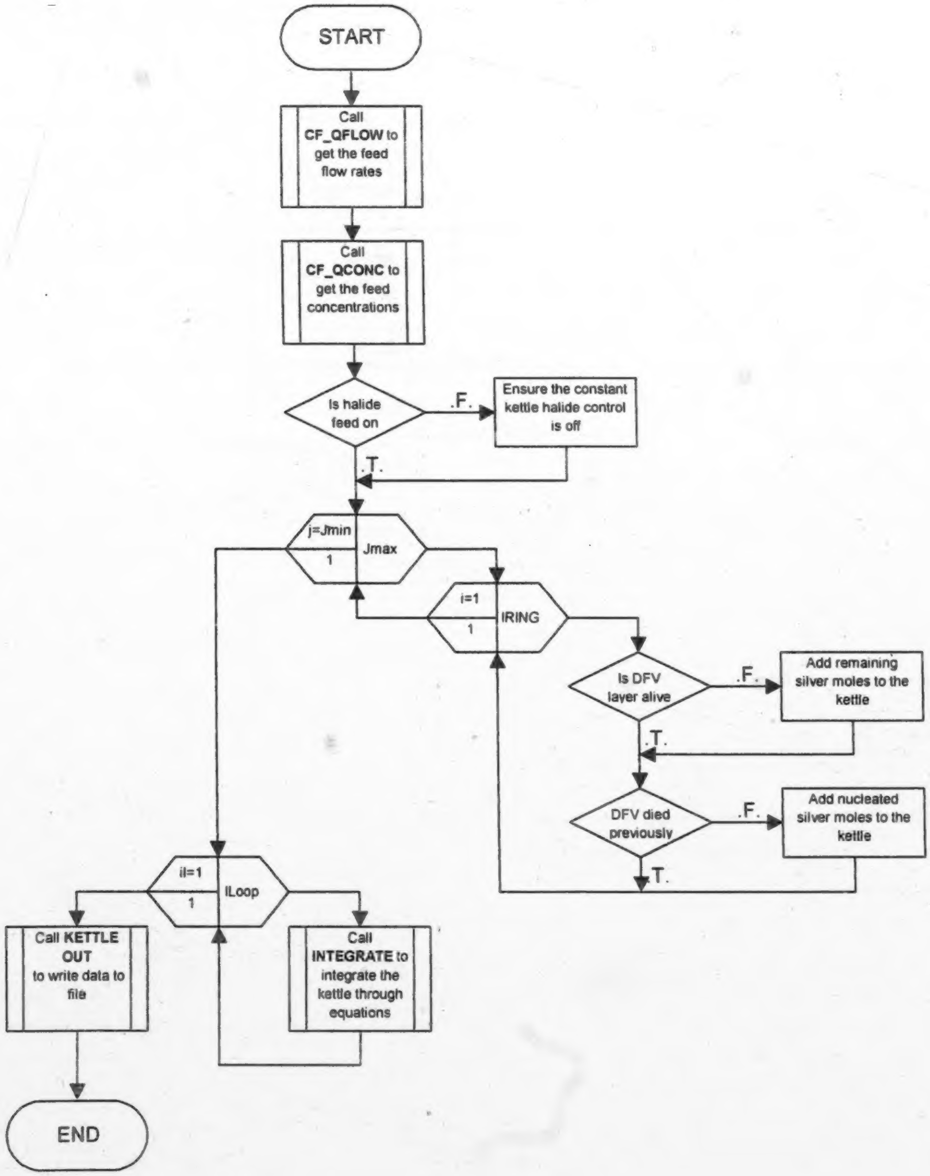
START
Call **CF_QFLOW** to get the feed flow rates
Call **CF_QCONC** to get the feed concentrations
Is halide feed on
.F.
Ensure the constant kettle halide control is off
.T.
j=Jmin
Jmax
1
i=1
IRING
1
Is DFV layer alive
.F.
Add remaining silver moles to the kettle
.T.
DFV died previously
.F.
Add nucleated silver moles to the kettle
.T.
il=1
ILoop
1
Call **KETTLE OUT** to write data to file
Call **INTEGRATE** to integrate the kettle through equations
END

## D.14.2 Kettle Output

- *Writes the kettle's species concentration, ionic strength and nucleation data to file.*

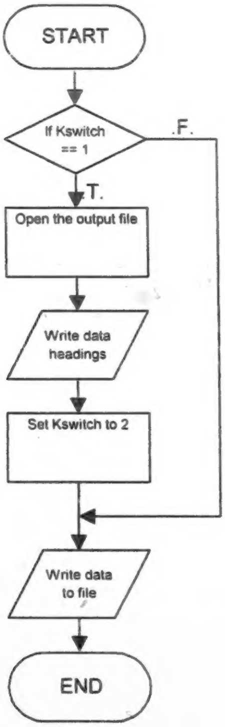
START
If Kswitch == 1
.F.
.T.
Open the output file
Write data headings
Set Kswitch to 2
Write data to file
END

## D.15 Integrator

### D.15.1 Integrate

- *Integrate the kettle through the equations for species concentration, ionic strength, nucleation and growth for the time step, dt.*

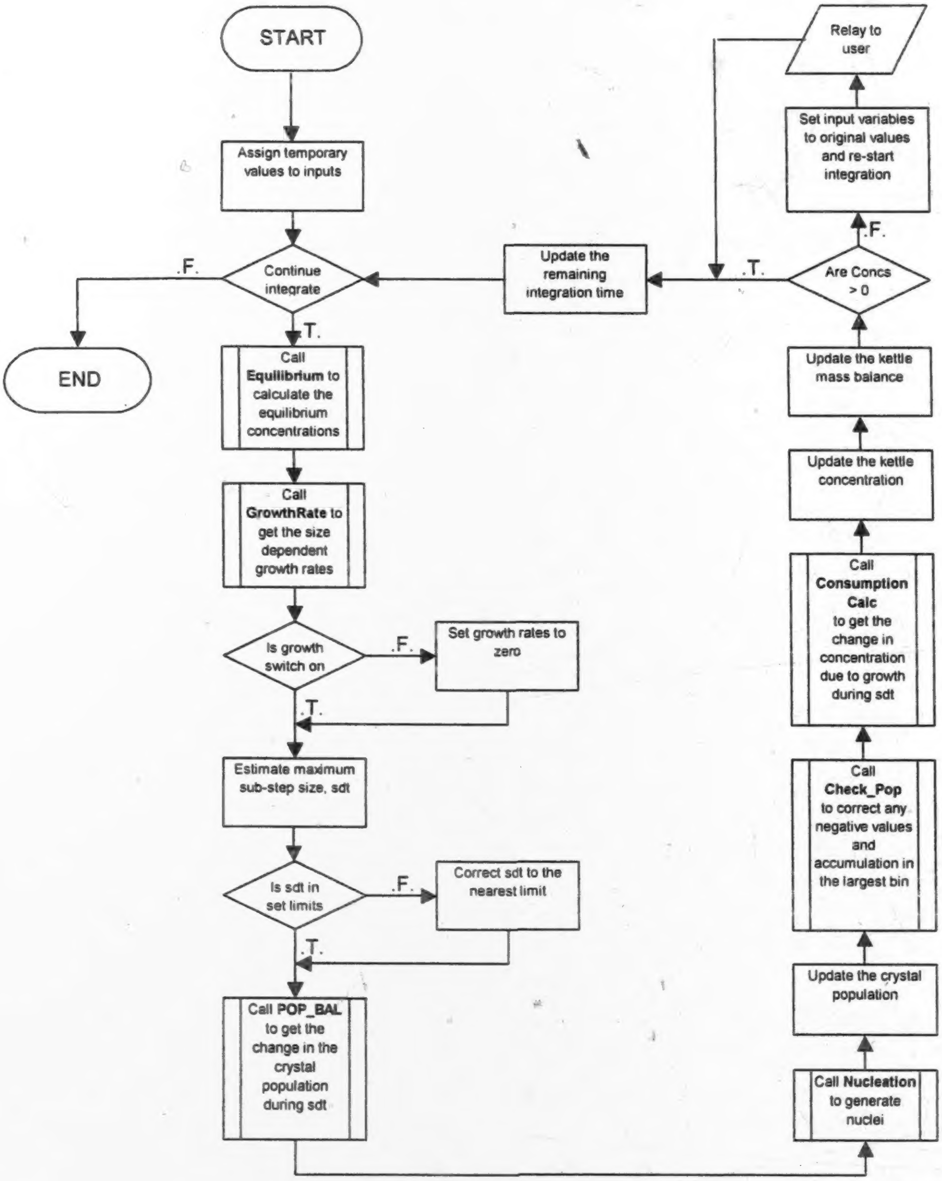
START
Assign temporary values to inputs
Continue integrate
.F.
END
.T.
Call **Equilibrium** to calculate the equilibrium concentrations
Call **GrowthRate** to get the size dependent growth rates
Is growth switch on
.F.
Set growth rates to zero
.T.
Estimate maximum sub-step size, sdt
Is sdt in set limits
.F.
Correct sdt to the nearest limit
.T.
Call **POP_BAL** to get the change in the crystal population during sdt
Call **Nucleation** to generate nuclei
Update the crystal population
Call **Check_Pop** to correct any negative values and accumulation in the largest bin
Call **Consumption Calc** to get the change in concentration due to growth during sdt
Update the kettle concentration
Update the kettle mass balance
Are Concs > 0
.F.
Set input variables to original values and re-start integration
Relay to user
.T.
Update the remaining integration time

## D.15.2 Calculate Nucleation Rate

- *Calculates the number of nuclei created and places them in the nucleation bin, for a given number of silver halide moles.*

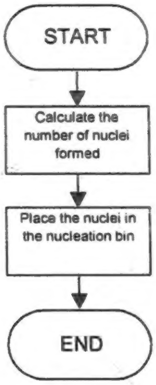
START
Calculate the number of nuclei formed
Place the nuclei in the nucleation bin
END

### *D.15.3 Calculate Growth Rate*

- *Calculates the size-dependent crystal growth rates according to the kinetic data from Wey and Strong (1977).*

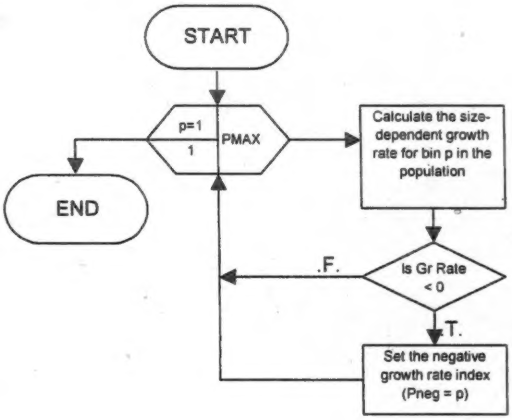
START
p=1
1
PMAX
END
Calculate the size-dependent growth rate for bin p in the population
Is Gr Rate < 0
.F.
.T.
Set the negative growth rate index (Pneg = p)

## *D.15.4 Population Balance*

- *Calculates the change in the population distribution during the time step, sdt (Hounslow, AIChE, pp.106-116, 1990).*

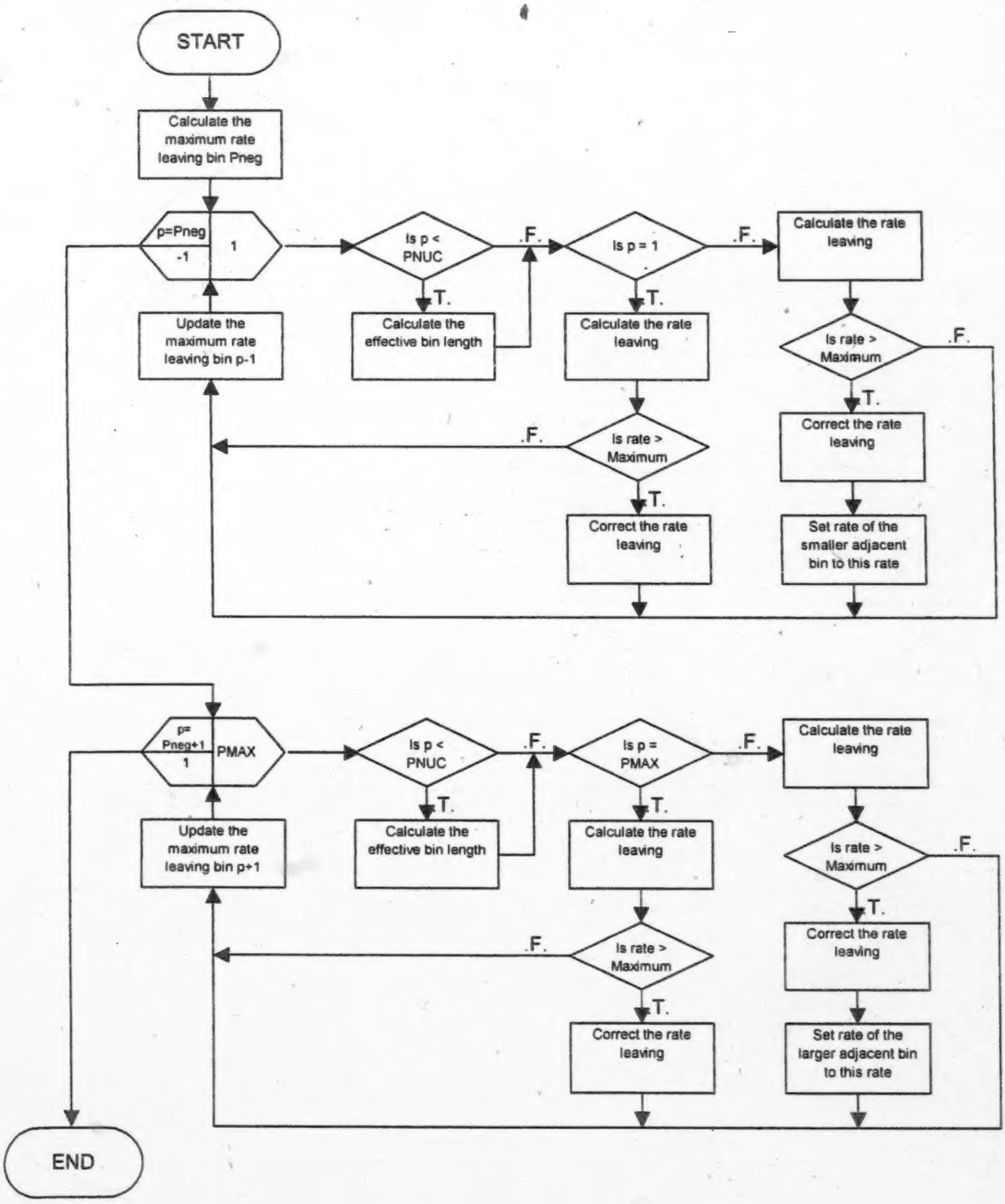
START
Calculate the maximum rate leaving bin Pneg
p=Pneg
-1
1
Is p < PNUC
.F.
Is p = 1
.F.
Calculate the rate leaving
.T.
Calculate the effective bin length
.T.
Calculate the rate leaving
Update the maximum rate leaving bin p-1
Is rate > Maximum
.F.
.T.
Correct the rate leaving
.F.
Is rate > Maximum
.T.
Correct the rate leaving
Set rate of the smaller adjacent bin to this rate
p= Pneg+1
1
PMAX
Is p < PNUC
.F.
Is p = PMAX
.F.
Calculate the rate leaving
.T.
Calculate the effective bin length
.T.
Calculate the rate leaving
Update the maximum rate leaving bin p+1
Is rate > Maximum
.F.
.T.
Correct the rate leaving
.F.
Is rate > Maximum
.T.
Correct the rate leaving
Set rate of the larger adjacent bin to this rate
END

## D.15.5 Check Population Balance

- *Corrects the change in population if negative crystal counts are found and warns the user if accumulation is occurring in the largest bin size.*

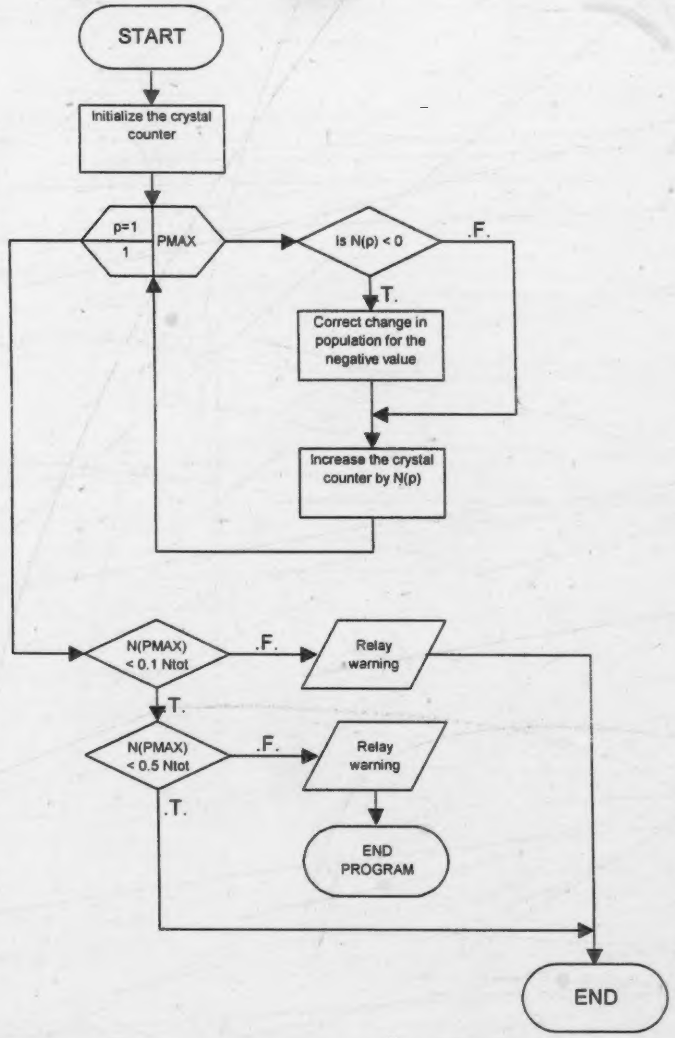
START
Initialize the crystal counter
p=1
1
PMAX
Is N(p) < 0
.F.
.T.
Correct change in population for the negative value
Increase the crystal counter by N(p)
N(PMAX) < 0.1 Ntot
.F.
Relay warning
.T.
N(PMAX) < 0.5 Ntot
.F.
Relay warning
.T.
END PROGRAM
END

### *D.15.6 Calculate Consumption Rate*

- *Calculates the amount of silver halide consumed for the given change in the population.*

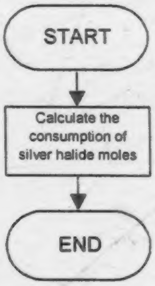
START
Calculate the consumption of silver halide moles
END

## D.16 Write Output

- *Writes the raw crystal size distribution, crystal size distribution descriptive statistics and mass balance data to file.*

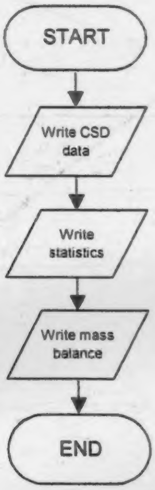
START
Write CSD data
Write statistics
Write mass balance
END

## D.17 Mass Balance

- *Determines the free, nucleated, crystallized and total moles of both silver and halide in the kettle.*

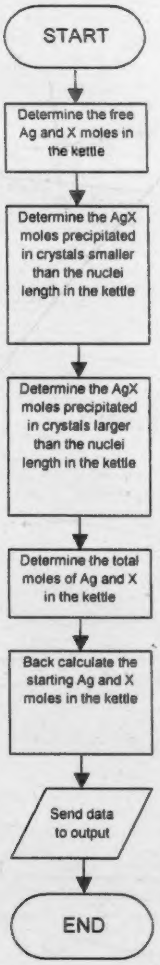
START
Determine the free Ag and X moles in the kettle
Determine the AgX moles precipitated in crystals smaller than the nuclei length in the kettle
Determine the AgX moles precipitated in crystals larger than the nuclei length in the kettle
Determine the total moles of Ag and X in the kettle
Back calculate the starting Ag and X moles in the kettle
Send data to output
END

## D.18 Population Statistics

- *Determines the descriptive statistics for each of the modes in the crystal size distribution.*

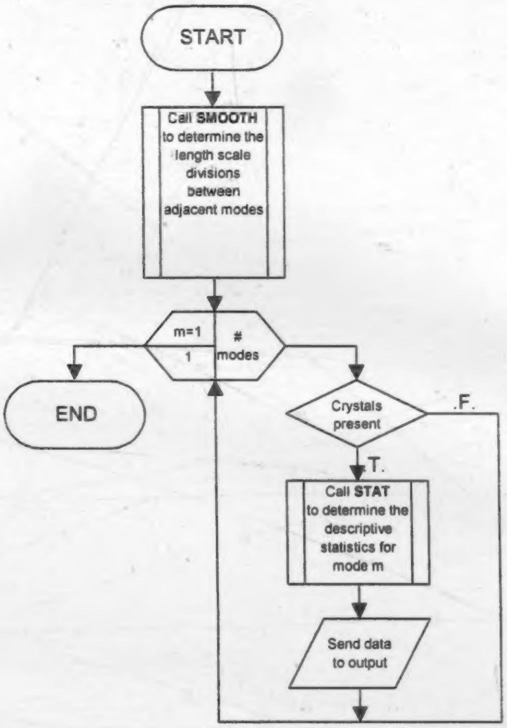
START
Call **SMOOTH** to determine the length scale divisions between adjacent modes
m=1
#
1
modes
END
Crystals present
.F.
.T.
Call **STAT** to determine the descriptive statistics for mode m
Send data to output

## D.19 Array Update

- *Repacks the working DFV arrays after every 1000 DFVs released.*

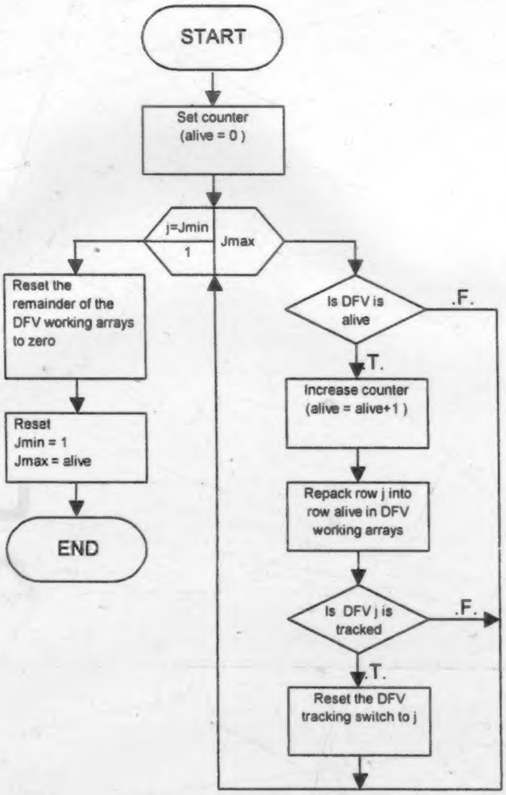
START
Set counter
(alive = 0 )
j=Jmin
1
Jmax
Reset the remainder of the DFV working arrays to zero
Reset
Jmin = 1
Jmax = alive
END
Is DFV is alive
.F.
.T.
Increase counter
(alive = alive+1 )
Repack row j into row alive in DFV working arrays
Is DFV j is tracked
.F.
.T.
Reset the DFV tracking switch to j

## D.20 Statistics

### D.20.1 Statistics Transformations

- *Calculates the arithmetic and geometric means and standard deviations for a given data set, or from the arithmetic or geometric input.*

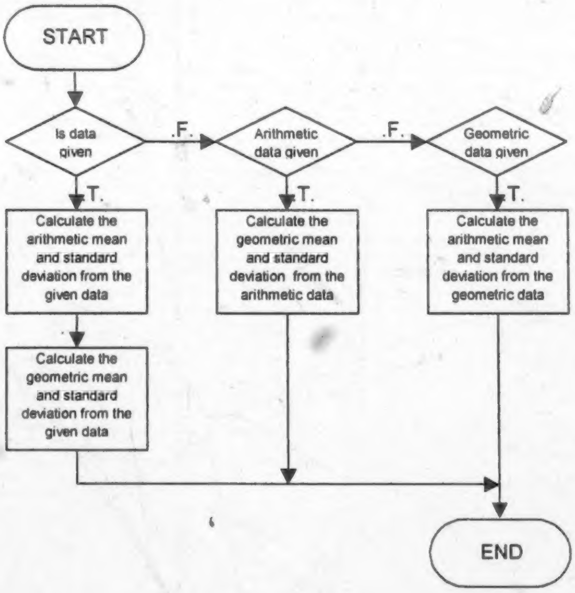
START
Is data given
.F.
Arithmetic data given
.F.
Geometric data given
.T.
.T.
.T.
Calculate the arithmetic mean and standard deviation from the given data
Calculate the geometric mean and standard deviation from the arithmetic data
Calculate the arithmetic mean and standard deviation from the geometric data
Calculate the geometric mean and standard deviation from the given data
END

## D.20.2 Calculate Probability

- *Calculates the probability of the continuous random variable, x, having a value within the interval (a..b), given the probability density function and using numerical integration.*

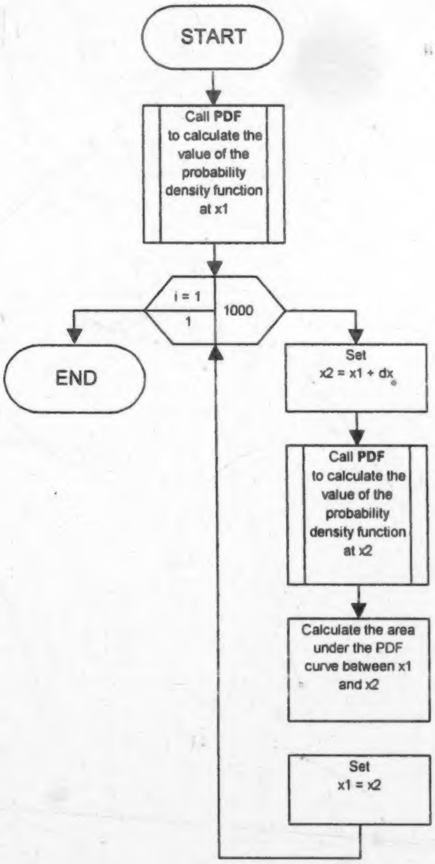
START
Call **PDF** to calculate the value of the probability density function at x1
i = 1
1
1000
END
Set x2 = x1 + dx
Call **PDF** to calculate the value of the probability density function at x2
Calculate the area under the PDF curve between x1 and x2
Set x1 = x2

### D.20.3 Probability Density Function

- *Calculates the specified probability density function at the given point, x.*

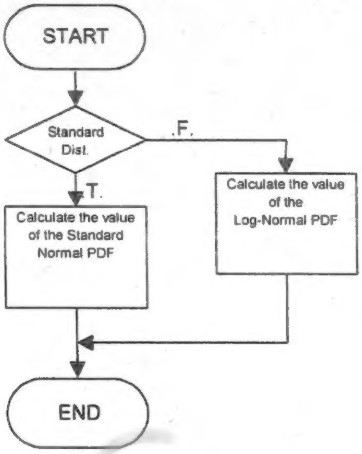
START
Standard Dist.
.F.
.T.
Calculate the value of the Standard Normal PDF
Calculate the value of the Log-Normal PDF
END

## D.20.4 Smooth Function

*First temporarily smoothes the given function, and then determines the divisions between adjacent modes.*

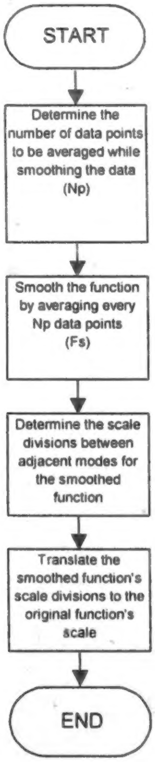
START
Determine the number of data points to be averaged while smoothing the data (Np)
Smooth the function by averaging every Np data points (Fs)
Determine the scale divisions between adjacent modes for the smoothed function
Translate the smoothed function's scale divisions to the original function's scale
END

# Appendix E

## Analytical Solutions for the Population Balance Equation

# Appendix E

## Analytical Solutions for the Population Balance Equation 317

**E.1 Method of Characteristics** 319

*Example 1:* Size-independent crystal growth rate. 321

*Example 2:* Linear size-dependent crystal growth rate. 321

*Example 3:* Inverse size-dependent crystal growth rate. 322

*Example 4:* The empirical ASL size-dependent crystal growth rate (Abegg et al. 1968). 323

*Example 5:* Diffusion controlled size-dependent crystal growth rate. 323

**E.2 Nomenclature** 324

**E.3 References** 325

The complete mathematical description of a crystal size distribution (CSD) undergoing nucleation, growth and agglomeration, for a well-mixed batch system of constant volume, is given by Randolph and Larson (1971) as

$$\frac{\partial n}{\partial t}+\frac{\partial (Gn)}{\partial L}=B_{o}-D_{o} \tag{E.1}$$

Few analytical solutions to Equation ( E.1 ) exist in the literature, and if a solution is given, it is usually under the conditions of steady state and size-independent crystal growth rates (Randolph and Larson 1971). In the following section, a solution method is given for transient conditions with size-dependent growth as determined by the method of characteristics. The method is straightforward provided that the inverse of the growth rate is integratable with respect to length, and the result can be solved for explicitly length.

## E.1 Method of Characteristics

From the method of characteristics, the solution to Equation ( E.1 ) for the conditions of pure growth is

$$f\left(t-\int^{L}\frac{1}{G(L)}dL\right)=f(\phi) \tag{E.2}$$

And this solution is related to the crystal number density function by equal areas, thus

$$n(t,L)dL=f(\phi)d\phi \tag{E.3}$$

Since,

$$\phi=t-\int^{L}\frac{1}{G(L)}dL \tag{E.4}$$

the following can be written,

$$\frac{d\phi}{dL} = -\frac{1}{G(L)} \qquad \text{( E.5 )}$$

so that now,

$$n(t,L) = -\frac{f(\phi)}{G(L)} \quad \text{or} \quad f(\phi) = -n(t,L)G(L) \qquad \text{( E.6 )}$$

Using the initial condition $n(t=0,L) = n_{o}(L)$ gives

$$f(\phi) = -n_{o}(L)G(L) \qquad \text{( E.7 )}$$

and then solving $\phi$ for L, remembering that t = 0, and denoting the result as $L^{\cdot}(\phi)$, gives

$$f(\phi) = -n_{o}(L^{\cdot}(\phi))G(L^{\cdot}(\phi)) \qquad \text{( E.8 )}$$

which gives the final result

$$n(t,L) = n_{o}(L^{\cdot}(\phi))\frac{G(L^{\cdot}(\phi))}{G(L)} \qquad \text{( E.9 )}$$

***Example 1:*** Size-independent crystal growth rate.

$$G = a$$

$$\phi = t - \int^{L} \frac{1}{a} dL = t - \frac{L}{a}$$

$$L^{\cdot}(\phi) = -\phi a$$

For the initial condition of a standard normal distribution with a mean crystal length $\bar{L}$, variance $\sigma^2$, and total crystal count $N_T$, the final solution is

$$n(t,L) = \frac{N_T}{\sigma\sqrt{2\pi}} \exp\left[-\left(\frac{L^{\cdot}(\phi) - \bar{L}}{\sigma\sqrt{2}}\right)^2\right]$$

$$= \frac{N_T}{\sigma\sqrt{2\pi}} \exp\left[-\left(\frac{\phi a + \bar{L}}{\sigma\sqrt{2}}\right)^2\right]$$

***Example 2:*** Linear size-dependent crystal growth rate.

$$G = aL + b$$

$$\phi = t - \int^{L} \frac{1}{aL + b} dL = t - \frac{\ln(aL + b)}{a}$$

$$L^{\cdot}(\phi) = \frac{e^{(-\phi a)} - b}{a}$$

For the initial condition of a standard normal distribution with a mean crystal length $\bar{L}$, variance $\sigma^2$, and total crystal count $N_T$, the final solution is

$$n(t,L)=\frac{N_T}{\sigma\sqrt{2\pi}}\exp\left[-\left(\frac{L^{*}(\phi)-\bar{L}}{\sigma\sqrt{2}}\right)^2\right]\frac{G(L^{*}(\phi))}{G(L)}$$

$$=\frac{N_T}{\sigma\sqrt{2\pi}}\exp\left[-\left(\frac{e^{(-\phi a)}-b-a\bar{L}}{\sigma\sqrt{2}a}\right)^2\right]\frac{e^{(-\phi a)}}{(aL+b)}$$

***Example 3:*** Inverse size-dependent crystal growth rate.

$$G=\frac{a}{L}$$

$$\phi=t-\int^{L}\frac{L}{a}dL=t-\frac{L^2}{2a}$$

$$L^{*}(\phi)=\sqrt{-2\phi a},\quad -\sqrt{-2\phi a}$$

The condition that $L^{*}(\phi)$ must equal L when t = 0 gives

$$L^{*}(\phi)=\sqrt{-2\phi a}$$

For the initial condition of a standard normal distribution with a mean crystal length $\bar{L}$, variance $\sigma^2$, and total crystal count $N_T$, the final solution is

$$n(t,L)=\frac{N_T}{\sigma\sqrt{2\pi}}\exp\left[-\left(\frac{L^{*}(\phi)-\bar{L}}{\sigma\sqrt{2}}\right)^2\right]\frac{G(L^{*}(\phi))}{G(L)}$$

$$=\frac{N_T}{\sigma\sqrt{2\pi}}\exp\left[-\left(\frac{\sqrt{-2\phi a}-\bar{L}}{\sigma\sqrt{2}}\right)^2\right]\frac{L}{\sqrt{-2\phi a}}$$

**Example 4:** The empirical ASL size-dependent crystal growth rate (Abegg et al. 1968).

$$G = G_o(1+\gamma L)^b \qquad b<1$$

$$\phi = t - \int^{L} \frac{1}{(a+bL)^c}\,dL = t - \frac{(1+\gamma L)^{(1-b)}}{G_o\gamma(1-b)}$$

$$L^{*}(\phi) = \frac{\left(\dfrac{1}{\phi G_o \gamma (b-1)}\right)^{\left(\frac{1}{b-1}\right)} - 1}{\gamma}$$

**Example 5:** Diffusion controlled size-dependent crystal growth rate.

$$G = \frac{a}{1+bL}$$

$$\phi = t - \int^{L} \frac{1+bL}{a}\,dL = t - \frac{L + \frac{b}{2}L^2}{a}$$

$$L^{*}(\phi) = \frac{-1+\sqrt{1-2\phi ab}}{b}, \quad \frac{-1-\sqrt{1-2\phi ab}}{b}$$

The condition that $L^{*}(\phi)$ must equal L when t = 0 gives

$$L^{*}(\phi) = \begin{cases} \dfrac{-1+|1+bL|}{b}, & \text{for } b>0 \\ \dfrac{-1-|1+bL|}{b}, & \text{for } b<0 \end{cases}$$

$$L^{*}(\phi) = \frac{-1+\frac{b}{|b|}\sqrt{1-2\phi ab}}{b}$$

## E.2 Nomenclature

| | |
|---|---|
| $B_o$ | nucleation rate, $m^{-3}\,m^{-1}\,s^{-1}$ |
| $D_o$ | crystal death rate, $m^{-3}\,m^{-1}\,s^{-1}$ |
| $G$ | linear crystal growth rate, $m\,s^{-1}$ |
| $L$ | cubic crystal edge length, m |
| $n$ | crystal count per size interval per unit size, $m^{-3}\,m^{-1}$ |
| $n_o$ | initial crystal number density function, $m^{-1}$ |
| $t$ | time, s |

***Greek***

| | |
|---|---|
| $\phi$ | characteristic curve of constant n in the L-t plane |

## E.3 References

Abegg C.F., J.D. Stevens and M.A. Larson, 1968, *Crystal Size Distributions in Continuous Crystallizers When Growth Rate is Size-Dependent*, AIChEJ, **14**, 118-122.

Mullin J.W., 2001, *Crystallization*, 4th ed., Butterworth-Heinemann Ltd., **Oxford**, Great Britain.

Randolph A.D. and M.A. Larson, 1971, *The Theory of Particulate Processes*, Academic Press, New York.